Karlsruher Institut für Technologie

Microwave Control of the Tin-Vacancy Spin Qubit in Diamond with a Superconducting Waveguide

Zur Erlangung des akademischen Grades eines

Doktors der Naturwissenschaften
(Dr. rer. nat.)

von der KIT-Fakultät für Physik des
Karlsruher Instituts für Technologie (KIT)

genehmigte
Dissertation

von

M.Sc. Ioannis Karapatzakis

Tag der mündlichen Prüfung: 16. Mai 2025
1. Referent: Prof. Dr. Wolfgang Wernsdorfer
2. Referent: Prof. Dr. David Hunger

Abstract

For quantum communication and computing to work reliably, qubit systems need to perform at their best. The underlying processes are highly complex, and even tiny errors can cause major disruptions, making the 'quantum' disappear. In recent years, many different qubit platforms have been explored, with color centers playing a major role in enabling scalable quantum networks. Among these, the negatively charged tin-vacancy (SnV) center in diamond has emerged as a promising candidate for optically addressable spin qubits due to its stable optical transitions and long spin coherence times. In this thesis we investigate coherent microwave control of SnV centers within superconducting waveguides, addressing key challenges such as phonon-induced decoherence, strain effects, and microwave induced heating.

We first analyze the fundamental electronic and spin properties of SnV centers, deriving an effective Hamiltonian that accounts for spin-orbit coupling, strain, and Zeeman interactions. With precise experimental measurements of the optically allowed and forbidden transitions in a magnetic field, we determine the quantization axis of the SnV center with unprecedented precision. This allows us to describe the quenched orbital-Zeeman interaction in the spin-orbit doublets of the optical ground and excited states. Since the performance of the SnV center as a qubit relies heavily on the stability of its optical transitions, we outline a rigorous method for identifying suitable emitters, in diamond samples with low surface quality and low yield of stable emitters. Further, we analyze the spin dynamics of the SnV center with regard to spin initialization, readout, and phonon-induced decoherence. We specifically focus on the effects of an externally applied magnetic field to identify the optimal measurement conditions for coherent control. By using the SnV center as a calibrated temperature sensor we characterize the losses of normal and superconducting coplanar waveguides, allowing us to evaluate the role of superconducting coplanar waveguides in mitigating thermal effects and maintaining qubit performance. By leveraging dynamical decoupling techniques, we demonstrate improved coherence times, setting a record for the SnV center platform of $T_2 = 10\,\mathrm{ms}$.

These results contribute to the development of robust spin-photon interfaces and hybrid quantum computing architectures, and demonstrate the potential of SnV centers for quantum networking and distributed quantum computing applications.

Zusammenfassung

Damit Quantenkommunikation und -rechnung zuverlässig funktionieren, müssen Qubitsysteme ihre maximale Leistungsfähigkeit erreichen. Die zugrunde liegenden Prozesse sind äußerst komplex, und selbst kleinste Fehler können erhebliche Störungen verursachen, wodurch das „Quantum“ verschwindet. In den letzten Jahren wurden zahlreiche Qubitplattformen erforscht, wobei Farbzentren eine zentrale Rolle bei der Realisierung skalierbarer Quantennetzwerke spielen. Unter diesen hat sich das negativ geladene Zinn-Fehlstellenzentrum (SnV) in Diamant als vielversprechender Kandidat für optisch adressierbare Spinqubits erwiesen, insbesondere aufgrund seiner stabilen optischen Übergänge und langen Spinkohärenzzeiten. In dieser Arbeit untersuchen wir die kohärente Mikrowellenkontrolle von SnV-Zentren in supraleitenden Wellenleitern und adressieren dabei zentrale Herausforderungen wie phononinduzierte Dekohärenz, Verspannungseffekte und mikrowelleninduzierte Erwärmung.

Zunächst analysieren wir die fundamentalen elektronischen und spindynamischen Eigenschaften der SnV-Zentren und leiten einen effektive Hamiltonoperator her, welcher Spin-Bahn-Kopplung, Verspannung und Zeeman-Wechselwirkungen berücksichtigt. Durch präzise experimentelle Messungen der optisch erlaubten und verbotenen Übergänge im Magnetfeld bestimmen wir die Quantisierungsachse des SnV-Zentrums mit bisher unerreichter Genauigkeit. Dies ermöglicht es uns die unterdrückte orbitale Zeeman-Wechselwirkung in den Spin-Bahn-Dupletts des optischen Grund- und angeregten Zustands zu beschreiben. Da die Leistungsfähigkeit des SnV-Zentrums als Qubit stark von der Stabilität seiner optischen Übergänge abhängt, stellen wir eine rigorose Methode vor, die zur Identifikation geeigneter Emitter in Diamantproben mit schlechter Oberflächenqualität und geringem Ertrag Erfolg verspricht. Darüber hinaus analysieren wir die Spindynamik des SnV-Zentrums im Hinblick auf Spininitialisierung, Auslese und phononinduzierte Dekohärenz. Besonderes Augenmerk legen wir auf die Auswirkungen eines externen Magnetfelds, um die optimalen Messbedingungen für eine kohärente Kontrolle zu identifizieren. Durch die Verwendung des SnV-Zentrums als kalibrierten Temperatursensor charakterisieren wir die Verluste normal- und supraleitender koplanarer Wellenleiter, was uns ermöglicht, den Beitrag supraleitender Wellenleiter zur Minderung thermischer Effekte und zur Erhaltung der Qubitleistung zu untersuchen. Mithilfe von dynamischen Entkopplungstechniken demonstrieren wir verbesserte Kohärenzzeiten und setzen mit $T_2 = 10\,\mathrm{ms}$ einen neuen Rekord für die SnV-Zentrum-Plattform.

Diese Ergebnisse tragen zur Entwicklung robuster Spin-Photonen-Schnittstellen und hybrider Quantencomputerarchitekturen bei und zeigen das Potenzial von SnV-Zentren für Quantennetzwerke und verteiltes Quantencomputing auf.

Acknowledgements

Some months before the outbreak of the COVID pandemic, I started my master's thesis in Wolfgang's group. Back then I was quite sure that I would not follow up with a PhD. But as luck would have it, I decided to join the small optics-subgroup where I was supervised by Marcel. Looking back, I realize it was your great mentoring skills that paved the path towards my PhD. You gave me the freedom to explore the lab and discover the excitement of research, while always making sure I never felt lost. Today, I am very grateful that I chose to pursue a PhD and I hope you continue to successfully apply your great skills at Qinu.

Of course, I want to thank Wolfgang for offering me a position in his group. I think it's great that you trust your students so much and allow them to develop throughout the years. Your work ethic is truly inspiring, and your knowledge, especially your expertise in cryogenics, has enabled the group to form successful subgroups across so many fields. For me, it was the occasional motivational boosts, often in the form of unsettling questions, that allowed me to realize my potential.

During a diamond platform meeting at our institute, 18 months into my PhD, I presented some of my results on superconducting waveguides. It was a key moment for me, as I realized that my work was of interest to people outside of my group. I specifically remember David's kind words. Over the past few years, you have been an incredible support. Seeing you get excited whenever we shared our newest results was a huge motivational boost. I really benefited from the knowledge and expertise you shared with me, especially as you filled in all the blanks on the optics side of the experiment. The combined input from the joint supervision of Wolfgang and David was unique and it's what allowed me to benefit throughout the years.

A couple of months after the diamond meeting, David sent Jeremias to me to take a look at a diamond sample in one of our cryostats. At first, it just looked like another one of the many shabby samples that come along in a PhD's lifetime, but after some magic treatment, it turned out to be *the* sample of my PhD. Jeremias and I ended up working together for the next two years, and I truly mean it when I say that it's been the greatest time working with you. I don't think there's anyone else who could put up with my constant nagging and turn it into such a successful and fun work experience like you do.

A major part of a PhD is, of course, drinking mate and coffee with your colleagues, and I have to say, the work environment and atmosphere in this group have been amazing. So thank you to all the great people: Christoph, Dennis, Luca, Simon, Kerim, Evgenij, Safa, Sagar, Daniel, Janick, Tino, Tim, Sophie, Appu, Tajamul, Amer, Julian, the other Julian, Sonja, Svenja, Markus, Aljoscha, Peter and anyone I may have forgotten.

Of course, I'm also very grateful for the many long and often random conversations with my office friends: Thomas, Luis, Viktor, Babydaniel, Baby-Chris and Csongor. From deep philosophical debates to the most absurd topics, you made the office a place where work felt a lot less like work. Thanks for all the laughs, the support, and the much needed distraction.

During my time as a student I have moved five times in total. In the end, I ended up with a great roommate, Alex. It is a pleasure to live with you and I'm always happy when I come home and there's something great to eat.

Playing Doppelkopf was a big part of my time as a student, and the weekly cooking and get-togethers with my friends have been an incredible source of support over the past few years. So thank you Lina, Isi, Felix and Tobi.

I'd say the greatest support came from my friends Tobi and Zorni, whom I've known since school. Our almost daily TeamSpeak sessions with Felix, Marvin, and Jannik have been an absolute blast and often the most exciting part of the day. Together, we've had the most decadent vacations, from visiting Greece almost every year to unforgettable skiing trips. I've had such a great time hanging out with you! Tobi is also making the best coffee in town, so if you ever get the chance to meet him, you should definitely pay him a visit. And if you're lucky, you might even get to taste one of the amazing breads baked by Theresa.

Finally, I want to express my gratitude to my family. As the youngest of five, I've had the privilege of growing up in a home filled with support, love, and encouragement. All of my siblings have helped me throughout the years and have always been excited to spend time with me, so thank you for everything you've done. I also want to specifically thank my parents, who have supported me unconditionally and have always been enthusiastic about my decision to pursue a PhD. So thank you, Mom and Dad.

List of Publications

Parts of Chapter 2 and Chapter 4 are extended work of the following publications:

[1] **I. Karapatzakis**†, J. Resch†, M. Schrodin, P. Fuchs, M. Kieschnick, J. Heupel, L. Kussi, C. Sürgers, C. Popov, J. Meijer, C. Becher, W. Wernsdorfer, and D. Hunger, "Microwave control of the tin-vacancy spin qubit in diamond with a superconducting waveguide", Phys. Rev. X **14**, 031036 (2024).

[2] **I. Karapatzakis**, D. Hunger, "Supraleitende Mikrowellenkontrolle von Zinn-Fehlstellen", Physik in unserer Zeit **56**, 6–7 (2025).

Authors marked with † have contributed equally. Chapter 3 is based on unpublished work. The following publications are in preparation:

1. J. Resch†, **I. Karapatzakis**†, M. Schrodin, P. Fuchs, M. Kieschnick, J. Heupel, L. Kussi, C. Sürgers, C. Popov, J. Meijer, C. Becher, W. Wernsdorfer, and D. Hunger, "Coherent Control of a Carbon-13 spin near a Tin-Vacancy Center in Diamond".
2. **I. Karapatzakis**, J. Resch, D. Hunger, and W. Wernsdorfer, "Ohmic Heating in Normal and Superconducting Waveguides".

Contents

List of Figures

List of Tables

Part I.

Overview and Main Results

1. Introduction and Motivation

The evolution of color centers in quantum science reads like a quiet reminder from nature that sometimes, flaws are a beautiful feature. In the early 20th century, researchers observed a peculiar phenomenon: glass developed distinct hues when exposed to radioactive or X-radiation [3–5]. This was the beginning of the study of F-centers [6], eventually leading to some of the most exciting advancements in quantum science. The term *F-center*, originates from the German word *Farbzentrum* meaning *color center*.

At first glance, these color centers appear as nothing more, than tiny defects where electrons are trapped at vacant lattice sites within an ionic crystal [7]. Yet these 'flaws' revealed an atomic-like behavior, almost as if nature had locked single atoms inside the crystal's framework. In a twist of irony, the gemstone industry's pursuit of more vivid colors fueled research into a new direction: color centers in diamond. Scientists seized the opportunity and systematically studied radiation damage in diamond [8], that eventually led to one of the most intriguing discoveries: the nitrogen-vacancy (NV) center [9, 10], a defect consisting of a substitutional nitrogen atom adjacent to a carbon-atom vacancy. The NV center marked a major turning point for quantum technologies, as researchers began to unravel the electronic structure and dynamics of this defect [11, 12].

By the 1990s, researchers had reached an exciting milestone: they isolated single NV centers and characterized them with optical microscopy [13]. Soon, its potential for quantum computing was recognized [14], and scientists demonstrated its capability as a room-temperature quantum bit (qubit). The first landmark experiments in the 2000s, demonstrated coherent control of single NV center spins and entanglement with nearby nuclear spins[15, 16]. These achievements established a foundation for using color centers as spin qubits in quantum information, sparking further excitement about their potential [17].

However, the very features that made the NV center rise as a quantum technology also led to limit its performance. The strong sensitivity to nearby spins, impurities and electromagnetic noise [18] make it difficult to achieve stable and narrow optical lines, an important requirement for scalability in the complex world of quantum optics technologies.

Since the random changes in its local electrostatic environment disturb the optical transition frequency, the question was whether there is a way around this problem. Consequently, throughout the 2000s and 2010s, researchers broadened their scope and explored other color centers in diamond with their attention gradually shifting to group-IV color centers around 2010-2015 [19, 20]. In these defects a group-IV element (silicon, germanium, tin, or lead) substitutes for two carbon atoms in a split-vacancy configuration within the diamond

lattice. The inversion-symmetric configuration of these defects causes electric field shifts to largely cancel out, leading to much more stable transition frequencies [19, 21]. For this very reason, the negatively charged silicon-vacancy (SiV^-) center literally emerged as a bright star and alternative to NV centers due to its exceptionally stable optical emission.

In 2014, experiments showed that SiV centers could generate coherent single photons with nearly identical spectra, even when the photons originated from separate emitters [22, 23]. The discovery hinted at the possible "impact on the application of single-photon sources for quantum optics and cryptography"[22].

Over the last decade, there have been further advancements in the quantum networking and quantum computing frontier, for both, the NV center and the SiV center in diamond.

State-of-the-art demonstrations for **NV centers** show

- remote entanglement of two qubits over a spatial separation of three meters [24],
- loophole-free Bell test over a distance of 1.3 km [25],
- entanglement distillation of distant electron-nuclear two-qubit nodes [26],
- deterministic delivery of remote entanglement [27],
- and a three-node quantum network built on NV centers [28].

For **SiV centers** key demonstrations are:

- memory-enhanced quantum communication [29],
- a two-qubit quantum network node with integrated error detection [30],
- and a two-node quantum network each composed of a SiV^- electron spin and a strongly coupled nuclear spin [31].

Unfortunately, the SiV center struggles with its own set of challenges: it demands ultra-low temperatures in the mK-regime to function reliably [32]. This limitation stems from the electronic structure of group-IV defects [33], where their symmetry grants them an extra degree of freedom: a second orbital branch [34]. The separation between these branches dictates the phonon coupling, and thus the temperature at which these defects can be efficiently operated [35].

This is where the real opportunity lies: by engineering the orbital branch separation [36], tuning the qubit-phonon coupling [37], or leveraging defects with naturally larger splittings [38], we can push beyond the SiV center's constraints. And that's precisely where heavier group-IV centers shine. Germanium-, tin-, or lead- vacancy centers stand out by nature, with greater orbital separation and enhanced spin-orbit coupling, drastically reducing phonon-induced decoherence and expanding their operational temperature range.

Now, lets leave history behind us and dive deeper into the remarkable properties that make group-IV defects a driving force in the future of quantum technologies.

1.1. Distributed Quantum Computing with Color Centers

Have we ever truly questioned our own drive to explore exotic quantum systems like color centers? Beyond the academic fascination, what do these defects in diamond have to offer — practically, technologically, even socially? Are they just a curiosity, or could they be the key to something revolutionary?

We want to motivate our research with one particularly promising application: distributed quantum computing, where color centers play a crucial role in enabling scalable quantum networks. In the following, we will explore the fundamental principles behind this concept, the role of color centers and why it could shape the future of computation. For interested readers, we refer to [39] for a summary on this topic and for more elaborate surveys detailing algorithms, networking, compiling and simulation to [40], as well as for a technical overview to [41]. For a summary on quantum networks based on color centers in diamond, we suggest [42].

1.1.1. The Vision of Distributed Quantum Computing

Quantum computing is believed to offer a benefit over classical computing in certain tasks by taking advantage of quantum mechanical properties like superposition and entanglement [43]. Through the smart design of quantum operations and algorithms, it enables the potential for exponential speedups in various fields, including machine learning, chemistry, optimization and secure communication [44].

However, in the currently available quantum devices[1], many application require thousands of qubits and simply scaling a monolithic (one single) device is not an effective solution, as maintaining quantum coherence gets exponentially harder due to environmental noise and excessive coupling complexity [46]. [2] These factors make it extremely difficult to build large scale quantum computers on a single chip.

This led to the idea, of building a modular quantum computer, consisting of many smaller processors that are connected within a quantum network just like classical computer clusters. This architecture is referred to as Distributed Quantum Computing (DQC), allowing to increase the computational power of the system through networking, rather than brute-force increasing the number of qubits on one chip. As an example, IBM is "developing ways to link processors together into a modular system capable of scaling without physics limitations", and for 2025, plans to "introduce the 1,386-qubit multi-chip processor, *Kookaburra*. With its communication link support for quantum parallelization, three *Kookaburra* chips can connect into a 4,158-qubit system." [47]

[1] We are currently in a state that is referred to as the noisy intermediate-scale quantum (NISQ) era characterized by qubits, that are noisy and suffer from loss of information [45]

[2] In addition, engineering constrains arise, such as extensive control wiring and increased heat load in cryogenic setups.

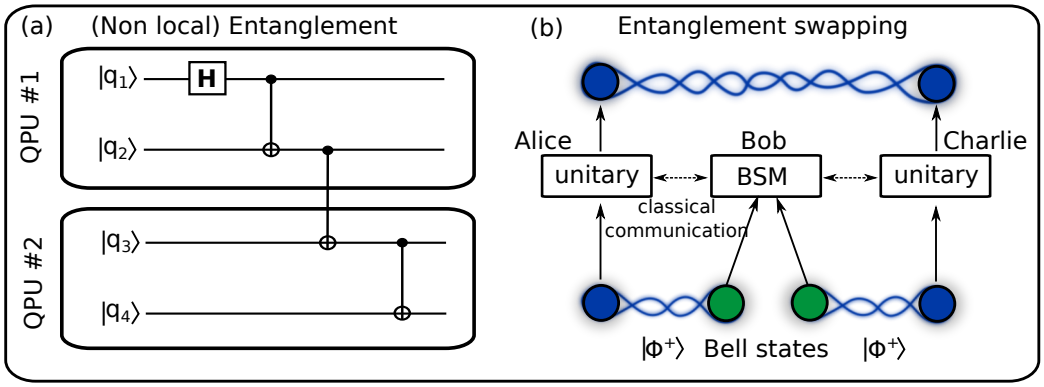

Figure 1.1.: Quantum circuit model and entanglement swapping. (a) depicts a quantum circuit acting on two QPUs. The circuit describes the single qubit H-gate to $|q_1\rangle$ and three two-qubit $CNOT$-gates successively applied from $|q_1\rangle$ to $|q_2\rangle$, from $|q_2\rangle$ to $|q_3\rangle$ and last from $|q_3\rangle$ to $|q_4\rangle$. All qubits are entangled after the gates are processed. The second $CNOT$-gate is non-local between the two separate QPUs. (b) shows the process of entanglement swapping between distant users. Bob possesses two flying qubits (green dots), each entangled separately, one with Alice and one with Charlie. Acting as a relay, Bob performs Bell measurements and communicates the outcomes to Alice and Charlie via a classical channel. Based on this information, they apply the appropriate quantum gates to their qubits. Consequently, Alice and Charlie establish an entangled state, contingent on Bob's measurement results. Figure (a) is inspired by [40] and (b) by [41].

But how exactly should we imagine such a cluster of different quantum processors, and what conditions must it fulfill? In 2000 David DiVincenzo proposed the famous criteria that have to be satisfied for a quantum computer to work, but besides the commonly known first five, he included two additional criteria necessary for quantum communication [48]. The criteria state, that a competitive quantum computer must have:

1. A scalable physical system with well characterized qubits;
2. The ability to initialize the qubit states to a simple state, i.e., $|0000...\rangle$;
3. Long relevant decoherence times, much longer than the gate operation time;
4. A "universal" set of quantum gates;
5. A qubit-specific measurement capability;
6. The ability to interconnect stationary and flying qubits;
7. The ability to properly transmit flying qubits from one location to another.

The ability to interconnect stationary and flying qubits means to transfer quantum information between two types of qubits: stationary qubits, that store and process data within a quantum processor (QPU) and flying qubits, that carry quantum information over distances, usually using photons.

Currently, there is no single platform of stationary qubits, that excels in all criteria: Superconducting [49, 50] are currently leading the race in terms of scalability, and error correction progress, semiconducting qubits [51–53] offer promising prospect due to fully industrial processing [54], but both lack efficient native interfaces for quantum networking.

Trapped ions [55, 56] lead in gate fidelity, but scaling the amount of qubits to large numbers is challenging. Neutral atoms in optical tweezers [57] are great in scalability, but lack behind in gate-fidelity. Color centers in solid state lack in scalability, but stand out in quantum networking with several state of the art demonstrations, due to their natural photonic interface [28, 31]. The point is that it is difficult to meet all the criteria within a single processor, but distributing the computational task across (distant) devices, might just do the trick.

Quantum gates and processes across multiple processors can be tricky to describe for larger systems. That's why we first focus on explaining quantum gates on a single device for which we partly follow the description in [40]. Quantum logic gates are the basic circuit operations on a qubit and are described by unitary matrices relative to some basis, meaning, a quantum operation is always reversible. The unitary operations (U) describe rotations and the most relevant single-qubit operation is the Hadamard-gate (H). It transform the basis state vectors to a superposition state with equal amplitudes:

$$H|0\rangle = \frac{|0\rangle + |1\rangle}{\sqrt{2}} \quad \text{and} \quad H|1\rangle = \frac{|0\rangle - |1\rangle}{\sqrt{2}} \tag{1.1}$$

For a multi qubit system, we can describe the total state as a tensor product of the individual quantum states, e.g. for a two-qubit system, we can write $|a\rangle \otimes |b\rangle = |ab\rangle$. Now lets assume that we have a two-qubit system consisting of a *control qubit* ($|\varphi_c\rangle$) that determines whether an operation should happen to a *target qubit* ($|\varphi_t\rangle$), if some condition is fulfilled. A quantum gate following this idea is the controlled not gate (CNOT), and the operation is described by the following condition:

$$\begin{cases} I|\varphi_t\rangle, & \text{if } |\varphi_c\rangle = |0\rangle \\ X|\varphi_t\rangle, & \text{if } |\varphi_c\rangle = |1\rangle . \end{cases} \tag{1.2}$$

with I denoting the identity operation (where nothing happens) and X the Pauli X-gate that rotates the state around the x-axis by π (flipping the state). The combination of the H- and $CNOT$-gates is the key to entanglement. It allows us to create a state that cannot be described as a simple product of individual qubit states. For example, if we start with two qubits in the state $|00\rangle$ and apply a H-gate to the first qubit, it will transform into a superposition state. If we follow with a $CNOT$-gate, with the first qubit as control qubit, we obtain

$$\frac{|00\rangle + |10\rangle}{\sqrt{2}} \xrightarrow{CNOT} \frac{|00\rangle + |11\rangle}{\sqrt{2}} = |\Phi^+\rangle . \tag{1.3}$$

The resulting state is the Bell state $|\Phi^+\rangle$ and the two qubits are now entangled. [3] We can generalize this process to entangle multiple qubits by iteratively applying $CNOT$-gates to the remaining qubits. For instance, in the case of three qubits, after entangling the first two, the second qubit would serve as the control while the third qubit acts as the target for the next $CNOT$-gate.

[3] The collection of all four Bell states are $\{|\Phi^+\rangle, |\Phi^-\rangle, |\Psi^+\rangle, |\Psi^-\rangle\}$ and are given by applying the described operations on the two qubit states $\{|00\rangle, |10\rangle, |01\rangle |11\rangle\}$

To visualize multiple quantum gates and describe different quantum circuit operations in a simply manner, we can use the widely adopted quantum circuit model [58], where quantum operators are represented as quantum gates. An example of this is shown in Figure 1.1 (a), which illustrates a quantum circuit. The circuit includes a single-qubit H-gate applied to $|q_1\rangle$ and three two-qubit $CNOT$-gates represented by a line connecting a dot and a circled cross, one of which is non-local, between two separate QPUs.

We now aim to explain, how such a non-local operation is conducted. In order to communicate between several QPUs, within the same or over different nodes, an interface is required for entanglement distribution. This interface is provided by the so-called flying qubits, which act as carriers for transmitting quantum information between different devices. These qubits must be highly mobile and efficiently coupled to the respective quantum platform [41]. Several proposed implementations include short distance electronic states in semiconductor devices [59], cold microwave links for superconducting devices [60] and single photons for ion traps, neutral atoms and color centers [42].

For evident reasons, photons are the optimal carriers of quantum information over long distances. They interact weakly with the environment and can travel at the speed of light without decohering. The biggest limitation is given by the loss in the optical fibers over many kilometers distance.[4] Photons also provide multiple degrees of freedom for encoding quantum information. For instance, qubit states can be represented using polarization or the spin degree of freedom. Additionally, standard telecom fiber technology can transmit these qubits with minimal loss.

1.1.2. Entanglement Swapping

One important entanglement-based communication protocols is entanglement swapping via Bell-state measurements (BSM). [5] An example is depicted in Figure 1.1 (b). Alice and Charlie send a flying qubit (green dot), entangled with a material qubit in their node (blue dot), to Bob. Bob performs a BSM that un-entangles the two qubits. [6] As Alice's and Charlie's qubits collapse into an unpredictable entangled state, Bob informs them of the BSM outcome through the classical channel. By applying a unitary correction to their qubits Alice and Charlie now share an known entangled state, making further quantum operations reliable.

[4] State of the art experiments use bidirectional quantum frequency conversion (QFC), to convert the photons from visible light into telecom wavelength (O-band), where attenuation is much lower ($< 0.3\,\mathrm{dB\,m^{-1}}$ in a conventional telecom single-mode fiber [31]).

[5] A second protocol is quantum teleportation, where an unknown quantum state is transferred from one node to another, without physically sending the state itself [61].

[6] In general, Bob performs a BSM by simply applying a $CNOT$-gate with one of his qubits as the control and the other as the target. Following a H-gate on the control qubit a measurement in the basis states of the qubit is performed. Specifically for photonic entanglement swapping, we refer to the proposal of [62] and the experimental demonstration in [24].

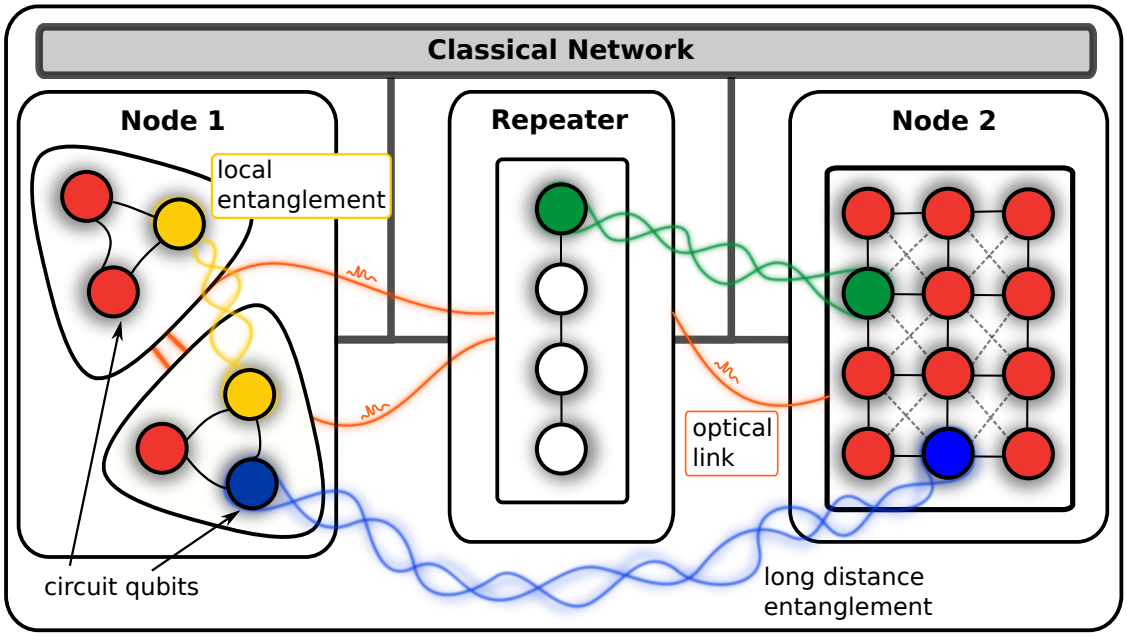

Figure 1.2.: Schematic representation of a DQC architecture. The system consists of two nodes. At the center, a quantum repeater facilitates the connection between Node 1 and a Node 2. Both nodes do not necessarily have to be of the same quantum hardware. A classical network enables communication between the different modules.

Finally, we present a schematic representation of a DQC architecture in Figure 1.2. A classical network enables communication between different modules and nodes by transmitting measurement outcomes and control signals. This allows for the coordination of quantum operations and implementation of entanglement-based tasks such as quantum teleportation and entanglement swapping. The system consists of two nodes. Node 1 includes two QPUs, which could, for example, be two interconnected color center systems linked via an optical cavity. At the center, a quantum repeater facilitates the connection between Node 1 and a second node, which does not necessarily have to be composed of the same quantum hardware. For instance, Node 2 could consist of trapped ions. Intra-chip connectivity for the second node is exemplified by the solid and dashed lines connecting different qubits. Solid lines represent strong connections, typically observed between nearest neighbors, while dashed lines indicate weaker connections to more distant qubit pairs. The limitations in connectivity arise due to factors such as overall noise effects and physical space constraints resulting in a reduction in coupling strength. [40].

Given that no single platform is perfect, a practical approach to Distributed Quantum Computing may involve such a hybrid architecture. By combining different quantum systems, each leveraging its unique advantages in terms of scalability, coherence times, and gate fidelities, performance for specific computational tasks can be optimized. Hybrid architectures facilitate fault tolerance by simply distributing workloads across the specialized platforms. As a consequence, the future of quantum computing is expected to be modular, with quantum nodes interconnected through quantum and classical channels.

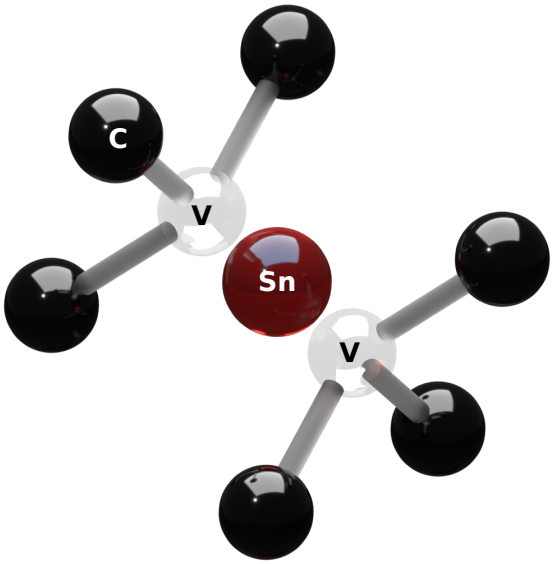

Figure 1.3.: Structural representation of a group-IV color center in diamond, where a group-IV atom (Si, Ge, Sn, or Pb) replaces two carbon atoms in a split-vacancy configuration (here represented with a red tin atom). This unique defect structure provides inversion symmetry, leading to stable optical transitions and long spin coherence, making it a promising candidate for quantum technologies.

1.2. Group-IV Color Centers

With a broader perspective in mind, we now shift our attention to group-IV defects in diamond and provide an overview of their key properties and differences. Rather than arguing that one particular defect is superior to the others, an approach that would miss the bigger picture, we aim to briefly highlight the unique advantages and trade-offs of each system.

Group-IV defects refer to structural defects in which an element (Si, Ge, Sn, or Pb) is positioned between two vacant carbon sites in the diamond lattice. The structural representation of a group-IV color center in diamond, created in Blender, is illustrated in Figure 1.3. We are interested in the negatively charged state of these defects and from this point forward, we refer specifically to the negatively charged color center when discussing these defects. Their split-vacancy configuration provides a unique combination of stable optical transitions and accessible spin degrees of freedom arising from their inversion symmetry [63, 64]. This offers a crucial advantage, which protects their optical transitions from linear Stark shifts, though not from quadratic Stark effects, as we will explore in Section 2.4.1. The insensitivity to electric field fluctuation results in narrow zero-phonon lines (ZPLs) with high Debye-Waller factor (η_{DW}), which quantifies the fraction of emission into the ZPL.

For example, the SiV center exhibits a Debye-Waller factor of approximately $\sim 70\,\%$ [65], orders of magnitude higher than the 3-4 % of the nitrogen-vacancy (NV) center [66]. Since quantum communication requires a high yield of coherent photons. We additionally need

to consider the quantum efficiency (η_{QE}), defined as the ratio of radiative to total decay. Among group-IV defects, the SnV center leads in this metric, with a quantum efficiency of $\sim 80\,\%$ [67]. In total, when assessing their suitability for quantum technologies, we must consider the total ZPL emission rate $\eta_{\mathrm{DW}} \times \eta_{\mathrm{QE}}$ and the overall excited state lifetime (τ), which impacts the repetition rate of quantum protocols.

Another interesting characteristic of group-IV defects is the fine structure of their optical transitions. The ground and excited states of these defects experience an internal splitting due to spin-orbit interaction (λ^{g}). This results in multiple closely spaced ZPL transitions, with splittings that strongly depend on the specific defect type. For example, the SiV center features a ground-state splitting of 50 GHz [65], while SnV center exhibits a significantly larger splitting of 820 GHz [68]. This difference has far-reaching implications: SiV centers require ultra-low temperatures (in the milli-Kelvin) to prevent phonon-induced relaxation of spin states [19]. Contrary, the larger splittings in SnV centers and PbV centers naturally suppress phonon interactions, allowing operation at higher temperatures [69, 70], potentially avoiding the need for dilution refrigeration.

The fabrication and charge stabilization of these color centers in diamond present additional challenges, which vary for each impurity. Due to differences in atomic size and properties, a single fabrication technique is universally not applicable. For example, GeV centers have been successfully incorporated into diamond via both in-situ doping during chemical vapor deposition growth and ion implantation of Ge^+ ions. In contrast, incorporating Sn into diamond is more difficult due its larger atomic radius compared to carbon, which increases the probability of introducing lattice defects [63]. While high-temperature annealing under high pressure has been shown to produce high-quality SnV centers [68], it comes at the cost of diamond surface quality, presenting an additional trade-off.

At last, we want to discuss qubit performance as a key metric. The relaxation time T_1 and coherence times T_2^* and T_2 are temperature dependent due to the orbital doublet in the ground state [71]. However, all group-IV centers exhibit impressive coherence when sufficiently cooled. For instance, the SnV center can achieve spin relaxation times exceeding 1 s at an operating temperature of $T_{\mathrm{op}} \sim 1\,\mathrm{K}$ [1]. The spin coherence time, in diamonds with a natural ^{13}C abundance of 1.1 %, is in the range of $T_2 \approx 1.5\,\mu\mathrm{s}$ to $2.5\,\mu\mathrm{s}$ [72]. Furthermore, by using dynamical decoupling techniques, coherence times exceeding 10 ms have been demonstrated [1, 72]. In Table 1.1, we offer a summary of the key characteristics of the different group-IV defects, including the NV center as a reference.

In summary, group-IV defects have emerged as a highly promising qubit platform among diamond color centers, offering a pathway to scalable quantum systems. They achieve an optimal balance between spin coherence and optical performance, exhibiting bright and stable emission with a high fraction of coherent photons. Moreover, they have already demonstrated key milestones, such as distant entanglement and continue to show great potential. As techniques for their fabrication and control advance, group-IV defects are set to have a bright future.

Table 1.1.: Summary of the key characteristics of the different group-IV defects, including the NV center as a reference. The table has been adapted from [73] and [42].

	λ_{ZPL} (nm)	η_{QE}	η_{DW}	τ (ns)	λ^g (GHz)	T_{op} (K)
SiV	737 [29]	0.10 [74]	0.7 [65]	1.7[74]	50 [65]	0.1 [19]
GeV	602 [20]	0.4 [75]	0.6 [75]	1.4 – 6 [75]	170 [75]	0.4
SnV	620 [1, 67]	0.8 [67]	0.57	4.5 – 7 [76, 77]	820 [1, 67]	1.2 [69]
PbV	550 [78]	-	-	>3.5 [78]	3900 [78]	8
NV	637 [79]	>0.85 [80]	0.03 [66]	11 – 13 [81, 82]	NA	NA

1.3. Outline of this Thesis

The SnV center has emerged as a promising candidate for optically addressable spin qubits [1, 69, 70], yet its full potential relies on precise control of its electronic and spin properties. Key challenges include mitigating phonon-induced decoherence and microwave control bottlenecks. In order to solve these and many other problems, a combination of different tasks have to be addressed, such as strain engineering, optimizing spin initialization by precise magnetic field alignment and overcoming thermal limitations by using superconducting materials. These key points, along with several other factors, play a crucial role in determining the qubit performance of the SnV center and its suitability for scalable quantum technologies. As part of this work, we will address and analyze all important aspects in detail. In the following, we outline the key aspects along with the sections where each is addressed:

- **Basic properties of the SnV center (Chapter 2)**: In this chapter we discuss the basic properties of the SnV center as an optically addressable spin qubit.
- **Effective Hamiltonian and the fine structure**: To understand the effects of the different interaction terms the derivation of the effective Hamiltonian is necessary (Section 2.2). The fine structure governs the resonance conditions of the optical- and magnetic transitions in the electronic ground and excited states of the SnV center (Section 2.3). It assists us to asses the optical linewidths, which impact spin-photon interface efficiency [32, 38].
- **Magneto-optical properties (Section 2.4)**: The stability of optical transitions over time (Subsection 2.4.1) is affected by charge fluctuations and strain variations. Spectral diffusion, primarily caused by charge noise, degrades optical coherence and impacts the efficiency of spin-photon interfaces [36, 63]. The fine structure is strongly modified by external magnetic field interaction. For example, the qubit's frequency is determined by the Zeeman interaction in the magnetic field and further influenced by spin-orbit coupling and strain. It requires precise knowledge of the several interactions to control the qubit [1] (Subsection 2.4.3).
- **Spin Dynamics of the SnV Center (Section 2.5)** When a qubit is prepared in a pure quantum state (e.g., $|0\rangle$), the accuracy of the preparation is described as the initialization fidelity. For SnV centers, both initialization and readout fidelity are

strongly dependent on the magnetic field orientation. Low-fidelity readout can limit efficient coherent control [65, 83](Subsection 2.5.1). In addition, the time over which a spin qubit relaxes from the initialized state back to its thermal equilibrium state is described by the spin relaxation time T_1. This parameter reflects the lifetime of the qubit and is influenced by phonon-induced relaxation and environmental coupling [35] (Subsection 2.5.2)

- **Microwave line and heating effects (Chapter 3)**: In this chapter we discuss the properties of the microwave transmission line for spin qubit control (Section 3.1). By using the SnV center as a calibrated temperature sensor (Subsection 3.2) we characterize the losses of normal and superconducting coplanar waveguides (Subsection 3.3).
- **Coherent control and its necessary requirements (Chapter 4)**: The rate of coherent oscillation between the qubit's spin states under an external driving field (e.g., microwave pulses) [84] is defined as the Rabi frequency Ω (Section 4.1). A high Ω enables fast qubit gates, but excessive driving can introduce heating and dephasing [65, 69]. The time over which a qubit loses phase coherence due to fluctuating magnetic fields or interactions with nuclear spins is determined by the coherence times T_2^* and T_2. The coherence can be extended using techniques like spin-echo or dynamical decoupling (Section 4.2). The distinction between T_2^* (free induction decay time) and T_2 (spin-echo coherence time) is crucial for evaluating noise sources. [71]

2. Tin-Vacancy Center: From Orbital Structure to Spin Dynamics

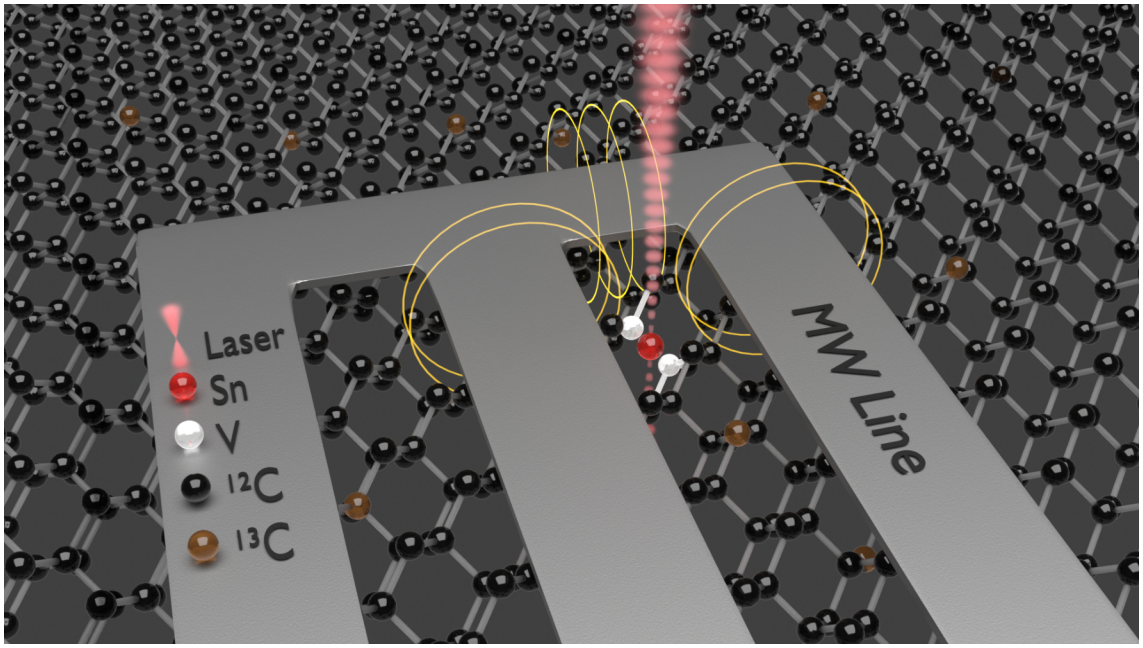

Figure 2.1.: Illustration of the SnV center in diamond with an integrated microwave line for spin manipulation. A tin atom (Sn, red) positioned between two vacancies (V, white) forms an SnV center. This SnV center is embedded in a diamond lattice composed of ^{12}C (black) and ^{13}C (brown) atoms. The system is optically addressed with a laser (red beam) and coherently controlled via a coplanar microwave line (gray structure). The dimensions of this model are exaggerated to visualize the idea of the SnV center as a spin qubit in diamond.

First of all, we would like to draw attention to the illustration of the SnV center in diamond as an optically addressable spin qubit, as depicted in Figure 2.1. The 3D model presents a tin atom (Sn, red) positioned between two vacancies (V, white), forming the SnV center within the diamond lattice. This defect is positioned within the gap of a coplanar microwave structure, where the microwave line generates localized oscillating magnetic fields to enable coherent spin manipulation. Optical addressing is achieved by a (resonant) laser, represented by a red beam. The diamond lattice is composed of ^{12}C (black) and ^{13}C (brown) atoms, with the latter highlighting the potential use of the ^{13}C nuclear spin for multi-qubit applications. The dimensions of the model are exaggerated to enhance the visualization of the SnV center as a spin qubit in diamond. In the following we start by discussing the electronic structure of the SnV center.

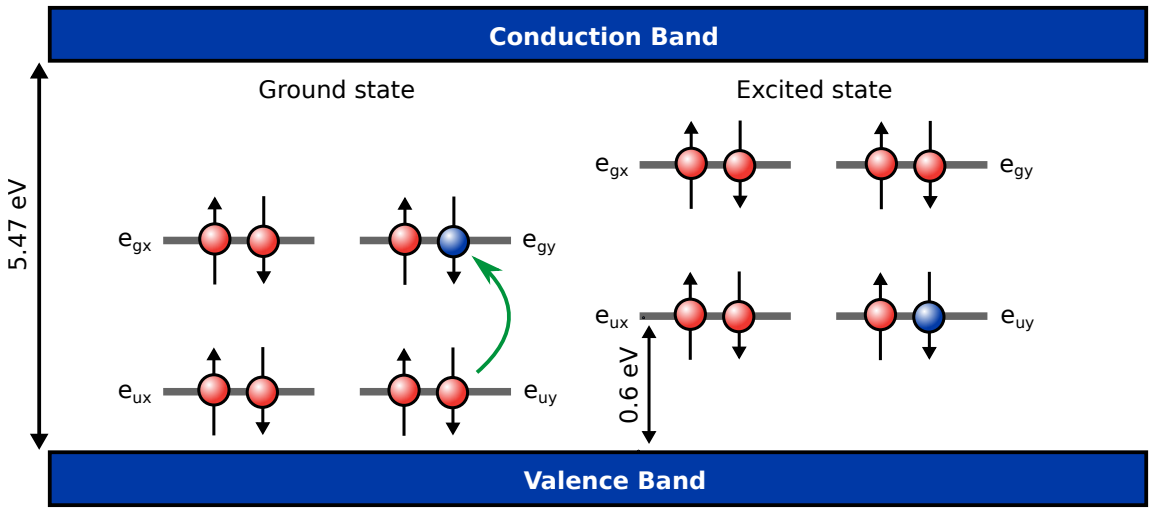

Figure 2.2.: Energy-level diagram depicting the ground and excited state configurations of the negatively charged tin-vacancy (SnV^-) center in diamond. The defect states are formed by e_g and e_u molecular orbitals, which arise from the interaction of dangling bonds on carbon atoms and tin atomic orbitals. Electrons (red spheres), holes (blue spheres), and their associated spins (black arrows) are displayed. Optical excitation is represented by the green arrow, promoting an electron from the e_u orbitals to one of the e_g orbitals.

2.1. Electronic and Orbital Structure

The electron configuration of the SnV center is determined by the symmetry of its molecular structure. The defect consists of six neighboring carbon atoms and two vacant sites, with a tin atom occupying an interstitial lattice position between the vacancies. The dangling bonds of the carbon atoms can be schematically described as sp^3-orbitals, which, together with the tin atomic orbitals, form the defect and determine its symmetry and invariance under symmetry operations. Using group theory and the identified symmetries, the SnV center can be assigned to the D_{3d} point group.[1] The constructed irreducible representations include two non-degenerate representations, A_{1g} and A_{2u}, along with two two-fold degenerate representations, E_g and E_u. The subscripts 'g' (gerade) and 'u' (ungerade) denote even and odd parity, respectively.

The notation with capital letters refers to the irreducible representations as defined by group theory. These irreducible representations describe the symmetry properties of the molecular orbitals in an abstract manner. Essentially, they tell us how a set of orbitals or wavefunctions transforms under the symmetry operations of the molecule's point group (such as rotations or reflections). The actual physical orbitals that are derived from these irreducible representations are denoted with small letters. These are the specific molecular orbitals that electrons occupy, derived from symmetry-adapted linear combinations (SALCs) of atomic orbitals. SALCs are constructed by combining atomic orbitals in ways

[1] For a thorough derivation of the symmetry-adapted linear combinations (SALCs), which are constructed by combining atomic orbitals to respect the symmetry of the molecule or defect, of the dangling bond orbitals using the D_{3d} group as described for silicon-vacancy centers, we refer to the doctoral thesis of C. Hepp [34].

that reflect the symmetry properties of the molecule's point group, allowing them to transform according to irreducible representations. The electron density is delocalized within the SALC orbitals corresponding to a particular irreducible representation, rather than being confined to a single atomic orbital. The molecular orbitals form orthogonal eigenstates, hence they do not overlap, are independent and are denoted as a_{1g}, a_{2u}, e_u, e_g. In the neutral state of the SnV center, the orbitals contain ten valence electrons: six from the dangling bonds of the carbon atoms and four from the Sn atom. In the relevant negatively charged state, SnV^-, an additional electron is captured from nearby donors, resulting in eleven electrons in total. From here on, we will refer to this negatively charged state. Considering the spin degree of freedom, each orbital can accommodate two electrons of opposite spin $\{\uparrow, \downarrow\}$. Density functional theory (DFT) calculations [38] indicate that the a_{1g} and a_{2u} orbitals are energetically located within the valence band of the diamond. As a result, these orbitals do not contribute to the electronic states within the bandgap and are excluded from the perturbation analysis.

The two-fold degenerate orbitals e_g and e_u can be expressed by two orthogonal eigenstates $e_{gx/y}$ and $e_{ux/y}$, again with an additional spin degree of freedom. These orbitals are positioned within the bandgap, as shown in Fig. 2.2, with the $e_{ux/y}$ orbital close to the valence band edge. In the ground state configuration, the $e_{gx/y}$ orbitals are occupied by three electrons, leaving a hole in one of the four e_g states. This state is described by the $e_u^4 e_g^3$ ($2E_g$) configuration [34]. The defect's properties are determined by the state of the hole, leading to a spin of $S = 1/2$ for the SnV center. When an electron is excited from the e_u state to the e_g state, as indicated by the green arrow, the resulting configuration for the excited state is $e_u^3 e_g^4$ ($2E_u$). The degenerate orbitals e_g and e_u, can be described by the four possible states that the hole can occupy. Each hole state is represented by a basis vector, including both orbital and spin information. The basis sets for the ground and excited state orbitals are as follows:

$$2E_g \text{ ground state: } \{|e_{gx}\uparrow\rangle, |e_{gx}\downarrow\rangle, |e_{gy}\uparrow\rangle, |e_{gy}\downarrow\rangle\} \tag{2.1}$$

$$2E_u \text{ excited state: } \{|e_{ux}\uparrow\rangle, |e_{ux}\downarrow\rangle, |e_{uy}\uparrow\rangle, |e_{uy}\downarrow\rangle\}. \tag{2.2}$$

The defined eigenstates provide a basis for analyzing the effect of various perturbations on the system. First, we consider internal perturbations such as spin-orbit coupling that introduces mixing between the orbital components while preserving spin degeneracy. In addition, strain can modify the orbital overlap, leading to changes in the energy spectrum. By applying external magnetic fields, we can split or shift the energy levels via the Zeeman effect, directly affecting the spin components of the eigenstates. These perturbations allow us to explore the complex interactions within the SnV center. In the next section we will derive a matrix representation of the Hamiltonian, focusing on the ground state for simplicity. This derivation applies equivalently to the excited state.

2.2. Derivation of the Effective Hamiltonian

The Hamiltonian for Group-IV defects was initially derived from measurements on silicon-vacancy centers [19] and subsequently extended to predict the behavior of heavier Group-IV elements [38]. However, due to the lack of necessary experimental data to validate the ab initio calculations, certain interactions have not been accurately predicted or have instead been incorrectly defined by assuming that average pre-factors could be used [1]. The aim of this section is to derive the effective spin Hamiltonian in a manner analogous to [38]. The key difference is that we present the various contributions in a matrix representation for the SnV center's electron spin Hamiltonian. This approach is more intuitive from an experimental perspective and helps illustrate why averaging the different contributions is incorrect in certain cases. By doing so, we aim to achieve a comprehensive characterization of the SnV center's experimentally observed optical and magnetic properties shown in section 2.4.

The interaction terms of the system can be described by four contributions, namely, the spin-orbit coupling $\hat{H}^{\mathrm{g,u}}_{\mathrm{SO}}$, the strain components $\hat{H}^{\mathrm{g,u}}_{\mathrm{JT+strain}}$, where we absorb the Jahn-Teller effect into the interaction term of the strain Hamiltonian, the orbital Zeeman effect $\hat{H}^{\mathrm{g,u}}_{\mathrm{ZL}}$ and the spin Zeeman effect $\hat{H}^{\mathrm{g,u}}_{\mathrm{ZS}}$. Hence, the effective Hamiltonian is:

$$\hat{H}^{\mathrm{g,u}}_{\mathrm{eff}} = \hat{H}^{\mathrm{g,u}}_{\mathrm{SO}} + \hat{H}^{\mathrm{g,u}}_{\mathrm{JT+strain}} + \hat{H}^{\mathrm{g,u}}_{\mathrm{ZL}} + \hat{H}^{\mathrm{g,u}}_{\mathrm{ZS}}. \tag{2.3}$$

While deriving a matrix representation of the Hamiltonian, we focus on the ground state for simplicity, noting that the same derivation applies to the excited state. Additionally, we set $\hbar = 1$ throughout the derivation and indicate the basis used for determining the interactions using superscript notation. The xy-basis is defined by equations 2.1.

Spin-orbit coupling With an interaction strength of approximately 820 GHz [67, 68, 85], spin-orbit coupling is the most significant perturbation across the majority of investigated and utilized SnV centers. It is a relativistic effect arising from the interaction of the electron with its orbital motion. In the potential of the Sn nucleus, the electron experiences a magnetic field in its rest frame due to its orbital motion around the nucleus. This leads to a spin-orbit interaction, where the electron's spin magnetic moment couples to its orbital angular momentum. As a result, the four-fold degeneracy of both the ground and excited states is lifted. The energy levels are split into two, corresponding to the two possible total angular momentum states. In the $\{xy\}$-basis of the electronic states, the Hamiltonian for spin-orbit coupling is thus given by [34, 86]:

$$\hat{H}^{xy}_{\mathrm{SO}} = -\lambda^{\mathrm{g}} \hat{L}_z \hat{S}_z. \tag{2.4}$$

This term accounts for the effective spin-orbit splitting, with the strength of the spin-orbit coupling given by λ^{g} for the orbital ground states. The negative sign was introduced in [34] due to the fact that we are dealing with a hole. $\hat{L}_z$ and $\hat{S}_z$ are the z-components of the angular

momentum operator $\hat{\boldsymbol{L}} = (\hat{L}_x,\ \hat{L}_y,\ \hat{L}_z)^{\mathrm{T}}$ and the Pauli-matrix vector $\hat{\boldsymbol{S}} = \frac{1}{2}(\hat{\sigma}_x,\ \hat{\sigma}_y,\ \hat{\sigma}_z)^{\mathrm{T}}$. The transverse components of the $\hat{L}$ operator vanish, as they do not couple the e_{g} and e_{u} states.

The $\hat{L}_z$ and $\hat{\sigma}_z$ operators are given by the matrices [34]:

$$\hat{L}_z = \begin{pmatrix} 0 & i \\ -i & 0 \end{pmatrix} \text{ and } \hat{\sigma}_z = \begin{pmatrix} 1 & 0 \\ 0 & -1 \end{pmatrix}, \tag{2.5}$$

respectively.

The spin-orbit splitting Hamiltonian follows as

$$\hat{H}_{\mathrm{so}}^{xy} = -\lambda^{\mathrm{g}} \hat{L}_z \hat{S}_z = \begin{bmatrix} 0 & 0 & -\frac{i\lambda^{\mathrm{g}}}{2} & 0 \\ 0 & 0 & 0 & \frac{i\lambda^{\mathrm{g}}}{2} \\ \frac{i\lambda^{\mathrm{g}}}{2} & 0 & 0 & 0 \\ 0 & -\frac{i\lambda^{\mathrm{g}}}{2} & 0 & 0 \end{bmatrix}, \tag{2.6}$$

which is derived by performing the outer product between the $\hat{L}_z$ operator and the $\hat{\sigma_z}$ Pauli matrix. The non-zero off-diagonal elements indicate that the spin-orbit interaction results in coupling between different components of the orbital states. By diagonalizing the matrix one can determine the Eigenvectors and Eigenvalues in the basis dominated by the spin orbit interaction as:

$$|e_+ \uparrow\rangle = \frac{1}{\sqrt{2}} \left(|e_{\mathrm{g}x} \uparrow\rangle + i |e_{\mathrm{g}y} \uparrow\rangle \right) \text{ with } E_1 = +\frac{\lambda^{\mathrm{g}}}{2}, \text{ and with } E_1 = -\frac{\lambda^{\mathrm{g}}}{2} \tag{2.7}$$

$$|e_- \downarrow\rangle = \frac{1}{\sqrt{2}} \left(|e_{\mathrm{g}x} \downarrow\rangle - i |e_{\mathrm{g}y} \downarrow\rangle \right) \text{ with } E_2 = +\frac{\lambda^{\mathrm{g}}}{2}, \text{ and with } E_2 = -\frac{\lambda^{\mathrm{g}}}{2} \tag{2.8}$$

$$|e_- \uparrow\rangle = \frac{1}{\sqrt{2}} \left(|e_{\mathrm{g}x} \uparrow\rangle - i |e_{\mathrm{g}y} \uparrow\rangle \right) \text{ with } E_3 = -\frac{\lambda^{\mathrm{g}}}{2}, \text{ and with } E_3 = +\frac{\lambda^{\mathrm{g}}}{2} \tag{2.9}$$

$$|e_+ \downarrow\rangle = \frac{1}{\sqrt{2}} \left(|e_{\mathrm{g}x} \downarrow\rangle + i |e_{\mathrm{g}y} \downarrow\rangle \right) \underbrace{\text{with } E_4 = -\frac{\lambda^{\mathrm{g}}}{2}}_{\text{in accordance with [34]}}, \underbrace{\text{and with } E_4 = +\frac{\lambda^{\mathrm{g}}}{2}}_{\text{according to [38]}} \tag{2.10}$$

In the ab initio calculations of G. Thiering and A. Gali, the ordering of the eigenvalues has been swapped. Specifically, they note "the negative sign which originates from the three-electron many-body E_{g} and E_{u} states. As a consequence, $E_{\mathrm{g,u}}^{3/2}$ is lower in energy than the $E_{\mathrm{g,u}}^{1/2}$, in contrast to the previous assignments." [38] Here, the total effective angular momentum is expressed as the sum of the orbital angular momentum and the spin quantum numbers $m_j = m_l + m_s = \{\pm\frac{1}{2}, \pm\frac{3}{2}\}$. We will follow this ordering from here on with a side note: we will later see from the experimental measurements, that are shown in Section 2.4.4, that the qubit frequency of the lower $E_{\mathrm{g,u}}^{3/2}$ doublet scales stronger in an external magnetic field than that of a free electron, with $\omega = 28\,\mathrm{MHz\,mT^{-1}}$. This indicates that the orbital and spin momentum are aligned in the lower doublet. Unlike

in the hydrogen atom, where the $j = \frac{1}{2}$ state with anti-aligned orbital and spin momenta lies lower in energy, the defect system shows the opposite behavior. When the orbital and spin angular momenta are aligned (e.g. $\{+ \uparrow\}$), the state's energy is reduced, whereas anti-alignment (e.g. $\{- \uparrow\}$) results in a higher energy state. Finally, we can display the Hamiltonian in the new $\{so\}$-basis with states

$$\{e_+|\uparrow\rangle, e_-|\downarrow\rangle, e_-|\uparrow\rangle, e_+|\downarrow\rangle\}, \tag{2.11}$$

$$\text{as } \hat{H}_{\text{so}}^{so} = \begin{bmatrix} -\frac{\lambda^{\text{g}}}{2} & 0 & 0 & 0 \\ 0 & -\frac{\lambda^{\text{g}}}{2} & 0 & 0 \\ 0 & 0 & \frac{\lambda^{\text{g}}}{2} & 0 \\ 0 & 0 & 0 & \frac{\lambda^{\text{g}}}{2} \end{bmatrix}. \tag{2.12}$$

It is evident that the originally four-fold degenerate states are split into the two spin-degenerate doublets $E_{\text{g,u}}^{3/2}$ and $E_{\text{g,u}}^{1/2}$, with their Eigenvalues in the upper and lower half of the matrix diagonals, respectively. We connect the $\{xy\}$-basis and the $\{so\}$-basis with a transformation matrix T, which diagonalizes $\hat{H}_{\text{so}}^{xy}$ with the relation:

$$T^{-1} \cdot \hat{H}_{\text{so}}^{xy} \cdot T = \hat{H}_{\text{so}}^{so}. \tag{2.13}$$

Solving this equation results in the matrix

$$T = \begin{bmatrix} i & 0 & -i & 0 \\ 0 & -i & 0 & i \\ 1 & 0 & 1 & 0 \\ 0 & 1 & 0 & 1 \end{bmatrix}. \tag{2.14}$$

One can now describe the remaining interactions in the basis that is more intuitive from an experimental approach. The transformation matrix allows to easily switch between the two bases to combine the different interactions into a single Hamiltonian.

Jahn-Teller effect and strain The Jahn-Teller effect (JT) involves the coupling of the electronic states to vibrational modes (phonons) of the crystal lattice, leading to symmetry-breaking distortions and lower symmetry of the system [87]. This coupling leads to a dynamic JT effect, where the energy barriers between different nuclear configurations are low enough for the system to tunnel between them. As a result, the electronic wavefunction becomes delocalized over multiple configurations, affecting properties like the g-factor by effectively quenching spin-orbit coupling and altering magnetic parameters [38, 88], and is referred to as the Ham-reduction [87]. The JT effect induces a linear displacement of the nucleus, similar to the effect of strain, and thus is often incorporated into the strain Hamiltonian. It is experimentally indistinguishable from strain-induced symmetry lowering [34].

The response of the electronic levels to strain has been investigated in [36] for SiV centers, by changing its static strain environment with a nano-electro-mechanical system. The description of the ground and excited state is independent, due to the different parities. Hence, H_{strain} is identical in form for E_{g} and E_{u} [36], with differing numerical values. The strain components with respect to the symmetry of the Group-IV defect, based on equations 2.1 follow as:

$$\epsilon_{A_1} = t_\perp \left(\epsilon_{xx} + \epsilon_{yy}\right) + t_\parallel \epsilon_{zz} \tag{2.15}$$
$$\epsilon_{E_x} = d(\epsilon_{xx} - \epsilon_{yy}) + f\epsilon_{zx} \tag{2.16}$$
$$\epsilon_{E_y} = -2d\epsilon_{xy} - f\epsilon_{yz}\,, \tag{2.17}$$

The strain response of the orbital states can be fully described by the four strain-susceptibility parameters $t_\perp$, $t_\parallel$, d, and f, which are determined for the SnV center in density functional theory (DFT) calculations by X. Guo [69]. These parameters account for how the orbital states respond to both perpendicular and parallel components of the strain. The strain Hamiltonian can be written in the form:

$$\hat{H}^{xy}_{\text{strain}} = \begin{pmatrix} \epsilon_{A1} - \epsilon_{E_x} & \epsilon_{E_y} \\ \epsilon_{E_y} & \epsilon_{A1} + \epsilon_{E_x} \end{pmatrix} \otimes \begin{pmatrix} 1 & 0 \\ 0 & 1 \end{pmatrix}, \tag{2.18}$$

The wave function's spin component is represented by an identity matrix in the strain Hamiltonian since lattice deformation mainly modifies the Coulomb energy of the orbitals, leaving the spin characteristics unaffected [36]. The diagonal elements ϵ_{A1} accounts for a global emission wavelength shift [69] and will be ignored. Further, since we cannot experimentally distinguish ϵ_{E_x} from ϵ_{E_y} for individual SnV centers, we sum up the contributions in an effective term α^{g}. This strain parameter causes mixing and relative shifts of the spin-orbit eigenstates $\{|e_+\rangle, |e_-\rangle\}$, transforming them back to pure $\{|e_x\rangle, |e_y\rangle\}$ orbitals for mainly transverse-oriented strain [36]. Hence, we place the strain component in the diagonals of the $\{xy\}$-basis with opposite sign. The strain Hamiltonian in both bases is given by:

$$\hat{H}^{xy}_{\text{strain}} = \begin{bmatrix} \alpha^{\text{g}} & 0 & 0 & 0 \\ 0 & \alpha^{\text{g}} & 0 & 0 \\ 0 & 0 & -\alpha^{\text{g}} & 0 \\ 0 & 0 & 0 & -\alpha^{\text{g}} \end{bmatrix}, \; \hat{H}^{so}_{\text{strain}} = \begin{bmatrix} 0 & 0 & -\alpha^{\text{g}} & 0 \\ 0 & 0 & 0 & -\alpha^{\text{g}} \\ -\alpha^{\text{g}} & 0 & 0 & 0 \\ 0 & -\alpha^{\text{g}} & 0 & 0 \end{bmatrix} \tag{2.19}$$

Note that we also include effects from Jahn-Teller interaction in the same coupling constant α.

Orbital-Zeeman effect Earlier, we mentioned that the dynamic Jahn-Teller effect suppresses the orbital moment, thereby effectively quenching the spin-orbit coupling. The same interaction reduces the orbital-Zeeman interaction of the SnV center by a factor $f^{\mathrm{g}}_{m_j}$, that will be further explained in the following based on parts from Karapatzakis, Resch et al. Phys. Rev. X 14, 031036 [1]. We can express the orbital Zeeman interaction in the form:

$$\hat{H}_{\mathrm{ZL}} = \mu_B \left(f^{\mathrm{g}}_{m_j}\right)_{\{\pm\frac{1}{2},\pm\frac{3}{2}\}} \cdot \hat{L}_z B_z \tag{2.20}$$

The term includes the Bohr magneton μ_B and the quenching factor $f^{\mathrm{g}}_{m_j}$, which adjusts the orbital Landé g-factor to account for the reduced splitting compared to the expected value for a quantized magnetic moment. The quenching factor can be expressed as $f^{\mathrm{g}}_{m_j} = p^{\mathrm{g}}_{m_j} \cdot g^{\mathrm{g}}_l$, where $p^{\mathrm{g}}_{m_j}$ represents the contribution from the dynamic Jahn-Teller effect, also known as the Ham effect, and g^{g}_l is Steven's orbital quenching factor, which arises due to the reduced symmetry of the system [38]. We cannot distinguish between these two components in our measurements, but we can determine the overall magnitude of the orbital quenching $f^{\mathrm{g}}_{m_j}$ separately for the total effective angular momentum $m_j = \{\pm\frac{1}{2}, \pm\frac{3}{2}\}$. The states with quantum number $m_j = \pm\frac{1}{2}$ correspond to the spin-orbit doublet with higher energy $+\frac{\lambda^{\mathrm{g}}}{2}$, while $m_j = \pm\frac{3}{2}$ corresponds to the doublet with energy $-\frac{\lambda^{\mathrm{g}}}{2}$. Within the orbital-Zeeman interaction, the states are further split by the applied external magnetic field B_z.

This approach is different from all previous publications, where the quenching factor of the two doublet states has been merged within an average quenching factor $f^{\mathrm{g}}_{\mathrm{average}} = \frac{1}{2} \cdot (f^{\mathrm{g}}_{\frac{1}{2}} + f^{\mathrm{g}}_{\frac{3}{2}})$. Generally, this approach provides an almost accurate characterization for SiV centers, where the crystal strain is comparable to or much greater than the spin-orbit coupling of approximately $\sim 48\,\mathrm{GHz}$, for defects utilized in experiments such as [65, 89]. Strain of a similar order to spin-orbit coupling induces mixing of the pure m_j eigenstates, thereby averaging the effective quenching factors.

However, the same approach fails to accurately describe the level structure of the SnV center, which is typically found in low to moderate strain environments relative to the spin-orbit coupling, as demonstrated in [69, 70]. This discrepancy arises from the significantly stronger spin-orbit coupling in these defects of approximately $\sim 820\,\mathrm{GHz}$, making much stronger strain necessary, to yield the same orbital mixing effect. Therefore, we assign separate quenching factors to the doublet states with corresponding m_j. Finally, by leveraging the differing degrees of orbital mixing across varying strain environments, from unstrained to highly strained emitters, we accurately determine orbital quenching.

We will see in Section 2.4.4 that, for an unstrained emitter, the qubit frequency corresponding to the splitting of the $E^{3/2}_{\mathrm{g}}$ doublet is purely determined by the $m_j = \pm\frac{3}{2}$ orbitals. As the strain magnitude increases, the $m_j = \pm\frac{1}{2}$ states start to contribute more significantly, allowing for an indirect determination of the corresponding quenching factor.

Following the ordering of the eigenstates as defined in Equation 2.11, we can construct the matrix representation of the orbital-Zeeman effect in the spin-orbit basis in a straightforward way:

$$\hat{H}_{\mathrm{ZL}}^{so} = \gamma_l B_{\parallel} \begin{bmatrix} f_{32}^{\mathrm{g}} & 0 & 0 & 0 \\ 0 & -f_{32}^{\mathrm{g}} & 0 & 0 \\ 0 & 0 & -f_{12}^{\mathrm{g}} & 0 \\ 0 & 0 & 0 & f_{12}^{\mathrm{g}} \end{bmatrix}. \tag{2.21}$$

We have the gyromagnetic factor $\gamma_l = 14\,\mathrm{GHz\,T^{-1}}$ [90], the magnetic field component parallel to the SnV-center's quantization axis $B_{\parallel}$ and the quenching factor $f_{m_j}^{\mathrm{g}}$ where the fractional line has been omitted for better readability. For the following matrix representation in the $\{xy\}$-basis, we will also omit the superscript g:

$$\hat{H}_{\mathrm{ZL}}^{xy} = \frac{\gamma_l B_{\parallel}}{2} \begin{bmatrix} -f_{12} + f_{32} & 0 & if_{12} + if_{32} & 0 \\ 0 & f_{12} - f_{32} & 0 & if_{12} + if_{32} \\ -if_{12} - if_{32} & 0 & -f_{12} + f_{32} & 0 \\ 0 & -if_{12} - if_{32} & 0 & f_{12} - f_{32} \end{bmatrix}. \tag{2.22}$$

We can directly see the similarities to the spin-orbit Hamiltonian $\hat{H}_{\mathrm{so}}^{xy}$, meaning that the orbital-Zeeman effect mixes the orbitals of the eigenstates in the $\{xy\}$-basis, while leaving the spin unaffected.

Spin-Zeeman effect Unlike the orbital-Zeeman effect, the spin-Zeeman interaction leads to mixing of the spin states in both bases when a transverse magnetic field component $B_{\perp}$ is applied, relative to the quantization axis of the SnV center. In contrast, parallel field components $B_{\parallel}$ result in the splitting of the m_j doublets without mixing the spin states. The performance of a spin qubit is very sensitive to spin mixing effects, such as enhanced coupling to phonon modes, as we will discuss in detail in Section 2.5.2. In both cases, the orbitals remain unaffected by the magnetic field. This results in zero 2x2 blocks in the off-diagonal positions. The spin-Zeeman Hamiltonian with the gyromagnetic factor $\gamma_s = 28\,\mathrm{GHz\,T^{-1}}$ [91] in both bases is expressed as:

$$\hat{H}_{\mathrm{ZS}}^{xy} = \frac{\gamma_s}{2} \begin{bmatrix} B_{\parallel} & B_{\perp} & 0 & 0 \\ B_{\perp} & -B_{\parallel} & 0 & 0 \\ 0 & 0 & B_{\parallel} & B_{\perp} \\ 0 & 0 & B_{\perp} & -B_{\parallel} \end{bmatrix}, \; \hat{H}_{\mathrm{ZS}}^{so} = \frac{\gamma_s}{2} \begin{bmatrix} B_{\parallel}\gamma_s & 0 & 0 & B_{\perp}\gamma_s \\ 0 & -B_{\parallel}\gamma_s & B_{\perp}\gamma_s & 0 \\ 0 & B_{\perp}\gamma_s & B_{\parallel}\gamma_s & 0 \\ B_{\perp}\gamma_s & 0 & 0 & -B_{\parallel}\gamma_s \end{bmatrix} \tag{2.23}$$

Effective Hamiltonian The derivation of the effective Hamiltonian perturbations aimed to establish a matrix representation capable of accurately explaining the experimentally observed interactions of the SnV center with its environment. Using this matrix-based approach, we were able to analyze the Hamiltonian in both the xy and so-basis, depending on which basis could explain the interaction more intuitively, with the eigenvalues

corresponding directly to the energy level structure of the SnV center. The description of the SnV center's fine structure, along with an experimental verification, is provided in Section 2.3. In order to obtain an accurate and reliable description of the SnV center, certain parameters of the Hamiltonian must be constrained or known in advance, otherwise it is underdetermined. For instance, we use a three-axis vector magnet with precisely calibrated coil-generated field strengths. The field strengths are initially estimated through simulations based on the geometric configuration and then calibrated through experimental measurements of the nuclear spin bath surrounding the SnV center. This allows us to optimize alignment of the magnetic field with the spin dipole, as we will show in Section 2.4.3. In addition, multiple emitters with varying strain parameters are analyzed, enabling the successive and iterative determination of accurate quenching factors. The followed procedure is described in Section 2.4.4 and involves the measuring of optically allowed and forbidden transition frequencies between the ground and excited states E_g and E_u under different strain and magnetic field configurations.

Having derived and discussed the individual contributions to the SnV center's interactions we now combine these terms to construct the total Hamiltonian. Finally, the effective Hamiltonian, formulated in both the xy and so bases is given by:

$$\hat{H}_{xy} = \frac{1}{2}\begin{bmatrix} (\gamma_l(f_{32}-f_{12})+\gamma_s)B_\parallel + 2\alpha & \gamma_s B_\perp & i\gamma_l(f_{12}+f_{32})B_\parallel - i\lambda^\mathrm{g} & 0 \\ \gamma_s B_\perp & (\gamma_l(f_{12}-f_{32})-\gamma_s)B_\parallel + 2\alpha & 0 & i\gamma_l(f_{12}+f_{32})B_\parallel + i\lambda^\mathrm{g} \\ (-i\gamma_l(f_{12}+f_{32}))B_\parallel + i\lambda^\mathrm{g} & 0 & (\gamma_l(f_{32}-f_{12})+\gamma_s)B_\parallel - 2\alpha & \gamma_s B_\perp \\ 0 & -i\gamma_l(f_{12}+f_{32})B_\parallel - i\lambda^\mathrm{g} & \gamma_s B_\perp & (\gamma_l(f_{12}-f_{32})-\gamma_s)B_\parallel - 2\alpha \end{bmatrix}, \tag{2.24}$$

$$\hat{H}_{\mathrm{so}} = \frac{1}{2}\begin{bmatrix} (2f_{32}\gamma_l+\gamma_s)B_\parallel - \lambda^\mathrm{g} & 0 & -2\alpha & \gamma_s B_\perp \\ 0 & (-2f_{32}\gamma_l-\gamma_s)B_\parallel - \lambda^\mathrm{g} & \gamma_s B_\perp & -2\alpha \\ -2\alpha & \gamma_s B_\perp & (-2f_{12}\gamma_l+\gamma_s)B_\parallel + \lambda^\mathrm{g} & 0 \\ \gamma_s B_\perp & -2\alpha & 0 & (2f_{12}\gamma_l-\gamma_s)B_\parallel + \lambda^\mathrm{g} \end{bmatrix}. \tag{2.25}$$

We note that we can rewrite this Hamiltonian by introducing the commonly used mean reduction factors $f^{\mathrm{g,u}} = \frac{f_{12}^{\mathrm{g,u}}}{2} + \frac{f_{32}^{\mathrm{g,u}}}{2}$, and the mean asymmetries $\delta = \frac{f_{32}^{\mathrm{g,u}}}{2} - \frac{f_{12}^{\mathrm{g,u}}}{2}$, as well as $\gamma_l = \gamma_s/2$, leading to:

$$\hat{H}_{\mathrm{so}} = \begin{bmatrix} (f\gamma_l+\delta\gamma_l+\frac{\gamma_s}{2})B_\parallel - \frac{\lambda^\mathrm{g}}{2} & 0 & -\alpha & \frac{\gamma_s B_\perp}{2} \\ 0 & (-f\gamma_l-\delta\gamma_l-\frac{\gamma_s}{2})B_\parallel - \frac{\lambda^\mathrm{g}}{2} & \frac{\gamma_s B_\perp}{2} & -\alpha \\ -\alpha & \frac{\gamma_s B_\perp}{2} & (-f\gamma_l+\delta\gamma_l+\frac{\gamma_s}{2})B_\parallel + \frac{\lambda^\mathrm{g}}{2} & 0 \\ \frac{\gamma_s B_\perp}{2} & -\alpha & 0 & (f\gamma_l-\delta\gamma_l-\frac{\gamma_s}{2})B_\parallel + \frac{\lambda^\mathrm{g}}{2} \end{bmatrix}. \tag{2.26}$$

This matrix, accounting for the freedom to rearrange the columns, corresponds to the same Hamiltonian as reported in [38].

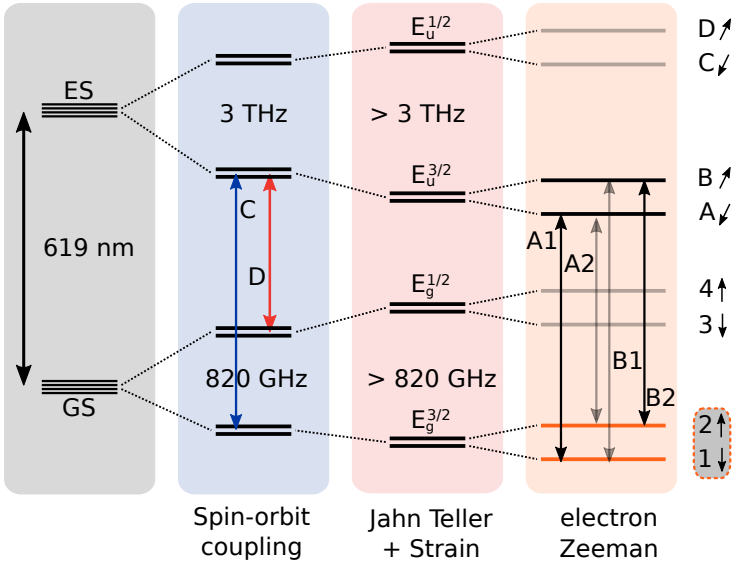

Figure 2.3.: Energy level diagram of a strained SnV center in a magnetic field. The figure illustrates the progression of energy levels for a SnV center under different interactions. In the grey panel, the unperturbed ground and excited states are shown as four-fold degenerate levels. The blue panel depicts these levels under additional spin-orbit interaction. The labeled transitions C and D highlight the prominent zero-phonon line (ZPL) transitions at low temperature and are indicated by blue and red arrows for clarity. The red panel represents the Jahn-Teller effect and strain, which further modify the level structure. Finally, in the orange panel, an applied magnetic field introduces further splitting of the spin states. The optically allowed transitions are marked by black arrows, and the forbidden transitions by grey arrows. The qubit states are represented by the orange-colored energy levels. This figure is adapted from Figure 1 in Reference [1].

2.3. Energy Level Structure

To best understand the electronic properties of the SnV center, it is helpful to validate the effective Hamiltonian, derived in the previous Section 2.2 through a synergistic approach combining the group-theoretical analysis with experimental data. The group-theoretical description provides a foundational framework, enabling a systematic characterization of the defect's electronic states. Experimental observations, in turn, supply critical parameters and constraints to refine the theoretical model and address interaction strengths that are difficult to predict. This interdependence ensures that the Hamiltonian accurately captures both the symmetry-driven properties and experimentally observed perturbations, resulting in a consistent and clear description of the SnV center's electronic structure. Building upon the derivation, we now explore the progression of the SnV center's energy levels under varying perturbations. Following, we incorporate experimental results from Karapatzakis, Resch et al. Phys. Rev. X 14, 031036 [1] to visualize the underlying interactions. For information on the devices and the sample fabrication we refer to Appendix B. For details on the experimental setup, please see Appendix C.

Fine structure of the SnV center Figure 2.3 schematically illustrates the evolution of the SnV center's energy level structure under the influence of spin-orbit coupling, strain, Jahn-Teller effects, and an applied magnetic field, with the interaction strengths decreasing

from left to right. Each subsequent interaction introduces characteristic splittings that define the optical and spin properties of the defect. The unperturbed four-fold degenerate ground (GS) and excited (ES) states, are depicted as four solid lines in the grey panel. The energy required to excite an electron from the GS to the ES is $E = 2.0\,\text{eV}$, corresponding to a wavelength of $\lambda = 619\,\text{nm}$. Spin-orbit coupling splits these states into two-fold degenerate levels (blue panel), with separations of $\lambda^{\text{g}} = 820\,\text{GHz}$ for the ground states (E_{g}) and $\lambda^{\text{u}} \sim 3\,\text{THz}$ for the excited states (E_{u}) [68, 85]. Upon optical excitation, decay occurs primarily via the prominent zero-phonon line transitions C and D, highlighted by blue and red arrows, respectively, in sub-10 K environments [85]. The splitting is further increased by strain and Jahn-Teller interaction, that are experimentally indistinguishable contributions in our experiment. The interactions are collectively represented in a single strain term, as we are only interested in the effective combined interaction. These strain parameters $\alpha^{\text{g,u}}$ are related to the experimentally measurable splitting of the ZPLs (of the C and D transitions) by the relation

$$\Delta_{\text{g,u}} = \sqrt{(\lambda^{\text{g,u}})^2 + 4(\alpha^{\text{g,u}})^2}. \tag{2.27}$$

Given that the spin-orbit interaction values are well-established from measurements in high-pressure and high-temperature (HPHT) samples [68], a first estimation of the strain magnitude of the ground state can be extracted from relatively uncomplicated experimental measurements, such as a photoluminescence (PL) spectrum.

In the same panel, the total angular momentum $m_j = m_l + m_s$ is indicated as superscript for the ground and excited states and is assigned accordingly to the lower and upper degenerate doublet levels, denoted as $E^{3/2}_{\text{g,u}}$ and $E^{1/2}_{\text{g,u}}$, respectively. The electron Zeeman interaction, consisting of the orbital-Zeeman and spin-Zeeman effects, is illustrated in the rightmost panel, completing the fine structure. The $E^{m_j}_{\text{g,u}}$ doublets are split, fully lifting the degeneracy of the SnV center. The resulting energy levels are labeled on the right in accordance with their energetic order. The most relevant levels for utilizing the SnV center as a spin qubit in diamond at operating temperatures below 4 K are the qubit states $|1\rangle$ and $|2\rangle$ of the ground state, represented by orange solid lines with corresponding spin states $\{\downarrow, \uparrow\}$, respectively. In the lower excited state, the relevant levels consist of $|A\rangle$ and $|B\rangle$, each additionally associated with spin states $\{\downarrow, \uparrow\}$. However, these spin states are represented as tilted relative to those in the ground state. The quantization axis in the excited state is assumed to be slightly misaligned due to the stronger spin-orbit interaction, if a transverse magnetic field is applied.

To effectively manipulate the qubit levels, initialization is essential. This is achieved by driving the spin-conserving optically allowed transitions A1 or B2. However, under certain conditions, such as strong transverse magnetic fields, the spin-flipping (optically forbidden) transitions A2 and B1 can also be driven. The allowed and forbidden transitions are shown as black and grey arrows, respectively. The process of spin initialization and readout is elaborated in detail in Section 2.5.1.

Zero-phonon line transitions As noted earlier, upon optical excitation, decay occurs mainly via the prominent zero-phonon line (ZPL) transitions C and D. These transitions

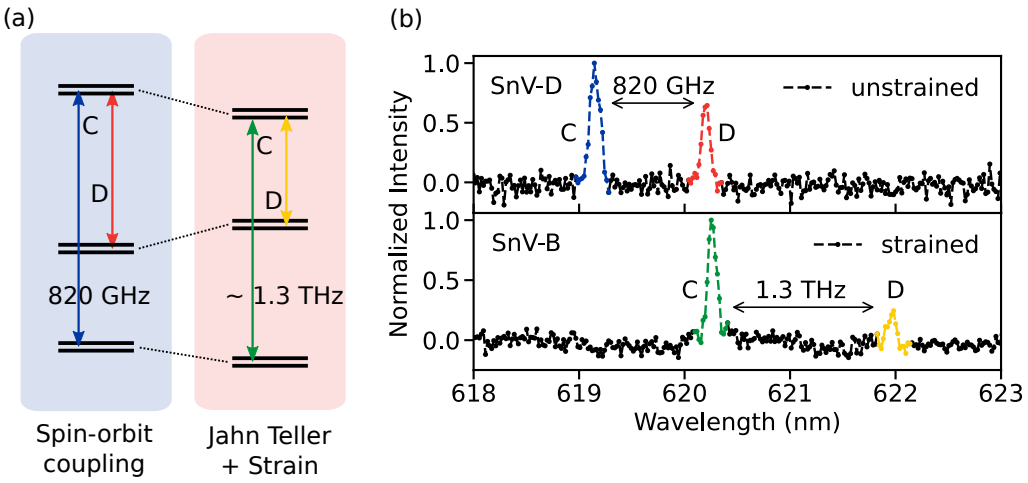

Figure 2.4.: (a) Reduced energy level diagram of an unstrained SnV center (blue panel) and a strained SnV center (red panel). The relevant ZPL transitions are shown for both cases, color-coded to match the transitions visible in the graphs in (b). (b) PL spectrum of an unstrained SnV center (SnV-D), with the C (blue) and D (red) transitions marked in the top graph. Below, the PL spectrum of a strained SnV center (SnV-B) is shown. The measurements were performed at 4 K, where the C and D transitions are the dominant ones. This figure is adapted from Figure 1 in Reference [1].

are depicted in a reduced energy level diagram for an unstrained SnV center (blue panel) and a strained SnV center (red panel), in Figure 2.4 (a). The ZPLs are highlighted with blue and red arrows for the unstrained case and with green and yellow arrows for the strained case. To gain further insight, we now focus on these ZPL transitions from an experimental perspective.

Following off-resonant excitation, such as illumination with high-energy light at a typical wavelength of 532 nm, decay of the electron occurs predominantly via the ZPL transitions, especially below 10 K. The resulting fluorescence from the SnV center can be observed in a photoluminescence spectrum captured by a spectrometer. Figure 2.4 (b) presents such a measurement. The top graph shows the PL spectrum of an unstrained SnV center (SnV-D), highlighting the C (blue) and D (red) transitions. Below, the PL spectrum of a strained SnV center (SnV-B) is displayed for comparison. The ground-state splitting Δ_g can be easily determined by fitting the ZPL transitions and measuring their spectral separation. Then, via Equation 2.27, the pure spin-orbit interaction for the ground state can be determined from measurements on unstrained emitters, such as SnV-D. We determine $\lambda^g = 822(1)$ GHz [1], matching previous reports for HPHT treated samples [68].

In the next section, we will explore the magneto-optical properties of the SnV center. To do so, we must first identify the optical transition frequencies. This will allow for the characterization of the optical stability and for the selection of the best SnV centers, which will then enable us to study the separated optical transitions in a magnetic field environment.

2.4. Magnetic and Optical Properties

In this section, we examine the magneto-optical properties of the SnV center, which play a critical role in its suitability as a qubit for quantum information applications. We begin by characterizing and identifying suitable SnV centers based on their optical properties and explaining how the Stark effect influences the spectral stability of the defects. Building on the insights gained from the fine-structure analysis in the previous Section 2.3, we explore how the energy levels respond to external magnetic fields and how the quantization axis can be determined by leveraging the SnV center's symmetry. We categorize the SnV centers based on the strain magnitude and investigate the orbital quenching factors, which influence the splitting of the ground and excited states under magnetic field perturbations. The goal is to provide a comprehensive understanding of the spin behavior to implement efficient protocols for initialization, manipulation, and readout of the SnV center's electron spin.

Pulsed resonant lifetime and photoluminescence excitation of the SnV center Once the fine structure lines of the ZPLs have been identified via spectroscopy, a narrow-band laser is used to probe the exact optical transition frequency (see Appendix E.1 for details). At cryogenic temperatures, the electron relaxes into the lower ground-state doublet $E_g^{3/2}$, making the C-transition the relevant resonance. A photoluminescence excitation (PLE) spectrum is then recorded by sweeping the laser frequency across the estimated resonance, while detecting emission through the phonon sideband (PSB). When the laser is resonant with the optical transition, the SnV center is driven into excitation, and spontaneous emission via the PSB provides a direct signal of resonance.

By actively driving the identified optical transition on resonance and thereby exciting the electron into the ES, the lifetime τ of the defect can be determined by measuring the decay time of the fluorescence signal after the resonant laser pulse is switched off. Figure 2.5 (a) shows such a measurement for SnV-B, yielding a lifetime of $\tau = 5.22(15)$ ns. The pulsed resonant lifetime of this SnV center has been measured by Jeremias Resch using an electro-optic modulator (EOM). The relationship between the excited-state lifetime τ and the line's full width at half maximum (FWHM) in the energy domain, derived from an exponentially decaying state amplitude is:

$$\Gamma = \hbar\Delta\omega_{\mathrm{FWHM}} = \frac{\hbar}{\tau} \text{ or } \Delta\nu = \frac{1}{2\pi\tau}. \tag{2.28}$$

With a measured lifetime of $\tau = 5.22(15)$ ns, a linewidth of $\Delta\nu = \frac{1}{2\pi\cdot 5.22\cdot 10^{-9}s} = 30.49\,\mathrm{MHz}$ follows in the Fourier-limit. In Figure 2.5 (b), an exemplary measurement of a single-scan photoluminescence excitation spectrum of SnV-B is depicted. Interestingly, despite the considerable strain in SnV-B, its optical properties remain unaffected, demonstrating the suitability of SnV centers for quantum optical integration [74]. The linewidth matches the theoretical lifetime limit, indicating that it is Fourier-limited. The PLE measurement is performed by resonantly sweeping the laser across the optical transition at a scanning speed of $\sim 28\,\mathrm{MHz\,s^{-1}}$. Typically, a low resonant laser power of 1-10 nW is used to excite

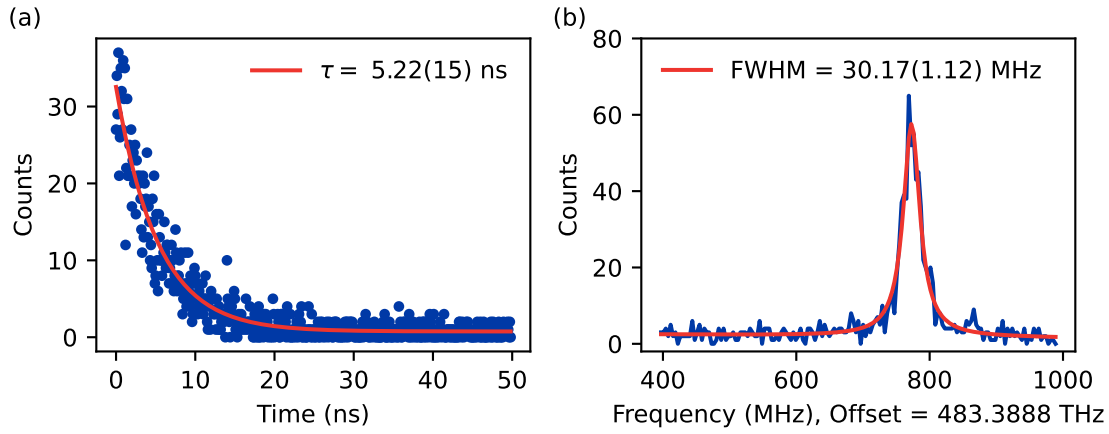

Figure 2.5.: Pulsed resonant lifetime measurement and single PLE scan. (a) shows a pulsed resonant life time measurement, yielding a lifetime of $\tau = 5.22(15)$ ns. (b) single-scan photoluminescence excitation spectrum in of a SnV center. The spectrum is obtained by sweeping the laser across the resonance of the C transition. The data is fitted with a Lorentzian, revealing a lifetime-limited width of 30.17(112) MHz.

the defect and to avoid power broadening.[2] The low excitation power, combined with a stable charge environment of the emitter, allows the resonance to be probed without the need for charge repumping, as commonly required in comparable studies [70, 73]. This capability is highly advantageous for subsequent coherent control measurements on the SnV center (see Section 4), where initialization is achieved by continuously and resonantly driving of the electron until emission occurs via an optically spin-flipping transition (see Section 2.5.1). The reduced need for a repump pulse significantly simplifies the measurement scheme, facilitating the overall experimental process.

2.4.1. Spectral Stability

In the following we will identify and discuss the factors that negatively impact the optical properties of Group-IV defects. There are two primary factors limiting optical stability. The first is charge instability, which is caused by a transition of the SnV center into the non-resonant charge state SnV^{2-} [92], with differing energy levels from the SnV^{-} center [93]. This instability complicates long-term operation, necessitating periodic charge-state reset via off-resonant repump pulses to maintain the emitter in the desired charge state SnV^{-} [69, 70]. The second limiting factor is spectral diffusion, which manifests as fluctuations in the optical transition frequency over time. These fluctuations arise from electric field variations near the defect, mainly caused by electrons hopping between adjacent vacancies or lattice defects [63].

We focus on the spectral stability by considering the sensitivity of atom-like defects to static electric fields. Atom-like defects are sensitive to static electric fields via the well-known

[2] We use $\frac{p}{p_{\text{sat}}} < 1$, where p_{sat} is the saturation power of the defect. We discuss the influence of the excitation power on initialization and emission in detail in Section 2.5.1.

DC Stark effect. However, unlike non-inversion symmetric color centers, such as the nitrogen vacancy center in diamond, the inversion symmetry of the SnV center suppresses the linear Stark effect, resulting in a negligible linear response and a pronounced nonlinear Stark effect [64]. This characteristic allows Group-IV defects to be effectively integrated into nanostructures while preserving their favorable optical properties, including low spectral diffusion and near lifetime-limited emission [94].

In the following, we will discuss the influence of varying electric fields. The Stark shift to the electronic transition, induced by an electric field F acting on the defect, is described to second order by:

$$h\Delta\nu = -\Delta\mu F - \frac{1}{2}\Delta\alpha F^2, \tag{2.29}$$

with Planck's constant denoted by h and the frequency shift $\Delta\nu$. Further, $\Delta\mu$ is the change in the dipole moment and $\Delta\alpha$ represents the polarizability difference between the excited and ground states [64, 95]. Due to the inversion symmetry of the SnV center the permanent dipole moments of the ground and excited state are negligible, i.e. there is no charge separation within the system. On the other hand, the polarizability describes how easily a dipole moment can be induced (by distorting the electron cloud) through an external electric field. The greater the difference in polarizability between the ground state and the excited state, the more pronounced the change in the transition frequency due to the quadratic scaling of the interaction. Therefore, if $\Delta\alpha$ dominates, we can estimate the influence of a localized charge e in the proximity of the SnV center by

$$h\Delta\nu \sim \frac{\Delta\alpha}{r^4} \tag{2.30}$$

where the spectral shifts scale with the fourth power of the inverse distance r of the charge. This relationship implies that the SnV center is insensitive to background electric field noise but highly sensitive to nearby charges. In particular, bistable charges jumping between damaged lattice sites, introduced during ion implantation, can significantly affect the spectral stability [63].

Two studies, one by De Santis et. al [64] and the other by Aghaeimeibodi et. al [96], investigated the Stark effect in the SnV center through direct current electrical tuning, accurately measuring the resonance frequency shift as a function of the local electric field at the defect. These investigations demonstrate that the permanent electric dipole moment and polarizability of the SnV center are several orders of magnitude smaller compared to NV centers in diamond [96] and mark the first direct confirmation of the inversion symmetry protection characteristic of Group-IV defects [64]. The results indicate an almost negligible permanent electric dipole moment and low polarizability. The quadratic shift coefficients reported range from $\delta\alpha = 0.051\,\mathrm{MHz\,m^2\,MV^{-2}}$ [3] [64] to $\delta\alpha = 0.275\,\mathrm{MHz\,m^2\,MV^{-2}}$ [4] [96],

[3] In [64], the original value is directly given as the quadratic frequency shift.

[4] The original polarizability value in [96] is given by $\Delta\alpha = 0.55\,\mathrm{MHz\,m^2\,MV^{-2}}$, which corresponds to a frequency shift $2 \cdot \Delta\nu$, therefore, we use half of this value for $\delta\alpha$.

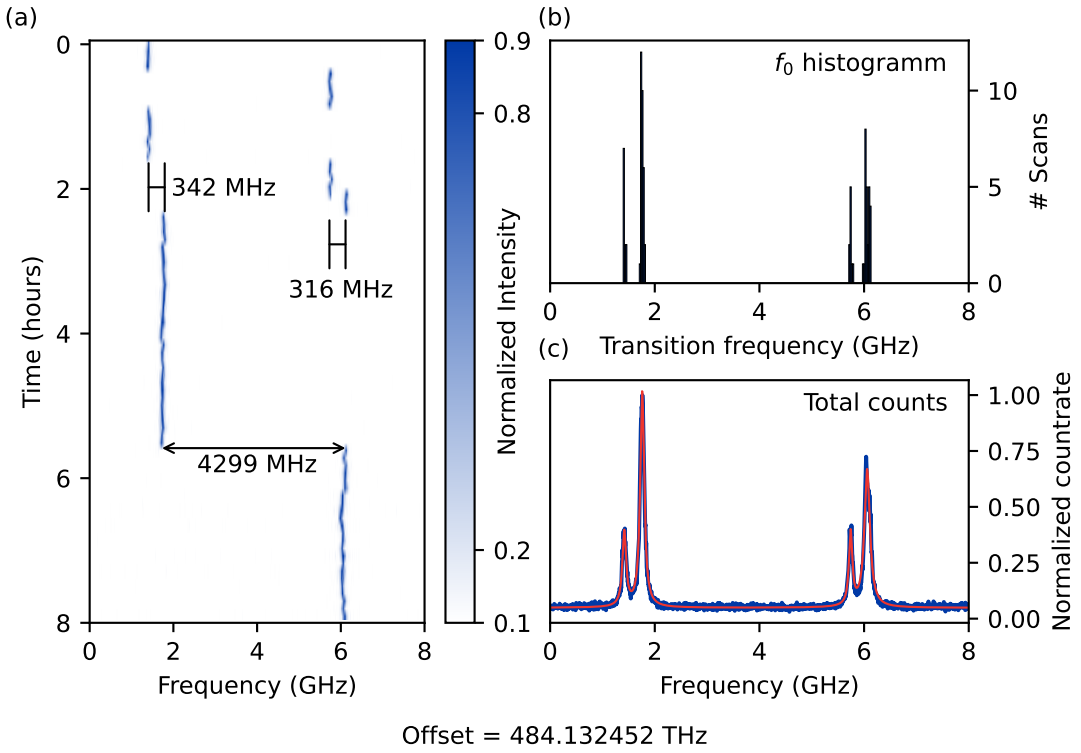

Figure 2.6.: Multistable SnV center. (a) shows 8 h photoluminescence excitation measurement of an SnV center, showing two stable optical positions separated by ∼ 4.3 GHz and ∼ 330 MHz. In (b) the central positions of the fitted PLE scans from (a) are histogrammed, illustrating the distribution of the observed spectral shifts. In (c) the total counts of all PLE scans that are fitted with Lorentzian curves highlight the distinct optical resonances.

respectively. Thereby, the quadratic frequency shift induced by an effective electric field F_{eff} acting on the SnV center, is expressed as:

$$\Delta\nu = -\delta\alpha \cdot F_{\text{eff}}^2. \tag{2.31}$$

We can estimate the electric field F_{C} from a nearby point charge q in the diamond acting on the SnV center using Coulomb's law [97], where the electric field amplitude follows as:

$$F_{\text{C}} = \frac{q}{4\pi\epsilon_0\epsilon_r} \cdot \frac{\vec{r}}{r^3}. \tag{2.32}$$

where q is the charge, ϵ_0 is the vacuum permittivity and $\epsilon_r = 5.7$ the relative permittivity for diamond [98] . Here, $\vec{r}$ is the vector pointing from the point charge to the SnV center, and r is the magnitude of this vector, representing the distance between the charge and the defect.

We want to make a simple assumption, namely, that electrons hop from far away into lattice defects or vacancies near the SnV center, and we aim to estimate the distance of the charge to the SnV center. To achieve this, we shift our attention to an SnV center with multistable optical transition frequencies, depicted in Figure 2.6 (a). This SnV center

exhibits clear signs of spectral jumps with separations of approximately 4.3 GHz and 330 MHz. These frequency shifts suggest changes in the local electric field due to a nearby charge.

Using the magnitude $\Delta\nu$ of the spectral shifts, we estimate the distance of the charge from the SnV center by calculating the electric field with Equation 2.32 that would cause such a spectral jump, as determined through Equation 2.31. For the estimation of the distance r, we assume a mean value of $\delta\alpha = 0.2\,\mathrm{MHz\,m^2\,MV^{-2}}$, consistent with the order of magnitude reported in the studies by De Santis and Aghaeimeibodi. For the determined frequency shifts, we obtain the distances:

$$
\begin{aligned}
r &= \left(-\frac{\delta\alpha}{\Delta\nu} \cdot \left(\frac{q}{4\pi\epsilon_0\epsilon_r} \right)^2 \right)^{\frac{1}{4}} \\
\rightarrow r\big|_{\Delta\nu=4.3\,\mathrm{GHz}} &= 1.32\,\mathrm{nm} \\
\text{and } r\big|_{\Delta\nu=0.33\,\mathrm{GHz}} &= 2.5\,\mathrm{nm}.
\end{aligned}
$$

The narrow histogrammed transition frequencies in Figure 2.6 (b) of the PLE scans from (a) demonstrate that the jumps are discrete, with no indication of overall spectral diffusion, even after the long scanning duration of eight hours. Additionally, the summed counts of all PLE scans are shown in (c) and are fitted with Lorentzian curves to highlight the distinct optical resonances. Interestingly, the investigated SnV center maintains its charge state over the entire duration of the scan, making sequential off-resonant repumping unnecessary, as required in comparable studies [70, 73, 93], except in rare cases[5]. The use of low resonant excitation power in the nanowatt range, combined with an overall stable charge environment of the emitter, thus allows the resonance to be probed continuously without the need for charge repumping.

In the following, we pursue a simple idea: if the lattice environment of the SnV center is as defect-free as possible, then the spectral diffusion should be minimal, and the charge stability correspondingly higher. This is because the SnV center would be less likely to ionize by losing its charge to nearby lattice defects or vacancy. Hence, we meticulously characterize all detected SnV centers following the workflow diagram in Figure 2.7, to determine suitable SnV centers for coherent control and precise fine-structure analysis. The process begins with a spatial scan of the area of interest under resonant excitation. The spatial scan under resonant excitation is to be understood as a scan where SnV centers coincidentally match the set laser frequency, thereby identifying emitters around ~ 619.2 nm. For unstrained samples, we limit the search range to approximately ± 100 GHz around 484.130 THz, aiming to find SnV centers comparable to the high-quality SnV centers identified in high-temperature, high-pressure samples from the study by Narita et al. [68].

[5] In general, it is advisable to optimize for parameters such as spatial position, z-focus and excitation power of the resonant laser in a way that yields optimal countrates while maintaining the charge state of the SnV center unaffected during a continuous excitation of several minutes. This enables the acquisition of long-term PLE measurements, or more complex coherent control measurements, where the charge state remains stable for several days.

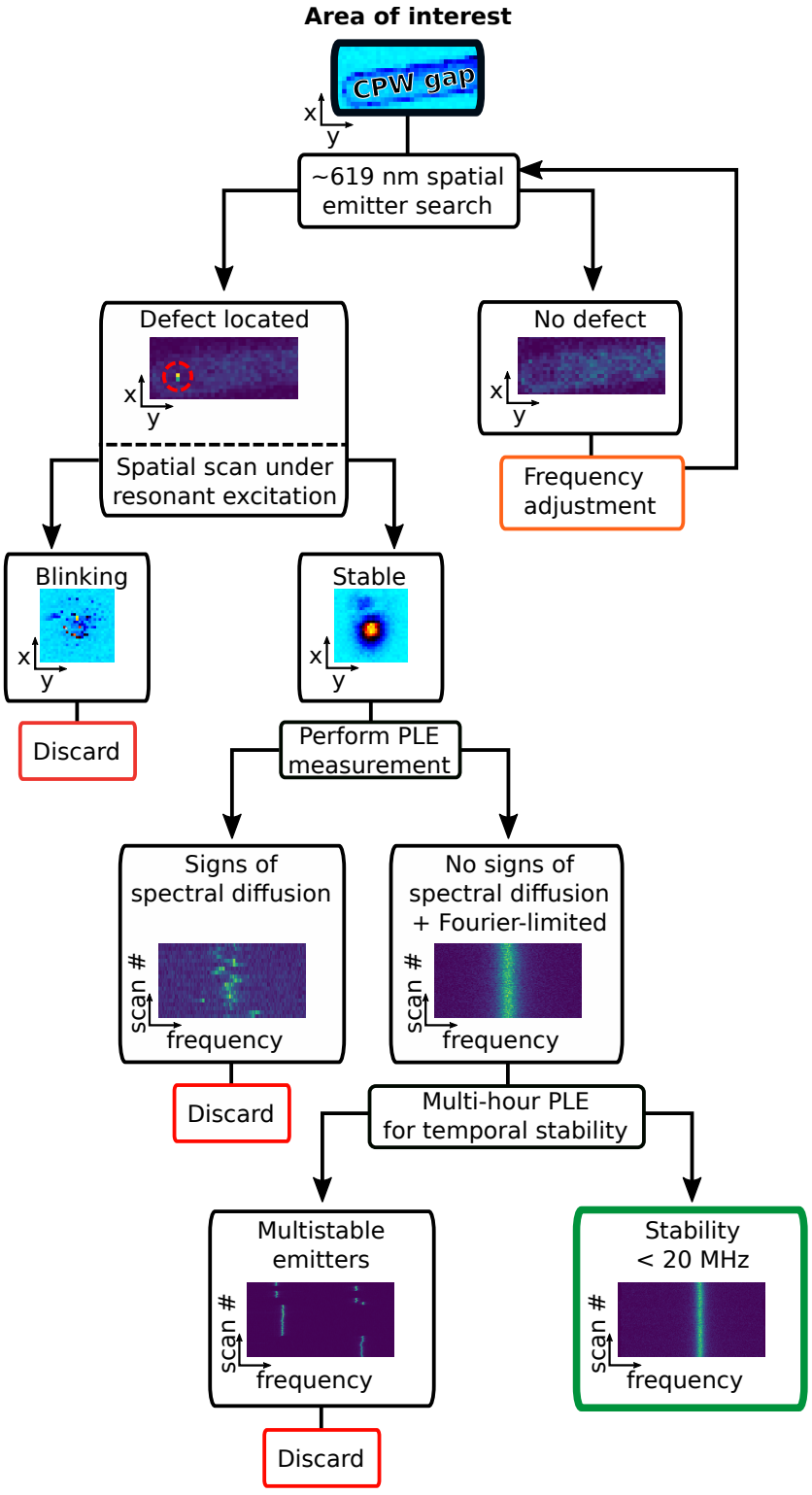

Figure 2.7.: Workflow for identifying and characterizing emitters. The process begins with a spatial scan under resonant excitation, identifying emitters around ~ 619 nm within the are of interest (here: coplanar waveguide gap). Emitters are categorized by stability, with SnV centers exhibiting any instability immediately discarded. Multi-hour PLE measurements are conducted on Fourier-limited defects for temporal stability verification. Defects showing multistability or spectral diffusion exceeding > 20 MHz are also discarded.

In the example shown in the referenced figure, we scan one end of the coplanar waveguide gap to locate all SnV centers within this specific region. If an emitter has a resonant transition matching the laser frequency, we detect a burst of fluorescence counts. If no fluorescence is detected, we adjust the laser frequency in small steps of 50 – 100 MHz and rescan the same region. In the first step, we categorize all detected SnV centers by checking for a stable emission count rate under resonant excitation. If we observe any signs of telegraph-like fluorescence[6] or blinking behavior[7], we discard the defect immediately. If the SnV center shows a stable emission, we perform initial PLE measurements to determine the linewidth and check for signs of spectral diffusion or narrow spectral jumps. We discard all emitters that are not Fourier-limited or exhibit short term spectral diffusion. In the final step, we conduct multi-hour PLE measurements to assess the long-term stability of the SnV center. Defects exhibiting multistability or spectral diffusion exceeding 20 MHz are also discarded. Although this entire process is time-consuming and yields a low number of suitable emitters[8] we believe the effort is justified. The use of carefully selected SnV centers significantly simplifies subsequent measurements and ensures high-quality results. We observe that defects identified through this process remain spectrally stable even when a charge repump is required, as there are no nearby defects that can be populated by excited electrons to cause spectral jumps. To regain the SnV^- charge state, if lost, we use an excitation power of $\sim$ 50 nW for the off-resonant 532 nm laser pulse. This ensures that the overall surrounding charge environment of the SnV center remains unchanged. Using higher off-resonant excitation powers can shuffle the local charge environment [93] and cause an offset in the effective transition frequency. Although this is an interesting aspect that could be used to spectrally overlap two defects with simple means, it is counterproductive in our case.

In Figure 2.8, the linewidth and optical stability of the highly strained SnV center (SnV-B), which fulfills all the aforementioned criteria, are illustrated. This defect is used in the subsequent coherent control measurements in Section 4. Panel (a) shows the photoluminescence excitation of the C transition recorded over a period of four hours. Notably, the defect's transition line remains visible across 400 individual sweeps without the need for charge state repumping, again demonstrating the exceptional stability and potential of the SnV center. The center position of the resonance is tracked for all sweeps and the resonance's frequency shift is histogrammed in Figure 2.8 (b). This benchmarks the stability of the resonance position, revealing a stable behavior. In this particular defect, the center position drifts less than 20 MHz over the whole duration of the PLE scans. In addition, we histogram the linewidth and fit the data to a log-normal distribution. The fitted histogram is shown in Figure 2.8 (c), yielding a mean Fourier-limited linewidth of 28.05(344) MHz. This analysis is necessary to confirm the spectral quality of the SnV

[6] If the SnV center exhibits discrete spectral jumps, the fluorescence will display telegraph-like behavior, as the resonance of the defect moves off and on the laser frequency.

[7] Under strong resonant excitation, some SnV centers exhibit blinking behavior, likely due to charge state transfer [93].

[8] In the diamond samples used for the measurements in this thesis, we achieve a yield of less than 1 %

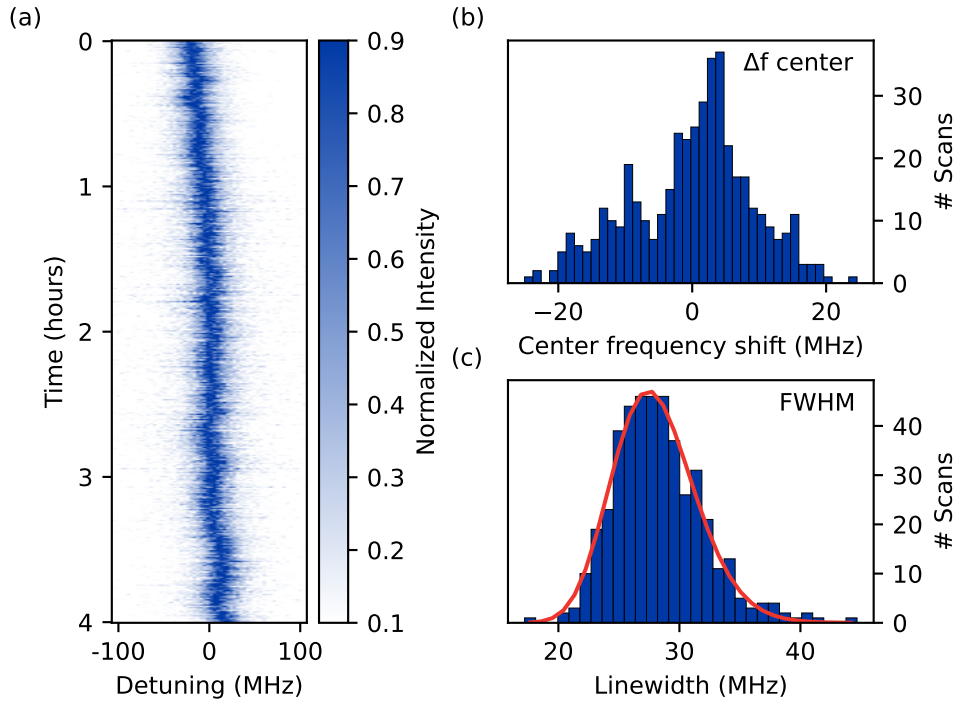

Figure 2.8.: Linewidth and optical stability of the SnV center. (a) displays the PLE of the C transition over a duration of four hours, consisting of a total of 400 single sweeps. (b) illustrates the stability of the resonance position, showing spectral diffusion below 20 MHz. (c) Histogram of the linewidth from the PLE scans. The data are fitted to a log-normal distribution with a mean Fourier-limited linewidth of 28.05(344) MHz.

center, as a Fourier-limited linewidth indicates minimal phonon-mediated dephasing and highlights the defect's suitability for high-fidelity quantum operations.

2.4.2. Magnetic Field Interaction

To utilize the SnV center as a potential candidate for quantum information applications, it is necessary to quantify the properties of the ground and excited states under strain. More importantly, the relevant qubit transitions must be determined and characterized, particularly in the presence of an external magnetic field, where the fine structure of the electron levels becomes fully resolved. We will first explore the fine structure of the SnV center under two very specific configurations of the external magnetic field to gain an initial understanding of the defect's magnetic properties. Figure 2.9 (a) illustrates the energy levels of the SnV center under a magnetic field $B_{\parallel}$ parallel to the SnV-center's quantization axis. In (b), a matching PLE measurement for a parallel magnetic field sweep from $-100\,\mathrm{mT}$ to $100\,\mathrm{mT}$ is shown. In contrast, Figure 2.9 (c) presents a PLE measurement of the SnV center during an angular DC magnetic field sweep for mainly perpendicular magnetic field $B_{\perp}$ at constant field strength.

Figure 2.9 (a) is key to understand the energy levels of the SnV center. It illustrates the reduced energy level diagram of a lower-strained SnV center in the left panel with a ground state splitting of $\Delta_{\mathrm{g}} \sim 825\,\mathrm{GHz}$, corresponding to a strain value of $\alpha^{\mathrm{g}} = 35\,\mathrm{GHz}$. In a magnetic field, the electron Zeeman effect lifts the remaining two-fold degeneracy, as illustrated in the right panel. The energy levels are adjusted to reflect the splitting differences for a magnetic field parallel to the SnV's quantization axis. This behavior can be intuitively derived from the final Hamiltonian in Equation 2.25 (Section 2.2), under the conditions of negligible strain and zero transverse magnetic field. In simple terms, the $E_{\mathrm{g,u}}^{3/2}$ doublets exhibit a stronger splitting for $B = B_{\parallel}$ due to the parallel alignment of the orbital and spin magnetic moments, while the $E_{\mathrm{g,u}}^{1/2}$ doublets shows a weaker splitting due to the anti-alignment of these moments. In this reduced energy level diagram, only $E_{\mathrm{g}}^{1/2}$ is depicted, for clarity. The resulting optically allowed transitions (A1 and B2) to the excited state are shown with solid arrows, while the forbidden transitions (A2 and B1) are indicated with dashed arrows.

Figure 2.9 (b) shows the diverging transitions of A1 and B2 with increasing magnetic field strength. From the energy level structure shown in (a) it is clear, that the spin Zeeman effect cancels out for the two transitions, and the difference translates directly to the deviation in the orbital Zeeman effect between the ground and excited state orbitals. We will discuss the details in the following section.

Figure 2.9 (c) aims to demonstrate the peculiar interaction of the SnV center with primarily transverse magnetic fields. The color plot displays all optical transitions (both allowed and forbidden) for an angular DC magnetic field sweep with a constant field strength of $B = 200\,\mathrm{mT}$ around the perpendicular axis of the SnV center. Without going into the experimental and theoretical details, we briefly discuss the key characteristics evident from the measurement.

One can observe that the optically forbidden transitions, whose progression are overlaid with dashed-line fits, are prominent when a purely perpendicular magnetic field ($\theta = 0°$) is acting on the SnV center. These transitions fade as the magnetic field deviates from

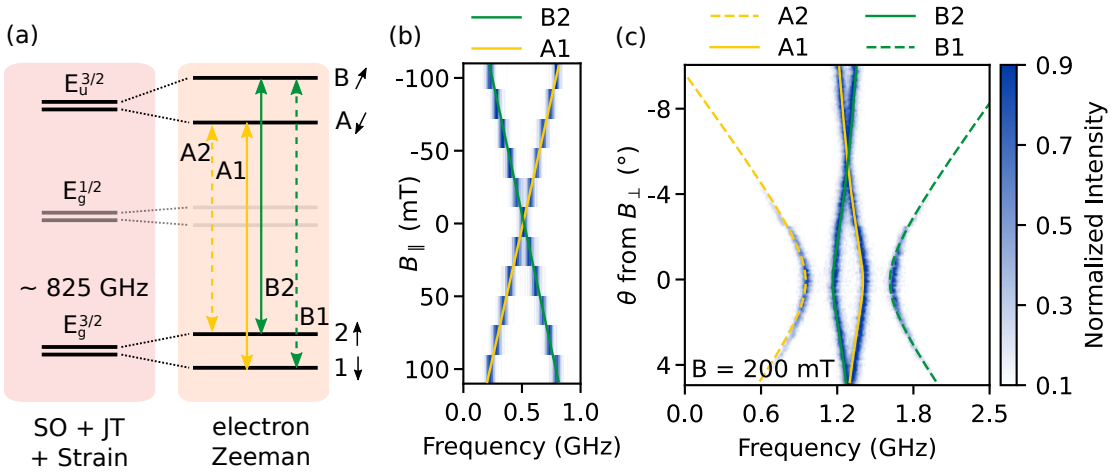

Figure 2.9.: Reduced energy level diagram with electron Zeeman effect. (a) shows the energy level diagram of a lower-strained SnV center (left panel) in a magnetic field environment (right panel). The electron Zeeman effect lifts the remaining two-fold degeneracy, with the lower ground state doublet used for quantum control. The optically allowed transitions (A1 and B2) to the excited state are shown with solid arrows, while the forbidden transitions (A2 and B1) are indicated with dashed arrows. (b) shows a matching PLE measurement for varying parallel magnetic field strength. In (c), optical transitions are shown for an angular DC magnetic field sweep around the perpendicular axis of the SnV center, displaying the crossings and anticrossings of the different transitions. Under this configuration, the selection rules are relaxed, making the forbidden transitions visible alongside the allowed ones.

the perpendicular direction, indicating a dependence of the transition cyclicity on the magnetic field orientation. This effect and its implications for the initialization properties of the SnV center will be discussed in more detail in Section 2.5.1.

For the allowed transitions, one would intuitively expect a crossing for perfect perpendicular field alignment, in the absence of strain. However, even in a weakly strained environment, the degeneracy is lifted under this configuration, and the crossing occurs when the magnetic field deviates from the perpendicular direction. The qubit frequency of the lower ground-state doublet can be directly determined by measuring the difference between the dashed and solid yellow transitions (A1 - A2) or the green transitions (B1 - B2), respectively. A clear minimum in the qubit frequency occurs near the perpendicular field orientation, with the frequency increasing as the field deviates from this orientation. Additionally, the splitting of the lower excited-state doublet can be determined in a comparable manner by calculating the difference between the transitions B1 - A1 or B2 - A2, respectively. We observe that the excited-state qubit frequency increases more rapidly as the magnetic field deviates from the perpendicular direction. This provides an initial intuition for the orbital quenching factors: since the $E_{g,u}^{3/2}$ doublet features aligned orbital and spin magnetic moments, the quenching factor for the excited state must be larger (indicating less quenching) than that for the ground state. This explains the faster increase in the excited-state qubit frequency compared to the ground state. We will now discuss how to determine the SnV center's quantization axis, strain and the quenching factors, in detail.

2.4.3. The SnV Center under Angular Magnetic Field Sweeps

In the following, we want to explore the magnetic properties of multiple SnV centers by analyzing their behavior under varying magnetic field configurations and strain conditions. Using detailed photoluminescence excitation measurements we create optical transition maps to illustrate how the magnetic field orientation influences the electronic ground and excited states. We begin by analyzing the response of an unstrained SnV center to angular magnetic field sweeps, highlighting the lifting of degeneracies and demonstrating how to determine its exact quantization axis, which is defined by the interplay of spin-orbit coupling and the diamond lattice symmetry. Subsequently, we examine the optical transitions of SnV centers under low-strain, and high-strain conditions. Next, we discuss the quenching factors for the ground and excited state doublets, which quantify the suppression of orbital magnetic moments due to symmetry and strain effects. By leveraging the symmetry of the Hamiltonian, we provide a straightforward method to approximate these parameters and gain insight into the orbital contributions to the magnetic response. Finally, by fitting the spin Hamiltonian to an extended set of experimental data of both optical and magnetic transitions, we achieve a precise determination of the strain and magnetic field parameters that dictate the energy level splittings.

The precisely determined quenching factors enable a straightforward method for estimating the strain magnitude in previously uncharacterized defects, by either measuring the qubit frequency or the two optically allowed transitions at a known magnetic field angle. This approach significantly simplifies the characterization process for new SnV centers and allows us to infer the optical and qubit transitions for all other angles, simplifying the experimental overhead. Together, the following analysis offers a comprehensive picture of the SnV center's magnetic characteristics that are essential for robust spin qubit applications.

Symmetry of the unstrained SnV center With the derivation of the effective Hamiltonian in Section 2.2, we expect to observe specific symmetries in the SnV center's properties during angular magnetic field sweeps. The optically allowed transitions A1 and B2 are the simplest to measure with high precision. With this in mind, we perform angular sweeps of the magnetic field while observing these transitions in the lab frame of our experimental setup. In practice, this involves fixing the magnetic field strength, for example to $B = 200\,\mathrm{mT}$ in the experiment, and rotating the field direction at first within the xy-plane of the lab system. Assuming, of course, that the magnetic coils are calibrated or that their field strength is known with sufficient certainty. Regarding the calibration of our coils we refer to Section C.3.2.

Since the diamond sample is glued with its surface approximately parallel to the xy-plane, aside from minor misalignments, we anticipate a rotationally symmetric pattern of the transitions. Given the four possible orientations of the SnV center in the diamond lattice, dictated by crystal symmetry, this sweep allows us to directly determine the projected orientation of the SnV center within the lattice on the xy-plane.

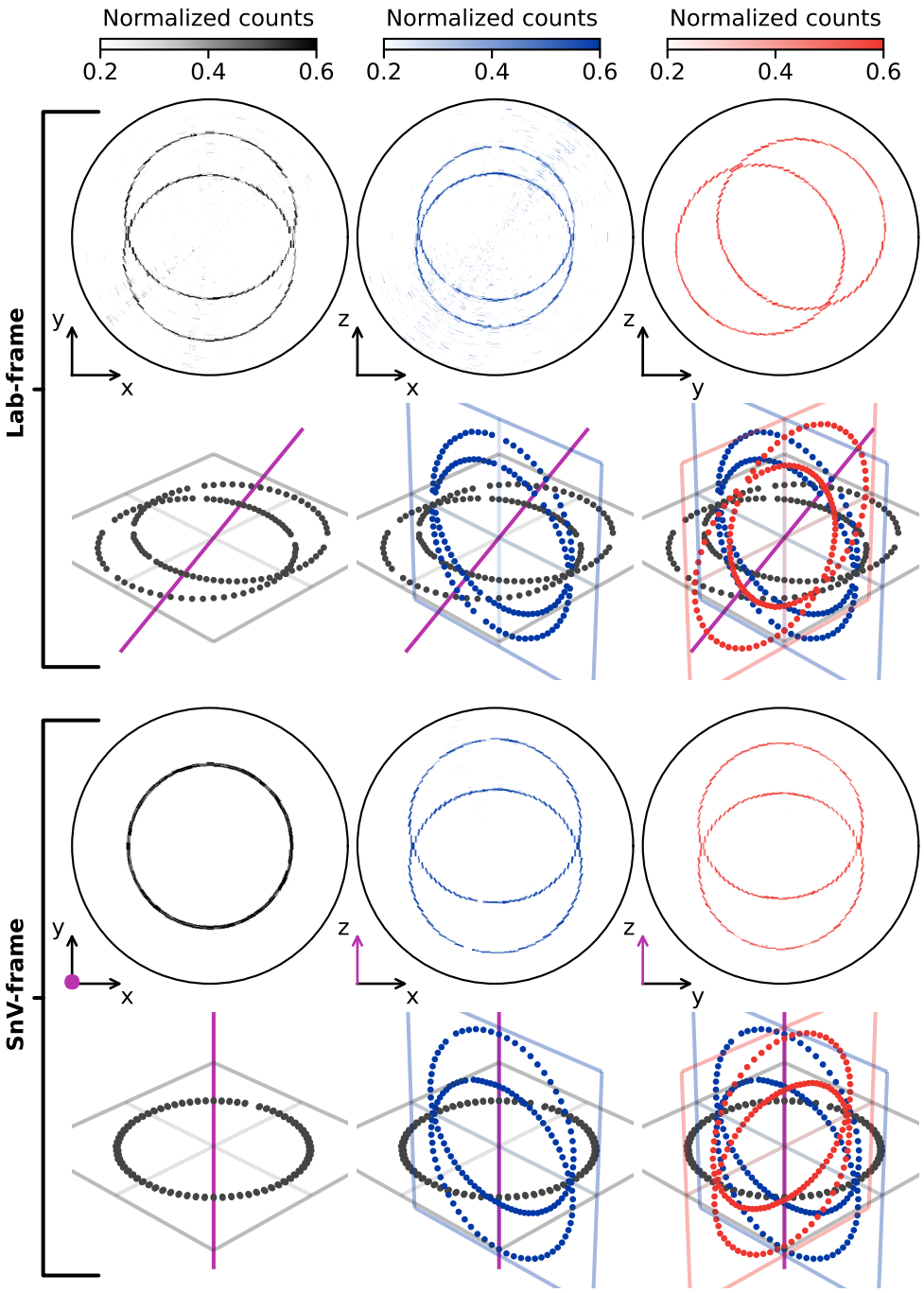

Figure 2.10.: Magneto-optical properties of an unstrained SnV center (SnV-E) under angular magnetic field sweeps. Lab frame: The magnetic field is swept in the three planes *xy*, *xz*, and *yz*, from left to right—in the laboratory frame, as defined by the axes of the 3D vector magnet. For each angle in the measurement plane, a single PLE measurement is performed, which determines the radial axis of the resulting polar plots. The resonance positions of the measured allowed transitions, A1 and B2, are plotted with color-coding in a 3D plot below each polar plot, with each plane added from left to right and the axis of the SnV center indicated in purple. SnV frame: The same measurements are conducted in the reference frame of the SnV center, aligned along the *z*-axis, demonstrating the system's radial symmetry. For all sweeps, the magnetic field is held constant at 200 mT.

In our experiment, we use a square diamond membranes with a width of 1 mm, cut along the $\langle 110 \rangle$ directions and oriented with a (001) surface. Hence, we expect the symmetry axis projected onto the xy-plane to be oriented either in the x or y direction, regardless of the spatial axis in which the defect is aligned along z.

As demonstrated in Figure 2.10, this behavior is clearly observable in the top-left polar plot. This image shows PLE measurements spanning a scan range of 3.3 GHz, where the laser scan frequency is represented on the radial axis, and the magnetic field direction is represented in polar coordinates. The resolution of the field direction, denoted as $\Delta\phi$, is 5°. Each PLE measurement is fitted with Lorentzians for each direction to precisely determine the transition frequencies of A1 and B2. The resonance positions of these allowed transitions are further depicted with color-coding in a 3D plot below the polar plot, aligned in the xy plane of the image.

While the axis of the SnV center in the lab frame is indicated by the purple line in the 3D plot, a single-plane scan is insufficient to determine this axis correctly. To achieve a precise determination, we repeat the measurement in the xz plane. The corresponding PLE measurements are shown in the top center panel, and the A1 and B2 transitions are added to the 3D plot below in blue. In theory, scanning two planes is enough to determine the exact quantization axis of the system. However, for greater reliability, especially if the scanned planes do not align closely with the SnV center's quantization axis, it is advisable to perform a third scan. Therefore, we conduct an additional measurement in the yz plane, depicted in the top right panel with red coloring. By combining all three scans, the quantization axis of the measured SnV center becomes clearly visible in the 3D plot. The measured vectors representing the SnV center's quantization axis $\vec{v}_{\parallel,z}$ and its corresponding perpendicular directions $\vec{v}_{\perp,x/y}$ are given by:

$$\vec{v}_{\parallel,z} = \begin{bmatrix} 0.0294 \\ 0.8419 \\ 0.5388 \end{bmatrix}, \quad \vec{v}_{\perp,x} = \begin{bmatrix} 0 \\ 0.5390 \\ -0.8423 \end{bmatrix}, \quad \vec{v}_{\perp,y} = \begin{bmatrix} -0.9996 \\ 0.0248 \\ 0.0158 \end{bmatrix}.$$

With the given vectors and the corresponding conversion factors for the magnetic coil's field strength, we can repeat the measurements in the SnV-frame. This serves two purposes: first, to validate the correct determination of the quantization axis, but more importantly, to precisely determine the energy levels of the defect. These energy levels are essential for the subsequent fitting of the Hamiltonian's quenching parameters.

The scans in the SnV-frame are illustrated in the lower half of Figure 2.10 and follow the same ordering as in the lab-frame. The z axis of the SnV center is shown as a purple dot in the coordinate axis pictogram and as a solid axis in the 3D plots. The rotational symmetry is clearly visible as a perfect circular transition band in the xy plane. For this unstrained emitter (SnV-E), the degeneracy of the doublets is nearly preserved, with only minimal splitting observed for a purely perpendicular magnetic field.

Since the qubit frequency is fundamentally defined by the difference between the optical transitions A1-A2 or B1-B2, it becomes immediately clear that for quasi-unstrained emitters,

operating at a field that is purely perpendicular to the quantization axis is unfavorable. This is because particularly high field strengths, which can negatively impact properties like the spin relaxation time T_1 (as discussed in Section 2.5.2), are required to achieve sufficient spectral separation of the transitions. Avoiding spectral overlap during electron spin initialization is essential to achieve high-fidelity control. Nevertheless, there are also advantages to performing the measurements with a perpendicular magnetic field. On the one hand, this orientation helps to isolate the SnV center from perturbations, such as the electron spin bath noise in the surrounding of the SnV center [9] [1, 70]. On the other hand, coherent control of the electron spin can be significantly more efficient under this field configuration [10] [84]. We will skip the details for now but will revisit and explain them later in the course of this work.

As the field orientation shifts from perpendicular to parallel, the transitions visibly separate, reaching a maximum energy splitting at $B = B_{\parallel}$. The polar scans in the xz and yz planes, are shown in the lower center and lower right panels, respectively. These scans further demonstrate the perfect rotational symmetry of the SnV center.

Strain-dependent optical transitions in SnV centers Figure 2.11 compares the optical transitions of an unstrained (SnV-E), lower-strain (SnV-A), and higher-strain (SnV-B) SnV center. These transitions are measured in the SnV-frame of each respective defect, using the same approach as described for SnV-E in the figure above. This comparison provides useful insight into the effects of strain on the system's optical properties. Here, the z axis aligns along the SnV center's symmetry axis and is marked in red. The unstrained SnV center, that is already described in the previous figure, serves as a reference for comparison with the strained defects. Introducing strain leads to the lifting of the degenerate states for perpendicular magnetic field. For the lower strain SnV center, both allowed and both forbidden transitions become visibly seperated. The strain-induced mixing of the orbital states relaxes the selection rules for this defect, making forbidden transitions accessible for measurement.

In the higher-strain case, the strain results in the splitting of the forbidden transitions to a level far beyond the scanning range of 3.3 GHz for an overall magnetic field strength of 200 mT. This highlights the sensitivity of the SnV center to strong strain together with a magnetic field.

In all, these results confirm that the symmetry of the SnV center remains intact, even under significant strain, and demonstrate the ability to probe both, allowed and forbidden transitions, depending on the strain environment. These measurements highlight the importance of understanding strain effects for optimizing the handling of SnV centers.

[9] The free electron Larmor precession scales faster than that of the SnV under perpendicular field orientation, effectively decoupling them. See Section 4.1.2 for details.

[10] Strain is essential for effective microwave control, enabling efficient driving of the electron spin for nearly arbitrary DC field orientations. See Section 4.1 for details.

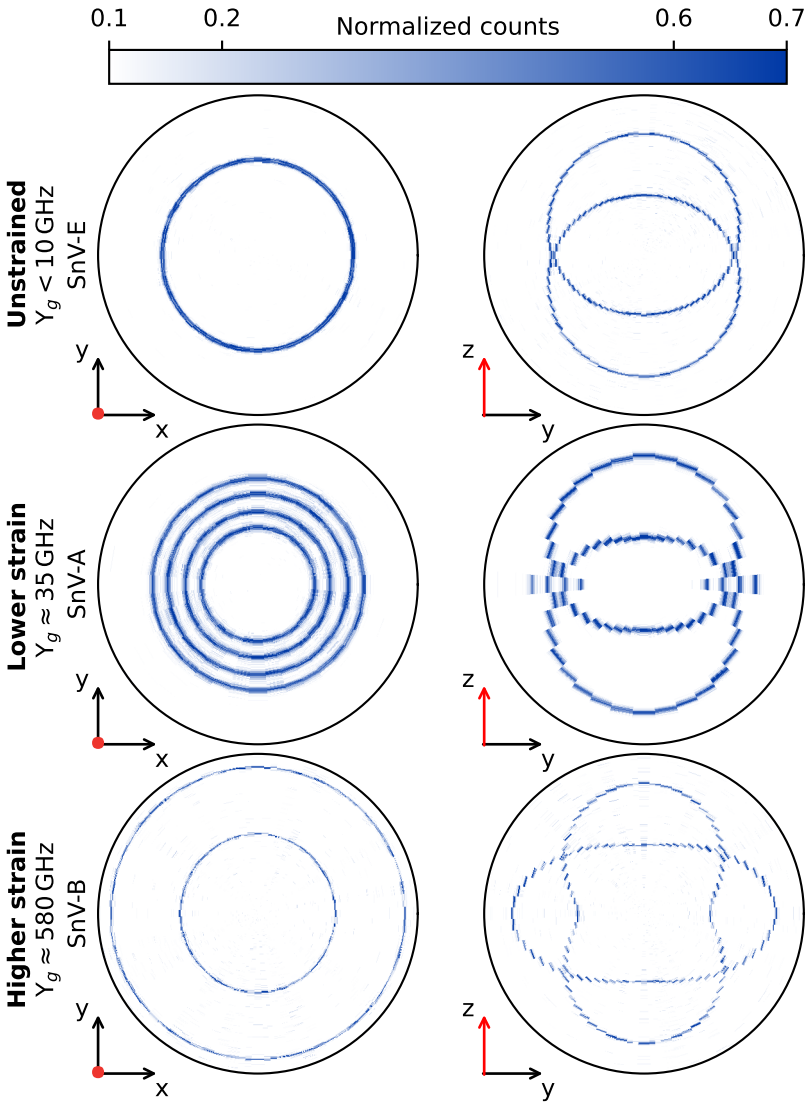

Figure 2.11.: Measured transitions of unstrained, lower strain and higher strain SnV centers. The magnetic field is rotated within the respective frame of the SnV center at constant strength of 200 mT, where the z axis aligns with the symmetry axis of the SnV center, as indicated in red. For the unstrained case, the resulting blue circles in the xy-plane correspond to the fourfold degenerate optical transitions. Under lower strain the degeneracy of the allowed and forbidden transitions is lifted and for this specific SnV center, the selection rules are relaxed, making the forbidden transitions visible alongside the allowed ones. In the case of higher strain, only the A1 and B2 transitions are visible, as the forbidden transitions are split far out of the scanning range. The measurements demonstrate that the symmetry of the SnV center is preserved in the strained environment. Parts of the figure are adapted from Figure 2 in Referece [1].

2.4.4. From Quick Estimates to Comprehensive Quenching Factor Analysis

In the following, we discuss the orbital quenching factors of the SnV center, introduced during the derivation of the Hamiltonian in Section 2.2. These parameters play a defining role in the orbital Zeeman interaction and are crucial to estimate the qubit frequency for arbitrary fields. This is particularly helpful for partly characterized or uncharacterized emitters, where finding the optical transition can be challenging below 4 K. Due to the long spin relaxation time of the SnV center at these temperatures, the optical transitions turn dark under resonant excitation when a magnetic field is applied. Continuous excitation eventually pumps the electron spin into the opposite state[11], making it difficult to identify the optical transition. This process is the same mechanism used to initialize the electron spin for coherent control measurements. Furthermore, if the optically allowed transition is not precisely hit, measuring the qubit transition becomes nearly impossible because the required population transfer cannot be probed.

To estimate the quenching factors through an intuitive approach, we explore the orbital and spin Zeeman interactions in combination with straightforward experimental measurements of the optically allowed transitions and the qubit frequency. This includes leveraging the symmetry of the Hamiltonian under specific constraints, such as the absence of strain. These measurements provide initial estimates for a precise determination by fitting the complete Hamiltonian to extended experimental data from SnV centers with varying strain magnitudes.

First, we want to recap the key points regarding the orbital quenching factors. Unlike the conventional approach, which averages the quenching factors across the doublet states, we assign separate values to each doublet, corresponding to their m_j values. This distinction is particularly important for SnV centers, given their strong spin-orbit coupling of approximately ~ 820 GHz. Especially in low to moderate strain environments averaging can lead to significant inaccuracies. By analyzing the orbital mixing across varying strain magnitudes, starting with unstrained emitters and progressing to highly strained ones, we achieve a precise determination of the orbital quenching.

We will follow the same approach as in Karapatzakis, Resch et al. Phys. Rev. X 14, 031036 [1], but provide a more detailed description of the process and visualize the results through straightforward measurements. The eigensvalues of the Hamiltonian described in Equation 2.25, correspond to the diagonal elements of the matrix under the constraints of negligible strain, $\alpha^{g,u} \ll \lambda^{g,u}$, and a purely parallel magnetic field, $B = B_{\parallel}$, since the off-diagonal elements vanish under these conditions. The energies of the two qubit levels can be directly extracted as the matrix elements $H^{g}_{11} = |2\rangle$ and $H^{g}_{22} = |1\rangle$ of the Hamiltonian $\hat{H}^{g}_{so}$ for the ground state. Accordingly, we can extract $H^{u}_{11} = |B\rangle$ and $H^{u}_{22} = |A\rangle$ of the Hamiltonian $\hat{H}^{u}_{so}$ for the excited state. For a visual representation of the electronic levels, we refer to Figure 2.3. Clearly, these energy levels depend solely on the quenching factors $f^{g,u}_{32}$, associated with $m_j = \pm\frac{3}{2}$.

[11] For example, when probing the A1 transition, a spin flip will bring the electron into resonance with the B2 transition.

The ground state qubit frequency can be directly determined as the energy difference between the two eigenstates:

$$\begin{aligned} B19 &= |2\rangle - |1\rangle \\ &= B_{\parallel}\left(2f_{32}^{\mathrm{g}}\gamma_l + \gamma_s\right), \quad \text{for } \alpha^{\mathrm{g}} \ll \lambda^{\mathrm{g}} \text{ and } B = B_{\parallel}, \end{aligned} \tag{2.33}$$

where we label the equations analogously to those in [1], such as $B19$, to allow for easier comparison. Examining this equation, we observe that the qubit frequency is determined by two contributions: the spin Zeeman term, $\gamma_s B_{\parallel}$, which is equivalent to that of a free electron in a magnetic field, and the orbital Zeeman term, $\gamma_l B_{\parallel}$, scaled by a factor $f_{32}^{\mathrm{g}} < 1$, thereby quenching its contribution. The factor of 2 arises from the alignment of both orbital and spin angular momentum in the spin-up direction for the state $|2\rangle$ and in the spin-down direction for the state $|1\rangle$. Since no other quenching factor contributes in this example, the value of f_{32}^{g} can be directly determined by measuring the qubit frequency of a low-strain emitter under a parallel external field. Figure 2.12 (a) shows such a measurement for SnV-A with $B_{\parallel} = 100\,\mathrm{mT}$, yielding a qubit frequency of $\omega_{21} = 3.55\,\mathrm{GHz}$ and $f_{32}^{\mathrm{g}} = 0.268$. The solid red line represents the expected qubit frequency for $f_{32}^{\mathrm{g}} \in [0, 1]$, with the position of the measured value indicated by the dashed crosshair.

The optically allowed transitions, such as $A1$, are defined as the energy difference between states in the excited and ground states. For instance, $A1 = |A\rangle - |1\rangle$. Consequently, the difference between both allowed transitions, $A1$ and $B2$, is given by:

$$\begin{aligned} B20 &= A1 - B2 \\ &= 2B_{\parallel}\left(f_{32}^{\mathrm{g}} - f_{32}^{\mathrm{u}}\right)\gamma_l, \quad \text{for } \alpha^{\mathrm{g,u}} \ll \lambda^{\mathrm{g,u}} \text{ and } B = B_{\parallel}. \end{aligned} \tag{2.34}$$

This equation is independent of the spin Zeeman effect and is solely determined by the difference in the orbital Zeeman effect between the ground and excited state orbitals. Essentially, the splitting of the allowed transitions reveals how much more the excited state qubit splits compared to the ground state. In other words, it reflects how much more the ground state levels are quenched relative to the excited state levels. For the ground state, we previously determined $f_{32}^{\mathrm{g}} = 0.268$. The value of f_{32}^{u} can now be obtained by measuring the difference in the optically allowed transitions under the same conditions. Figure 2.12 (b) shows the resulting measurement, which yields $f_{32}^{\mathrm{u}} = 0.485$.

To determine the quenching factors $f_{12}^{\mathrm{g,u}}$, associated with $m_j = \pm\frac{1}{2}$, it is necessary to first precisely determine the strain of the respective SnV center. By examining the Hamiltonian described in Equation 2.25, we simplify the calculation of the eigenvalues by setting $B = B_{\perp}$, in contrast to the previous considerations. Diagonalizing the Hamiltonian under this condition yields the qubit frequency of the ground state as:

$$\begin{aligned} B21 &= |2\rangle - |1\rangle \\ &= -\frac{1}{2}\Big(\sqrt{(\gamma_s B_{\perp} - 2\alpha^{\mathrm{g}})^2 + (\lambda^{\mathrm{g}})^2} \\ &\quad - \sqrt{(\gamma_s B_{\perp} + 2\alpha^{\mathrm{g}})^2 + (\lambda^{\mathrm{g}})^2}\Big), \quad \text{for } B = B_{\perp} \end{aligned} \tag{2.35}$$

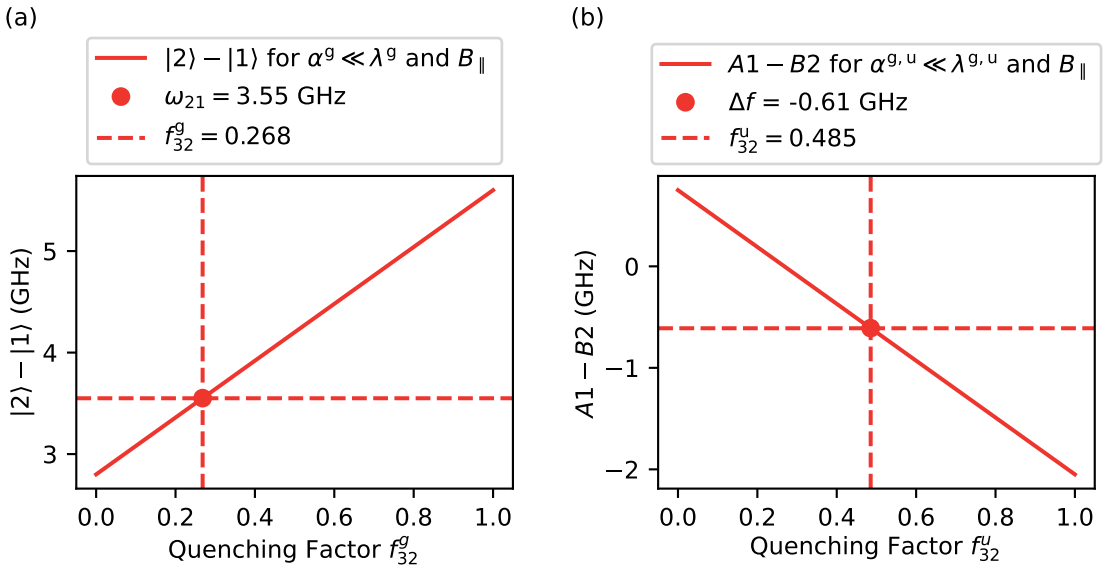

Figure 2.12.: Quenching factors $f_{32}^{g,u}$ for the lower ground and excited state doublets. (a) shows the resulting qubit frequency $|2\rangle - |1\rangle$ for a quenching factor f_{32}^g in the range from 0 to 1, in the case of negligible strain and a parallel magnetic field of $B_\parallel = 100$ mT. A single measurement point ω_{21} corresponding to SnV-A is plotted in red. In (b), the difference between the allowed transitions $A1 - B2$ is depicted for a quenching factor f_{32}^u in the range from 0 to 1 and the fixed value for $f_{32}^g = 0.268$ from the previous equation. A single measurement point is also depicted in red.

This equation[12] depends solely on the ground state strain α^g, the well-known value of the spin-orbit interaction λ^g, and the spin Zeeman interaction $\gamma_s B_\perp$.

Figure 2.13 (a) shows the qubit frequency as a function of the ground state strain, including measurements from two SnV centers. SnV-A, a defect with negligible strain, is represented by the red data point. This center exhibits a small splitting of $\omega_{21} = 0.24$ GHz for a 100 mT off-axis magnetic field, corresponding to a ground state strain of approximately $\alpha^g \sim 35$ GHz. In contrast, the highly strained SnV-B shows a qubit frequency nearly an order of magnitude larger, at $\omega_{21} = 2.25$ GHz, corresponding to $\alpha^g \sim 550$ GHz. This comparison highlights the significant sensitivity of the qubit's working point to strain under transverse magnetic fields.

[12] Note the corrected sign of the equation compared to [1]

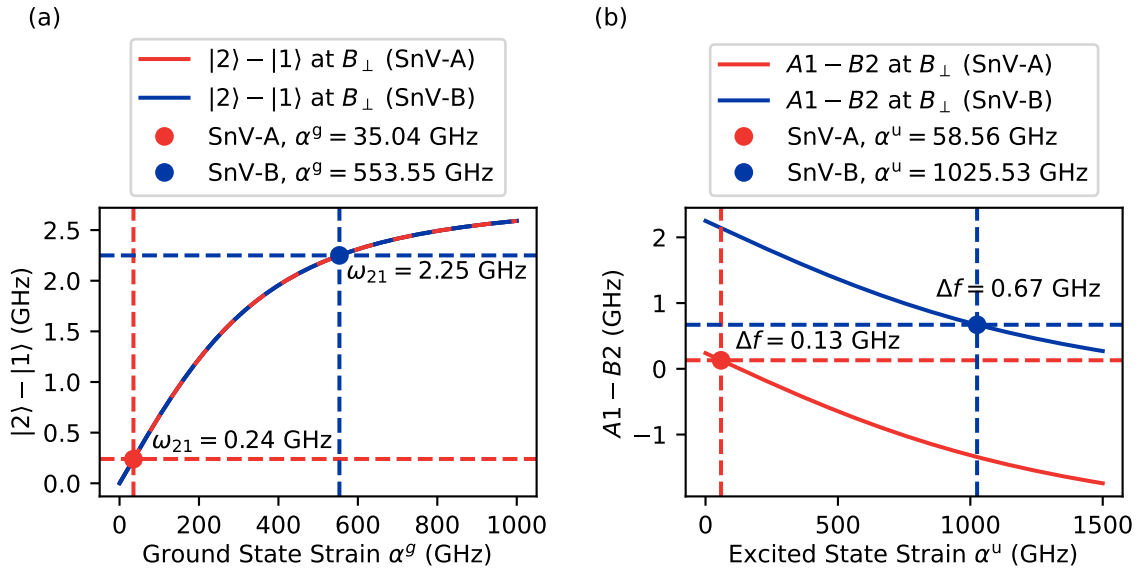

Figure 2.13.: (a) shows the resulting qubit frequency $|2\rangle - |1\rangle$ in the case of a perpendicular magnetic field, $B_\perp = 100\,\mathrm{mT}$. The red data point corresponds to a measurement on SnV-A with a coupling of $\alpha^g = 35.04\,\mathrm{GHz}$, while the blue point represents SnV-B with $\alpha^g = 553.55\,\mathrm{GHz}$. In (b), the excited state strain is determined using the previously obtained values of α^g, with red indicating SnV-A and blue indicating SnV-B.

Now that the ground state strain is determined, we turn our attention to the excited state strain. This value can be pinpointed by measuring the difference in the allowed transitions. Using the procedure and constrictions analogous to the previous measurement, we get:

$$\begin{aligned} B22 &= A1 - B2 \\ &= \frac{1}{2}\Big(\sqrt{(\gamma_s B_\perp - 2\alpha^u)^2 + (\lambda^u)^2} \\ &\quad - \sqrt{(\gamma_s B_\perp + 2\alpha^u)^2 + (\lambda^u)^2} \\ &\quad - \sqrt{(\gamma_s B_\perp - 2\alpha^g)^2 + (\lambda^g)^2} \\ &\quad + \sqrt{(\gamma_s B_\perp + 2\alpha^g)^2 + (\lambda^g)^2}\Big), \quad \text{for } B = B_\perp. \end{aligned} \tag{2.36}$$

For the spin-orbit interaction, we assume a value of $\lambda^u = 3\,\mathrm{THz}$, as determined in [85]. Figure 2.13 (b) presents the results of the measurements, yielding an excited state strain of $\alpha^u \sim 60\,\mathrm{GHz}$ for SnV-A and $\alpha^u \sim 1000\,\mathrm{GHz}$ for SnV-B. This demonstrates the significantly larger strain sensitivity of the excited state compared to the ground state, particularly for the highly strained SnV-B.

We have now pre-characterized all the necessary parameters to determine the quenching factors associated with $m_j = \pm\frac{1}{2}$. To achieve this, we take advantage of the fact that the high strain in SnV-B causes the $f_{12}^{g,u}$ parameters to contribute to the energy level structure when the Hamiltonian is diagonalized. Following the approach of the previous

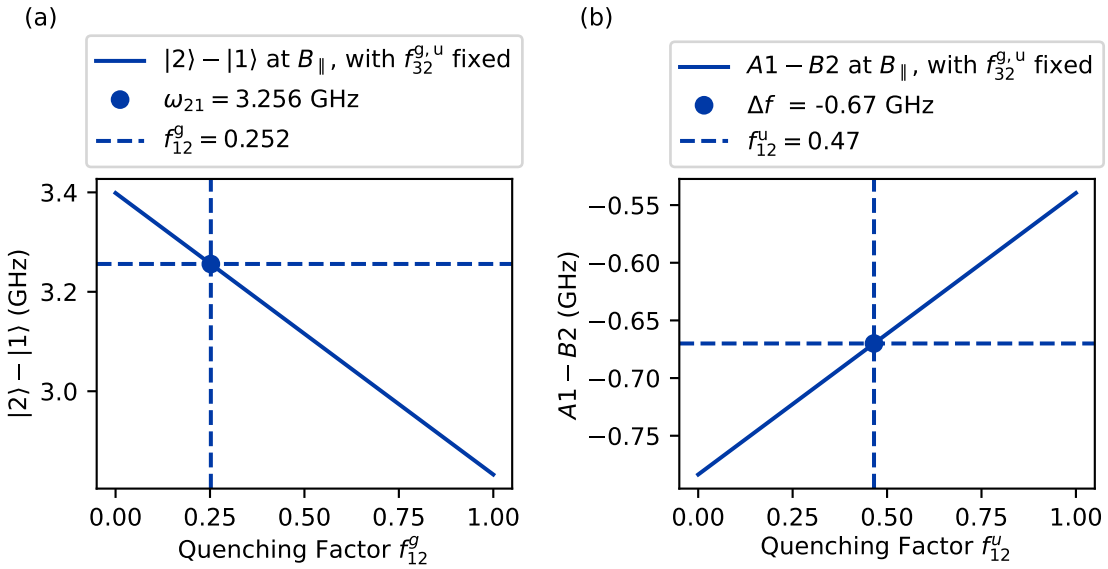

Figure 2.14.: Quenching factors $f_{12}^{g,u}$ for the lower ground and excited state doublets for fixed quenching factors $f_{32}^{g,u}$. (a) shows the resulting qubit frequency $|2\rangle - |1\rangle$ for a quenching factor f_{12}^{g} in the range from 0 to 1, in the case of substantial strain and a parallel magnetic field of $B_\parallel = 100$ mT. A single measurement point ω_{21} corresponding to SnV-B is plotted in the blue crosshair. In (b), the difference between the allowed transitions $A1 - B2$ is depicted for a quenching factor f_{12}^{u} in the range from 0 to 1 and the fixed value for $f_{12}^{g} = 0.482$ from the previous equation. A single measurement point is also depicted in the blue crosshair.

measurements, we first examine the qubit frequency for $B = B_\parallel$ of this strained emitter. The qubit frequency is defined by the following equation:

$$\begin{aligned} B23 &= |2\rangle - |1\rangle \\ &= -\frac{1}{2}\Big(\sqrt{\left(\lambda^{g} - \gamma_l B_\parallel \left(f_{12}^{g} + f_{32}^{g}\right)\right)^2 + 4(\alpha^{g})^2} \\ &\quad - \sqrt{\left(\lambda^{g} + \gamma_l B_\parallel \left(f_{12}^{g} + f_{32}^{g}\right)\right)^2 + 4(\alpha^{g})^2} \\ &\quad + 2\gamma_l B_\parallel \left(f_{12}^{g} - f_{32}^{g}\right) - 2B_\parallel \gamma_s\Big), \quad \text{for } B = B_\parallel. \end{aligned} \tag{2.37}$$

From this equation, it is evident that all parameters defining the Hamiltonian in the ground state play a role, with the quenching factor f_{12}^{g} being the last remaining unknown variable. Figure 2.14 (a) plots the qubit frequency as a function of $f_{12}^{g} \in [0, 1]$, with the measurement data point indicated in the blue crosshair.

Finally, we determine the remaining factor f_{12}^{u} for the excited state Hamiltonian by measuring the difference in the allowed transitions, as defined by the following equation:

$$\begin{aligned} B24 &= A1 - B2 \\ &= \frac{1}{2}\Big(2B_{\parallel}\left(f_{12}^{\mathrm{u}} - f_{12}^{\mathrm{g}} - f_{32}^{\mathrm{u}} + f_{32}^{\mathrm{g}}\right)\gamma_L \\ &\quad + \sqrt{4(\alpha^{\mathrm{u}})^2 + \left(-B_{\parallel}\left(f_{12}^{\mathrm{u}} + f_{32}^{\mathrm{u}}\right)\gamma_L + \lambda^{\mathrm{u}}\right)^2} \\ &\quad - \sqrt{4(\alpha^{\mathrm{u}})^2 + \left(B_{\parallel}\left(f_{12}^{\mathrm{u}} + f_{32}^{\mathrm{u}}\right)\gamma_L + \lambda^{\mathrm{u}}\right)^2} \\ &\quad - \sqrt{4(\alpha^{\mathrm{g}})^2 + \left(-B_{\parallel}\left(f_{12}^{\mathrm{g}} + f_{32}^{\mathrm{g}}\right)\gamma_L + \lambda^{\mathrm{g}}\right)^2} \\ &\quad + \sqrt{4(\alpha^{\mathrm{g}})^2 + \left(B_{\parallel}\left(f_{12}^{\mathrm{g}} + f_{32}^{\mathrm{g}}\right)\gamma_L + \lambda^{\mathrm{g}}\right)^2}\Big), \quad \text{for } B = B_{\parallel} \end{aligned} \tag{2.38}$$

Figure 2.14 (a) plots the difference as a function of $f_{12}^{\mathrm{u}} \in [0, 1]$, with the measurement data point indicated by a blue crosshair.

A closer examination of the previous equations reveals that the qubit frequency and the difference in allowed transitions mainly scale with the asymmetry of the quenching factors, specifically $\propto f_{32}^{\mathrm{g}} - f_{12}^{\mathrm{g}}$ and $\propto f_{32}^{\mathrm{u}} - f_{12}^{\mathrm{u}}$ and the sum of the quenching factors $\propto f_{32}^{\mathrm{g}} + f_{12}^{\mathrm{g}}$ and $\propto f_{32}^{\mathrm{u}} + f_{12}^{\mathrm{u}}$. We now understand why, for strongly strained SnV centers, the Hamiltonian can be described using averaged reduction factors $f^{\mathrm{g,u}} = \frac{f_{12}^{\mathrm{g,u}}}{2} + \frac{f_{32}^{\mathrm{g,u}}}{2}$. We can generalize the Hamiltonian, as described in Equation 2.26, consistent with the description derived by G. Thiering et al. [38], by including the mean asymmetries $\delta = \frac{f_{32}^{\mathrm{g,u}}}{2} - \frac{f_{12}^{\mathrm{g,u}}}{2}$. However, it is important to note that precise measurements are necessary to accurately determine their values. In the following, we will discuss how these quenching factors are determined with high accuracy by fitting to an extended dataset.

Figure 2.15 and Figure 2.16 present the complete measurements for SnV-A and SnV-B, respectively. The red data points represent the absolute value of the difference between the optically allowed transitions A1 and B2, extracted from the angular magnetic field sweeps described in Figure 2.11. For SnV-A, the forbidden transition difference B1-A2 is also shown in green within a narrow range around $B_{\perp}$. The qubit frequency of the ground state doublet, measured via optically detected magnetic resonance (ODMR)[13], is depicted as blue data points.

The quenching parameters are extracted by fitting the Hamiltonian to the observed optical and qubit transition frequencies using a comparable methodology to that described earlier and including the angle dependency. First, an initial guess for the strain magnitude is inferred from photoluminescence (PL) measurements of the respective SnV center. The ground state strain α^{g} is related to the ground state splitting via the equation $\Delta_{\mathrm{g}} = \sqrt{(\lambda^{\mathrm{g}})^2 + 4(\alpha^{\mathrm{g}})^2}$. The exact ground state strain magnitude is then refined by matching the strain to the minimum of the qubit transitions $\omega_{\mathrm{q}}(\theta)$ around $\theta = 90°$, as their frequency

[13] See Section 4.1.1 for details on the measurement technique

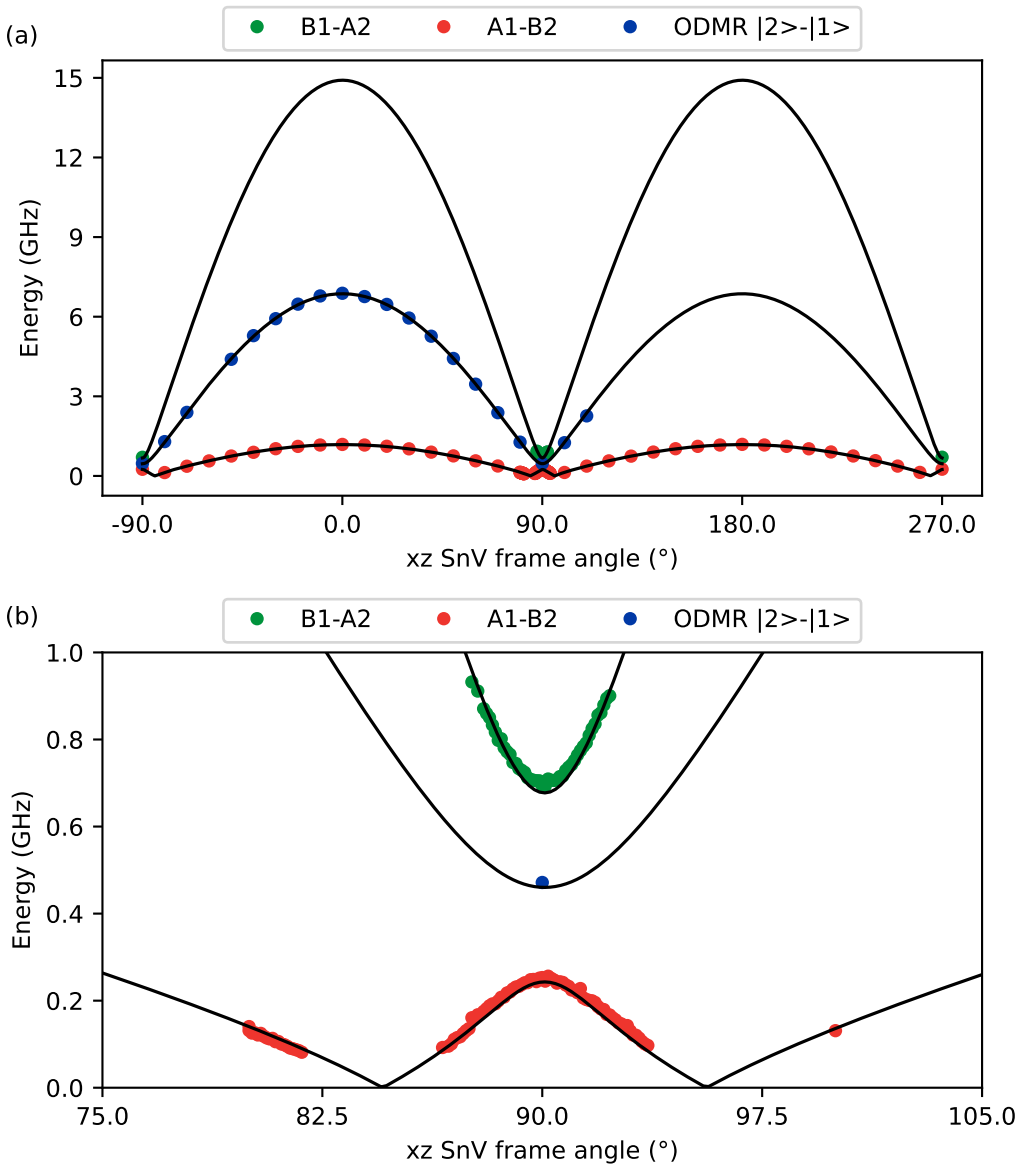

Figure 2.15.: Fit of the electronic energies of SnV-A to the observed optical spin-conserving transitions A1 and B2 in the SnV frame (red points) and the spin-forbidden transitions A2 and B1 (green points), as measured by PLE. The qubit transition frequencies (blue points) are measured in ODMR scans at 50 mK. (b) A zoom into the anticrossing around the perpendicular field orientation is shown. All measurements are performed at B = 200 mT. This figure is adapted from Figure 11 in Reference [1].

depends solely on α^{g} for a given magnetic field strength. For the excited state strain α^{u}, we fit the Hamiltonian to the measured allowed transition splitting (and forbidden splitting for SnV-A), assuming a spin-orbit coupling strength for the excited state of $\lambda^{u} = 3000$ GHz [38, 85]. Next, we determine f_{32}^{g} by fitting to all qubit transitions of the low-strain emitter (SnV-A) using the determined strain magnitude $\alpha^{g} = 35.0(15)$ GHz. This value is independent of all other quenching factors. Once f_{32}^{g} is fixed, we determine f_{32}^{u} by fitting it to all allowed transitions of SnV-A.

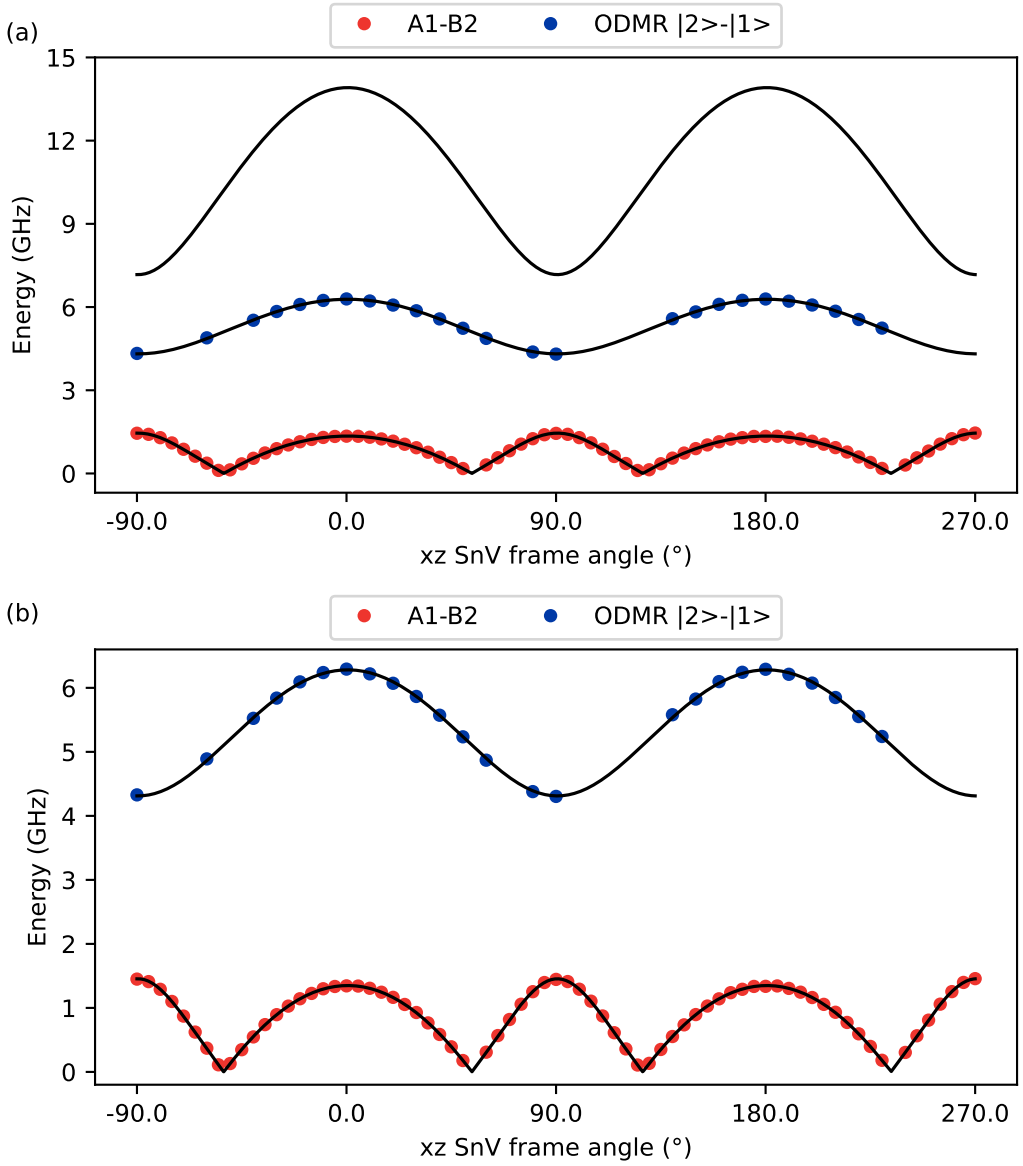

Figure 2.16.: (a) Fit of the electronic energies of SnV-B to the observed optical spin-conserving transitions A1 and B2 in the SnV frame (red points), as measured by PLE. The qubit transition frequencies (blue points) are measured in ODMR scans at 50 mK. The spin-forbidden transitions A2 and B1 are not measured due to their large splitting. (b) A zoom into the allowed and ODMR transitions is shown. All measurements are performed at B = 200 mT. This figure is adapted from Figure 11 in Reference [1].

The $f_{12}^{g,u}$ values cannot be determined in cases of low strain, as their influence is negligible due to the absence of orbital mixing. However, for moderate and high strain, where the condition $\alpha \ll \lambda$ no longer applies, the influence of the quenching factors associated with $m_j = \pm\frac{1}{2}$ becomes significant [1]. After determining the strain magnitude for the highly strained SnV-B using the same approach as for SnV-A, we leverage the previously determined values of $f_{32}^{g,u}$ from SnV-A to extract f_{12}^{g}. This is achieved by fitting the

Hamiltonian to the qubit transitions of SnV-B.[14] Finally, we determine f_{12}^{u} by fitting the Hamiltonian to the allowed transitions of SnV-B.

Precise Hamiltonian parameters are essential for understanding spin polarization, readout processes, and the angular dependence of optically allowed transitions, as well as the qubit frequency. Moreover, these parameters are invaluable when working with uncharacterized SnV centers, particularly in cases where the optically allowed transitions A1 and B2 become undetectable due to optical spin initialization at temperatures below 4 K.

The analysis of the potential error range for the quenching factors was conducted by Jeremias Resch as follows: An estimated uncertainty of ±0.5 % in the magnetic field amplitude was applied to the fitting results described above. The quenching parameters f were evaluated by varying the field strength within this error range, following the relation

$$B_{\mathrm{dc}}^{\parallel,\perp}(x) = B_{\mathrm{mean}}^{\parallel,\perp}(1 + x \cdot 0.5\,\%), \text{ where } x \in [-1, 1]. \tag{2.39}$$

This uncertainty is motivated by empirical observations: the measured qubit frequency deviates by approximately ±0.5 % when the magnetic field is cycled on and off. The effect is attributable to small hysteresis effects in the magnetic field coils. Further, uncertainties from the fits of the allowed and ODMR transitions were omitted, as these are at least an order of magnitude smaller than those associated with the magnetic field uncertainty.

[14] The f_{12}^{g} sublevel of the ground state significantly contributes to the qubit energy levels in the diagonalized Hamiltonian. However, it remains insensitive to f_{12}^{u} from the excited state [1].

Table 2.1.: Parameters of the SnV center Hamiltonian. The spin-orbit splitting λ^{g} is measured by PL measurements from an unstrained SnV center (SnV-D, Figure 2.4 (b)). For the magnetic field magnitude values, we estimate an error of 0.5 %. The strain components and orbital quenching factors are obtained by a fit to the electron spin Hamiltonian. This table is a reprint from Karapatzakis, Resch et al. Physical Review X 14, 031036.

Parameter	**Value**	**Fitted?**	**Source**
γ_l	14 GHz T^{-1}	-	[90]
γ_s	28 GHz T^{-1}	-	[91]
λ^{g}	822(1) GHz	yes	SnV-D
λ^{u}	3000 GHz	-	[38, 85]
f_{32}^{g}	0.268(13)	yes	SnV-A
f_{12}^{g}	0.251(12)	yes	SnV-A
f_{32}^{u}	0.486(15)	yes	SnV-B
f_{12}^{u}	0.500(8)	yes	SnV-B
	SnV-A	**SnV-B**	**SnV-C**
α^{g}	35.0(15) GHz	577.3(34) GHz	530.0(40) GHz
α^{u}	60.0(70) GHz	961.90(49) GHz	921.4(32) GHz
$B_{\parallel}$	193.44(97) mT	193.46(97) mT	193.47(97) mT
$B_{\perp}$	193.48(97) mT	189.03(95) mT	193.45(97) mT
$\delta\theta$	$-0.08(2)^{\circ}$	$-0.54(2)^{\circ}$	$-0.46(18)^{\circ}$

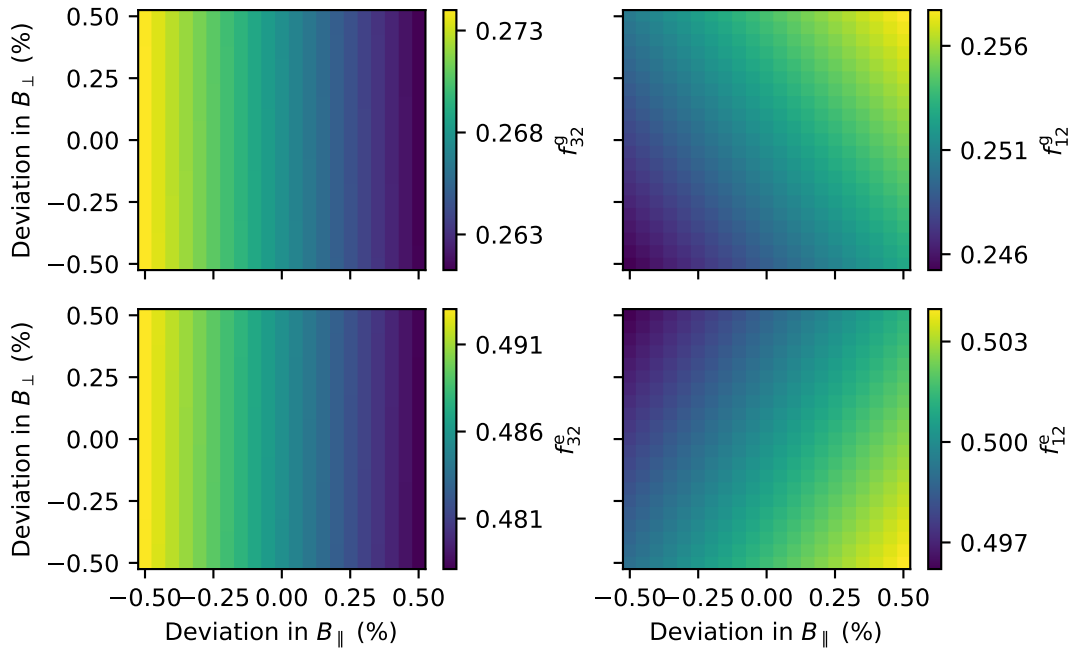

Figure 2.17.: The spread of the quenching parameters f derived from fits to SnV-A and SnV-B, assuming a ±0.5% uncertainty in the B-field amplitude, is illustrated. For each magnetic field strength, the Hamiltonian is fit, and the resulting f parameter is represented in the corresponding pixel. As outlined in this section, the fitting process proceeds sequentially: first f_{32}^{g} is determined, followed by f_{12}^{g}, f_{32}^{e}, and f_{12}^{e}, with each step incorporating the previously determined quenching parameter. The overall spread of the f parameters in each subplot is used to calculate the standard uncertainty for the respective parameter. This figure is adapted from Figure 12 in Reference [1].

Similarly, uncertainties in λ^{g} and strain α^{g} were considered negligible by comparison and were not propagated to the quenching parameters.

The resulting quenching parameters and their distributions, are shown in Figure 2.17. This figure illustrates the spread of the f parameters derived sequentially: f_{32}^{g}, followed by f_{12}^{g}, f_{32}^{u}, and f_{12}^{u}. At each step, the previously determined quenching parameters are incorporated into the fitting process. The spread of the f values in each subplot provides the basis for calculating their standard uncertainties. The final fitting parameters, along with their corresponding errors, are summarized in Table 2.1.

2.5. Spin Dynamics

In Section 2.3, we analyzed the energy structure of the SnV center, identifying the lower ground states $|1\rangle$ and $|2\rangle$ as optimal candidates for a spin qubit. In the following, we elaborate on the preparation and measurement of these qubit states. Efficient initialization of the qubit into one of the basis states is crucial to implement quantum gates and to enable reliable quantum computing operations. The quality and precision of both initialization and subsequent state readout are characterized by the initialization and readout fidelity, a measure which quantifies the accuracy in achieving the desired spin state.

In addition, we analyze the spin relaxation processes that can limit the coherence and fidelity of the SnV center. These processes become particularly significant when operating above 1 K, which will be discussed along with the following measurements.

2.5.1. Three-Level System Interactions

In the following, we describe the dynamics of a resonantly driven three-level system to analyze the emission and polarization properties of the SnV center, following the derivation presented in [99] and [100]. This allows for the simulation of spin initialization, which is facilitated by a spin-flipping transition. The three-level system is illustrated in Figure 2.17 and consists of the two ground states $|1\rangle$ and $|2\rangle$ forming the spin qubit and the excited state $|A\rangle$. In this simplified energy level diagram, an electron excited to $|A\rangle$ with frequency Ω relaxes from this state to the ground states $|1\rangle$ and $|2\rangle$ with probabilities P_{A1} (at a rate γ_{A1}) and P_{A2} (at a rate γ_{A2}), respectively. The transition $|A\rangle \rightarrow |1\rangle$ is a spin-conserving transition (allowed), while $|A\rangle \rightarrow |2\rangle$ is a spin-flipping transition (forbidden).

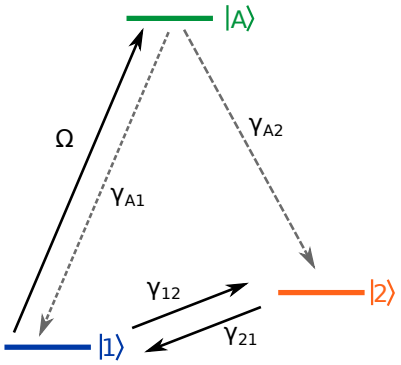

Figure 2.18.: Simplified energy level diagram of a driven the three-level system. The spin qubit is formed by the two ground states $|1\rangle$ and $|2\rangle$, with transition from $|1\rangle$ to the excited state $|A\rangle$ driven at frequency Ω. Relaxation from $|A\rangle$ occurs to $|1\rangle$ and $|2\rangle$ with rates γ_{A1} and γ_{A2}, respectively. To account for phonon-mediated interaction with the upper ground states $|3\rangle$ and $|4\rangle$ (excluded from this model), effective transitions between $|1\rangle$ and $|2\rangle$ are introduced, as characterized by the rates γ_{21} and γ_{12}. The energy levels are color coded to match the populations in the simulations of Figure 2.19. Figure adapted from [99].

The ratio of these probabilities is defined as the cyclicity $\Lambda = \frac{P_{A1}}{P_{A2}}$. It serves as a measure of state overlap. Using the cyclicity and the condition $P_{A1} + P_{A2} = 1$, the probabilities can be reformulated as [99]:

$$P_{A1} = \frac{\Lambda}{1+\Lambda}, \quad P_{A2} = \frac{1}{1+\Lambda}. \tag{2.40}$$

To account for phonon-mediated interactions between the lower ground states and the upper ground states $|3\rangle$ and $|4\rangle$ (in addition to spin flipping interaction within the qubit states), which are excluded from the model, an effective interaction term between $|1\rangle$ and $|2\rangle$ is introduced and characterized by the rates γ_{21} and γ_{12}, respectively. At the operating temperatures during the coherent control measurements of the electron spin, that are far below 1 K, these interactions can be neglected. At these cryogenic temperatures the spin relaxation time significantly exceeds the spin initialization time. However, as we will describe in detail later in Subsection 2.5.2, spin relaxation is highly dependent on magnetic field parameters, such as the strength of the off-axis component $B_\perp$ and the type of phonon interaction (single-phonon or two-phonon processes) [36]. For now, the introduced interaction serves as a means to quantitatively characterize the spin initialization by including this thermally induced absorption and emission process. The rates γ_{21} and γ_{12} are given by:

$$\gamma_{21} = \gamma_0\big(n(\omega)+1\big), \quad \gamma_{12} = \gamma_0 n(\omega). \tag{2.41}$$

Here, γ_0 denotes the interaction strength, and $n(\omega)$ is the phonon occupation number at frequency ω, determined by the Bose-Einstein distribution. The total transition rate $\gamma = \gamma_{21} + \gamma_{12}$ corresponds to the inverse of the spin relaxation time T_1.

To fully capture the the quantum behavior of the three-level system, including coherence effects and population dynamics, we need to describe the system using the density matrix ρ. While the state vector $|\psi\rangle$ describes pure states only, the density operator ρ allows the description of both pure and mixed states. Mixed states are far more common in experimental settings, especially when the preparation of the system is not fully known or entangled with another system.

For the three-level system described above, the basis for the description of the density matrix is given by the orthonormal vectors $\{|1\rangle, |2\rangle, |A\rangle\}$, which represent the pure states of the system. The density matrix in this basis can be written as:

$$\rho = \sum_{i,j=1}^{N} \rho_{i,j} \, |i\rangle \langle j| , \tag{2.42}$$

with the trace of the matrix $\sum_i \rho_{i,i} = 1$.

For a closed quantum system, the Hamiltonian H evolves according to the von Neumann equation (or Liouville-von Neumann equation) [101]:

$$\frac{d\rho(t)}{dt} = -i\big[H(t), \rho(t)\big]. \tag{2.43}$$

For an open quantum system, where a system interacts with an external environment or reservoir, such as our qubit interacting with its surroundings, the von Neumann equation must be extended to include dissipative and decoherence effects, since the interaction of the open system with the large reservoir is irreversible. [101] The most common generalization is the quantum master equation in Lindblad form (with $\hbar = 1$):

$$\frac{d\rho}{dt} = -i\big[H, \rho\big] + \mathcal{L}[\rho], \tag{2.44}$$

$$= -i[H, \rho] + \sum_k \gamma_k \left(L_k \rho L_k^\dagger - \frac{1}{2}\{L_k^\dagger L_k, \rho\} \right). \tag{2.45}$$

where $\mathcal{L}[\rho]$ represents the Lindblad superoperator and accounts for the interaction with the environment. L_k are the jump operators that characterize specific dissipative processes, such as relaxation, dephasing, or spontaneous emission and γ_k are the rates (with the dimension of an inverse time) associated with the dissipative channels. For a short introduction into the Lindblad master equation, see [102]. The Hamiltonian H is not necessarily the free Hamiltonian of the system S, but can also contain additional terms due to the coupling of the system to the environment, such as interaction with a resonant laser beam. In the following, we will describe the evolution of our three-level system in the rotating frame under resonant driving of the A1-transition. The Hamiltonian, with the energy of the lower ground state $|1\rangle$ set to zero, is expressed as [100]:

$$H = \Delta \, |A\rangle \langle A| + \delta \, |2\rangle \langle 2| + \frac{\Omega}{2}\big(\, |1\rangle \langle A| + |A\rangle \langle 1| \, \big). \tag{2.46}$$

Here, Δ denotes the laser detuning, Ω represents the strength of the driving frequency, and δ corresponds to the energy difference between $|2\rangle$ and $|1\rangle$ We can now model the system using the quantum master equation in Lindblad form. For the three-level system under consideration, the jump operators are given by:

$$L_{A1} = |1\rangle \langle A|, \quad \text{representing decay from } |A\rangle \text{ to } |1\rangle, \tag{2.47}$$

$$L_{A2} = |2\rangle \langle A|, \quad \text{representing decay from } |A\rangle \text{ to } |2\rangle, \tag{2.48}$$

$$L_{21} = |1\rangle \langle 2|, \quad \text{representing phonon-mediated relaxation from } |2\rangle \text{ to } |1\rangle, \tag{2.49}$$

$$L_{12} = |2\rangle \langle 1|, \quad \text{representing phonon-mediated excitation from } |1\rangle \text{ to } |2\rangle. \tag{2.50}$$

The optical decay rate is given by the lifetime of the state $|A\rangle$ and is defined as $\gamma = \gamma_{A1} + \gamma_{A2}$. Using these operators, the full dynamics of the system, including both coherent and dissipative processes, can be described. The resulting equations of motion for the density matrix elements are:

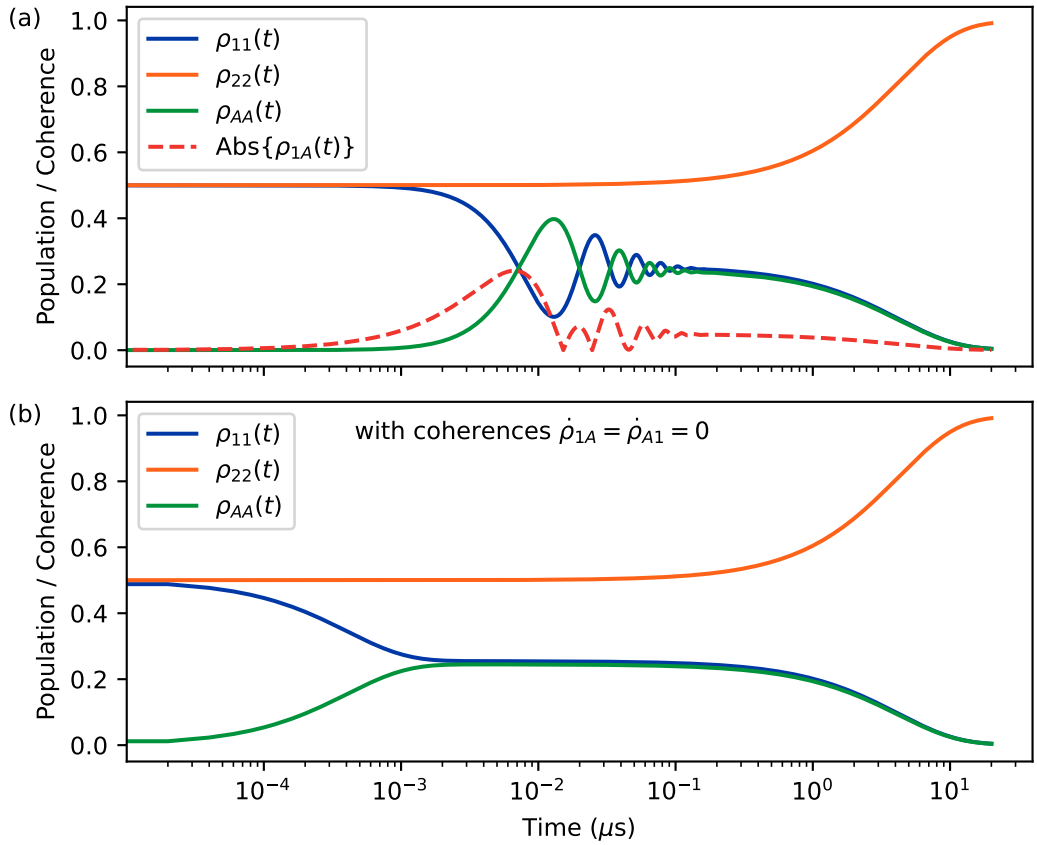

Figure 2.19.: Simulated dynamics of the driven three-level system. In (a) the coherences are included in the simulation, leading to short-term oscillations between the populations $\rho_{11}(t)$ and $\rho_{AA}(t)$, which decay on a timescale much shorter than the initialization duration. The coherence term Abs$\{\rho_{1A}(t)\}$ is also shown. (b) A quasistationary state is assumed, with coherences neglected by setting $\dot{\rho}1A = \dot{\rho}A1 = 0$. The resulting dynamics highlight the population transfer between $\rho_{11}(t)$, $\rho_{22}(t)$, and $\rho_{AA}(t)$ in the absence of coherent oscillations.

$$\dot{\rho}_{11} = -\gamma_{12}\rho_{11} + \gamma_{21}\rho_{22} + \gamma_{A1}\rho_{AA} - i\left(-\frac{\Omega\rho_{1A}}{2} + \frac{\Omega\rho_{A1}}{2}\right), \tag{2.51}$$

$$\dot{\rho}_{22} = \gamma_{12}\rho_{11} - \gamma_{21}\rho_{22} + \gamma_{A2}\rho_{AA}, \tag{2.52}$$

$$\dot{\rho}_{AA} = -\gamma_{A1}\rho_{AA} - \gamma_{A2}\rho_{AA} - i\left(\frac{\Omega\rho_{1A}}{2} - \frac{\Omega\rho_{A1}}{2}\right), \tag{2.53}$$

$$\dot{\rho}_{1A} = -\frac{\gamma_{12}}{2}\rho_{1A} - \frac{\gamma_{A1}}{2}\rho_{1A} - \frac{\gamma_{A2}}{2}\rho_{1A} - i\left(-\Delta\rho_{1A} - \frac{\Omega\rho_{11}}{2} + \frac{\Omega\rho_{AA}}{2}\right), \tag{2.54}$$

$$\dot{\rho}_{A1} = -\frac{\gamma_{12}}{2}\rho_{A1} - \frac{\gamma_{A1}}{2}\rho_{A1} - \frac{\gamma_{A2}}{2}\rho_{A1} - i\left(\Delta\rho_{A1} + \frac{\Omega\rho_{11}}{2} - \frac{\Omega\rho_{AA}}{2}\right). \tag{2.55}$$

These equations can be analytically solved under the condition $\dot{\rho}_{1A} = \dot{\rho}_{A1} = 0$. An analytical derivation of $\rho_{AA}(t)$ can be found in [100]. This quantity is proportional to the

fluorescence intensity and is thus the observable measured in the experiment. Note that the referenced derivation excludes phonon-mediated interactions.

To account for all interactions, we numerically simulate the dynamics of the driven three-level system using the `odeint` package in Python. The results, depicted in Figure 2.19, illustrate the temporal evolution of the driven three-level SnV system, including phonon-mediated interactions and spontaneous emission.

We distinguish between two simulation conditions:
(i) **Full coherence dynamics** (Figure 2.19 (a)), where the system evolves without constraints on coherence terms, and
(ii) **Quasistationary assumption** (Figure 2.19 (b)), where coherences are eliminated by imposing $\dot{\rho}_{1A} = \dot{\rho}_{A1} = 0$.

The simulation is initialized with the following density matrix elements:

$$\rho_{11}(0) = 0.5, \quad \rho_{22}(0) = 0.5, \quad \rho_{AA}(0) = \rho_{A1}(0) = \rho_{1A}(0) = 0.$$

Finally, the parameters governing the system dynamics are given by:

$$\begin{aligned}
\text{T}_1 \text{ relaxation rates:} &\quad \gamma_{12} = 1\,\text{kHz}, \quad \gamma_{21} = 1\,\text{kHz}, \\
\text{Excited-state decay:} &\quad \frac{\gamma}{2\pi} = 30.5\,\text{MHz} \\
\text{Branching ratio:} &\quad \Lambda = 100, \\
\text{State-dependent decay:} &\quad \gamma_{A2} = \frac{\gamma}{\Lambda + 1}, \quad \gamma_{A1} = \Lambda \cdot \gamma_{A2}, \\
\text{Detuning and driving:} &\quad \Delta = 0, \quad \Omega = 5 \cdot \gamma.
\end{aligned}$$

The parameters for the simulation are chosen to capture the short-term coherent oscillations between the populations $\rho_{11}(t)$ and $\rho_{AA}(t)$. However, in the experiment, we find weak resonant excitation below the saturation power of the SnV center to yield the best results regarding the readout fidelity, while maintaining a stable charge state of the SnV center over several hours of measurements. Below the saturation power, no significant coherences are generated. The good fidelity can be attributed to the long spin relaxation time of the electron and minimal leakage of the excitation laser into the collection path, which remains negligible at low laser powers. The readout fidelity F is given by [103]:

$$F = 1 - \frac{I_{t\to\infty}}{2 \cdot I_{\text{max}}}, \tag{2.56}$$

where I_{max} represents the maximum detected intensity during initialization, and $I_{t\to\infty}$ is the steady-state intensity. The factor of 2 is necessary when assuming a thermal equilibrium state distributed with 50/50 occupancy between the spin-up and the spin-down state. In general, the pre-factor depends on the initial population of spin states.

In the following, we determine the initialization fidelity of the highly strained SnV-B, that has been described in Figure 2.11. This SnV center is used for the coherent control measurements following in Section 4. In Figure 2.20, we show initialization measurements

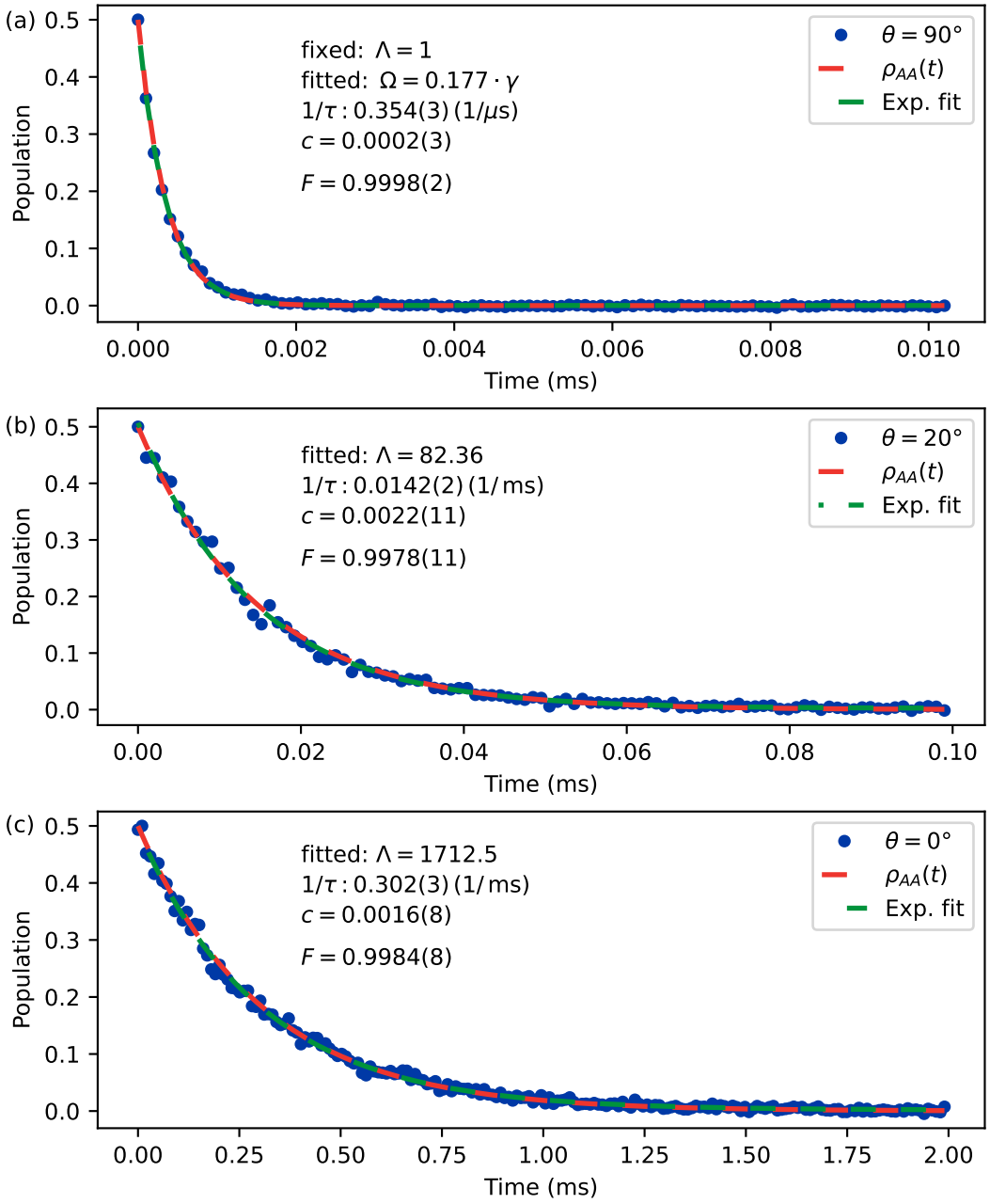

Figure 2.20.: Initialization fidelity measurements of SnV-B under three magnetic field orientations: perpendicular ($\theta = 90°$), at an angle ($\theta = 20°$), and parallel ($\theta = 0°$) to the SnV axis. Experimental data (blue points) are compared with fits derived from the Lindblad simulation (red dashed lines) and an exponential decay model (green dashed lines). The fixed and fitted parameters for the simulation are noted in each panel. In (a) we derive the Rabi frequency Ω by assuming the worst-case cyclicity of $\Lambda = 1$. In (b) and (c), we minimize $\rho_{AA}(t)$ against the data and extrapolate the corresponding value for the cyclicity. The initialization fidelity is determined through the exponential fit to the data.

on SnV-B with the external magnetic field oriented perpendicular in (a), at a 20° angle in (b), and parallel in (c). The angle is defined with respect to the SnV center's z-axis. The depicted initialization curves are extracted from Rabi measurements on the electron spin. Thereby, the resulting averaged population of the spin states are 50 % in the spin-up state and 50 % in the spin-down state.

The goal of the measurements is to estimate the lower bound of the cyclicity of SnV-B by fitting the simulated dynamics of the driven three-level system to the experimental exponential decay curves while optimizing the cyclicity value. First, however, it is necessary to determine the Rabi drive frequency Ω, as the dynamics strongly depend on this parameter. The Rabi frequency of the optical drive is related to the defect's saturation power p_{sat}.

We note that a measured saturation power of an inspected defect can vary significantly depending on the accuracy of the optical z-focus on the defect and the spatial alignment in x and y. While we carefully optimize the spatial positioning prior to each measurement batch to ensure optimal readout fidelity, even slight spatial misalignments, variations in power coupling, or temperature drifts can result in saturation power variations by several factors. Therefore, we determine p_{sat} through the initialization curve in (a) by assuming the minimal cyclicity of $\Lambda = 1$ and minimizing $\rho_{AA}(t)$ against the experimental data instead of directly measuring a saturation curve. [15] The minimized curve for $\rho_{AA}(t)$ is depicted as a dashed red line in the plots. Using [104]

$$\frac{p}{p_{\text{sat}}} = \frac{2\Omega^2}{\gamma^2} \rightarrow \Omega = \sqrt{\frac{p}{2p_{\text{sat}}}}\gamma \tag{2.57}$$

we find $\Omega = 0.177\gamma$ for an applied laser power of $p = 1\,\text{nW}$[16], which is the same power used in (b) and (c). The corresponding saturation power follows as $p_{\text{sat}} \approx 16\,\text{nW}$. The inferred saturation power obtained through the measurement of Ω in (a) is then applied to the measurements in Figure 2.20 (b) and (c), allowing the determination of cyclicity.

Using $p_{\text{sat}} \approx 16\,\text{nW}$, we determine the cyclicity to be $\Lambda(20°) = 82.36$ and $\Lambda(0°) = 1712.5$, representing the lower bound for the respective angles in (b) and (c). Additionally, we independently fit the normalized data to an exponential decay function, $I(t) = I_0 \cdot \exp\left(-\frac{t}{\tau}\right) + c$, with the fit shown as a dashed green line in the plots. We use Equation 2.56 to extract the fidelity via the exponential fit. For the parallel field orientation the fidelity is $F_{\parallel} = 99.84(8)\,\%$ demonstrating an almost perfect initialization. For perpendicular field orientation a fidelity of $F_{\perp} = 99.98(2)\,\%$ is achieved. The relatively longer initialization duration, compared to the decay time, for the perpendicular field orientation, allows for full initialization. The Fidelity is limited by the fitting error of the constant variable c, since we subtract the average dark count of the photon-detectors. To achieve higher initialization fidelity for parallel field orientation, one would have to increase the initialization time, but this comes at the cost of measurement time. All relevant fit values are noted within the plots for a clearer overview.

[15] If $\Lambda > 1$ is assumed, the ratio p/p_{sat} must be larger to achieve the same initialization time (i.e., a higher Ω), leading to higher cyclicity values for the measurements in (b) and (c). By assuming the worst-case cyclicity of $\Lambda = 1$, we can estimate the lower bound of the cyclicity for different angles.

[16] The optical power levels are defined in front of the input window of the cryostat.

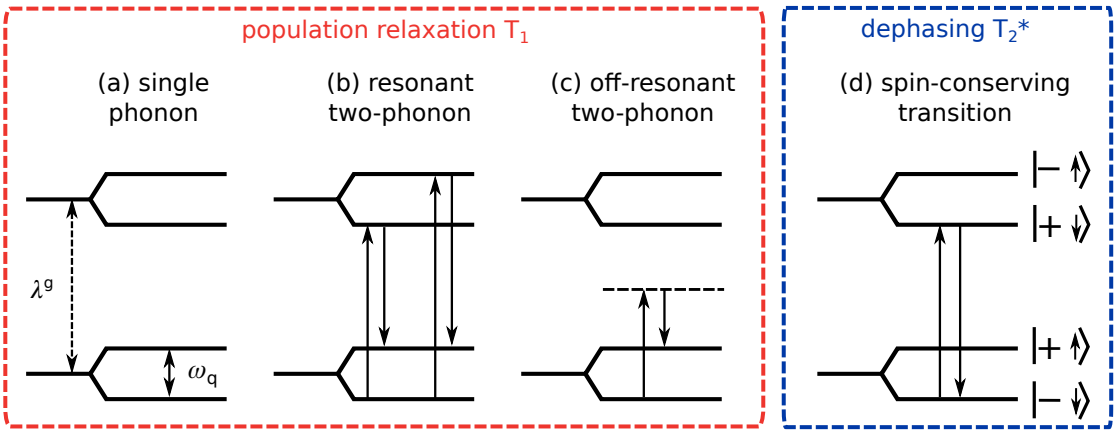

Figure 2.21.: Phonon-induced relaxation pathways. The red panel shows pathways for phonon-mediated spin flips, where direct relaxation via a single-phonon resonant to the qubit frequency ω_q is depicted in (a). The two possible channels for a two-phonon process involving the upper orbital branch are shown in (b). Off-resonant two-phonon processes are illustrated in (c). The blue panel shows spin-conserving transitions that are responsible for dephasing. The figure is based on figures 4(a) and 8 in [36].

2.5.2. Phonon-Induced Relaxation Pathways

In the previous discussion of the dynamics of a resonantly driven three-level system (see Section 2.5.1), we introduced the interaction between the qubit states $|1\rangle$ and $|2\rangle$ to quantitatively characterize the influence of spin relaxation on spin initialization. Here, we dive deeper into the spin relaxation mechanisms that determine the relaxation time T_1 of the SnV center in diamond. Specifically, we describe the coupling between spin states and lattice vibrations (phonons), that can limit qubit performance and coherence under varying strain, magnetic field, and temperature conditions. Our analysis combines theoretical models, following the work of S. Meesala [36] and I. Harris [71], with experimental data for validation[17]. Figure 2.21 illustrates phonon-mediated spin relaxation and dephasing mechanisms in SnV centers. The red panel highlights pathways for spin flips, e.g. single-phonon transitions resonant to the qubit frequency ω_q in (a). In addition, two-phonon processes are possible. Resonant transitions, are referred to as an Orbach process. Off-resonant Raman-scattering, involving the upper orbital branch or a virtual level are illustrated in (b) and (c), respectively. The blue panel shows spin-conserving transitions that are responsible for dephasing.

The ground states are labeled on the far-right of the energy levels with their respective orbital and spin angular momentum, e.g., $|-\downarrow\rangle$, differing from the nomenclature used in Figure 2.3, to clearly represent spin-conserving and spin-flipping transitions. In Section 2.2, we characterized these eigenstates as defined by the spin-orbit interaction, where the orbital and spin angular momentum are well-defined in the absence of off-axis strain or magnetic fields. Subsequently, we discussed the influence of strain and introduced the strain Hamiltonian, $\hat{H}_{\text{strain}}$, in Section 2.2. From the form of the strain Hamiltonian

[17] For readers interested in orbital relaxation dynamics involving spin conserving single-phonon transitions, we refer to the study of SiV centers by K. Jahnke [35]

given in equation 2.18, it is evident that E_x and E_y strain components induce mixing and relative shifts between orbitals, while the spin part of the wavefunction remains unaffected. Consequently, ac strain arising from thermal $E_{\mathrm{gx/y}}$ phonons can ease ground-state orbital transitions [36].

To model the decoherence processes, I. Harris [71] presents a simplified model of the group-IV fine structure, effectively describing it as a pair of coupled two-level systems:

$$\hat{H}_S = \frac{1}{2}\omega_Q \sigma_z^Q + \frac{1}{2}\omega_B \sigma_z^B + \frac{1}{4}\lambda_{\mathrm{eff}} \sigma_z^Q \sigma_z^B \tag{2.58}$$

where ω_B represents the branch degree of freedom associated with the spin-orbit coupling, and ω_Q corresponds to the qubit state splitting, determining whether the system resides in the upper or lower level within the branch. The parameter λ_{eff} is introduced as an effective coupling strength, interpreted as a shift in the qubit frequency dependent on the state of the branch degree of freedom. This formalism enables the derivation of transition rates γ_{ij} and provides insights into the dynamic processes of the system[18]. Within this model, the transition rates in the presence of a thermal phonon bath are given by:

$$\gamma_{ij} = 2\pi \sum_R |h_{ij}^R|^2 \chi_R |\omega_i - \omega_j|^3 n_{\mathrm{th}}(\omega_i - \omega_j), \tag{2.59}$$

where $|h_{ij}^R|$ represents the coupling strength, χ_R is the phonon absorption cross section, and $|\omega_i - \omega_j|$ is the frequency difference between states i and j. The thermal phonon occupation number at frequency $\omega = \omega_i - \omega_j$, $n_{\mathrm{th}}(\omega)$, is described by the Bose-Einstein distribution:

$$n_{\mathrm{th}}(\omega) = \begin{cases} \frac{1}{e^{\hbar\omega/k_B T}-1}, & \text{if } \omega > 0 \\ \frac{1}{e^{\hbar|\omega|/k_B T}-1} + 1, & \text{if } \omega < 0 \end{cases} \tag{2.60}$$

where $\hbar$ is the reduced Planck constant, k_B is the Boltzmann constant, and T is the temperature. The terms in $n_{\mathrm{th}}(\omega)$ reflect the asymmetry between phonon absorption and emission, depending on whether ω is positive or negative, respectively.

In an unperturbed environment, phononic transitions between eigenstates couple entirely to the orbital degree of freedom and remain spin-conserving. However, we are interested in the qubit population decay driven by spin-flipping phonon transitions, such as $|-\downarrow\rangle \rightarrow |-\uparrow\rangle$. These transitions require spin mixing, which occurs under the influence of an off-axis magnetic field even at zero strain. In this scenario, the qubit eigenstates transform into perturbed eigenstates, e.g., $|-\downarrow\rangle \rightarrow |-\downarrow\rangle'$. The perturbed spin-orbit eigenstates are determined using first-order perturbation theory, with the perturbed state expressed as [105]:

$$|n\rangle' = |n\rangle + \sum_{m \neq n} \frac{\langle m|V|n\rangle}{E_n - E_m} |m\rangle, \tag{2.61}$$

[18] For a detailed derivation of γ_{ij}, please refer to the work of I. Harris [71]

with the perturbation matrix $V = \frac{B_\perp \gamma_s}{2}(\sigma_x \otimes \sigma_x)$ describing the influence of the off-axis magnetic field, and the Pauli X-matrix σ_x. We find the eigenstates $|-\downarrow\rangle$ and $|+\uparrow\rangle$ of the qubit to transforms to[19]:

$$|-\downarrow\rangle' = |-\downarrow\rangle + \frac{\gamma_s B_\perp}{2\left(B_\parallel(f_{12}-f_{32})\gamma_l - B_\parallel\gamma_s - \lambda^{\mathrm{g}}\right)}|-\uparrow\rangle \approx |-\downarrow\rangle - \frac{\gamma_s B_\perp}{2\lambda^{\mathrm{g}}}|-\uparrow\rangle \tag{2.62}$$

$$|+\uparrow\rangle' = |+\uparrow\rangle + \frac{\gamma_s B_\perp}{2\left(-B_\parallel(f_{12}-f_{32})\gamma_l + B_\parallel\gamma_s - \lambda^{\mathrm{g}}\right)}|+\downarrow\rangle \approx |+\uparrow\rangle - \frac{\gamma_s B_\perp}{2\lambda^{\mathrm{g}}}|+\downarrow\rangle \tag{2.63}$$

where we approximate $B_\parallel(f_{12}-f_{32})\gamma_l - B_\parallel\gamma_s << \lambda^{\mathrm{g}}$, as the orbital and spin Zeeman terms are negligible compared to the spin-orbit splitting. This explains why the transverse magnetic fields cause spin mixing of the eigenstates and enable coupling to phonons resonant with ω_{q}.

We now calculate the perturbed eigenstates under the influence of strain, where $V_{\mathrm{strain}} = \hat{H}^{so}_{\mathrm{strain}}$ describes the effect of strain on the spin-orbit eigenstates. For example, we find $|-\downarrow\rangle$:

$$|-\downarrow\rangle' = |-\downarrow\rangle + \frac{-\alpha}{-B_\parallel(f_{12}+f_{32})\gamma_l - \lambda^{\mathrm{g}}}|+\downarrow\rangle \approx |-\downarrow\rangle + \frac{\alpha}{\lambda^{\mathrm{g}}}|+\downarrow\rangle, \tag{2.64}$$

We observe directly that strain perturbs only the orbital components, leaving the spin component unaffected, a property that becomes crucial for enabling coherent control of the spin qubit, as will be discussed in Section 4.

To conclude, we aim to determine the experimentally observable scaling of the transition rates. We begin by considering the spin-conserving transition rate, as defined by S. Meesala [36]:

$$\gamma_{\mathrm{up}}(\omega) = 2\pi\chi\rho\ \omega^3 n_{\mathrm{th}}(\omega). \tag{2.65}$$

Here, $2\pi\chi\rho\ \omega^3$ contains the bulk density of states (DOS) scaling with ω^2 and the electron-phonon coupling, which scales linearly with ω.

We focus again on the case of negligible strain and an off-axis magnetic field. In this scenario, single-phonon transitions, such as $|+\uparrow\rangle' \rightarrow |-\downarrow\rangle'$, become partially allowed due to spin mixing. The strain susceptibility of the spin transition, d_{spin}, can be expressed in terms of the ground-state orbital strain susceptibility d_{g}. Therefore, we calculate the fraction of the ac strain $\epsilon^{\mathrm{ac}}_{E_g}$ (the phonons) resonant with the qubit transition frequency ω_{q} that effectively drives the spin-flipping transitions of the qubit. This requires evaluating the overlap of the perturbed wavefunctions. The susceptibility of the qubit state is thus expressed as:

$$\frac{d_{\mathrm{spin}}}{d_{\mathrm{g}}} = \frac{\langle -\downarrow|' H_{\mathrm{strain}}|+\uparrow\rangle'}{\epsilon^{\mathrm{ac}}_{E_g}} = \frac{\gamma_s B_\perp}{\lambda^{\mathrm{g}}} \tag{2.66}$$

The rate for single-phonon transitions is given by $\left(\frac{d_{\mathrm{spin}}}{d_{\mathrm{g}}}\right)^2 \gamma_{\mathrm{up}}(\omega_{\mathrm{q}})$. Resonant two-phonon transitions, such as the decay from $|+\downarrow\rangle' \rightarrow |+\uparrow\rangle'$ require both nonzero static strain and

[19] Note that S. Meesala defines $\gamma_s = 14\,\mathrm{GHz\,T^{-1}}$, while we maintain $\gamma_s = 28\,\mathrm{GHz\,T^{-1}}$, to keep consistency with the definition in Section 2.2

an off-axis magnetic field. S. Meesala estimates the susceptibility as $\frac{d_{\mathrm{g,flip}}}{d_{\mathrm{g}}} \sim \frac{1}{\Delta^{\mathrm{g}}}$ leading to a decay rate of $4\left(\frac{d_{\mathrm{g,flip}}}{d_{\mathrm{g}}}\right)^2 \gamma_{\mathrm{up}}(\Delta^{\mathrm{g}})$, where Δ^{g} denotes the ground-state splitting. Finally, off-resonant two-phonon relaxation scales with $\left(\frac{B_\perp \omega_{\mathrm{q}}}{\Delta^{\mathrm{g}}}\right)^2 T^3$. A summary of all rates and their expected scaling is provided in Table 2.2.

Although off-resonant two-phonon relaxation is expected to become relevant primarily at elevated temperatures above $\sim 40\,\mathrm{K}$, we find that including this term is necessary to correctly fit the experimental data for SnV-F (blue curve) depicted in Figure 2.22. This suggests that the contribution of these off-resonant processes may be more pronounced in certain defect configurations or field conditions.

Figure 2.22 presents various T_1 measurements, highlighting the distinct physical mechanisms governing phonon-mediated relaxation in SnV centers. One immediately notices the bend for the low-strain SnV centers SnV-F and SnV-D (blue and green curves) around 2.5 K. This saturation-like behavior can be attributed to coupling with resonant single-phonon transitions. At temperatures below $\sim 200\,\mathrm{mK}$ the spin relaxation time is expected to increase significantly due to the polynomially decreasing density of states. However, for SnV-F (blue curve) under a strong off-axis magnetic field, we observe a capping of $T_1 \approx 270\,\mathrm{ms}$ at the 50 mK base temperature of the cryostat. This limitation is likely caused by heat radiation from the 4 K surroundings, including the objective and the magnetic field coils mounted on the 4 K radiation shields, which effectively limit the minimum achievable local sample temperature. To estimate this temperature limit, we adjust the measured temperature $T_{\mathrm{measurement}}$ by introducing a correction term that scales with an offset ΔT. The offset is multiplied with an exponential term effectively reducing its weight for increasing temperature of the cryostat to account for the enhanced cooling power at higher temperatures. The adjusted temperature $T_{\mathrm{effective}}$ is expressed as:

$$T_{\mathrm{effective}} = T_{\mathrm{measurement}}\left(1 + \Delta T \cdot e^{-\frac{T_{\mathrm{measurement}}}{\Delta T}}\right) \tag{2.67}$$

This expression introduces an exponential factor to account for deviations in the low-temperature regime. From the best fit, we determine $\Delta T = 335\,\mathrm{mK}$ which serves as the limit temperature.

Table 2.2.: Summary of phonon-mediated relaxation processes in the SnV center: (a) single-phonon relaxation, (b) resonant two-phonon channels via the upper orbital branch, and (c) off-resonant two-phonon pathways. This Table has been slightly adapted and reprinted with permission from Srujan Meesala, Physical Review B, 97, 205444 (2018). Copyright (2018) by the American Physical Society.

Channel	Rate	Regime	Expected scaling of rate
Direct	$\left(\frac{d_{\mathrm{spin}}}{d_{\mathrm{g}}}\right)^2 \gamma_{\mathrm{up}}(\omega_{\mathrm{q}})$	$k_B T/h \ll \omega_{\mathrm{q}}$	$B_\perp^2 (\Delta^{\mathrm{g}})^{-2} \omega_{\mathrm{q}}^3 \exp(-h\omega_{\mathrm{q}}/k_B T)$
Orbach	$4\left(\frac{d_{\mathrm{g,flip}}}{d_{\mathrm{g}}}\right)^2 \gamma_{\mathrm{up}}(\Delta^{\mathrm{g}})$	$k_B T/h \sim \Delta^{\mathrm{g}}$	$B_\perp^2 \Delta^{\mathrm{g}} [\exp(h\Delta^{\mathrm{g}}/k_B T) - 1]^{-1}$
Raman	$8\pi^3 \left(\frac{d_{\mathrm{g,flip}}}{d_{\mathrm{g}}}\right)^2 \chi^2 \rho^2 \omega_{\mathrm{q}}^2 \left(\frac{k_B T}{h}\right)^3$	$k_B T/h \gg \Delta^{\mathrm{g}}$	$B_\perp^2 (\Delta^{\mathrm{g}})^{-2} \omega_{\mathrm{q}}^2 T^3$

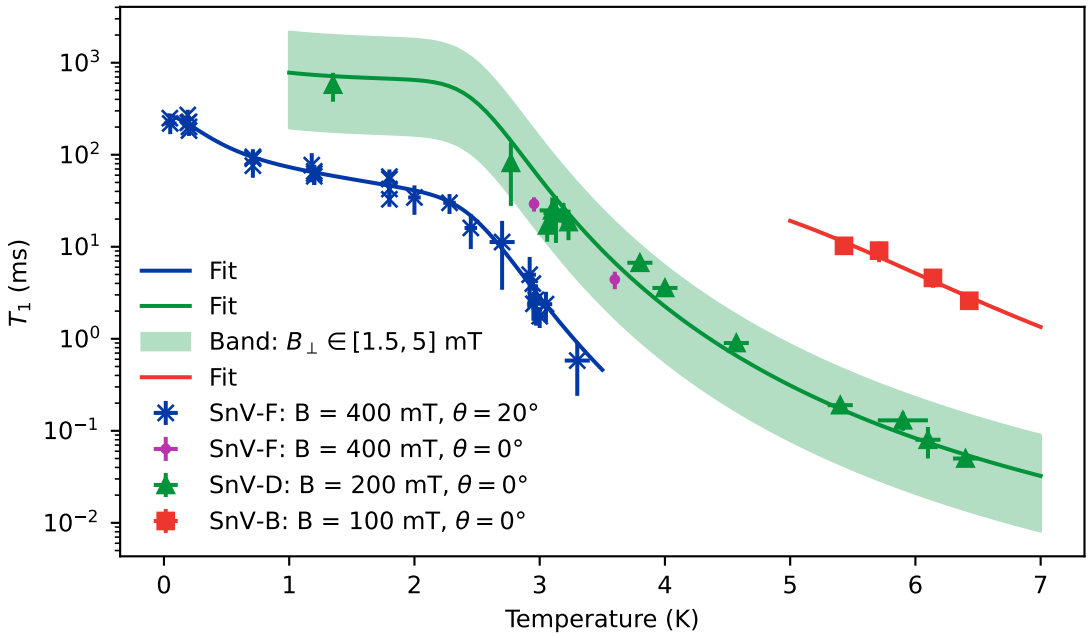

Figure 2.22.: Temperature dependence of the spin-lattice relaxation time T_1 for different SnV centers, illustrating key relaxation mechanisms. Around 2.5 K, T_1 exhibits saturation-like behavior due to coupling to resonant single-phonon transitions. At temperatures below ~ 300 mK, the observed T_1 of SnV-F (blue curve) saturates from thermal saturation of the sample temperature, due to heat radiation from the 4 K surrounding, effectively capping the minimum temperature achievable at approximately ~ 300 mK. The green band for SnV-D represents slight magnetic field variations of the off-axis magnetic field ($B_\perp \in$ 1.5 mT to 5 mT). The magnetic field is initially aligned along the quantization axis of the SnV center. However, small off-axis components may arise due to coil hysteresis effects.

The green band for SnV-D represents slight variations in the off-axis magnetic field ($B_\perp \in$ 1.5 mT to 5 mT). Initially, the magnetic field is aligned along the quantization axis of the SnV center ($\theta = 0°$). However, small off-axis components may arise due to coil hysteresis effects and imperfect field calibration.[20] We observe that even slight variations in $B_\perp$ induce significant changes in the spin relaxation time.[21] The red curve corresponds to T_1 measurements of the highly strained SnV-B, which exhibits orders of magnitude higher spin relaxation times compared to the unstrained emitters due to the enhanced ground-state splitting. This large splitting suppresses phonon-mediated relaxation processes as it shifts the system out of resonance with many low-energy phonons. The thermal occupation of high energy phonon states is significantly lower and their availability for phonon-driven transitions decreases. The spin state is effectively decoupled from the phonon bath, yielding an enhanced T_1. The fit values for SnV-F and SnV-D are summarized in Table 2.3.

[20] For details on the methods used for magnetic field calibration, refer to Section C.3.2.

[21] While a few millitesla variation in $B_\perp$ may appear small compared to $B_\parallel$, the coupling scales with $B_\perp^2$ meaning that even slight changes can effectively enhance the phonon-coupling by an order of magnitude.

Until now, we have not discussed the spin-conserving transitions, shown in the blue panel of Figure 2.21, which are responsible for dephasing (transverse relaxation). These transitions are particularly significant at higher temperatures where thermal phonon populations increase. Still, they contribute to dephasing even at cryogenic temperatures, as they introduce random phase shifts between the spin projections due to the different precession frequency of the qubit within the separate branches. The transverse relaxation time T_2, can be expressed as a combination of contributions from T_1 and dephasing processes T_Φ. For a phonon-limited environment, T_2 is given by:

$$\frac{1}{T_2} = \frac{1}{2T_1} + \frac{1}{T_\Phi} \tag{2.68}$$

with $T_\Phi = 1/\gamma_{\mathrm{up}}(\Delta^{\mathrm{g}})$, showing that coherence is effectively protected by strain. For readers specifically interested in temperature dependent spin-coherence measurements of T_2 and T_2^*, we refer to the work of A. Stramma [73] and to matching theoretical calculation published by I. Harris [71].

In summary, we have studied the spin dynamics of the SnV center, focusing first on the interactions within the relevant three-level system spanned by the qubit levels and one of the excited states to determine the cyclicity and initialization fidelity of the system, both of which are relevant factors for spin-qubit control. We specifically addressed phonon-induced relaxation pathways, looking primarily on processes that influence spin relaxation and decoherence. We have shown, that strain and off-axis magnetic field components mix the spin and orbital states, allowing resonant and off-resonant spin-flip transitions. We find the electron-phonon coupling responsible for spin-flipping transitions to be proportional to $\propto \frac{\gamma_s B_\perp}{\lambda^{\mathrm{g}}}$. Hence, the large intrinsic spin-orbit coupling allows SnV centers to maintain stable spin states at relatively higher operational temperatures setting it apart from the lighter SiV and GeV centers. These require additional strain to protect their properties due to the relatively small spin-orbit coupling of 50 GHz [65] and 170 GHz [75], respectively. Generally, additional strain further suppresses phonon-mediated relaxation mechanisms protecting lifetime and coherence.

Table 2.3.: Fit values for SnV-F and SnV-D. The parameters A_1(single-phonon), A_2(two-phonon), and A_3(off-resonant two-phonon) represent the amplitudes (pre-factors of the expected scaling rate) for the corresponding transition rates.

Parameter	SnV-F	SnV-D
A_1	4.033×10^{-7} kHz	5.697×10^{-4} kHz
A_2	1.355×10^{-5} kHz	1.710×10^{-3} kHz
A_3	190 kHz	0.0 (fixed)
$B_\perp$	136.8 mT (fixed)	2.5 mT (fixed)
Δ_{gs}	840 GHz (fixed)	825 GHz (fixed)
ω_s	13 GHz (fixed)	7 GHz (fixed)
ΔT	335.8 mK	-

2.6. Summary

In this chapter, we investigated the fine structure of the SnV center by first presenting a full matrix-representation of the relevant Hamiltonian. We supported the theoretical description by examining the interactions of spin-orbit coupling, strain and magnetic field separately via experimental measurements. We show a method to meticulously characterize all detected SnV centers to determine the suitable emitters for coherent control and precise fine-structure analysis. We showed stable optical transitions for various low to high strain SnV centers, demonstrating the pristine optical properties of the SnV center. With the enhanced control over the optical and magnetic states of the SnV center's electron, we measured 2D rotation maps of the optical transitions to reliably determine the SnV center's quantization axis within the laboratory system with an uncertainty of less than 1 %. Through variation of the magnetic field orientation we further contribute to a deeper understanding of the magneto-optical properties. By mapping the measurements to the electron-spin Hamiltonian with explicit ground and excited state doublets, we determined the orbital quenching factors. In addition we developed a fitting procedure for the optical and qubit transitions to easily characterize unknown emitters. We investigated the spin dynamics of the SnV center. Among them, we show an initialization and readout fidelity of $F_{\parallel} = 99.84(8)$ % for parallel field orientation and $F_{\perp} = 99.98(2)$ % for perpendicular field orientation, demonstrating an almost perfect initialization. We determined the lower bound of the cyclicity for SnV-B under parallel field orientation to be ~ 1700, an important property for the following coherent control measurements. At last, we analyzed the relaxation time for various defects under differing field compositions illustrating the key relaxation mechanisms.

3. Ohmic Heating in Normal and Superconducting Waveguides: Implications for Efficient Spin Control

Efficient and coherent microwave control of solid-state spin qubits requires careful engineering of the microwave delivery structure. In the following chapter, we discuss the advantages of a shorted coplanar waveguide (CPW) design, with a small gap fabricated directly on the diamond surface and positioned in close proximity to the emitters, in enabling strong and localized microwave fields. With an impedance matched geometry optimized for fast spin rotations, necessary for high-fidelity qubit operations, pulse errors due to reflections of the microwave signal are minimized.

Achieving fast control with conventional normal-conducting CPWs (NC-CPWs) often comes at the cost of significant Ohmic losses, due to the high microwave power required to achieve fast and efficient qubit operations. The local temperature of the surrounding diamond lattice can rise significantly and the local thermal fluctuations can degrade the properties of the SnV center, such as spin initialization fidelity and coherence time.

To address this challenge without compromising the efficiency of the microwave control, we fabricate superconducting coplanar waveguides (SC-CPWs) made from niobium. These structures eliminate Ohmic losses and thus enhance thermal stability, while maintaining the advantageous design parameters needed for efficient qubit manipulation.

To investigate the thermal impact of both NC-CPWs and SC-CPWs, we utilize the SnV center itself as a local temperature sensor. By analyzing the temperature dependence of the zero-phonon line position and linewidth broadening, we calibrate the SnV center as a local thermometer. This approach allows us to directly quantify and compare microwave-induced heating effects across the different CPW implementations.

We begin by introducing the finite-width coplanar waveguide (FW-CPW) structure in Subsection 3.1, that is used for the coherent control measurements discussing the major advantages of the simple structure for spin-qubit control. Following, we motivate the use of superconducting coplanar waveguides. Next, the temperature dependent PLE measurements, to quantify the SnV center's spectral response as a function of temperature, is presented in Subsection 3.2. To conclude, we examine the impact of microwave driving on the SnV center's spectral properties and spin relaxation time and conduct a direct

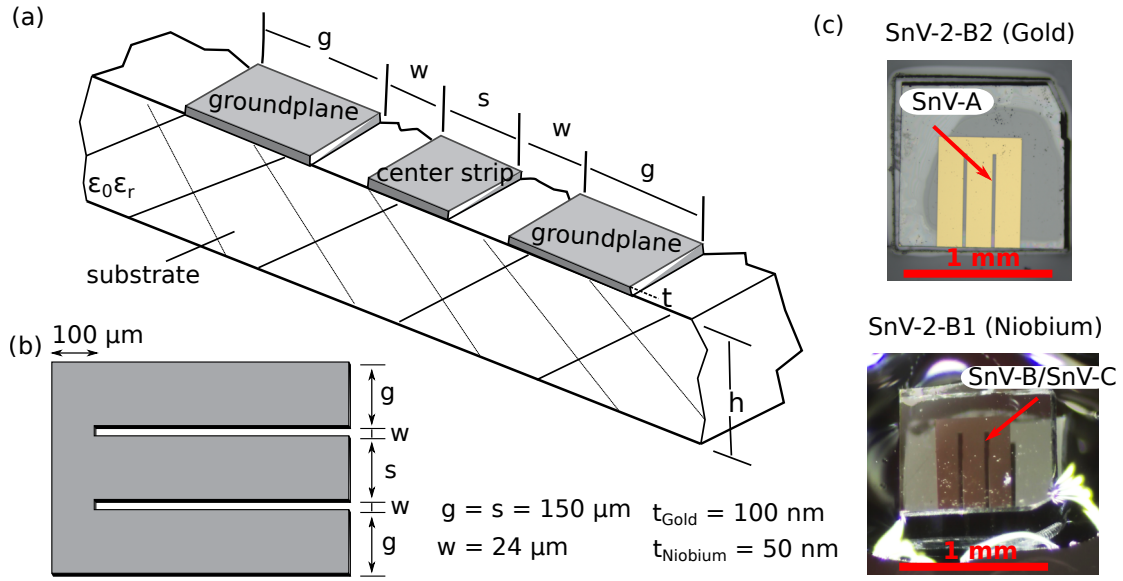

Figure 3.1.: The symmetrical coplanar waveguide (CPW). (a) presents a schematic of the finite-width coplanar waveguide (FW-CPW) on a dielectric substrate. This structure consists of a central strip conductor flanked by finite-width ground planes and supports a quasi-TEM mode of propagation, as described in [106]. Figure (b) shows the FW-CPW with the dimensions used for sample fabrication, accurately scaled to match the true proportions. (c) displays images of fabricated samples, including a normal-conducting CPW made of gold (top image) and a superconducting CPW made of niobium (bottom image).

comparison of NC-CPW to SC-CPWs. At last, we demonstrate the advantages of SC-CPWs in reducing microwave-induced heating with various experimental measurements in Subsection 3.3.

3.1. Coplanar Waveguides for Spin Qubit Control

The coplanar waveguide was first proposed by Cheng P. Wen in 1969 [107] and "consists of a strip of thin metallic film on the surface of a dielectric slab with two ground electrodes running adjacent and parallel to the strip." It is a specialized transmission line[1] that allows for the delivery of electromagnetic (EM) waves to a far destination, while mitigating radiation loss. [108]. Transmission lines consist of two or more conducting metals, effectively reflecting an energy carrying EM wave back and forth with minimal loss, while restricting the direction of propagation. One commonly known and used transmission line is the coaxial line consisting of a conducting wire and a surrounding cylindrical conducting shield with an insulating medium in between.

[1] The book *Understanding Electromagnetic Waves* of M. Kao and C. Chang offers a friendly introduction into the theory of transmission lines [108].

An important property of transmission lines is the characteristic impedance Z_0 that is defined as the voltage to current ratio along the line direction z:

$$Z_0 = \frac{V(z)}{I(z)} = \text{constant} \tag{3.1}$$

The characteristic impedance of transmission lines is influenced by their geometric parameters, as well as the dielectric of the substrate between the conductors. In general, one tries to match Z_0 of different connected transmission lines for a simple reason: If the characteristic impedance of two lines is different, the voltage to current ratio has to adapt on the interface to yield the same ratio for both lines. This is only possible, if a partial reflection of the EM wave occurs on the interface. Since the aim is lossless EM wave propagation to the destination of the transmission line, one has to mitigate these reflection. This is achieved by designing the geometry of different lines to yield the same characteristic impedance. Usually, the commercially bought electronic components are designed to have $Z_0 = 50\,\Omega$.

The transmission line that we are interested in is a variation of the first proposed CPW structure and is depicted in Figure 3.1 (a). It consists of a center conductor with two finite-width ground planes. In (b) the design of the FW-CPW with the dimensions used for the sample fabrication is shown in the top view, accurately scaled to match the true proportions. The waveguide is shorted at the end, to reflect the EM wave, and create a standing wave with the following conditions:

$$V_+ = -V_- \rightarrow V_\mathrm{L} = 0 \tag{3.2}$$

$$I_+ = I_- \rightarrow I_\mathrm{L} = 2I_+ \tag{3.3}$$

Here, V_+ and V_- represent the forward and reflected voltage waves, respectively, while I_+ and I_- denote the corresponding current components. The subscript L stands for the load of the short.[2] At the shorted end ($Z_L = 0$) of the CPW, the voltage must vanish ($V_L = 0$) according to equation 3.1, enforcing a perfect reflection with a 180° phase shift between the incident and reflected waves. On the other hand, the current components add constructively, resulting in a current maximum at the shorted termination ($I_L = 2I_+$). This means, that a traveling wave (on transmission) needs four times more power than a shorted circuit to deliver the same peak current at the sample. Since minimizing heat dissipation in the cryostat is desired over the extend of the transmission line, the reduced power requirements enabled by this effect is advantageous.[3]

To mitigate reflections before the shorted end of the CPW, the characteristic impedance is matched to $Z_\mathrm{CPW} = 50\,\Omega$ by individually adapting the geometric dimensions of the

[2] The load is the circuit or electrical device connected at the end of the line that receives or reflects the transmitted power. Here, it corresponds to the shorted end of the CPW, while the CPW has a matched impedance of $Z_\mathrm{CPW} = 50\,\Omega$.

[3] The power is defined as $P = Z_0 I^2$, hence to achieve a peak current I_L at the load an input power of $Z_0 I_\mathrm{L}^2$ is necessary for a traveling wave. In contrast, for a shorted circuit where the standing-wave effect doubles the current at the load, the same peak load current is achieved with only $\frac{1}{4} Z_0 I_\mathrm{L}^2$ of input power.

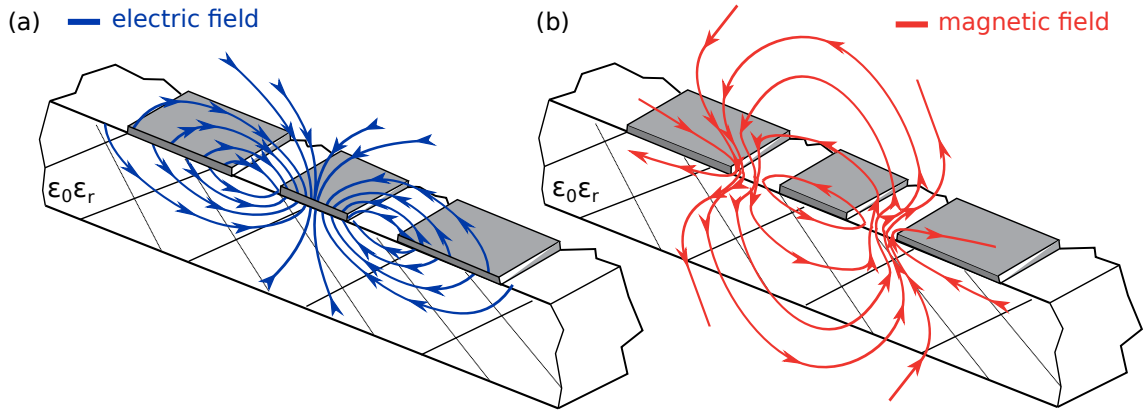

Figure 3.2.: Electric and magnetic field distribution of the CPW. The electric and magnetic field lines of the even mode in the cross section of the coplanar waveguide are depicted in blue (a) and red (b), respectively. The electric-field lines extend across the conductor gaps while the magnetic field lines are oriented perpendicular to the air-dielectric interface within the gap. Obviously, the magnetic field is strongest in this region, making it the optimal location to investigate SnV centers. Additionally, it is observed that the electric field lines on the right half of the structure are mirrored in direction relative to those on the left half, while the magnetic field lines circulate around the central conductor. Inspired by [106]

center strip, the groundplanes, the gap and the height of the substrate with permittivity ϵ_r. The characteristic impedance of the CPW can be precisely derived, along with its attenuation constant, using the conformal mapping method [109]. The detailed impedance and attenuation calculations are provided in Appendix D and will be skipped at this point of the work.

The elaborate discussion about the electric current component is due to a straightforward fact: the alternating component of the magnetic field that drives the electron spin of the SnV center is directly proportional to the current I. The electric along with the magnetic field distribution of the CPW are drawn in Figure 3.2 (a) and (b), respectively. It is clear, how the magnetic field is forced into the narrow gap between the center conductor and the ground planes, making the field strongest in this region and thus, the optimal location to investigate SnV centers. The ability of the CPW to efficiently deliver microwave fields with high spatial confinement makes them interesting for spin qubit applications, where strong electromagnetic fields are essential for efficient spin manipulation. The structure supports a quasi transverse electromagnetic (TEM) mode of propagation. Therefore, there is no low-frequency cutoff and dispersion is minimized, enabling low loss transmission of radio frequency and microwave signals. The planar geometry allows for simple, on-chip fabrication and makes them very tempting for applications on diamond substrates with color centers close to the surface. Ergo, when investigating SnV centers we focus on defects in proximity of the shorted end of the FW-CPWs. Two different samples are depicted in Figure 3.1 (c), one with a normal-conducting CPW made of gold (top image) and one with a superconducting CPW made of niobium (bottom image). The different SnV centers that are characterized within the respective samples, are indicated.

Lastly, the attenuation of the EM waves due to conductor losses and dielectric losses in the diamond are discussed in a quantitative manner. Dielectric losses originate from the finite

conductivity and imperfect insulating properties of materials such as the silicon wafer substrate, the adhesive between the diamond sample and the diamond itself. Additionally, polarization losses arise from the reorientation of dipoles within the substrate in response to the oscillating electromagnetic field. Conductor losses in normal-conducting metals, such as gold which is used in the fabrication of the NC-CPWs, originate from Ohmic dissipation. Electromagnetic fields affecting the metal will induce currents that oscillate and decay as a function of depth into the metal. This is known as the skin effect. In thick conductors,[4] these losses increase with frequency due to this effect, which confines the current flow to the metal's surface, leading to increased resistance. [110] However, for the thin gold layer used in NC-CPWs, with a thickness of approximately $t_{\text{gold}} \approx 100\,\text{nm}$, the skin depth δ_{nf} remains significantly larger than the conductor thickness up to several tens of GHz. As a result, the frequency dependence of NC-CPW losses is negligible for thin conductor layers.

For superconductors, the direct current (DC) resistance of the metal drops to zero below the superconducting critical temperature T_c, which for bulk niobium is $T_{\text{c}}^{\text{bulk}} \approx 9.3\,\text{K}$ [111]. In the case of thin films with a thickness of approximately $t \approx 50\,\text{nm}$, the critical temperature is slightly reduced to $T_{\text{c}}^{50\,\text{nm}} \approx 8.6\,\text{K}$ [112]. Hence, the question arises, how a superconductor behaves under the effect of electromagnetic waves. In 1940, Heinz London showed high-frequency resistance for superconducting tin. He explained the resistance through the "simultaneous presence of superconducting and normal electrons" [113] as presumed in a previous paper in 1934 [114]. The effect is phenomenologically described by the two-fluid model, which assumes that a superconductor consists of a fraction of normal electrons that experience resistance and inertial effects just like they do in a normal metal and a fraction of superconducting electrons that show inertial effects but flow without dissipation[115]. The relative number of these normal to superconducting electrons change as a function of temperature with the total number per unit volume given by:

$$n(T) = n_{\text{s}}(T) + n_{\text{n}}(T). \tag{3.4}$$

Here, the total density n is equal to that of the metal in the normal state. Once the superconductor is cooled below T_c, the number of superconducting electrons increases from zero to $n_{\text{s}} = n$ at $T = 0\,\text{K}$ and the number of normal electrons decreases accordingly. For DC current, the superconducting electrons can flow without resistance, carrying the total current and mitigating dissipative losses. However, as soon as an alternating field is applied the normalconducting electrons contribute to the current and power is dissipated. This is attributed to the non-zero impedance of the superfluid [110].

To finally compare NC-CPW with SC-CPW, we can consider the frequency dependence of the dissipated power for a normal-conductor and a superconductor. The power dissipation is given by:

$$P_{\text{n}} \propto \omega^{1/2} \text{ and} \tag{3.5}$$

$$P_{\text{s}} \propto \omega^{2} \tag{3.6}$$

[4] For example in printed circuit boards, the conductor thickness of the transmission lines made of copper typically exceeds 18 µm.

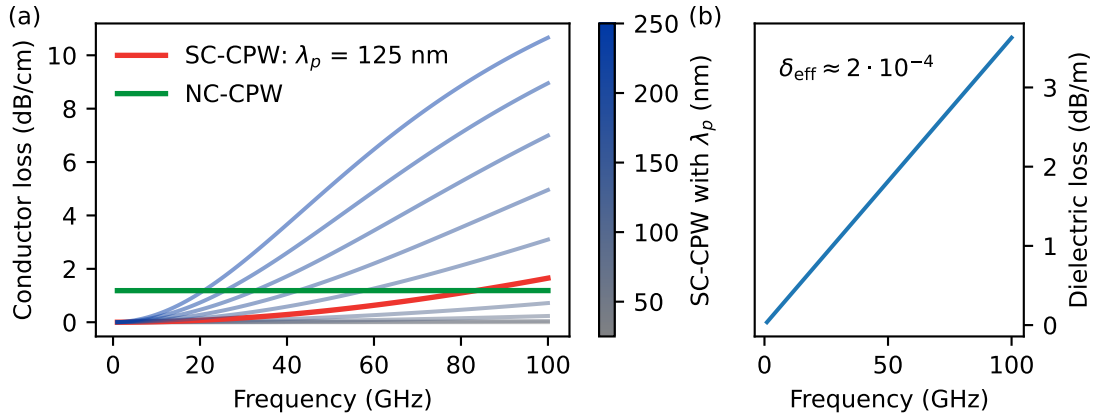

Figure 3.3.: Attenuation characteristics of NC-CPW and SC-CPW. (a) Conductor losses as a function of frequency for normal-conducting (NC-CPW) and superconducting (SC-CPW) coplanar waveguidesexpressed in dB cm^{-1}. The SC-CPW losses strongly depend on the magnetic penetration depth λ_{p}, with a crossover point where SC-CPW losses exceed NC-CPW losses at approximately 80 GHz for $\lambda_{\text{p}} = 125$ nm. (b) Dielectric losses as a function of frequency, expressed in dB m^{-1}. The dielectric loss is dominated by the adhesive material, with an assumed effective loss tangent of $\delta_{\text{eff}} \approx 2 \times 10^{-4}$.

respectively. Since most of the current is carried by the superconducting electrons far below T_{c}, the superconductor starts with much smaller loss but can eventually exceed the losses of normal metals for very high frequencies. However, this frequency is typically above several tens of GHz.

The conductor losses for both NC-CPW and SC-CPW are calculated using equation D.15[5] (see Section D.2) and are depicted in Figure 3.3 (a), with the geometric parameters given in Figure 3.1 (b). As discussed earlier, the losses in the normal-conducting CPW (green curve) remain frequency-independent as long as the normal skin depth satisfies $\delta_{\text{nf}} \gg t_{\text{gold}}$. In contrast, the conductor losses of the superconducting CPW (grey-blue gradient) strongly depend on the magnetic penetration depth λ_{p}. The calculated losses are shown for penetration depths in the range $\lambda_{\text{p}} \in [25, 250]$nm. Assuming a moderate penetration depth of $\lambda_{\text{p}} = 125$ nm (red curve), the crossover frequency, where the SC-CPW losses exceed those of the NC-CPW occurs at approximately ≈ 80 GHz for the given geometry.[6]

The calculated dielectric losses are shown in Figure 3.3 (b). As described by equation D.12, they exhibit a linear dependence on frequency. For diamond, the loss tangent ($\tan(\delta_{\text{l}})$, which is a measure of signal loss) is exceptionally low, ranging from 10^{-6} to 10^{-5} [119]. However, for some materials, such as polyimide in flexible printed circuit board (PCB)

[5] Note that the equation includes the characteristic impedance, which accounts for the weighting of the effective dielectric factor, that is determined by the contribution of the diamond's and the substrate's dielectric constants.

[6] Values of the magnetic penetration depth for thin film niobium range from 25 to > 250 nm depending on the thickness and purity of the material. For studies on niobium films with equivalent thickness of 50 nm and a purity defined via the residual resistance ratio $RRR = R(300\,\text{K})/R(T_{\text{c}})$ where we measure a value of $RRR \approx 3.5$ the magnetic penetration depth ranges from $\lambda_{\text{p}} \in [100, 150]$nm [116–118]. Therefore, we take the mean value for the simulation.

structures that are used for microwave transmission between the separated cryogenic stages within the cryostat, or polymers like PMMA used as adhesives for the samples, the loss tangent is significantly higher, typically between 10^{-3} and 10^{-1} at room temperature [120]. Reports indicate that these losses are drastically reduced in cryogenic environments, by up to a factor of 100 [121]. In the graph presented, an average dielectric loss of $\delta_{\text{eff}} \approx 2 \times 10^{-4}$ is used, as determined via the separate contribution of the diamond and the adhesive. The contribution of the diamond and the adhesive to the dielectric losses is a function of their respective filling factors, a measure of the amount of electric field in the respective material. The calculation of the filling factor is explained in Appendix D.2. Note that the dielectric losses in this graph are expressed in $\mathrm{dB\,m^{-1}}$, in contrast to the conductor losses.

For coherent control measurements, we typically need frequencies below 10 GHz. As an example, we want to give the specific values for the conductor and dielectric losses for the most used frequency during this work of around 3 GHz, for NC-CPWs and SC-CPWs. For the normal-conducting CPW we determine a conductor loss of of $\alpha_{\text{c}}^{\text{n}} \approx 1.2\,\mathrm{dB\,cm^{-1}}$, For the superconducting CPW we calculate $\alpha_{\text{c}}^{\text{s}} \approx 0.002\,\mathrm{dB\,cm^{-1}}$, a 600-fold difference. The dielectric losses are the same for both materials and account for $\alpha_{\text{d}} \approx 0.001\,\mathrm{dB\,cm^{-1}}$ at 3 GHz.

To get a first impression of the temperature- and power-dependent behavior of niobium CPWs, we fabricate a 50 nm-thick waveguide on a bulk diamond substrate via electron-beam evaporation and measure the insertion loss (IL) through the cryostat, with the microwave power monitored directly in front of the cryostat. The waveguide used in these measurements operates in a transmission configuration, making it an S_{21} measurement.[7] In Figure 3.4, we investigate the high-frequency performance of this superconducting CPW from DC to 10 GHz in a zero-field environment. Figure 3.4 (a) shows the IL during cooldown from room temperature to 7 K, revealing a distinct enhancement in transmission for reduced temperatures and a sharp IL drop below 9 K due to the superconducting phase transition and the vanishing resistive losses of niobium.[8] The extracted data at 3 GHz (red box) are plotted in (b), illustrating the significant decrease in IL once the niobium becomes superconducting. In (c), the IL is depicted for input powers of 19 dBm (red) and 19.2 dBm (black), demonstrating that the IL remains low until a critical power level is reached. Above approximately 19.2 dBm, superconductivity is suppressed, restoring the waveguide's normal-state losses, as shown in (d).

While the preceding results highlight the temperature- and power-dependent behavior of niobium CPWs, these metrics alone do not fully determine their viability for quantum applications. Ultimately, even though conductor and dielectric losses can be calculated precisely, the critical question is whether SC-CPWs actually benefit spin qubits by mitigating microwave-induced heating in the GHz regime and operating under the magnetic fields

[7] In microwave engineering, S_{21} refers to the scattering parameter that characterizes the transmission of a signal from port 1 (input) to port 2 (output). It quantifies how much power is lost through the device and is often measured in decibels (dB).

[8] Note that the insertion loss includes the losses of the coaxial lines and the flexible PCB line.

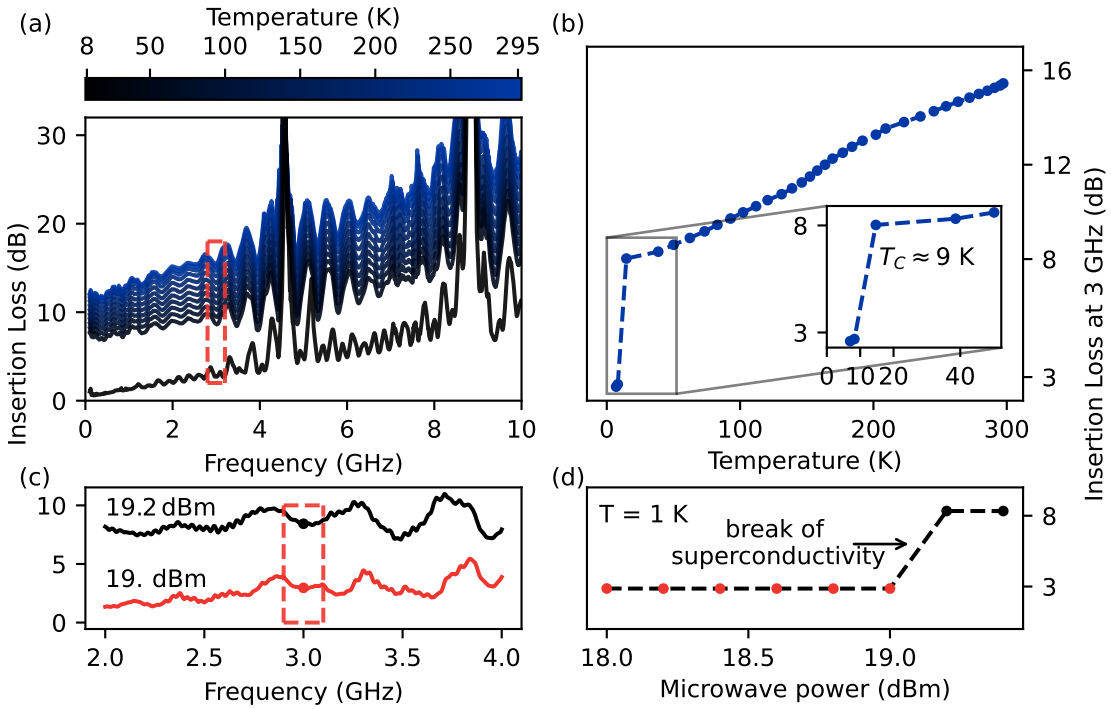

Figure 3.4.: Properties of superconducting niobium waveguides in zero-field environment. In (a) the measured insertion loss of a superconducting CPW is depicted from DC to 10 GHz. The enhanced transmission at less than or close to 9 K is caused by the superconducting phase transition and the vanishing resistance of the niobium. The red box indicates the data points at 3 GHz that are extracted for the graph in (b). (c) Breaking of superconductivity at a power of 19.2 dBm. The red line shows the IL while the waveguide is still in the superconducting state. The red box indicates the data points at 3 GHz that are extracted for the graph in (d). Graphs (b) and (d) are adapted from Figure 3 in Reference [1].

required for reasonable qubit splitting. If SC-CPWs fail to outperform NC-CPWs in the actual operational environment, their implementation becomes unnecessary. To address this, we employ the SnV center as a highly sensitive temperature probe by calibrating its temperature response to characterize the thermal impact of both NC-CPWs and SC-CPWs on the local cryogenic environment.

3.2. Temperature Calibration of the SnV Center

Group-IV defects, such as the SnV center, are sensitive to temperature because electron–phonon interactions shift and broaden their zero-phonon lines. By measuring the linewidth and line position as a function of the temperature, one can observe distinct polynomial scaling laws that capture these phonon-driven processes. In this section, we explore how temperature affects the C-transition of the SnV center, focusing on both its shift in energy and its broadening.

The temperature dependent behavior of group-IV defects (including the SnV center) has been investigated by several groups, and a summary of these results is provided in table 3.1. Most of these studies observe linewidths that follow a dominant $\propto T^3$ dependence, with a weaker $\propto T^7$ contribution, while the ZPL shift typically scales as a combination of $T^2 + T^4$. A theoretical model explaining these polynomial laws via electron–phonon interactions was introduced by V. Hizhnyakov [122, 123]. The temperature dependence of the ZPL linewidth is explained as a modulation of the ZPL frequency by long-wave acoustic phonons. For nondegenerate electronic levels this results in a $\propto T^7$ dependency. For degenerate electronic levels and in the presence of the linear dynamic Jahn-Teller effect, this yields a $\propto T^5$ dependence, that is only observed in two investigations of SiV center ensembles [124, 125]. The suggested model of V. Hizhnyakov extends the theory to include the quadratic electron–phonon coupling in the presence of a "strong softening of elastic springs" [9] in the excited state. In the case of linear Jahn–Teller interaction the adiabatic potential energy surface (APES) is shaped like a Mexican hat in the excited state with a single minimum [38, 88]. The inclusion of quadratic terms disrupts the axial symmetry and produces three minima, that are separated by very shallow energy barriers if the interaction is small. This instability results in a significant peak of the local phonon density of states at a low frequency. In turn, this leads to a significant change in the temperature dependence of the ZPL shift (T^2 instead of T^4) and width (T^3 instead of T^7). One can picture the system as being extra sensitive, since a small increase in temperature leads to a large increase in the amplitude of these phonon mode fluctuations, which in turn dramatically increase the dephasing rate. This unusual sensitivity is what the authors refer to as anomalous temperature dependence.

We now focus on the examination of the temperature dependent shift and broadening of the C-transition for SnV-F in the range of 1 to 20 K. We will establish a precise temperature calibration for this SnV center, also clarifying the underlying electron–phonon interactions. In turn, this approach will allow us to evaluate how normal-conducting and superconducting coplanar waveguides influence the local cryogenic environment.

Figure 3.5 presents an extensive PLE measurement of the C-transition of SnV-F measured over a temperature range from 20 down to 1 K. Note that the temperature axis is non-linear due to the non-linear nature of the temperature curve during cooling. For this reason, the mapped temperature values are given at close intervals. We want to briefly

[9] Elastic springs are a way to picture the interatomic bonds.

Table 3.1.: Temperature behavior of group-IV defects. Abbreviations: Ref. = reference; S.e. = single emitter; Ens. = ensemble.

Defect center	Ref.	Temperature range (K)	Defect type	Linewidth scaling	Lineshift scaling
SiV	[35]	4–350	S.e.	< 20 K: T^1; > 20 K: T^3	T^3
SiV	[21]	5–295	S.e. and Ens.	T^3	Ens.: $T^2 + T^4$; S.e.: T^4
SiV	[124]	5–300	Ens.	$T^3 + T^5 + T^7$	$T^2 + T^4$
SiV	[125]	5–80	Ens.	$T^3 + T^5$	$T^2 + T^4$
GeV	[126]	20–180	Ens.	T^3	$T^2 + T^4$
GeV	[127]	100–400	Ens.	T^a ($a \approx 2.8$)	T^3
SnV	[128]	80–300	Ens.	$T^3 + T^7$	$T^2 + T^4$
SnV	[85]	5–200	S.e. and Ens.	T^3	$T^2 + T^4$
PbV	[78]	6–260	Ens.	T^3	$T^2 + T^4$
SnV	this work	1–20	S.e.	$T^3 + T^7$	$T + T^2 + T^4$

discuss the accuracy of the temperature of the thermometers: In our setup, temperature measurements are performed using ruthenium oxide resistive thermometers in a four-terminal measurement configuration. These resistors have been calibrated by previous group members using certain reproducible fixed points in cryogenic thermometry, such as the boiling point of liquid helium at standard atmospheric pressure, e.g. by immersing the thermometer in a bath of liquid helium. In addition, to extend the calibration to a wider temperature range, especially below 4 K, the thermometers were cross-calibrated with instruments from other cryostats. Therefore, the absolute accuracy of the temperature is difficult to estimate, also partly because the thermometers and the sample are spatially separated. The thermometer is mounted directly onto the milli-Kelvin plate, while the sample is mounted onto the piezo-stack. Thus, to minimize the temperature gradient between the temperature sensor and the sample, the cooling from 20 down to 1 K is performed over a relatively long duration of ~ 150 min.

The spectral response is normalized and displayed on a logarithmic scale with an adapted range of the colormap, allowing a clearer illustration of the subtle spectral features at higher temperatures. As the temperature decreases, the ZPL reveals a blueshift of the C-transition. The temperature dependency of the ZPL shift can be attributed to the modulation of the electronic states due to changes in the lattice environment and enhanced electron–phonon interactions, but in parts also due to the thermal expansion of the diamond [128]. The broadened linewidth at higher temperatures reinforces how thermal effects not only shift the transition but also introduce broadening. The center of the ZPL transition is marked with a red line, providing a reference point to quantify the shift. This detailed temperature-dependent mapping is key to calibrate the SnV center for its role in temperature sensing.

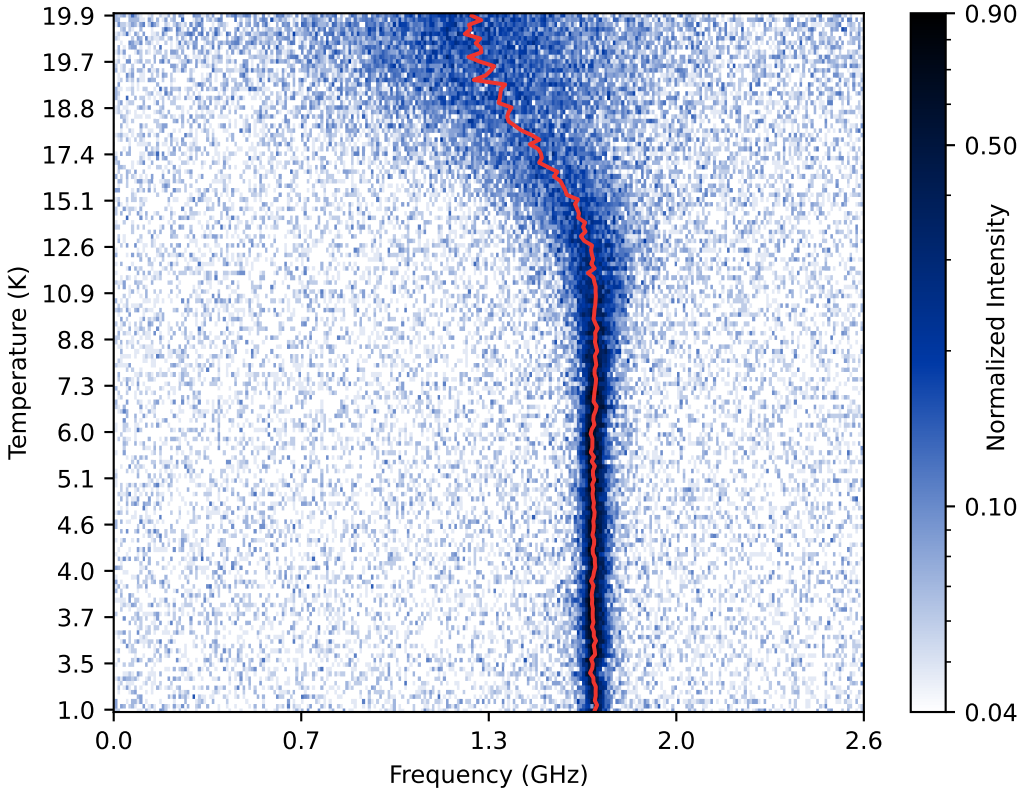

Figure 3.5.: PLE measurement of the C-transition of SnV-F as a function of temperature. The 2D plot shows the spectral response from 20 K down to 1 K, illustrating the evolution of the transition linewidth and position. In order to better visualize the transitions at elevated temperatures, the data have been normalized and plotted on a logarithmic scale. The transition shows a redshift with increasing temperature, accompanied by a broadening of the linewidth. The center position of the transition is indicated with a red line. Please note that the temperature axis is non-linear due to the non-linear nature of the temperature curve during cooling.

It sets the foundation for the more specific analysis of the following lineshift (Figure 3.6) and linewidth (Figure 3.7).

In Figure 3.6, the zero-phonon lineshift is plotted against temperature and fitted to a polynomial model of the form $c_0 + c_1 T + c_2 T^2 + c_4 T^4$. Unlike previous studies, the inclusion of the $c_1 T$ term is crucial here, as the inset demonstrates. The linear component is necessary to capture the nuanced behavior of the ZPL shift, which shows a negative trend up to around 5 K, reverses to positive up to 10 K, and then becomes negative again as the T^4 term dominates above this temperature. The origin of the $c_1 T$ term is unclear and is not discussed in any of the referenced literature in Table 3.1, where measurements below 4 K were not performed. In addition, it is very challenging to achieve gradually stable temperatures in the range between 1.2 and 4 K, complicating a precise measurement of this contribution. [10] The described contributions limit this SnV center's effectiveness for

[10] Temperatures can be reduced below 4 K by pumping on the helium bath, but the steep vapor-pressure curve in this range makes stable control difficult. Accessing $\sim$ 1 K typically relies on a Joule–Thomson expansion stage, which is not optimized for fine regulation between $1 - 4$ K.

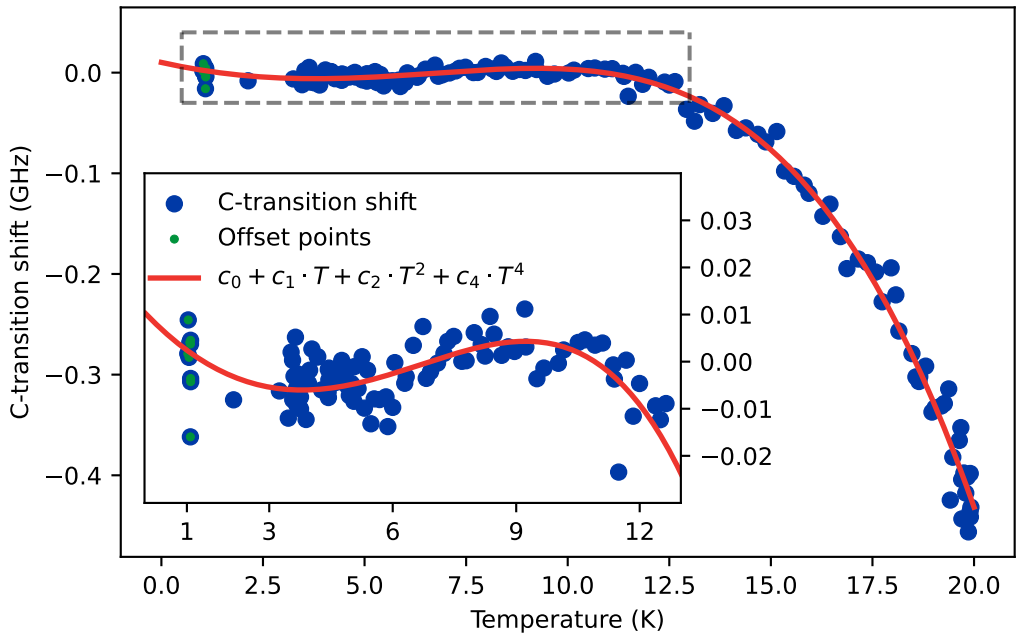

Figure 3.6.: Temperature dependence of the C-transition lineshift. The blue dots show the extracted lineshift from the PLE measurements during the cooldown from 20 K to 1 K. The main figure reveals a pronounced lineshift above 12 K. The solid red lines show the polynomial fit ($c_0 + c_1 T + c_2 T^2 + c_4 T^4$). The inset zooms in on the low-temperature regime from $1 - 13$ K, highlighting the positive T^2 contribution.

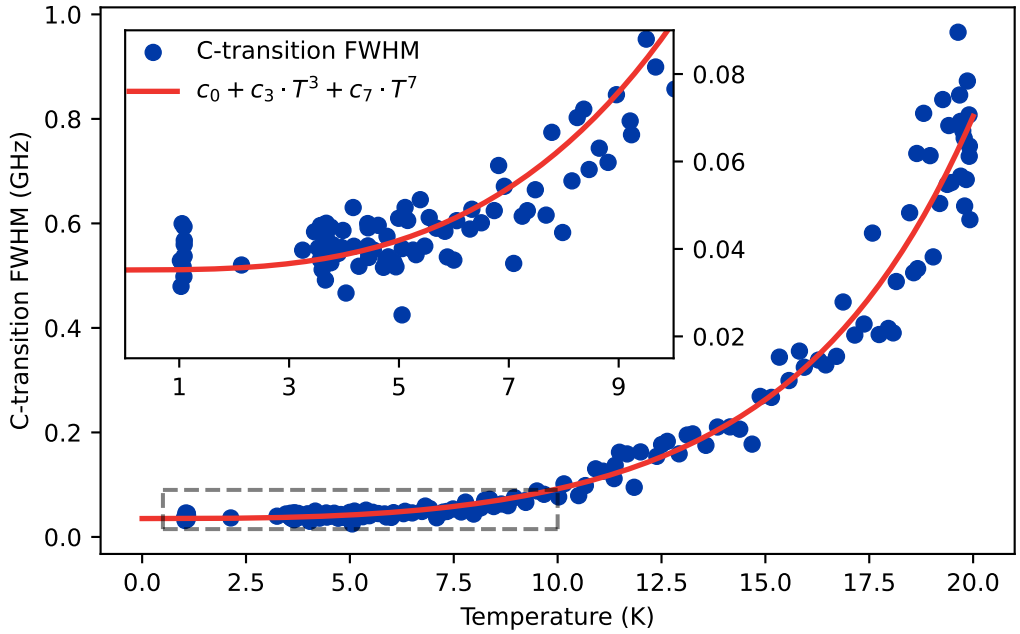

Figure 3.7.: Temperature dependence of the C-transition linewidth. The blue dots show the extracted linewidth from PLE measurements over 20 K to 1 K. The main figure reveals a pronounced broadening above 5 K. The solid red line shows the fit using a polynomial model $c_0 + c_3 T^3 + c_7 T^7$. The inset zooms in on the low-temperature region from $1 - 10$ K, highlighting the low temperature precision of the polynomial fits.

Table 3.2.: Fit parameters for the C-transition lineshift and linewidth functions of SnV-F. The uncertainties are given as standard errors.

Parameter	Value
Lineshift: $c_0 + c_1 T + c_2 T^2 + c_4 T^4$	
c	10.2(50) MHz
c_1	$-9.07(170)$ MHz/K^1
c_2	1.34(13) MHz/K^2
c_4	$-4.97(17) \times 10^{-3}$ MHz/K^4
Linewidth: $c_0 + c_3 T^3 + c_7 T^7$	
c	35.2(56) MHz
c_3	$54.1(51) \times 10^{-3}$ MHz/K^3
c_7	$26.3(35) \times 10^{-6}$ MHz/K^7

precise temperature calibration via the ZPL position in the regime below 12 K due to the observed insensitivity of the lineshift below this temperature.

The extracted linewidth from the same PLE measurements is examined in Figure 3.7. Here, the data is well described by a polynomial of the form $c_0 + c_3 T^3 + c_7 T^7$ with both the T^3 and T^7 terms contributing positively. This results in a monotonic increase in linewidth with temperature. The inset, which zooms in on the low-temperature range below 9 K, shows that the linewidth begins to broaden above 5 K. The steady and predictable broadening makes the linewidth a more reliable metric for temperature estimation in the lower temperature regime. The fit values of the ZPL position and linewidth are summarized in Table 3.2.

By combining these measurements with the temperature-dependent spin–lattice relaxation analysis discussed in Section 2.5.2 and depicted in Figure 2.22 for SnV-F, we can extend the range in which the SnV center can be used to measure the local temperature inside the diamond. This allows temperature sensing from the mK regime up to beyond 20 K by optimizing the measurement conditions for this specific defect. In summary, the SnV center enables local temperature sensing across this entire range through the following measurement approaches:

- **Ultra-low temperatures, measure** T_1 ($\sim 50\,\text{mK} - 4\,\text{K}$, blue curve in Figure 2.22)
  - Apply a strong magnetic field with an off-axis component (400 mT, $\theta = 20°$).
- **Low-temperature range, measure** T_1 ($2.5 - 6.5\,\text{K}$, green curve in Figure 2.22)
  - Apply a moderate magnetic field parallel to the SnV axis ($100 - 200$ mT, $\theta = 0°$).
- **Moderate temperatures** ($6 - 20\,\text{K}$, Figure 3.7)
  - Measure the linewidth of the SnV center.
- **High temperatures** (12 K to > 20 K, Figure 3.6.)
  - Measure the line position of the SnV center.

3.3. Microwave-Induced Heating in Normal and Superconducting Waveguides

Microwave-induced heating from the microwave line is a critical factor influencing the performance and stability of the SnV center in diamond, particularly in high-power applications. In this section, we demonstrate that "heating-related effects could be mitigated by using superconducting microwave waveguides" [129], highlighting the advantages of superconducting systems in reducing thermal dissipation.

By leveraging the SnV center's temperature-dependent properties like the spin–lattice relaxation times, linewidth variations, and zero-phonon line shifts under optimized measurement conditions, we utilize the SnV center in diamond as a highly sensitive local temperature sensor. The broad range from the mK regime up to beyond 20 K is covered to thermally map the waveguides under microwave excitation. We are particularly interested in understanding superconducting systems, especially when operated under strong magnetic fields. In the course of this thesis, we will demonstrate the suitability of on-chip superconducting waveguides for direct high-power microwave manipulation of spin qubits in diamond, as outlined in our published study (see [1]). To the best of our knowledge, no comparable demonstrations have been reported to date. However, their thermal response under these conditions has not been thoroughly investigated so far, making precise temperature sensing critical to assess their stability and efficiency. In the following, an approach is demonstrated that allows for real-time detection of localized heating effects, allowing the distinction between normal and superconducting states with high temporal resolution.

We first discuss the losses associated with normal-conducting coplanar waveguides, as they offer a more intuitive understanding. We aim to estimate the temperature of the diamond, if we assume that all dissipated microwave losses are entirely converted into heat. Under the additional assumption that the diamond is initially in thermal equilibrium, i.e. its temperature is equal to the base temperature of the cryostat, we perform a simplified calculation to determine the temperature after depositing an energy Q within a relatively short time of a few ms. We first consider the diamond to be thermally isolated from its surroundings, effectively modeling it as a lumped thermal capacitance.

Given the small dimensions of the diamond 24 µm × 1 mm × 1 mm and its high thermal conductivity at low temperature [130], that is in par with that of thin-film gold [131], and significantly greater than that of the polymer adhesive [132], the temperature is expected to be nearly uniform throughout the diamond. This assumption is further justified by the fact that the waveguide covers a major fraction of $\sim$ 30 % of the surface, resulting in distributed Ohmic losses over the entire sample. Additionally, the exceptionally high thermal diffusivity of diamond at temperatures below 20 K, owing to its extremely low heat capacity, reinforces the assumption of uniform temperature distribution. By contrast, heat diffusion into the surrounding adhesive and through the bonding wires connecting the diamond waveguide to the flexible coplanar waveguide transmission line can be considered orders of magnitude slower than the internal heat propagation within the diamond itself.

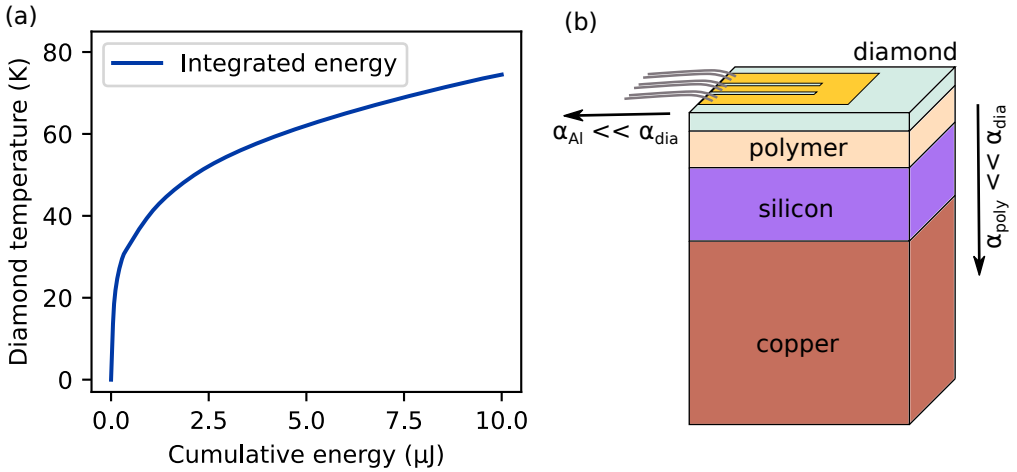

Figure 3.8.: In (a) the temperature variation of the diamond as a function of deposited energy is illustrated. In (b) the schematic representation of the sample structure is provided. The thermal diffusivity α of diamond is several orders of magnitude higher compared to the surrounding materials, leading to a thermal equilibrium within the diamond.

While this model does not account for the high thermal conductivity of the metallic layer, which could transport heat away from the sample, we momentarily disregard this effect, as our primary objective is to determine the collective temperature of the normal-conducting CPW gold layer and the diamond for a given deposited energy.

The specific heat c_p of a material is defined as

$$c_p = \frac{\Delta Q}{\rho V \Delta T} \quad (\mathrm{J\,kg^{-1}\,K^{-1}}), \tag{3.7}$$

where $\Delta Q = P_{\mathrm{MW}} \Delta t$ represents the energy deposited into the diamond for a continuous microwave signal dissipating a power P_{MW} over the pulse duration Δt. The density of diamond is denoted by ρ, and its volume V is determined by its geometric dimensions. The resulting temperature change is given by ΔT.

Since c_p is strongly temperature dependent, especially at low temperatures, we adapt the equation by considering the total energy required to heat the sample from absolute zero to a final temperature T. This leads to the integral form:

$$Q = \rho V \int_0^T c_p(T')\, dT'. \tag{3.8}$$

To solve for T, we use tabulated values of the heat capacity of diamond from [133, 134], interpolate the data points, and numerically integrate in small increments until the final temperature satisfies Equation 3.8.

Figure 3.8 (a) illustrates the thermal response of the diamond as a function of deposited energy from microwave-induced heating. The extremely low heat capacity of diamond below 10 K leads to a sharp temperature rise, even for minimal deposited energy. Above

20 K, the temperature deviates from the initial linear behavior due to the temperature dependence of the heat capacity, which increases significantly with temperature.

In (b), a schematic representation of the sample structure is provided. The diamond is in contact with materials of considerably lower thermal diffusivity α, including the photopolymer adhesive beneath it and the bonding wires connecting it to the transmission line. Given that the thermal diffusivity of diamond is several orders of magnitude higher than that of the surrounding materials, heat rapidly distributes within the diamond, justifying the assumption of a nearly uniform temperature distribution before significant dissipation occurs into the surroundings.

The sharp temperature spikes for even minimal energy dissipation, negatively impact the coherence properties of the spin qubit, at least until the sample rethermalizes. To gain an intuitive understanding of the temporal evolution of these temperature fluctuations, we extend the simplified lumped thermal capacitance model by simulating the heat equation in one dimension. This allows us to account for the previously ignored effect of thermal diffusivity, and estimate the temperature gradient over time.

In our simulation of the 1D heat equation, we define the diamond as the origin of the coordinate system, where the initial heat pulse is modeled as a source term $f(x,t)$ that remains nonzero for the duration of the microwave pulse. To describe the time dependence of this heat source, we assume that heating occurs directly within the diamond. Therefore, we express the source term as $f(x,t) = \delta(x)h(t)$, [11] where the heat is applied from $t = 0$ to $t = t_{\text{source}}$. Here, $\delta(x)$ denotes the Dirac delta function.

Again, we justify this description with the assumption of poor thermal diffusivity into the surrounding materials. Given the rapid absorption of Ohmic losses, the diamond is effectively heated homogeneously (within the time frame in which the heat source is on) and is assumed to have the same temperature as the gold layer as long as the heat source remains active, i.e., while the microwave signal is on. It is important to emphasize that, in contrast to studies such as [69, 129], we focus on the heat dissipation of long microwave pulses on the millisecond timescale. In the referenced works, the simulations primarily consider ultrashort pulses on the order of tens of nanoseconds, where the spatial separation between the heat source and the SnV center must be explicitly accounted for. In such cases, the pulse duration can be significantly shorter than the time required for the heat-pulse to propagate to the SnV center, yielding an inhomogeneous heat distribution. For many such short microwave pulses with small temporal separation a temperature equilibrium is reached, e.g. during dynamical decoupling sequences. Therefore, a measurement with quasi continuous-wave (CW) microwaves represents the upper limit of the sample temperature.

In our case, even though the applied pulse duration is only a few milliseconds, this timescale is orders of magnitude longer than the characteristic thermal diffusion time required for heat to reach the SnV center. This justifies the assumption of treating the diamond as

[11] Ideally we want this function to result in a temperature evolution that is described by a combination of the lumped thermal capacitance model and a diffusion term.

the origin of the 1D coordinate system and using the one-dimensional heat equation to simulate the thermalization process of the entire sample.

The one-dimensional heat equation with a source term is given by [135]

$$u_t(x,t) = \alpha u_{xx}(x,t) + f(x,t), \tag{3.9}$$

where, $u_t(x,t)$ denotes the partial derivative of temperature u with respect to time t and $u_{xx}(x,t)$ is the second partial derivative with respect to the position x and α is the thermal diffusivity. The heat source function $h(t)$ is defined as

$$h(t) = \begin{cases} 1, & \text{if } 0 \leq t \leq t_{\text{source}}, \\ 0, & \text{if } t > t_{\text{source}}. \end{cases} \tag{3.10}$$

The fundamental solution of the homogeneous heat equation is given by

$$\Phi(x,t) = \frac{1}{\sqrt{4\pi\alpha t}} \exp\left(-\frac{x^2}{4\alpha t}\right). \tag{3.11}$$

If the system is described as semi-infinite, meaning that heat dissipates only in one direction, this solution must be multiplied by a factor of two [136]. However, in this simplified model, we assume a single effective thermal diffusivity α and include additional heat dissipation pathways, such as thermal transport through the bonding wire connections back to the microwave line in this effective term.

To find the inhomogeneous solution we make use of Duhamel's principle. The principle interprets the inhomogeneous problem as a continuous resetting of homogeneous problems while the heat source remains active, with the total solution obtained by integrating over the specified duration [135]. Then, the temperature at a point x and time t is given by

$$u(x,t) = \begin{cases} \int_0^t \Phi(x,\tau)\, d\tau, & \text{if } 0 < t \leq t_{\text{source}}, \\ \int_{t-t_{\text{source}}}^t \Phi(x,\tau)\, d\tau, & \text{if } t > t_{\text{source}}. \end{cases} \tag{3.12}$$

The motivation for simulating the one-dimensional heat equation is to understand how the spin-state selective count rate evolves under continuous microwave driving. In the following experiment, we continuously initialize an SnV center (SnV-A) into the dark spin state by exciting the A1 transition at a base temperature of $T = 50\,\text{mK}$. We use a magnetic field of $\sim 200\,\text{mT}$ with an angle of $\theta = 60°$ to split the optically allowed transitions as well as the qubit transitions. We then apply an off-resonant continuous-wave microwave pulse at 3 GHz of 10 ms duration followed by a 190 ms break. If the sample heats up due to microwave induced heating, the increased temperature should lead to a higher count rate. This effect arises from the temperature dependence of the spin relaxation time T_1, which decreases significantly with increasing temperature. By comparing the simulated temperature profile with the observed count rate, we can infer the local heating dynamics and validate the thermal model.

First, we use the result of the one-dimensional heat equation to examine the temperature evolution of the system. Although no physical parameters, such as the real dissipated power, have been explicitly integrated into the equation, we illustrate its implications by considering an example where the microwave pulse heats the sample to a peak temperature of 20 K. Since the given form of the equation makes the time evolution independent of power, this example is simply to provide insight into the thermal response of the system.

Figure 3.9 (a) presents the simulated temperature profile obtained by solving the one-dimensional heat equation, where the diamond is set as the origin and reaches a peak temperature of 20 K.

In the next step, shown in (b), we simulate the PLE spectrum as a function of the temperature variation obtained from the heat equation, starting from $T = 0$ K. For this, we use the fit parameters for the ZPL position and linewidth of SnV-F, as determined in Section 3.2 and listed in Table 3.2.

The simulation clearly illustrates the pronounced shift and broadening of the spectral line with increasing temperature during the duration of the microwave pulse. The intensity of the Lorentzian lineshape is normalized to reflect the physical intensity under resonant excitation at constant excitation power. Additionally, since the experiment is conducted under an applied magnetic field, we include the effect of the spin relaxation time T_1 by superimposing the intensity with an exponential decay, where the weight of the exponent gradually increases below approximately 7 K, effectively reducing the spin-selective count rate for decreasing temperature.[12] We refrain from simulating the T_1 curve over the previously determined spin relaxation rates, as this would overcomplicate the procedure.

In the experiment the laser frequency is fixed, therefore, we extract the count rate at the central frequency of the PLE spectrum and plot its evolution over time in (c). The measured count rates for various microwave power levels are shown in (d).

Examining the count rate evolution, we observe two different regimes. For power levels $\leq$ 10 dBm, the spin-selective count rate increases during the first 10 ms in which the microwave is turned on. In this regime, the local temperature rises from the cryostat's base temperature of $T = 50$ mK to several Kelvin. This temperature increase activates T_1 relaxation processes that restore the selected spin state, enabling continuous optical pumping and gradually raising the count rate throughout the duration of the microwave pulse. For power levels exceeding 10 dBm the temperature surpasses the T_1 threshold faster than we can probe and a pronounced drop in the count rate is observed within the first 10 ms of microwave application. This is contrary to what we would intuitively expect. However, the effect can be attributed to the strong spectral shift induced by heating, which shifts the optical transition so significantly that the excitation laser becomes off-resonant with the "hot" ZPL position.

[12] The used weight function $w = 0.5\left(1 + \tanh\frac{T-T_0}{\Delta}\right)$ smoothly shifts from 0 (for $T \ll T_0$) to 1 (for $T \gg T_0$), where $\Delta = 1.5$ K defines the temperature range over which the scaling shifts, and T_0 the transition temperature. The scale factor is defined as $s = w + (1 - w)e^{T-T_0}$ and boosts the Lorentzian at low T to model T_1 effects. The final profile is $I = s \times$ Lorentzian.

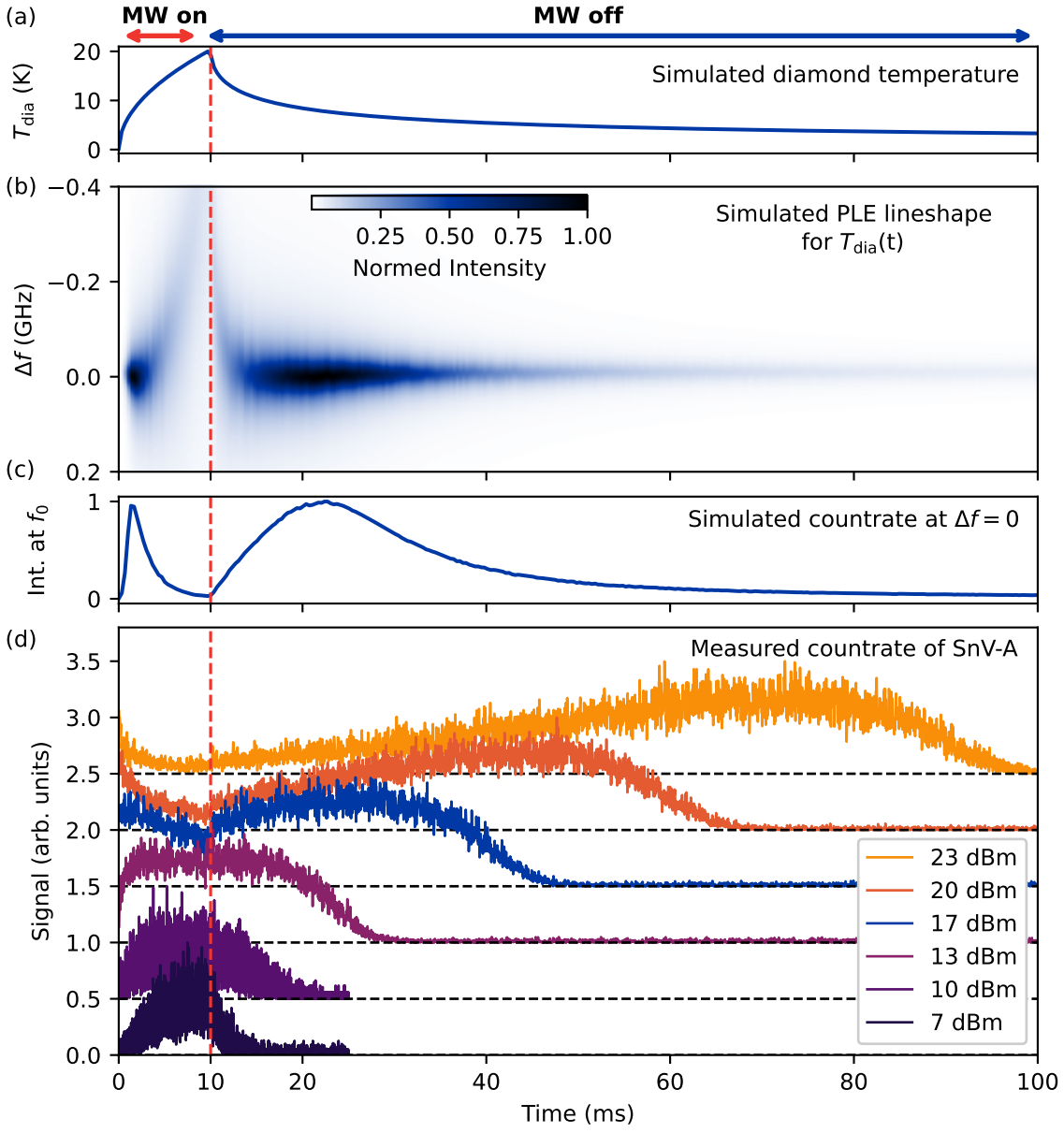

Figure 3.9.: Heating effects of the NC-CPW due to microwave-induced Ohmic losses. (a) Simulated temperature profile obtained from the one-dimensional heat equation, with the diamond set as the origin and a peak temperature of 20 K. (b) Simulated PLE spectrum as a function of temperature variation in the diamond, determined from the 1D heat equation in (a). (c) Count rate intensity at the central frequency of the PLE spectrum in (b). A significant drop in count rate is observed within the first 10 ms of microwave application due to strong line shift and broadening. The count rate recovers immediately after the microwave is turned off and subsequently decays as the sample thermalizes below $\approx$ 7 K where the spin relaxation time T_1 increases. (d) Measured count rate at a base temperature of T = 50 mK for various microwave powers. The data for P = 17 dBm (blue curve) shows good agreement with the simulation.

In our publication [1], we state: "Interestingly, for high microwave powers above 10 dBm, the count rate rises continuously even after the microwave is switched off." With the insights gained from the thermal model, we can now qualitatively explain this behavior of the fluorescence signal: As soon as the microwave is turned off, the count rate immediately recovers as the spectral line shift resets. Within the first milliseconds, the temperature decreases quickly to around $\approx 10\,\mathrm{K}$, according to the heat equation. However, the thermalization process slows down significantly and the temperature remains above a critical threshold where the low spin relaxation time T_1 maintains a high count rate. Only as the sample gradually cools below approximately 7 K does T_1 become long enough to suppress the count rate.

Finally, the data for P = 17 dBm (blue curve) shows excellent agreement with the simulated results, validating the thermal model. These findings emphasize the strong impact of microwave-induced heating on spin readout fidelity and highlight the importance of mitigating Ohmic losses in transmission line configurations.

Next, we want to discuss another statement: "We attempt the same measurement for the high-strain SnV-B with the SC-CPW; however, no increase in count rate could be observed, even for microwave powers that break the superconductivity. We attribute this result to the noticeably higher spin lifetime of SnV-B due to the larger ground-state splitting." With the insights gained from our measurements, we can now clarify that the absence of a count rate increase is not primarily due to the longer spin lifetime but rather the thermal properties of the system. Specifically, as we will show in the following measurements on SC-CPWs, below the critical power threshold where superconductivity breaks down, the dissipated heat is negligible, and the sample remains close to the base temperature. At microwave frequencies ($> 1\,\mathrm{GHz}$), we observe a gradual degradation of superconductivity close to the critical current density. In the previously performed measurements on SC-CPWs this effect was insufficient to cause a significant increase in count rate. On the other hand, upon breakdown of superconductivity, the temperature instantly increases to the point where the excitation laser becomes off-resonant with the shifted ZPL position. We will show with the following measurements that, superconductivity breaks rather abruptly within a band of $1 - 2\,\mathrm{dB}$, providing further insight into the thermal behavior of superconducting waveguides.

For the following measurements, we use a newly fabricated SC-CPW (on the diamond sample SnV-2-B2) with a constriction to narrow the conductor widths and gaps. The utilized sample, hosting the relevant SnV-F, is depicted in the two upper right images of Figure B.1. The fabricated waveguide on this sample has a conductor width of $g = s = 30\,\mu\mathrm{m}$ at the shorted end and a gap width of $w = 5\,\mu\mathrm{m}$. The measured input return loss (RL) for the specific device is shown in Figure 3.12 (a) with an inset for the relevant frequency regime in (b).

Before presenting the measurements performed to benchmark the SC-CPW, we first provide a schematic illustration of the measurement configuration in Figure 3.10. This visualization clarifies the relative orientation of the SnV center (SnV-F) within the superconducting coplanar waveguide structure and the applied magnetic field directions, serving as a reference for interpreting the subsequent experimental results. For simplicity,

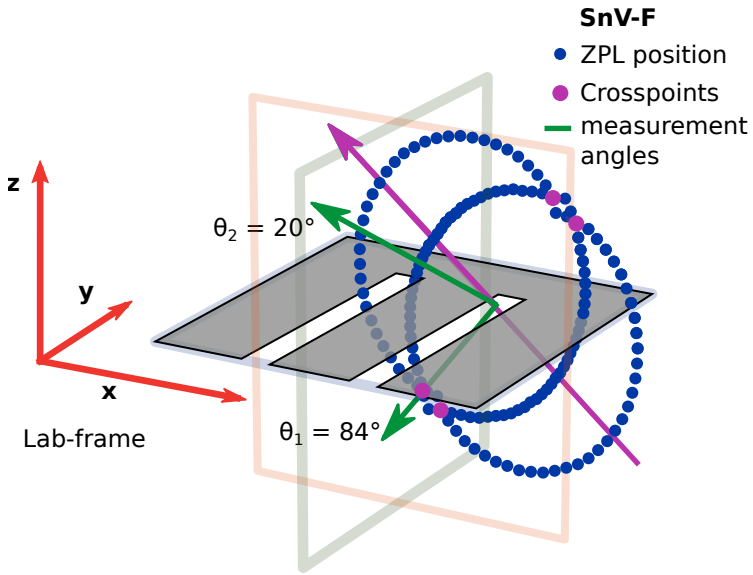

Figure 3.10.: Schematic illustration of the allowed transition of SnV-F extracted from angular sweeps, as explained in Figure 2.10 (blue data points), and the relative orientation of the transitions with respect to the SC-CPW structure (grey CPW) on the diamond. The SnV axis is indicated by the purple arrow, while the green arrows denote the external magnetic field orientations applied in subsequent measurements. For $\theta_2 = 84°$, the allowed transitions intersect (purple points), ensuring their visibility in PLE measurements even at temperatures below 4 K, where the spin relaxation time is high. The lab frame is represented by the red coordinate system. The actual sample, hosting the relevant SnV-F, is depicted in the two upper right images of Figure B.1.

the waveguide has not been drawn with a consticton. The figure shows the allowed optical transitions of SnV-F (blue data points), extracted from angular PLE sweeps, equivalent to the description in Figure 2.10. These transitions are depicted in a three-dimensional representation, including the superconducting coplanar waveguide structure on the diamond to visualize the absolute orientation of the SnV center within the experimental setup. The SnV axis is indicated by the purple arrow. The two external magnetic field orientations that are applied in the subsequent measurements are shown as green arrows. For a field orientation of $\theta_2 = 84°$, the allowed transitions intersect (purple points), ensuring their visibility in PLE measurements even at temperatures below 4 K, where the spin relaxation time is long. The lab frame coordinate system is represented in red.

The idea of the following measurements is to determine the local temperature and observe the breakdown of superconductivity in the SC-CPW by observing the shift of the A1-transition in PLE measurements. We apply microwave pulses of varying power and short duration at three different frequencies: 20 MHz, 1 GHz, and 2 GHz. The pulses have a duty cycle of 20 % (pulse duration: 10 µs, off-time: 40 µs), ensuring periodic heating while allowing for partial thermal relaxation between pulses. We track the position and linewidth of the C-transition under three distinct configurations:

1. No magnetic field: The transition remains visible at all times.
2. $B = 400$ mT, $\theta_1 = 84°$: Allowed transitions cross, ensuring continuous visibility.

3. $B = 400\,\mathrm{mT}$, $\theta_2 = 20°$: The transition remains dark when pumping A1 due to spin initialization effects.

As soon as the current density, which scales with power as $P \propto j^2$, becomes high enough to disrupt superconductivity, we expect the ZPL to shift and broaden. Under the third configuration, the transition should also regain visibility as the spin initialization condition is altered. T_1 is massively reduced by the elevated temperature, once superconductivity breaks down.

The measurements are presented in Figure 3.11 and are performed at a base temperature of $T \approx 1.1\,\mathrm{K}$.[13] The data are arranged in a three-row grid, with each row corresponding to a distinct measurement set. In each row, the primary panels display the 2D PLE plots of normalized intensity as a function of frequency (x-axis) and microwave power (y-axis). The Custom colormaps are applied to distinguish the three aforementioned frequency regimes: red for 20 MHz, blue for 1 GHz, and green for 2 GHz. The rightmost panel in each row overlays the extracted center frequency and full-width at half-maximum trends, which are depicted with circle and cross markers, respectively, in matching colors. For both, the values have been offset to zero, therefore the x-axis corresponds to the absolute frequency shift Δf. Note that the center frequency experiences a redshift for increasing temperature ($\Delta f < 0$), while the FWHM shows an increasing trend from the lifetime limit ($\Delta f > 0$). Moreover, a short color-coded line on the right y-axis marks the power, at which the superconductivity breaks. The horizontal brackets above the columns and vertical brackets along the rows indicate panel groupings. Please note, that the depicted power corresponds to the power level at the input of the cryostat and is not corrected for the input return loss. The measured RL for the specific measurement configuration and device can be extracted from Figure 3.12 (b).

In the first measurement configuration without an applied magnetic field, we are not able to observe the breakdown of superconductivity at a frequency of 20 MHz, as the required power exceeds the maximum output of 19 dBm of the utilized microwave source. At higher frequencies of 1 GHz and 2 GHz, superconductivity breaks down at 18 dBm and 17.2 dBm, respectively. The observed difference of 0.8 dB between these two frequencies is significant, as it hints to additional loss mechanisms that have not been discussed so far. When correcting for the frequency-dependent RL extracted from Figure 3.12 (b), the difference is rather $0.8\,\mathrm{dB} + \frac{2.76-1.94}{2}\,\mathrm{dB} \approx 1.2\,\mathrm{dB}$. This is a large discrepancy compared to the predicted total losses of $\alpha^{\mathrm{s}}_{\mathrm{tot}} \approx 0.003\,\mathrm{dB\,cm^{-1}}$ at 3 GHz which are derived from the two-fluid model alone. Before discussing potential origins of these losses, we first examine the measurement performed under strong magnetic fields.

In the second and third configurations, with $B = 400\,\mathrm{mT}$, superconductivity is suppressed at much lower powers across all frequencies. For a field orientation of $\theta_1 = 84°$ the breakdown occurs upwards 8 dBm, while for $\theta_2 = 20°$ it begins at 10 dBm. This shows that the direction of the magnetic field plays an additional role in the loss mechanisms.

[13] This is to take advantage of the higher cooling power provided by the Joule–Thomson-Effect. At the cryostat's base temperature of about 50 mK, the heat load would exceed the available cooling power and disrupt the dilution mixture.

Without diving into extensive detail, which lies beyond the scope of this work and the capabilities of single SnV center measurements, we discuss the most probable origin of the observed losses. Niobium is an elemental type-II superconductor and allows magnetic flux to penetrate above a critical magnetic field threshold B_{c1}, over which ideal diamagnetism ends [137]. Between this lower critical field and the upper critical field B_{c2},[14] the material enters the so-called mixed or vortex state [138]. In this regime, magnetic flux penetrates the superconductor in the form of quantized vortices [139], forming small cylindrical regions that are locally normal-conducting [140].

These vortices can move under the influence of Lorentz forces [141], and this motion leads to ohmic losses due to the driven normal-conducting electrons. However, defects in the material can pin the vortices, preventing their motion [142]. In this pinned state, only the superconducting electrons contribute to current flow, and no energy dissipation occurs under DC conditions.

In contrast, under alternating fields or currents, such as in our microwave measurements, the changing magnetic environments induce electromotive forces, leading to energy dissipation [143]. Vortex motion thus limits the critical current density for AC currents, potentially reducing it by orders of magnitude [144]. This effect is particularly pronounced when the magnetic field is oriented perpendicular to the film [144]. This is exactly the case for the measurements under $\theta_1 = 84^\circ$, which explains the earlier breakdown of superconductivity compared to $\theta_2 = 20^\circ$, where the field is predominantly in-plane. This behavior explains the rapid breakdown of superconductivity under applied magnetic fields. The formation and motion of vortices introduce additional dissipation channels that are absent in the zero-field case.

However, even with an applied field, the measurements confirm that superconductivity breaks rather abruptly. Therefore, we are particularly interested in understanding the system's behavior for power levels close to the critical threshold. To investigate this, we measure the spin relaxation time T_1 for the three microwave frequencies under the third configuration ($B = 400\,\mathrm{mT}$, $\theta_2 = 20^\circ$) at a temperature of $T = 1.8\,\mathrm{K}$.[15] This configuration allows us to directly relate the extracted T_1 values to the previously determined temperature dependence, as discussed in Section 2.5.2

The results are presented in Figure 3.13. The main panels display the normalized decay dynamics. The data points represent the recovery of the count rate as determined by a readout pulse after an initialization pulse and are plotted as a function of the time interval between the pulses. The corresponding curve fits are overlaid to extract the characteristic relaxation times. The data is color-coded to match the previous PLE measurements for the respective frequencies. For better clarity, some of the data are grayed out to visualize the trend of the saturation curves with increasing microwave power without overloading the plot. The insets provide a dual-axis view showing how the measured T_1

[14] In Appendix D.3 we briefly discuss critical field measurements of B_{c2} by investigating the input return loss.

[15] At this temperature and magnetic field configuration, the spin relaxation time T_1 is approximately 40 ms, allowing for reasonable measurement durations.

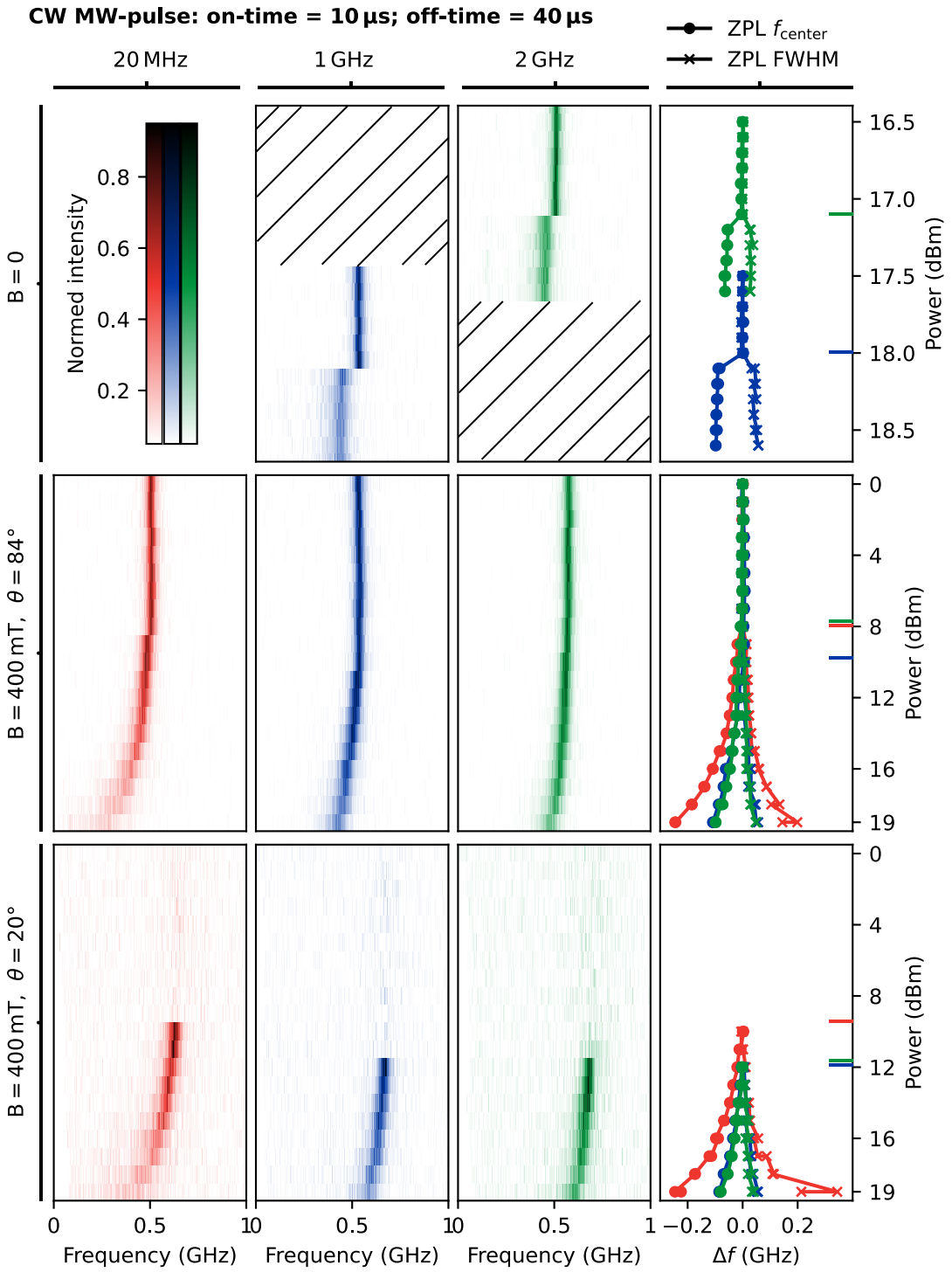

Figure 3.11.: Comparison of PLE measurements across various experimental conditions, highlighting the impact of microwave heating and the consequent breakdown of superconductivity in SC-CPWs. The data are arranged in a grid of three rows, with each row corresponding to a distinct measurement set. In each row, the primary panels display 2D PLE plots showing normalized intensity as a function of frequency (x-axis) and MW power (y-axis). Custom colormaps are used to differentiate the frequency regimes: red for 20 MHz, blue for 1 GHz, and green for 2 GHz. The rightmost panel in each row overlays the extracted center frequency and FWHM trends depicted with circle and cross markers, respectively in matching colors. The horizontal brackets on top of the columns and vertical brackets along the rows describe the panel groupings. Note, that measurements were only taken for a limited range within the first row.

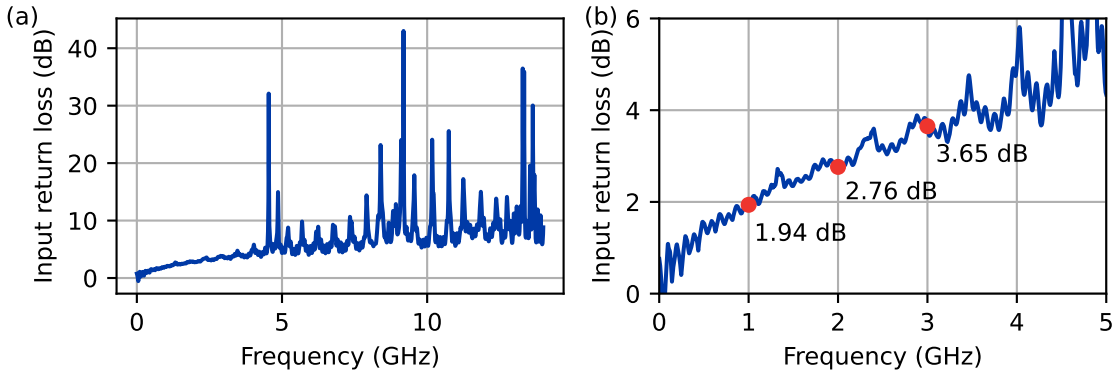

Figure 3.12.: Input return loss of the microwave lines and the sample used to benchmark the SC-CPW (sample SnV-2-B2). The fabricated waveguide on this sample and configuration has a conductor width of $g = s = 30\,\mu m$ at the shorted end and a gap width of $w = 5\,\mu m$.

values (left y-axis) correlate to both applied power (x-axis) and the corresponding sample temperature (right y-axis). We observe, that for 20 MHz, the T_1 time remains stable for increasing microwave power. We are not able to determine a gradual degradation of the superconductor at this frequency for measurements with 0.1 dBm increments. Above 9.4 dBm the superconductivity breaks abruptly and no T_1 can be acquired.

On the other hand, for 1 GHz, we observe a decrease in T_1 above 8 dBm, corresponding to a temperature increase from 1.8 K to 3 K in the range of 8 dBm to 11 dBm. At higher powers, measuring T_1 is no longer possible, as superconductivity fully breaks down. A similar trend is observed for 2 GHz. However, the degradation occurs more gradually, beginning at approximately 7 dBm.

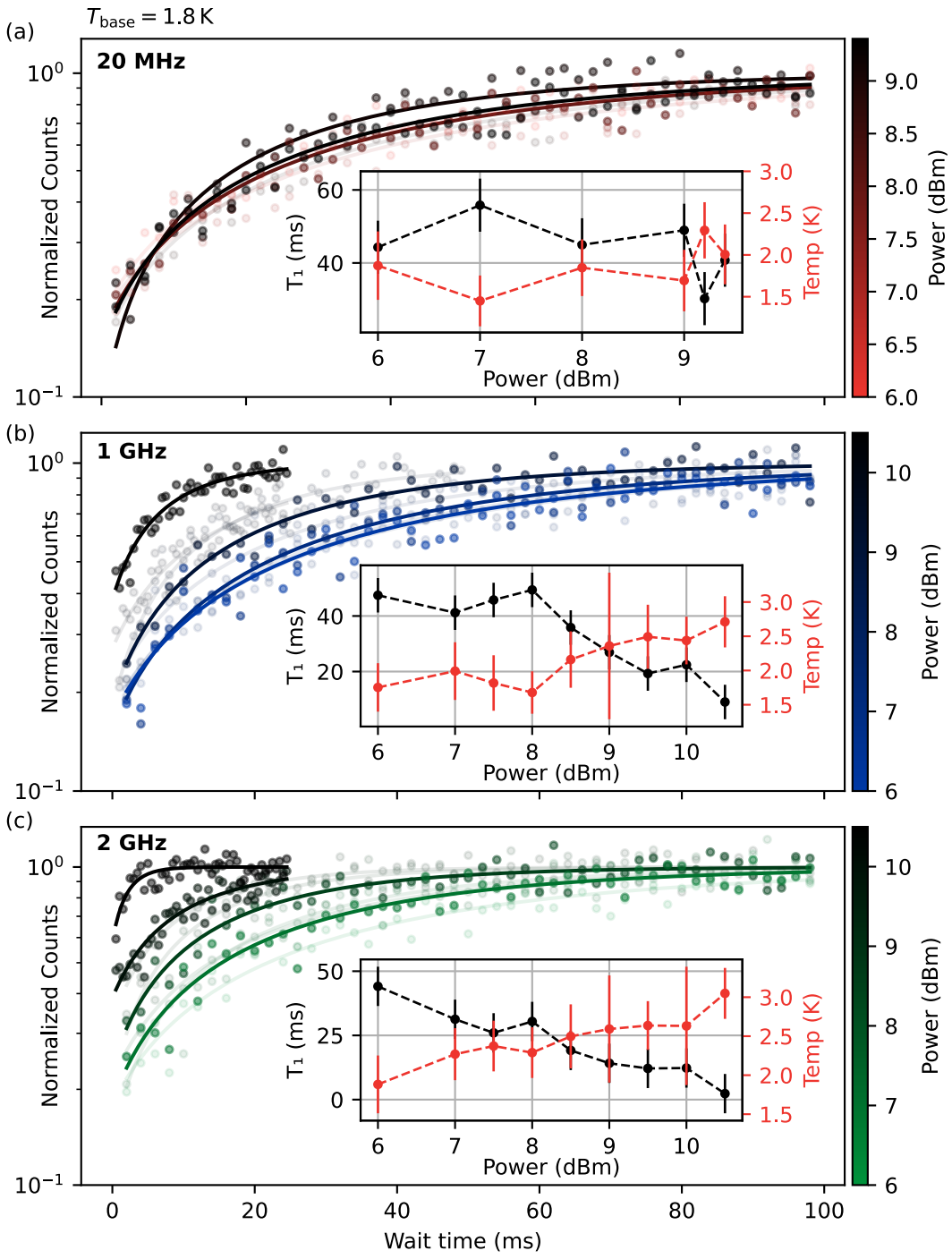

Figure 3.13.: Overview of the T_1 relaxation behavior in SC-CPWs specifically addressing the intermediate regime of superconductivity breakdown across different frequency ranges. The data are color-coded in line with previous measurements shown in Figure 3.11 (red: 20 MHz, blue: 1 GHz, green: 2 GHz). The main panels display the normalized decay dynamics with corresponding curve fits. For better clarity, some of the data are grayed out to visualize the trend of the saturation curves with increasing microwave power without overloading the plot. The insets provide a dual-axis view showing how the measured T_1 values correlate to both applied power and the corresponding sample temperature. The insets contain the grayed out data of the main panels.

3.4. Summary

In this chapter, we examined the heating effects of NC-CPWs and the superconducting stability of SC-CPWs under microwave excitation, with the main focus on their suitability for spin qubit control. Our measurements show that superconductivity in SC-CPWs breaks abruptly at a critical power threshold, and the presence of strong magnetic fields further limits the maximum applicable microwave power. Despite this, we demonstrated that SC-CPWs exhibit significantly reduced Ohmic losses below this threshold compared to their normal-conducting pendants. With carefully optimized measurement conditions, their advantages can be fully leveraged.

In the previous Chapter 2 we identified the most favorable configuration for preserving the spin properties of the SnV center: aligning the magnetic field parallel to its quantization axis. In this configuration, fields of approximately 100 mT are sufficient to spectrally separate the optical and microwave transitions, four times lower than the fields applied during our rigorous measurement conditions. For the SnV center, this corresponds to qubit frequencies around 3 GHz to 3.5 GHz. Within this regime and for the waveguide geometries used, up to 14 dBm to 17 dBm of microwave power can be transmitted without compromising superconductivity.

We are convinced, that these findings are particularly promising for nuclear spin control. As shown, RF driving at frequencies up to several tens of MHz causes no measurable heating as long as the critical power is not exceeded, an ideal foundation for the long pulses required for coherent nuclear spin manipulation. This could assist in removing a major bottleneck in scaling hybrid quantum systems that rely on both photonic interfaces and nuclear spin coherence as spin memories.

In the following chapter, we extend these results to electron spin control, showing how superconducting waveguides can enable fast qubit operations while maintaining thermal stability. This is also assisted by to the short microwave pulse durations and long initialization times of the electron spin, allowing any minor AC losses to dissipate before the next pulse arrives.

4. Tin-Vacancy Center: Coherent Microwave Control

In the preceding chapters, we have examined the spin properties of the SnV center and identified the key components required to harness its full potential as a spin qubit for quantum information applications. However, we have yet to define what a qubit actually is, how to intuitively represent it and how to manipulate it.

Fundamentally, a qubit is a quantum mechanical two-level system that can be realized using various physical properties, such as spin, charge, or flux, provided there is a mechanism to induce transitions between the two levels. The ability to control the state is essential for its function in quantum operations.

For the SnV center, we define the qubit using the two lower spin-orbit eigenstates defined in Equation 2.7: [1]

$$|1\rangle = |- \downarrow\rangle \quad \text{and} \quad |2\rangle = |+ \uparrow\rangle .$$

A pure ideal qubit state can be described as a complex superposition of the two states:

$$|\psi\rangle = \alpha\,|1\rangle + \beta\,|2\rangle \quad \text{with} \quad |\alpha|^2 + |\beta|^2 = 1 \tag{4.1}$$

and can be represented on the surface of the Bloch sphere via:

$$|\psi\rangle = \cos\frac{\theta}{2}\,|1\rangle + e^{i\phi}\sin\frac{\theta}{2}\,|2\rangle . \tag{4.2}$$

Here, θ and ϕ are the polar and azimuthal angles, respectively. The state is mapped onto a point on the surface of the Bloch sphere with $|1\rangle$ indicating the north pole with $\theta = 0$ and $|2\rangle$ the south pole with $\theta = \pi$.

To describe a real qubit, it is important to take into account destructive processes that lead to the loss of coherence, such as spin-relaxation and dephasing. These phenomena, which arise from the qubit's coupling to its environment, were discussed in Section 2.5.2. As a result, qubits are typically represented using the density matrix formalism, where the Bloch vector $\vec{r}$ satisfies $\vec{r} \leq 1$. If $|\vec{r}| = 1$, the qubit is in a pure state, located on the surface of the Bloch sphere. If $|\vec{r}| < 1$, the qubit is in a mixed state, within the interior of the Bloch sphere, representing a loss of coherence.

[1] Please note that we deviate from the standard description of the qubit in the computational basis with $|0\rangle = (1, 0)^T$ and $|1\rangle = (0, 1)^T$, to match the description in Figures 2.3 and 2.18.

4.1. Microwave Spin Control

Now that we have established a description of the qubit, we can examine how it behaves under the influence of a resonant driving field. A two-level quantum system subject to such a field undergoes a coherent, cyclic evolution known as Rabi oscillations. The drive frequency Ω of a Rabi oscillation for the SnV center is expected to scale proportional to the expectation value $\langle 1| H_{\mathrm{MW}} |2\rangle$ [145]. According to the selection rules for magnetic dipole transitions, microwave excitation preserves the orbital angular momentum of the state. We have seen, that the lower ground-state qubit has different orbital momenta for the spin-orbit eigenstates $|1\rangle = |- \downarrow\rangle$ and $|2\rangle = |+ \uparrow\rangle$, thereby preventing first-order microwave control.

In Section 2.5.2, we discussed the spin-orbit eigenstates in a perturbed environment, and specifically show in Eq. 2.64, how the eigenstates under strain transform: $|- \downarrow\rangle' \approx |- \downarrow\rangle + \frac{\alpha}{\lambda_{\mathrm{g}}} |+ \downarrow\rangle$. This indicates that direct microwave driving becomes feasible in the presence of strain. Nevertheless, due to the substantial spin-orbit interaction in SnV centers compared to their lighter counterparts, the SiV and GeV centers, achieving efficient microwave control requires significant strain. For unstrained or weakly strained SnV centers, the required driving power for effective qubit manipulation induces excessive heating, which degrades the spin properties, making the system unusable for quantum operations, when normalconducting transmission lines are used.

Initial demonstrations of microwave control in SnV centers leveraged highly strained defects [69, 70]. More recently, G. Pieplow and M. Belhassen [84] highlighted the critical interplay between strain and the vectorial characteristics of the applied magnetic fields. Specifically, they describe the time evolution of the system by decomposing the static field (dc) used to lift spin degeneracy and the time-dependent field (ac) responsible for microwave driving, resulting into the effective Hamiltonian:

$$H_{\mathrm{eff}} = H_{\mathrm{dc}} + H_{\mathrm{ac}}(t) \tag{4.3}$$

$$= -\frac{\omega_{21}}{2}\sigma_z - \mathbf{S} \cdot \hat{\mu} \cdot \mathbf{B}_{\mathrm{ac}}(t), \tag{4.4}$$

where ω_{21} is the Larmor frequency of the qubit (with $\hbar = 1$). We define the analytical solution of the qubit-splitting in equations 2.35 and 2.37 for $B_\perp$ and $B_\parallel$, respectively. For arbitrary fields, we need to solve the Hamiltonian in equation 2.25 with the strain magnitude of the specific defect numerically, to determine the qubit frequency.[2] In the second term, $\boldsymbol{S} = \frac{1}{2}(\hat{\sigma}_x,\ \hat{\sigma}_y,\ \hat{\sigma}_z)^{\mathrm{T}}$ is the Pauli-matrix vector, the magnetic moment $\hat{\mu}$ is a 3×3 matrix that depends on the vectorial dc field components $\mathbf{B}_{\mathrm{dc}}$ and vectorial and time dependent ac field components $\mathbf{B}_{\mathrm{ac}}(t) = \mathbf{B}_{\mathrm{ac}} \cos \omega t$ with $\mathbf{B}_{\mathrm{dc/ac}}$ in spherical coordinates [84].

We can visualize a microwave drive as a rotation of the state vector (Bloch vector) on the Bloch sphere about an axis that is defined by the effective magnetic field in the

[2] G. Pieplow provides a general solution for ω_{21} using an average quenching factor.

rotating frame of the electron spin. The Hamiltonian as described in the rotating wave approximation (RWA) takes the form:

$$H_{\mathrm{RWA}} = \frac{1}{2}\Delta\omega\sigma_z + \frac{1}{2}\Omega_{\mathrm{R}}\sigma_x = \frac{1}{2}\begin{pmatrix}\Delta\omega & \Omega_{\mathrm{R}} \\ \Omega_{\mathrm{R}} & -\Delta\omega\end{pmatrix}, \tag{4.5}$$

where Ω_R is the Rabi frequency and $\Delta\omega = \omega_{21} - \omega$ is the detuning from the qubit's resonance frequency. The term σ_x drives rotations about the x-axis, while a z-component is added by the magnitude of the detuning.

The Rabi frequency is given by:

$$\Omega_{\mathrm{R}} = \gamma_s B_{\mathrm{ac}} \Lambda, \tag{4.6}$$

where $\Lambda = \Lambda(x, \theta_{\mathrm{dc}}, \theta_{\mathrm{ac}}, \phi)$ accounts for the coupling strength, considering the full vectorial attributes of the magnetic fields. In the description of Λ, the variable $x = \arctan(\xi/\lambda)$ accounts for the orbital state overlap where ξ stands for the strength of the strain interaction and λ for the spin-orbit coupling. The angles θ_{dc} and θ_{ac} are defined as the polar angles relative to the SnV center's quantization axis, as detailed in Section 2.4.3. The azimuthal angle difference, $\phi = \phi_{\mathrm{dc}} - \phi_{\mathrm{ac}}$, represents the relative angle between the plane spanned by the quantization axis and the ac field vector to the dc field vector [84].

One can determine the time evolution of the state $|\Psi(t)\rangle$ by applying the unitary transformation:

$$|\Psi(t)\rangle = e^{-iH_{\mathrm{RWA}}t}\,|\Psi(0)\rangle \tag{4.7}$$

which results in the oscillation of the state vector around the field vector $\vec{n}$ (see [84] for a detailed description of the involved vectorial components). The probability of measuring the qubit along the z-axis of the Bloch sphere, if we initially prepare it in $|2\rangle$[3], is given by:

$$P_{|1\rangle}(t) = \frac{\Omega_{\mathrm{R}}^2}{\Omega^2}\sin\left(\frac{\Omega}{2}t\right), \quad \text{with} \quad \Omega = \sqrt{\Omega_{\mathrm{R}}^2 + \Delta\omega^2}. \tag{4.8}$$

The generalized Rabi frequency Ω is derived by finding the eigenvalues of the Hamiltonian for the off-resonantly driven two-level system.

In the experiment, we apply rotations around the x-, y-, and z-axes of the Bloch sphere, allowing full control over the qubit's state. These rotations form the fundamental building blocks of quantum operations. For example, if we want to achieve population inversion[4] of the initial state, we need to rotate around an equatorial axis by a duration t_π such that $\Omega t_\pi \longrightarrow \theta = \pi$. In Equation 4.5, rotations around the x-axis arise from the σ_x term. By introducing a phase offset in the ac field $\cos\omega t \longrightarrow \cos(\omega t + \varphi)$, we can freely choose the rotation axis as $\sigma_x \longrightarrow \sigma_x \cos\varphi + \sigma_y \sin\varphi$.

We now have a full description of how an external driving field influences a qubit's state on the Bloch sphere. The frequency of the field determines the angle of rotation in the xz-plane. The phase decides the angle of rotation in the xy-plane. Finally, the amplitude and duration of the field control how fast and how far the qubit moves along its trajectory.

[3] This initialization corresponds to pumping the A1-transition. See Section 2.5.1 for details.
[4] A full inversion is only possible under resonant drive.

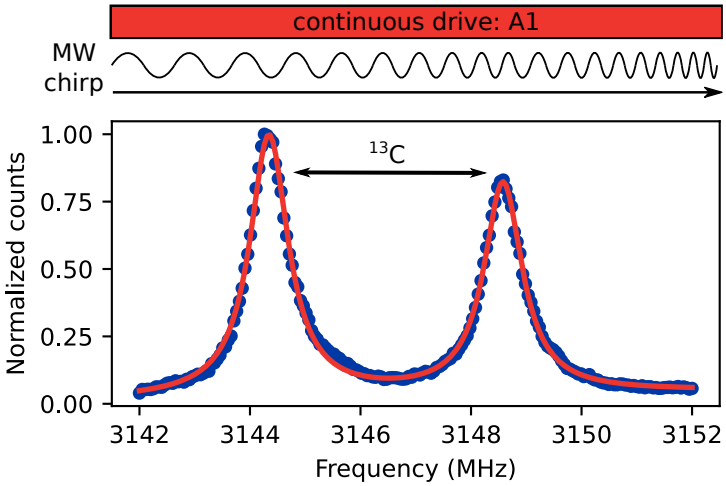

Figure 4.1.: ODMR measurement of SnV-B under continuous optical excitation of A1 and parallel magnetic field orientation of $B = 96\,\mathrm{mT}$ magnitude. A continuous microwave chirp is applied across the target frequency range. The two observed resonances, one at $f_1 = 3144.34(22)\,\mathrm{MHz}$ and another at $f_2 = 3148.58(26)\,\mathrm{MHz}$, indicate strong coupling to a nearby ^{13}C nuclear spin. This figure is adapted from Figure 4 in Reference [1].

Measurement conditions All subsequent measurements are performed on SnV-B (Sample SnV-2-B1, see Figure 3.1 (c)), taking advantage of the SC-CPW for spin control. Unless stated otherwise, the following conditions apply: An external magnetic field $B_{\parallel} = 96\,\mathrm{mT}$ is aligned parallel to the quantization axis at a temperature of 50 mK. The electron spin is initialized by resonantly driving the allowed optical transition A1. Due to the high stability of the charge-state of SnV-B, no off-resonant repump pulse is included in the control sequences. If charge stabilization is required, a 532 nm repump pulse with an excitation power below 100 nW is applied to avoid spectral diffusion caused by charge environment fluctuations.

4.1.1. Optically Detected Magnetic Resonance

The paramagnetic and optically active nature of the SnV center allows us to determine the resonance frequency ω_{21} of the spin qubit via optically detected magnetic resonance (ODMR). As described in Section 2.5.1, the SnV center can be optically initialized by driving one of the two allowed transitions. Exciting transition A1 initializes the system into state $|2\rangle$, turning the SnV center off-resonant to the laser frequency and thus undetectable at low temperatures. By applying a microwave pulse resonant with the qubit transition, the state $|1\rangle$ can be (partially) recovered. This permits continuous photon detection through repeated cycling.

Different implementations of this scheme are possible: In a pulsed-ODMR scheme, a microwave pulse of duration t_π is applied. The pulse is temporally separated from the

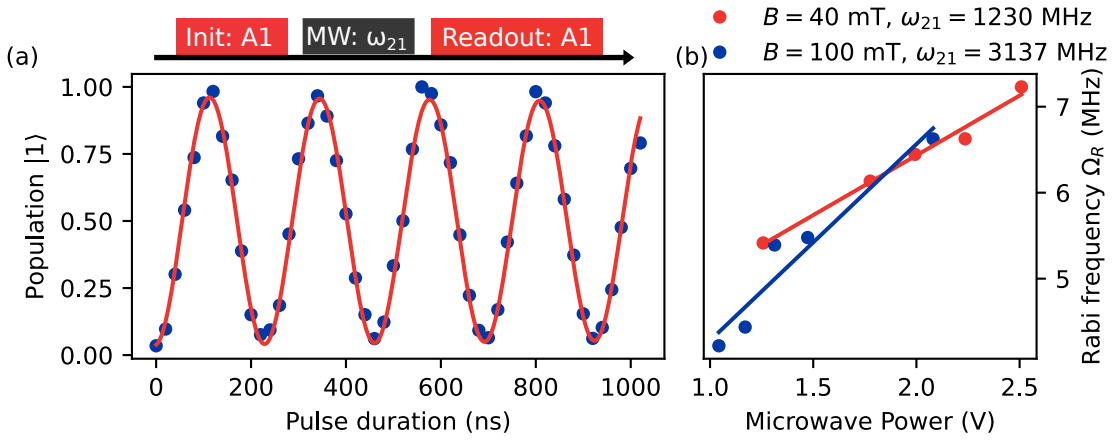

Figure 4.2.: Rabi oscillations and power dependence. The Rabi oscillations shown in (a) are measured at the midpoint of the two hyperfine transitions. The measurement scheme consists of alternating laser and microwave pulses. In principle, the readout pulse also serves as the initialization. (b) depicts the detuning-corrected Rabi frequency on the ac field amplitude. (a) is adapted from Figure 4 in Reference [1].

initialization pulse of the laser and fully recovers state $|1\rangle$. This maximizes the count rate per cycle while minimizing power broadening.

To implement this scheme, it is necessary to accurately identify the spin transition, which can be challenging for the SnV center. The strong dependence of the qubit frequency on the magnetic field orientation and strain magnitude makes it difficult to predict the transition frequency for uncharacterized defects. Therefore, a rapid method for scanning a broad frequency range is desirable.

A simplified ODMR measurement, as shown in Figure 4.1, addresses this challenge. We apply a continuous microwave chirp across the target frequency range, with its duration and power optimized based on the desired frequency span and spectral resolution. In our experiments, the microwave frequency is swept within $10 - 20$ ms under continuous resonant optical excitation of A1. In general, a low laser powers of approximately $1 - 5$ nW is used. For example, for a large frequency range of $(200 - 1000$ MHz), we use a chirp with an insertion power of approximately -5 dBm to efficiently detect the qubit during the brief interval when the chirp is resonant with the transition. This sequence is repeated until the desired signal-to-noise ratio is achieved.

For high spectral resolution, as in the measurement shown in Figure 4.1, a lower microwave amplitude is used (-40 dBm; 100 nW) and the span of the mw-chirp is adapted. Two resonances are observed, one at 3144.34(22) MHz and another at 3148.58(26) MHz with a linewidth of 841(78) kHz and 838(82) kHz, respectively. The frequency splitting suggests strong coupling to a proximal ^{13}C nuclear spin, which can serve as a long-lived quantum memory [89, 146].

4.1.2. Rabi Oscillations and Ramsey Experiment

With the qubit frequency identified, we apply resonant microwave pulses of variable duration to induce spin state oscillations. As observed in the ODMR measurement, a strongly coupled nuclear spin is present. Therefore, we set the microwave frequency to the midpoint between the two resonances and use a high Rabi frequency to minimize the influence of the nuclear spin state. The measurement scheme for a Rabi measurement is straightforward, consisting of alternating laser and microwave pulses. No charge repump is required between cycles.

Figure 4.8 (a) presents a Rabi measurement at an insertion power of 14 dBm, showing a Rabi frequency of $\Omega/2\pi = 4.31(28)$ MHz that corresponds to a π-pulse duration of 115 ns. The full contrast and slow decay demonstrate the high fidelity ($F_\pi = 99.1(+0.3)(-2.3)$ %) of the spin manipulation. Comparable fidelities have been reported in previous studies, including $F_\pi = 99.36(9)$ % by X. Guo and A. Stramma [69, 73] and $F_\pi = 99.1$ % by E. Rosenthal [70]. The gate fidelity is extracted from the decay of the Rabi oscillations by fitting to the full dataset. Notably, the fit does not fully match the amplitude around the third and fourth oscillation cycles. Increasing the statistics, either by performing more repetitions or by extending the pulse duration could improve the fit accuracy. Furthermore, the final data point shows a comparatively large deviation from the fit relative to the rest of the dataset. Indeed, if this point is excluded from the fit, the extracted gate fidelity improves to $F_\pi = 99.55(+0.2)(-1.9)$ %. Ideally, one needs to characterize the gate-fidelity via Randomised Benchmarking [147], which allows to track how errors build up over a sequence of operations and to extract a more reliable estimate of the gate performance.

Figure 4.8 (b), depicts the detuning-corrected Rabi frequency on the ac field amplitude. The data points are adjusted for the measured return loss at the respective qubit frequencies.[5] For microwave powers exceeding 19 dBm at the sample, the superconducting properties of the waveguide break down, leading to a complete loss of the qubit coherence. During the data acquisition, two important factors were unfortunately overlooked, which does not allow us to interpret the data accurately. First, different amplifiers were used depending on the applied magnetic field, as the qubit transition frequencies varied significantly.[6] Second, the arbitrary waveform generator (AWG70001A, Tektronix) for the pulse generation was calibrated for 3 GHz but not separately for 1 GHz. The delivered power of the AWG depends on the frequency, thus a wrong conversion of the amplitude can result in incorrect scaling. Ideally, the output power should have been verified for each measurement using a spectrum analyzer. Additionally, the strong hyperfine coupling to a proximal nuclear spin complicates data acquisition, as one must ensure that measurements are performed precisely at the midpoint between the split resonances. For further details on the measurement electronics, we refer to Appendix C.1.

[5] At 1.23 GHz the total RL is 3.0 dB, and at 3.14 GHz the total RL is 5.26 dB

[6] The following amplifiers from Mini-Circuits were used: ZHL-16W-43+ for $\sim$ 100 mT and ZVA-183-S+ for 40 mT.

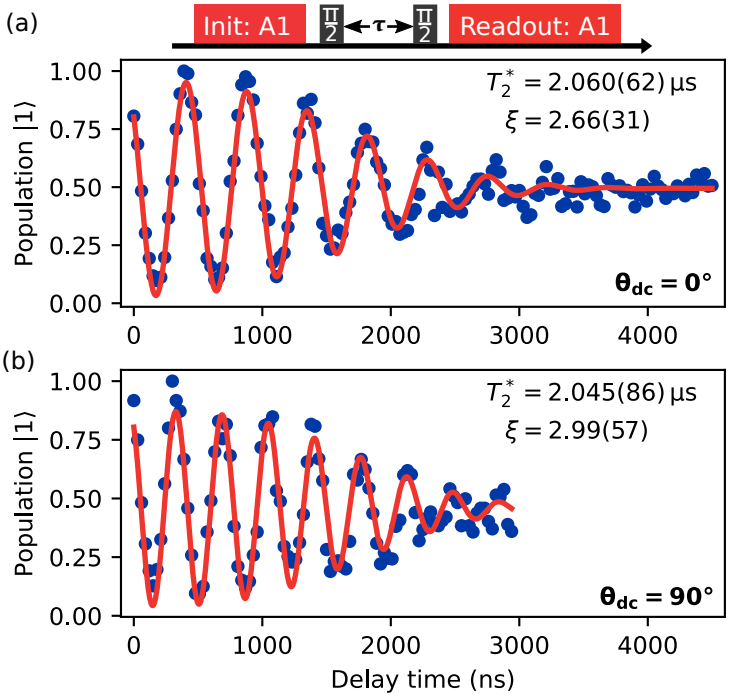

Figure 4.3.: Free induction decay measurement tuned to the center between the two resonances of the nuclear spin states at 100 mT dc field. The data are modeled by a sinusoid with decaying envelop $\propto e^{(-\tau/T_2^*)^\xi}$. (a) Parallel field alignment: The detuning $\Delta\omega/2\pi = 2.123(6)$ MHz perfectly matches the expected value of $(f_2 - f_1)/2 = 2.12$ MHz determined via ODMR in Figure 4.1. (b) Perpendicular field alignment: The detuning $\Delta\omega/2\pi = 2.775(10)$ MHz indicates stronger hyperfine interaction. (a) is adapted from Figure 4 in Reference [1].

Performing free-induction decay measurements allows to probe the dephasing time T_2^* of the qubit.[7] The spin dynamics are best described in the rotating frame of the qubit. First, the qubit is initialized into a superposition state by applying a $\pi/2$-rotation around the x-axis of the Bloch sphere. The spin is then allowed to freely precess for a variable duration τ. For a resonant microwave pulse ($\omega = \omega_{21}$), the experiment results in an exponential decay, for reasons explained in 2.5.2. If the microwave frequency is detuned, the Bloch vector precesses around the z-axis with frequency $\Delta\omega$. The probability of measuring the qubit in $|1\rangle$ is therefore given by:

$$P_{|1\rangle}(t) = \frac{1}{2}(1 + \cos(\Delta\omega t + \phi))e^{(-t/T_2^*)^\xi} \tag{4.9}$$

The additional phase ϕ is necessary, to account for the precession occurring during the pulse duration. The exponential stretching exponents, $\xi_\parallel = 2.66(31)$ and $\xi_\perp = 2.99(57)$, for parallel and perpendicular field alignment, deviate from the typically expected Gaussian envelope ($\xi = 2$), which is characteristic of dephasing dominated by low-frequency noise [149, 150]. The observed deviation suggests the presence of an altered noise bath,

[7] T_2^* is the decay time of the total in-plane magnetization for which the decay is reversible by applying a spin-echo pulse sequence. [148].

such as a cutoff of noise contributions for specific frequencies, multiple spin baths or simply imperfect pulse shapes. Further, the free induction can be analytically derived for short times to

$$P_{|1\rangle}(t) \propto e^{-M_1 t^2 + M_2 t^4 + \ldots} \tag{4.10}$$

"for noise spectra possessing a high frequency cutoff" [148]. We will analyze the spin bath properties in more detail in the following discussion of dynamical decoupling (Section 4.2).

For parallel field alignment, the detuning $\Delta\omega/2\pi = 2.123(6)$ MHz precisely matches the expected value of $(f_2 - f_1)/2 = 2.12$ MHz, as determined via ODMR in Figure 4.1. In contrast, for perpendicular field alignment, the detuning $\Delta\omega/2\pi = 2.775(10)$ MHz suggests a stronger hyperfine interaction.

From the envelope of the Ramsey experiment shown in Figure 4.3, we extract a dephasing time of $T_2^* = 2.06(6)\,\mu$s for the qubit. This value is comparable to that observed in isotopically pure overgrown diamond [69]. In the following, we further analyze the Rabi oscillations and free induction decay under variable detuned driving. The resulting chevron and 2D-Ramsey patterns for two field configurations are presented in Figure 4.4:

- **Top row:** Magnetic field aligned parallel to the quantization axis, with a qubit center frequency of 3135.2 MHz.
- **Bottom row:** Magnetic field aligned perpendicular to the quantization axis, with a qubit center frequency of 2152.0 MHz.

These measurements provide direct insight into the coupling strength of the electron spin and the proximal nuclear spin. In the chevron pattern of the top row, this interaction is revealed by the presence of two distinct resonance features, where the Rabi frequency reaches a minimum (around ±2 MHz). The observed pattern deviates from the expected structure of two independent, detuned Rabi oscillations, which would typically arise from a thermally populated nuclear spin state. However, the deviations is expected when the hyperfine coupling strength is comparable to the Rabi frequency of the driven electron spin.[8] In this regime, coherent driving of the electron spin induces nontrivial dynamics in the coupled nuclear spin state, leading to modifications in the oscillation pattern [151]. These interactions can be used for coherent nuclear spin control, offering an additional pathway for quantum memory applications [89].

As the driving frequency is detuned relative to the two transitions, the population in the Ramsey patters oscillates, forming a characteristic crown-like pattern. The periodic instances of complete coherence loss further confirm the influence of the hyperfine interaction with the nuclear spin.

From the measurements, we determine the Rabi frequencies for both magnetic field orientations. For parallel field alignment, we extract $\Omega_R/2\pi = 3.56$ MHz whereas for perpendicular alignment, we obtain $\Omega_R/2\pi = 5.28$ MHz. After correcting for the different

[8] For an electron spin coupled to a ^{13}C nuclear spin, the so called Hartmann-Hahn condition is given if the effective Rabi frequency of the qubit is tuned to match the Larmor frequency of the ^{13}C nuclear spins.

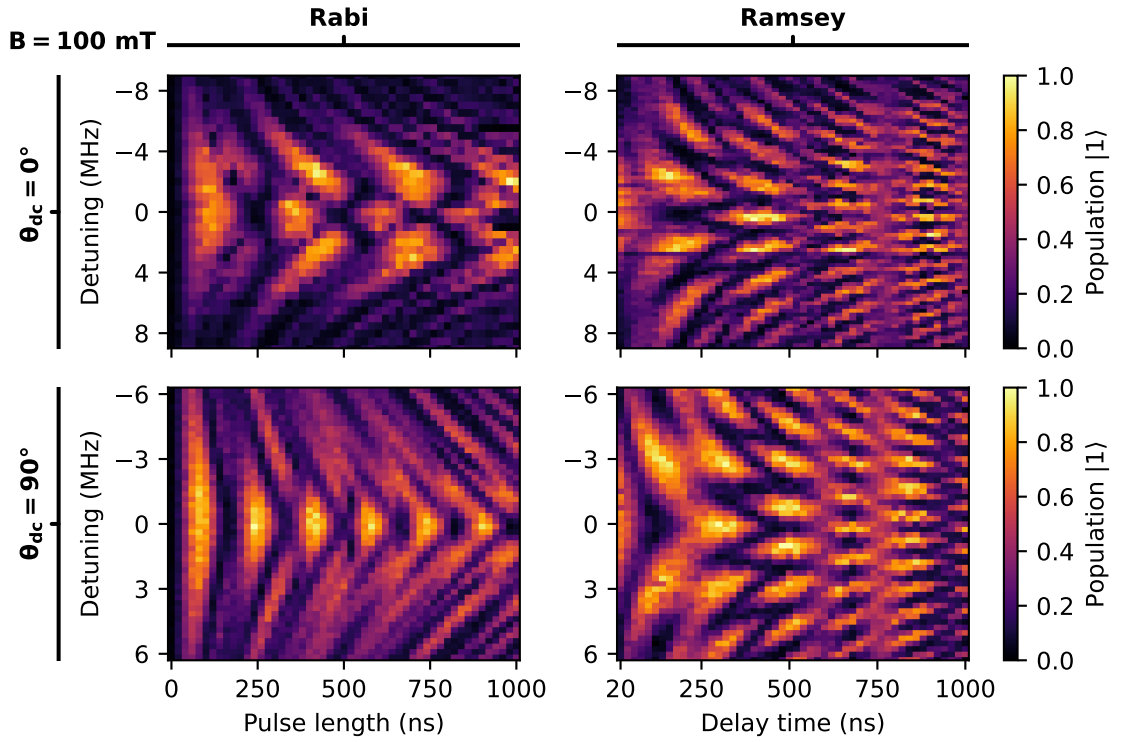

Figure 4.4.: Rabi chevron and 2D-Ramsey experiment. The top row shows the Rabi chevron and 2D-Ramsey pattern for parallel field alignment. The bottom row shows similar measurements for perpendicular field alignment. This figure is adapted from Figures (4, 17) in Reference [1].

input return losses, arising from the respective qubit frequencies, the Rabi frequency in the parallel configuration increases to $\Omega_R/2\pi = 4.42\,\text{MHz}$, yet remains substantially lower than that in the perpendicular case. This supports the dependence of the Rabi frequency on the magnetic field orientation, as introduced in Equation 4.6.

By analyzing the beating in the Ramsey fringes, we also extract the hyperfine interaction strength for both configurations: $I_{B_\parallel} = 4.24\,\text{MHz}$ and $I_{B_\perp} = 5.7\,\text{MHz}$. Here, I quantifies the strength of the coupling between the electronic spin of the SnV center and the nearby nuclear spin for parallel, and perpendicular field, respectively. However, the nature responsible for the difference in coupling strength was not investigated.

In the following, we will discuss the extension of the coherence time by making use of dynamical decoupling techniques and investigate the influence of the spin bath in more detail.

4.2. Dynamical Decoupling

The interaction between the qubit and its environment leads to the decay of in-plane magnetization. This interaction can be reversed almost completely by including decoupling pulses in between the $\pi/2$ pulses of the Ramsey sequence. These decoupling pulses consist of a variable number of π-pulses that invert the magnetization vector, thereby counteracting the environmental effects. The simplest sequence with one refocusing pulse ($\pi/2 - \tau - \pi - \tau - \pi/2$) is known as the Hahn-echo protocol. This method of dynamical-decoupling (DD) extends the dephasing time T_2^* by several orders of magnitude, yielding the spin coherence time T_2.

The irreversible decoherence time T_2 is limited by time dependent fluctuations within the time intervals τ, which are characterized by the correlation time τ_c [148]. We can think of these fluctuations as a modulating magnetic field component that changes the qubit's energy splitting and thus its Larmor precession over τ_c. Then, we can understand, how for $\tau_c \gg \tau$ the refocusing pulse simply reverses the error of the 'detuning' by effectively canceling out the accumulated phase error, as the fluctuation behaves like a quasi-static field: the accumulated phase during the first delay time τ is equal and opposite in sign to the phase that is acquired during the second delay time τ [149]. However, for $\tau_c \leq \tau$ the accumulated phase in the first τ is no longer canceled in the second τ, since the phase is randomly accumulated. As a consequence the refocusing pulse becomes less effective and the qubit irreversibly loses its coherence.

From a theoretical standpoint, there are no factors that prevent us from reducing the delay time to $\tau \leq \tau_c$, until the noise appears quasi-static again. And indeed, a common approach is to apply a train of periodic π-pulses in between the $\pi/2$-pulses ($\pi/2 - [\tau - \pi - \tau]_{\text{repeat}} - \pi/2$) with decreasing delay times and increasing repetitions, such that the total delay time $t = 2n\tau$ remains constant. A common pulse sequence is the Carr-Purcell-Meiboom-Gill sequence (CPMG), for which the π-pulses are 90° phase-shifted to the $\pi/2$-pulses. In principle, reducing the delay time to $\tau \ll \tau_c$ averages out fast-fluctuating noise for the reasons explained above. Experimentally, this approach is limited by pulse imperfections, finite pulse durations, and increased power dissipation.

In the following, we will discuss the decoherence properties in a more mathematical though compact approach, by elaborating the key mechanisms arising from the qubit's coupling to environmental noise. For interested readers, we refer to various very detailed studies of electron spin dynamics: by R. Sousa on "the microscopic mechanisms for reversible and irreversible decay of spin coherence" [148], by R. Hanson on coherent dynamics of a single NV-center interacting with a spin bath [149] and G. Lange on DD of a single NV-center from a spin bath [150]. In addition, A. Stramma's doctoral thesis offers a detailed insight into the spectroscopy of noise via different dynamical-decoupling sequences on SnV-centers [73].

We will follow the investigation of Ł. Cywiński on "how to enhance dephasing time in superconducting qubits" [152]. The description of Ł. Cywiński develops the theoretical foundations from an experimentally more intuitive perspective.

First, we consider a situation, where spin relaxation of the qubit is negligible and decoherence is dominated by pure dephasing ($T_1 \gg T_2$). The Hamiltonian to describe the interaction of the qubit with its environment is given by:

$$H = \frac{1}{2}[\omega_{21} + \beta(t)]\sigma_z \tag{4.11}$$

with qubit frequency ω_{21} and the two-level fluctuators (TLFs) described by a random classical variable $\beta(t)$ (and assuming $\hbar = 1$). This variable represents the fluctuation of the energy splitting due to the coupling of the SnV-center's electron spin to the bath. Components $\propto \sigma_{x,y}$ are neglected in this approach, as they are assumed to be of much smaller magnitude.

Visually, the system can be described as a central spin system, and the bath can consist of electron spins (including P1 centers, di-vacancies, interstitial defects etc.) and nuclear spins (host nuclear spin, N-nuclear spins, but mostly ^{13}C nuclear spins), interacting with each other by long-range dipolar forces. These dynamics result in spin-flip processes, if their interaction is of comparable strength. These so called flip-flop processes can then lead to the described fluctuation of the field as seen by the SnV-center's electron.

In this semiclassical approach, the theory assumes that flip-flop processes can be modeled as random telegraph noise (RTN). The noise function is then expressed as:

$$\beta(t) = \sum_i v_i \xi_i(t), \tag{4.12}$$

where $\xi_i(t) = \pm 1/2$ represents the RTN signal and v_i the coupling strength of the i-th TLF.

To characterize these fluctuations, one evaluates the two-point correlation function, which quantifies how noise at different times is related. Its Fourier transform gives the spectral density, describing how different frequency components contribute to the overall noise. If the fluctuations follow Gaussian statistics, the noise spectrum is fully described by:

$$S(\omega) = \int_{-\infty}^{\infty} e^{i\omega t} \langle \beta(t_1)\beta(t_2) \rangle. \tag{4.13}$$

To understand the influence of the noise spectrum on the qubit coherence, we consider the time evolution of a qubit that is initially prepared in a coherent superposition of its spin states:

$$|\Psi(0)\rangle = (c_{|1\rangle}\,|1\rangle + c_{|2\rangle}\,|2\rangle). \tag{4.14}$$

As the qubit evolves freely, it accumulates a phase due to the environmental noise, leading to the time evolution:

$$|\Psi(t)\rangle_{\mathrm{RWA}} = e^{-i\int_0^t \beta(t')dt'} \cdot c_{|1\rangle}\,|1\rangle + e^{i\int_0^t \beta(t')dt'} \cdot c_{|2\rangle}\,|2\rangle\,, \tag{4.15}$$

$$= e^{-i\varphi/2} \cdot c_{|1\rangle}\,|1\rangle + e^{i\varphi/2} \cdot c_{|2\rangle}\,|2\rangle\,. \tag{4.16}$$

Here, the fluctuating phase φ arises from the noise and leads to a loss of phase coherence over time. To quantify this decoherence, we introduce the function $W(t)$. To account for

all possible noise realizations, an averaging process is performed, by integrating over all possible fluctuations of φ. The expectation value of an exponential function of a zero-mean Gaussian variable (here, $\langle\varphi\rangle = 0$) is given by $\langle\exp(i\varphi)\rangle = \exp\left(-\frac{1}{2}\langle\varphi^2\rangle\right)$. This motivates the decoherence function

$$W(t) = e^{-\chi(t)}, \tag{4.17}$$

where the accumulated phase fluctuation is captured by $\chi(t)$.

Before describing $\chi(t)$ in detail, we first consider how the accumulated phase is altered by applying a δ-shaped π-pulse during the time evolution of the qubit. A π-pulse about the x-axis at time t_i swaps the amplitudes of $|1\rangle$ and $|2\rangle$, effectively flipping the sign of the accumulated phase up to that point. If we repeat this process for n pulses at the time t_i, the phase evolution is periodically inverted, counteracting the effects of slowly changing environmental noise. To describe this effect mathematically, we introduce a modulation function $f(t;t')$, defined using a Heaviside step function, which alternates between ±1 at the pulse timings t_i. This function characterizes the filter properties of the pulse sequence by determining how the qubit samples noise at different frequencies. In the simplest case of a free induction decay experiment, where no π-pulses are applied, $f(t) = 1$ for the entire evolution $t \in [0, \tau]$, forming a simple rectangular function over the delay time. This means the qubit continuously accumulates phase noise without interruption, making FID highly sensitive to low-frequency noise.

To better understand how different pulse sequences influence qubit decoherence, it is necessary to analyze the filter properties of their corresponding step functions. This process is made easier by the fact that a simple rectangular step function in time corresponds to a sinc function in the Fourier domain. Therefore for the FID, the Fourier transform of the step function is simply given by:

$$\tilde{f}(t;\omega) = \frac{\sin(\omega)}{\omega}. \tag{4.18}$$

The key idea is that the Fourier transform of any pulse sequence defines a filter function that determines how different noise frequencies affect the qubit.

Now we can return to the description of $\chi(t)$ in more detail. In the Gaussian noise approximation, the accumulated phase is related to the noise spectral density

$$\chi(t) = \int_0^\infty \frac{d\omega}{\pi} S(\omega) \frac{F(\omega t)}{\omega^2}. \tag{4.19}$$

Here, $F(\omega t)$ is the filter function, which describes how the different frequency components of the noise spectrum contribute to decoherence. The function is given by the squared Fourier transform of the step function of the respective pulse sequence:

$$F_{\text{sequence}}(\omega t) = \frac{\omega^2}{2} |\tilde{f}(t;\omega)|^2 \tag{4.20}$$

Each pulse sequence corresponds to a different modulation function that resulting in different filter functions, acting as a bandpass filter on the environmental noise.

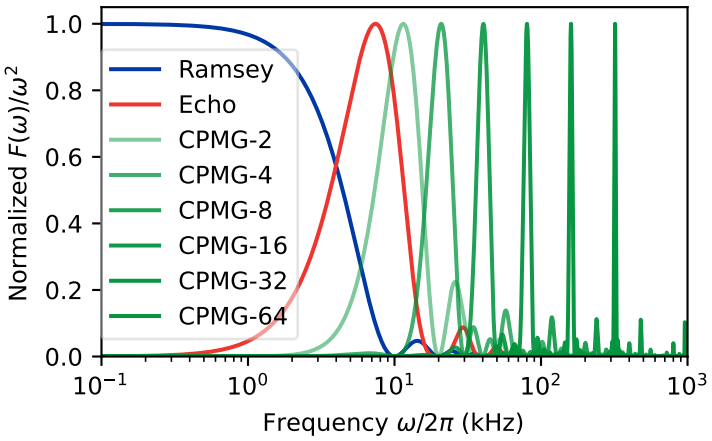

Figure 4.5.: Normalized filter functions for Ramsey, Hahn-Echo and CPMG for up to $n = 64$ pulses over frequency. The total delay time is kept constant at $T = 100\,\mu s$. The filter function for CPMG gets narrower for higher pulse numbers and sensitive to noise at frequency $f = \frac{n}{2T}$.

For the utilized pulse sequences, the filter functions are given as:

$$F_{\text{Ramsey}}(\omega t) = 2\sin^2\left(\frac{\omega t}{2}\right), \tag{4.21}$$

$$F_{\text{Echo}}(\omega t) = 4\sin^4\left(\frac{\omega t}{4}\right), \tag{4.22}$$

$$F_{\text{CPMG}}(\omega t) = 8\sin^4\left(\frac{\omega t}{4n}\right)\frac{\sin^2\left(\frac{\omega t}{2}\right)}{\cos^2\left(\frac{\omega t}{2n}\right)}, \tag{4.23}$$

where n is the number of π-pulses in the CPMG-sequence and is assumed to be an even number. The filter functions are depicted in Figure 4.5 for Ramsey, Hahn-Echo and CPMG for up to $n = 64$ pulses as a function of frequency $f = \omega/2\pi$. The total delay time is kept constant at $T = 100\,\mu s$, resulting in functions for CPMG that become narrower for higher pulse numbers and more sensitive to noise at higher frequencies around $f = \frac{n}{2T}$.

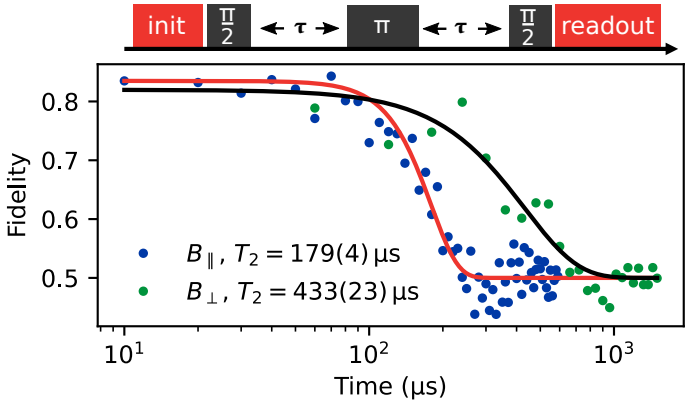

Figure 4.6.: Hahn echo measurements under a parallel and perpendicular applied magnetic field. The data are fit to a stretched exponential decay with a stretching factor of $\xi = 4$ (for parallel field orientation) and $\xi = 3$ (for perpendicular field orientation). This figure is adapted from Figure 5 in Reference [1].

4.2.1. Spin-Echo and CPMG Experiment

In this section, we present the experimental observations of the decoherence dynamics of the SnV center. We analyze how the noise bath influences the decay and coherence times. The modelling of the spin bath dynamics was carried out by Jeremias Resch.

Noise model and decoherence scaling In the previous discussion, we described the electron spin of the SnV center as a central spin system. Such a system is generally characterized by Ornstein-Uhlenbeck noise [153], which leads to a Lorentzian spectral density:

$$S(\omega) = \frac{b^2}{\pi} \frac{\tau_c}{1 + \omega^2 \tau_c^2}, \tag{4.24}$$

with the coupling strength b to the local spin and the bath correlation time τ_c [154, 155].

For CPMG sequences, only the high frequency tail of the Lorentzian is relevant. In this regime, the spectral density follows a power-law behavior:

$$S(\omega) \propto \omega^{-2}.$$

Generally, a power-law scaling $\propto \omega^{-\alpha}$ leads to decoherence envelopes of the form

$$W(t) = \exp\left[-\left(\frac{t}{T_2}\right)^{\xi}\right], \tag{4.25}$$

with a stretching factor $\xi = \alpha + 1$ [156]. Therefore, the coherence time under dynamical decoupling scales as

$$T_2^{\mathrm{DD}} = T_2^{\mathrm{HE}} \cdot n^{\kappa}, \tag{4.26}$$

where $\kappa = \frac{\alpha}{\alpha+1}$ and T_2^{HE} is the Hahn-Echo coherence time [156]. For an Ornstein-Uhlenbeck bath with a Lorentzian spectral density the decoherence is proportional to $\exp(-2t/T_2)$ and the scaling simplifies to

$$T_2^{\mathrm{DD}} = T_2^{\mathrm{HE}} \cdot n^{\frac{2}{3}}.$$

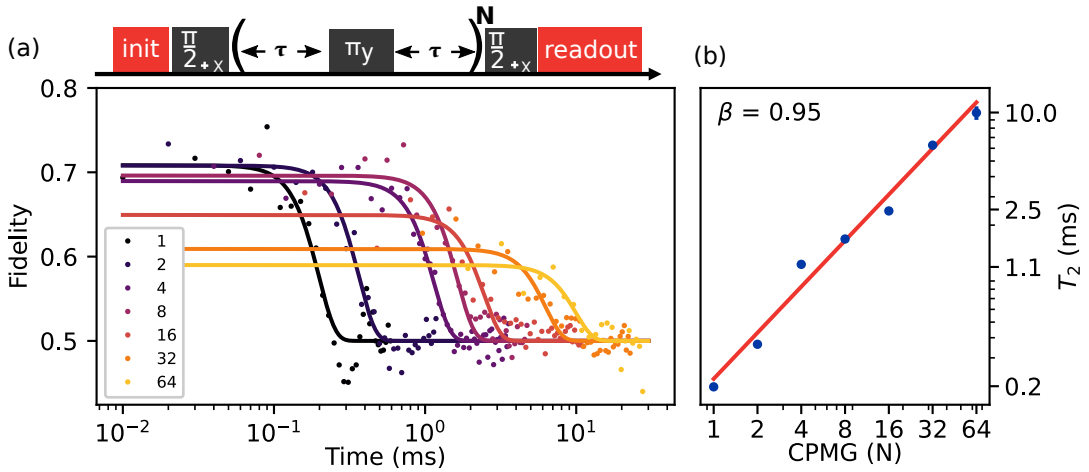

Figure 4.7.: CPMG sequence with varying number N refocusing pulses. In (a) the CPMG measurements are shown with the data fit to stretched exponential envelopes with $e^{-(t/T_2)^{\xi}}$ and $\xi = 4$. In (b) a double-logarithmic plot of the power-law behavior of T_2 is depicted. We find as scaling for the coherence proportional to $n^{0.95}$ with the pulse number. This figure is adapted from Figure 5 in Reference [1]

Experimental observations In Section 4.1.2 we presented FID measurements that deviated from the expected Gaussian envelope, and hinted that the data are better described by a Lorentzian noise bath with a high frequency cutoff. For a Hahn-Echo sequence where we drive resonantly to one nuclear spin resonance using a microwave power of 10 dBm (resulting in a Rabi frequency of 2.5 MHz), we observe a stretched exponential decay with a stretching factor of $\xi = 4$ (for parallel field orientation) and $\xi = 3$ (for perpendicular field orientation). As for the FID measurement, a stretching factor of $\xi = 4$ can only be explained by a Lorentzian noise bath with a high frequency cutoff [148]. In this case, the corresponding coherence times are $T_2^{\mathrm{HE}} \approx 179(4)\,\mu\mathrm{s}$ for the parallel case and $T_2^{\mathrm{HE}} \approx 433(23)\,\mu\mathrm{s}$ for the perpendicular case. These measurements are shown in Figure 4.6.

In addition, CPMG measurements with up to 64 refocusing pulses yield a coherence time of $T_{2,\mathrm{CPMG64}} = 10(1)\,\mathrm{ms}$, which is about a six-fold improvement over earlier work [69]. Interestingly, the scaling of T_2 with the pulse number follows an almost linear trend, with an exponent of $\kappa = 0.95(9)$, in contrast to the expected $\kappa = 2/3$ for a single nuclear spin bath [153, 155]. These measurements are shown in Figure 4.7. In the following, we will explain these deviations by an adapted expression of the spin bath.

Total bath expression In Sukachev et al. [65], it is already discussed that the altered stretched exponentials can be modeled by a double-Lorentzian bath, where

1. one bath is attributed to the nuclear spin environment, and
2. a second bath is originating from the electron spin environment.

For the electron spin bath a hard frequency cutoff is implemented. In our model of this double-Lorentzian bath, we set the cutoff frequency to

$$\omega_{\text{lim}} \approx 1 \times 10^4 \, \text{s}^{-1} \, ,$$

and apply the fast exponential cutoff to the electron spin bath [157].[9] The resulting total noise spectral density is then

$$S(\omega) = \frac{2b_1^2 \tau_{c1}}{1 + \omega^2 \tau_{c1}^2} + \frac{2b_2^2 \tau_{c2}}{1 + \omega^2 \tau_{c2}^2} \cdot \exp\left[- \left(\frac{\omega}{\omega_{\text{lim}}} \right)^4 \right] . \tag{4.27}$$

The first bath is attributed to the bulk environment of the SnV center. The coupling strength b_1 is related to the FID decay time:

$$b_1 = \frac{\sqrt{2}}{T_2^*} \approx 2\pi \times 100 \, \text{kHz} \, ,$$

and the correlation time is linked to the Hahn-Echo time for perpendicular field orientation:

$$\tau_{c1} = \frac{b_1^2}{12} \cdot \left(T_2^{\text{HE}} \right)^3 \approx 2.8 \, \text{s} \, ,$$

as discussed in [153]. These parameters agree well with reported measurements on the bulk spin bath with deep GeV centers under Ornstein-Uhlenbeck noise conditions [72].

The second spin bath can be explained by surface charges (of free electrons) due to the proximity to the surface [129, 154]. We use the measurement value of T_2^{HE} for parallel field alignment together with a coupling of

$$b_2 = 2\pi \times 30 \, \text{kHz} \, ,$$

to gain the correlation time

$$\tau_{c2} = 5 \, \mu\text{s} \, ,$$

which is comparable to the value reported for shallow NV and SiV centers [129, 154].

The total double-bath model reproduces the observed Hahn-Echo coherence time $T_2^{\text{HE}} \approx 180 \, \mu\text{s}$ (for parallel field alignment) with a stretching factor $\xi = 4$.

The simulation also yields a FID decay time of $T_2^* \approx 2.2 \, \mu\text{s}$ and a perpendicular (bulk bath only) Hahn-Echo coherence time of $T_2^{HE} \approx 440 \, \mu\text{s}$ with a stretching factor of $\xi = 3$. As these results are in good agreement with the measured values, they support the notion that one can cancel out the electron spin bath by detuning the qubit frequency from the free electron Larmor precession [70].

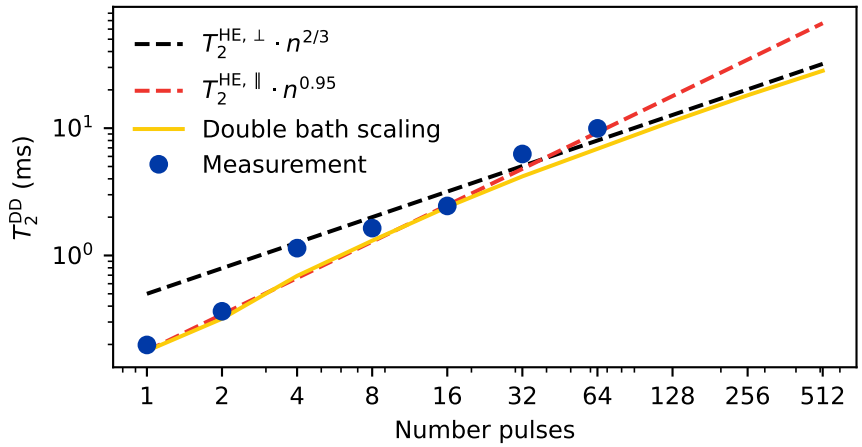

Figure 4.8.: Modeled scaling of the coherence times T_2^{DD} with the number of applied π-pulses. This figure is adapted from Figure 16 (b) in Reference [1]

Discussion of linear trend with pulse number Figure 4.8 shows the simulated scaling of the DD coherence time T_2^{DD} with the number of pulses n for two field configurations. For parallel field alignment, where both spin baths contribute, the scaling exponent is $\kappa \approx 0.95$. On the other hand, for perpendicular alignment, where the electron spin bath is decoupled, the scaling follows $\kappa \approx 2/3$, but with an increased initial value of T_2 (for $n = 1$). The simulated decoherence (defined at $W_{CPMG} = 1/e$) matches the experimental data (blue points), following the $\kappa \approx 0.95$ for parallel field alignment up to roughly 32 pulses. However, for higher pulse numbers, the simulated trend gradually deviates from $\kappa \approx 0.95$ and asymptotically approaches the perpendicular field scaling of $\kappa \approx 2/3$.

This result is intuitive: With a single noise bath, the initial coherence time is longer, while with two noise baths, the initial coherence is lower but compensated by faster scaling. As the number of pulses increases, the filter function progressively suppresses low-frequency noise and is more sensitive to noise at higher frequencies for a constant total delay time. This results into a higher residual coherence. Once the cutoff frequency drops below the frequency window sampled by the filter function, the electron spin bath becomes irrelevant. At this point, both cases converge, and the system behaves as if only the nuclear spin bath remains dominant. In addition, the filter functions become narrower for higher pulse numbers. Therefore, the electron spin is only sensitive to a gradually smaller frequency band for constant delay times and increasing pulse number.

[9] We implement the cutoff by simply multiplying with an exponential factor.

4.3. Summary

By utilizing a superconducting niobium CPW we achieve robust microwave control of the SnV spin qubit while suppressing drive-induced heating. We first identify the qubit transition via optically detected magnetic resonance. We demonstrate Rabi oscillations with frequencies in the MHz-range for parallel and perpendicular magnetic fields at a driving power of 10 dBm to 14 dBm, with high fidelity spin control ($F_\pi = 99.1(+0.3)(-2.3)$ %).

The free induction decay measurements, demonstrate coherence decay with an exponential stretching exponent of $\xi = 3$, deviating from the expected Gaussian envelope and suggesting the presence of an altered noise bath. Indeed, we show via Hahn-Echo measurements, that the electron spin bath can be canceled out by detuning the qubit frequency from the free electron Larmor precession, allowing extended coherence of $T_2 = 433(23)$ µs for $B = B_\perp$.

We further show that the altered stretched exponentials can be modeled by a double-Lorentzian bath with a hard frequency cutoff to the electron spin bath. In addition, via CPMG measurements with up to 64 refocusing pulses we achieve a coherence time of $T_{2,\mathrm{CPMG64}} = 10(1)$ ms, setting a a new record for the SnV center platform, to date.

5. Conclusion and Outlook

In this work, we investigated coherent microwave control of the SnV center in diamond, focusing on its fundamental properties, control mechanisms, and the limitations given by decoherence and microwave heating. We have shown stable optical transitions for various low- to highly strained SnV centers.

This property made it possible to achieve enhanced control over the optical and magnetic states of the SnV center's electron. Consequently, we measure 2D angular maps of the optical transitions that further contribute to a deeper understanding of the magneto-optical properties. In addition, varying the magnetic field orientation allowed us to reliably determine the SnV center's quantization axis within the laboratory system with an uncertainty of less than 1 %, regardless of the orientation of the diamond itself. Furthermore, we developed a fitting procedure for the optical and qubit transitions by mapping the measurement data to an electron spin Hamiltonian with explicit doublets for the orbital ground and excited states. This approach allowed for a qualitative determination of the orbital quenching factors. Parameters that are invaluable when working with previously uncharacterized SnV centers. We characterize the SnV center's spin dynamics. Among these, we show an initialization and readout fidelity of $> 99.8\,\%$ for both, parallel and perpendicular magnetic field orientation. We determined a spin relaxation time (T_1) exceeding 1 second at a temperature of $\sim 1\,\mathrm{K}$ for unstrained SnV centers and demonstrate how they can be decoupled from phonon-induced relaxation by introducing strain.

We calibrated an SnV center as a temperature sensor to characterize the microwave losses of normal and superconducting coplanar waveguides in a magnetic field environment. This allowed for the evaluation of superconducting coplanar waveguides in mitigating thermal effects and maintaining qubit performance. We demonstrated that, below the critical current threshold, superconducting coplanar waveguides offer significantly reduced Ohmic losses, minimizing microwave-induced heating and preserving long spin coherence times compared to normalconducting coplanar waveguides.

Microwave control was investigated using superconducting coplanar waveguides, where we demonstrated high-fidelity spin manipulation with a π-pulse fidelity of $F_\pi = 99.1\,\%$. We observe Rabi frequencies in the MHz-range with relatively low driving powers of $10 - 14\,\mathrm{dBm}$. The spin coherence time (T_2), measured under dynamical decoupling sequences, reached values of 10 ms, setting a new record for the SnV center platform.

Outlook In the near future, our primary goal is to achieve nuclear spin control of a nearby ^{13}C nucleus allowing us to use it as a memory qubit. We have already observed strong electron-nuclear coupling in our ODMR signal and coherence measurements as discussed in Chapter 4, and now we aim to leverage this interaction. One approach involves inducing coherent nuclear spin oscillations in the Hartman-Hahn regime, though this method is complex [89]. A more promising alternative is direct nuclear spin control using radio frequency pulses in the kHz to MHz range, which offer high fidelity. The advantage of the coplanar waveguide design is its compatibility with a broad frequency range, allowing seamless integration of both microwave and RF pulses. A significant challenge so far has been microwave-induced heating due to the long pulse durations, necessary to control the nuclear spin [65]. The fabricated superconducting waveguides show potential in mitigating this issue, and our recent advancements in this area, soon to be published, demonstrate substantial progress.

We are also working on refining our microwave structure design. While the current design emphasizes simplicity, we have successfully tested and optimized for narrower coplanar configurations to improve for nuclear spin control. However, a deeper understanding of the superconducting waveguide's loss behavior, particularly for short, high-power and high-frequency pulses, remains a key objective to be studied. Specifically, gaining insight into the mechanisms behind superconductivity breakdown is most important. The relevant question is whether the limitations arise solely from critical current constraints or if other factors are limiting the performance, such as the contact resistance at the wire-bonds. Further optimizations, including exploring alternative superconducting materials apart from niobium, could improve performance. In any case, the magnetic field requirements in combination with microwave frequencies remain loss factors that have to be considered.

Overall, this work provides essential insights into the control and stability of the SnV center. By leveraging strain engineering, precise magnetic field alignment, and superconducting waveguides for spin control, we have taken significant steps toward realizing a robust, scalable quantum technology.

Part II.

Detailed Information

A. Summary Table of all Measurements

Table A.1.: This table summarizes the properties of the different SnV centers that are used throughout this thesis. The figures in which the respective SnV centers are relevant are marked with X. For information on the figure contents, please see the List of Figures.

	SnV-A	**SnV-B**	**SnV-C**	**SnV-D**	**SnV-E**	**SnV-F**
Sample	B2	B1	B1	B1	B2	B2
CPW	Au	Nb	Nb	none	Nb	Nb
α^{g} (GHz)	35.0(15)	577.3(34)	530.0(40)	-	<15	42.2(17)
α^{u} (GHz)	60(7)	961.9(49)	921.4(32)	-	-	70(8)
ZPL (THz)	484.134	483.269	483.388	484.131	484.201	484.173
SnV Quantization Axes (Lab Frame)						
X	-0.081	0.011	-0.015	-	0.029	-0.810
Y	0.834	0.722	0.883	-	0.842	0.015
Z	-0.546	0.692	-0.468	-	0.539	0.586
Used in Figure						
Fig. 2.4	-	X	-	X	-	-
Fig. 2.5	-	X	-	-	-	-
Fig. 2.8	-	X	-	-	-	-
Fig. 2.9	X	-	-	-	-	-
Fig. 2.10	-	-	-	-	X	-
Fig. 2.11	X	X	-	-	X	-
Fig. 2.12	X	-	-	-	-	-
Fig. 2.13	X	-	-	-	-	-
Fig. 2.14	-	X	-	-	-	-
Fig. 2.15	X	-	-	-	-	-
Fig. 2.16	-	X	-	-	-	-
Fig. 2.17	X	X	-	-	-	-
Fig. 2.20	-	X	-	-	-	-
Fig. 2.22	-	X	-	X	-	X
Fig. 3.5	-	-	-	-	-	X
Fig. 3.6	-	-	-	-	-	X
Fig. 3.7	-	-	-	-	-	X
Fig. 3.9	X	-	-	-	-	-
Fig. 3.10	-	-	-	-	-	X
Fig. 3.11	-	-	-	-	-	X
Fig. 3.13	-	-	-	-	-	X
Fig. 4.1	-	X	-	-	-	-
Fig. 4.2	-	X	-	-	-	-
Fig. 4.3	-	X	-	-	-	-
Fig. 4.4	-	X	-	-	-	-
Fig. 4.6	-	X	-	-	-	-
Fig. 4.7	-	X	-	-	-	-
Fig. 4.8	-	X	-	-	-	-

B. Details on Devices and Sample Fabrication

B.1. Diamond Membrane Devices

The sample used in the experiments of the main text was an electronic-grade diamond membrane from *Element Six*, with dimensions $2\times2\times0.04$ mm. The initial surface roughness is 4 nm on side A and 2.3 nm on side B. Both sides are strain-relief etched via reactive ion etching (RIE) to remove damage from polishing. This procedure is done by Philipp Fuchs (Saarland University). The etching procedure follows these parameters:

- **Side A:** 50 min Ar/Cl_2 + 5 × (7 min Ar/Cl_2 + 13 min O_2)
- **Side B:** 20 min Ar/Cl_2 + 5 × (7 min Ar/Cl_2 + 15 min O_2) + 10 min Ar/Cl_2 + 15 min O_2

After etching, a total thickness of 7 µm is removed from each side, reducing the surface roughness to 3 nm (side A) and 2 nm (side B), as measured by Julia Heupel (University of Kassel).

Given its lower surface roughness, side B is selected for tin ion implantation. The implantation is performed by Michael Kieschnick (University of Leipzig) at the Felix-Bloch-Institute for Solid State Physics. The isotope ^{116}Sn is implanted with a fluence of 1×10^9 cm^{-2} at an energy of 65 keV. Post-implantation, the sample is annealed at 1200 °C for 4 h under a pressure of $< 1 \times 10^{-6}$ mbar, by Philipp Fuchs.

Surface cleaning is performed by boiling the sample in a tri-acid mixture (1:1:1 nitric acid:sulfuric acid:perchloric acid) at 400 °C.

Following this, the membrane is laser-cut into 4 pieces by *Diamond Materials*. The final preparation step involves baking the sample on a hotplate at 450 °C for 6 h, followed by cleaning in boiling piranha acid.

All measurements involving SnV centers are conducted within two pieces, SnV-2-B1 and SnV-2-B2, that are shown in Fig. AB.1 (c). The sample SnV-2-B2 (upper images) hosts SnV-A (with gold waveguide) and SnV-E and SnV-F where the sample has been recycled and used with a newly designed and fabricated Nb-waveguide for optimized electron and nuclear spin control.

The sample SnV-2-B1 (lower images) hosts SnV centers B, C, and D. Notably, SnV-D was measured in the central region of the sample before waveguide fabrication and without induced strain.

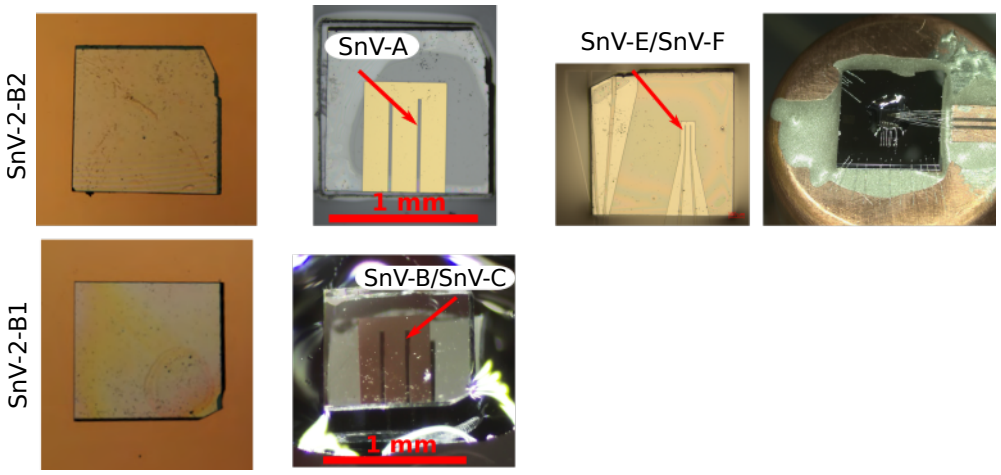

Figure B.1.: The figure shows the two main samples SnV-2-B2 (upper row) and SnV-2-B1 (lower row).

B.2. Coplanar Waveguide Fabrication

Coplanar waveguide design The coplanar waveguides used in this work is designed with two main constraints:

1. The gap between the conductors needs to be sufficiently large to accommodate a sufficient number of SnV-centers within the gap while simultaneously ensuring a high AC field density with minimal power consumption.
2. The impedance has to match the system components, which is achieved by designing the structure for 50 Ω.

The metallization thickness is 50 nm for niobium and 100 nm for gold due to photoresist limitations during deposition.

Preparation of the diamond samples To minimize background fluorescence and depending on the state of the sample, the diamonds are subject to different cleaning procedures:

- **Triacid cleaning:** Removes residual surface metallization and graphite via boiling in a mixture of nitric acid (68 %), sulfuric acid (98 %), and perchloric acid (70 %) in a ratio of 1 : 1 : 1 following the procedure described in [158].
- **Piranha cleaning:** In ratio of 2 : 1 a mixture of sulfuric acid and hydrogen peroxide (30 %) eliminates heavy organic contaminants through oxidation.
- **Sonication:** Removes organic solutes such as PMMA and photoresist via sequential sonication in acetone, 2-propanol, and deionized water.

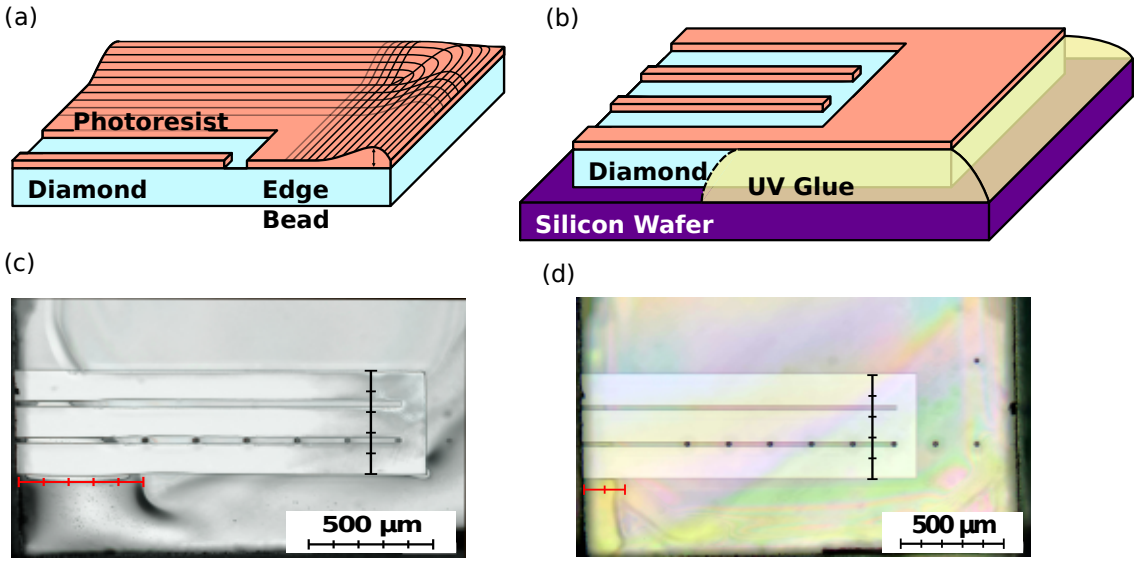

Figure B.2.: (a) A cross-sectional schematic of the diamond edge shows the formation of edge beads when coated with photoresist. (b) The application of UV glue as an additive edge bevel is depicted, reducing the edge bead effect. (c) A top-down microscope image of the developed photoresist without edge beveling reveals a pronounced edge bead along the left and bottom edges, causing overexposure at the waveguide's right end due to improper mask contact. (d) When an edge bevel is applied before spin coating, the edge bead is significantly reduced, leading to improved photoresist uniformity. This figure is from Julian Schaal's master's thesis [159].

Mitigating edge beads During spin coating, small samples develop edge beads due to uneven photoresist distribution, which can interfere with lithographic exposure by preventing proper mask contact. As part of the master's project of Julian Schaal, conducted under my supervision, we optimized the fabrication process for small diamond samples. A detailed discussion on the fabrication of small diamond samples can be found in his master's thesis [159]. Figure B.2 illustrates the developed technique of additive edge beveling to mitigate edge bead formation during spin coating. The sample shown on the lower row of the image is a single emitter CVD diamond with nine solid immersion lenses (SIL) fabricated along one edge. It was kindly provided by the Institute for Quantum Optics of Ulm University. The bake-out was performed by Johannes Lang and the SILs were fabricated by Petr Siyushev at Ulm University. The sample was used in Julian's thesis to benchmark on-chip superconducting coplanar waveguides made of niobium compared to normal-conducting coplanar waveguides made of gold. Due to the size of the sample of $2 \times 2 \times 0.5\,\mathrm{mm}$, it was helpful to study and improve edge bead formation. We have found the following approach to yield the best spin coating results:

- Small diamonds are glued onto larger silicon wafers to facilitate handling.
- The edge beveling technique is applied using UV-curing adhesive to reduce edge bead formation. The glue is carefully applied to the edges of the diamond sample.
- Care is taken to prevent the UV glue from protruding onto the diamond surface, to ensure a uniform resist layer.

Lift-off photolithography The waveguide fabrication follows a negative-tone lift-off photolithography process:

1. **Spin coating:** A negative photoresist (AZ 5214-E) is applied at 10 000 RPM for 60 s.
2. **Soft bake:** The coated substrate is baked at 110 °C for 50 s to evaporate the solvents.
3. **Exposure:** UV light exposure is performed using a Hg-Xe vapor lamp with a 300 nm filter for ≈ 11 s.
4. **Image reversal bake:** The sample is heated to around 120 °C for 60 s to crosslink the exposed areas.
5. **Flood exposure:** The entire sample is UV exposed. This step is uncritical as long as sufficient energy is applied to make the previously unexposed areas soluble.
6. **Development:** The sample is immersed in an AZ-Developer (1:1 solution with deionized water) for ≈ 33 s, followed by rinsing and ultrasonic cleaning in deionized water.
7. **Lift-off:** After metal deposition, the resist is dissolved in acetone to remove the resist.

Electron-beam physical vapor deposition Following photolithography, the sample is metalized using Electron-Beam Physical Vapor Deposition (EBPVD):

- **Surface cleaning** The sample surface is cleaned from organic/resist residues using a Kaufman ion source, which enables reactive ion etching (RIE) of the sample. This step is performed for 15 s before metallization.
- **Niobium purification:** The niobium crucible is cleaned immediately before deposition to minimize contamination. This process also purifies the vacuum chamber by reacting with residual oxygen, depositing the dirt onto the chamber walls.
- **Evaporation rate:** A high evaporation rate is preferred to minimize the thermal load from radiative heating of the hot crucible. An evaporation rate of $\approx 1\,\mathrm{nm\,s^{-1}}$ is aimed for.

C. Details on the Experimental Setup

C.1. Optical Setup

In Figure C.1, the optical setup is depicted. Some components are illustrated using elements from the *GW Optics Component Library* [160]. The optical setup is distributed across two optical tables. One table houses the resonant laser along with the necessary components for pulsing the beam. Resonant laser pulses are generated by a tunable continuous-wave laser source (C-WAVE vis, Hübner), locked to a wavemeter (WS7, HighFinesse), in combination with an acousto-optical modulator (3200-1214, G&H). We use the AOM in a double-pass configuration to achieve a higher extinction ratio (single pass $\sim -25\,\mathrm{dB}$, double pass $\sim -50\,\mathrm{dB}$). Trigger signals are provided using a fast transistor–transistor logic (TTL) unit (ADwin-Pro II, Jäger).

In case we need to restore the negative charge state of the SnV center, charge repumping is performed using a continuous-wave 532 nm laser (Ventus MPC6000, Laser Quantum), triggered by a separate TTL logic (ADwin Gold II, Jäger).

We emphasize that once the experiment is finely tuned, that is, resonant laser power optimized, objective z-focus (MPLN100X, Olympus)[1] and spatial (xy) alignment adjusted, we utilize a separate custom-made motorized beam block using a digital high speed servo (Horizon Hobby: $0.06\,\mathrm{s}/60°$), mounted on the main table, to fully block the green laser. We observe even minimal leakage to lead to increased charge instability.

For the green laser, we use a single-mode fiber (P3-460B-FC-1, Thorlabs), while the red laser is coupled through a polarization-maintaining fiber (PM-S405-XP, Thorlabs). The green beam is collimated via an air-spaced doublet collimator (F810FC-543, Thorlabs), whereas the red beam is out-coupled using an achromatic doublet lens (AC127-025-A-ML, $f = 25\,\mathrm{mm}$, Thorlabs). To suppress higher-wavelength background excitations in the fibers, we apply bandpass clean-up filters (green: FBH530-10; red: FBH620-10, Thorlabs).

Both beam paths are combined on the main optical table using a dichroic mirror (Semrock, Di03-R532-t1-25x36).[2] The light is subsequently directed through a $90:10$ beam

[1] Over the course of several years, we have tested several objectives from various reputable manufacturers. The specified model is the only one that has consistently survived multiple cooldown cycles without failure.

[2] To ensure precise spatial overlap of the green and red laser beams on the sample, both beams are projected onto a distant wall. The two mirrors positioned before the dichroic mirror are then carefully aligned using a walking beam technique. This step requires high precision to guarantee proper beam overlap at the sample position.

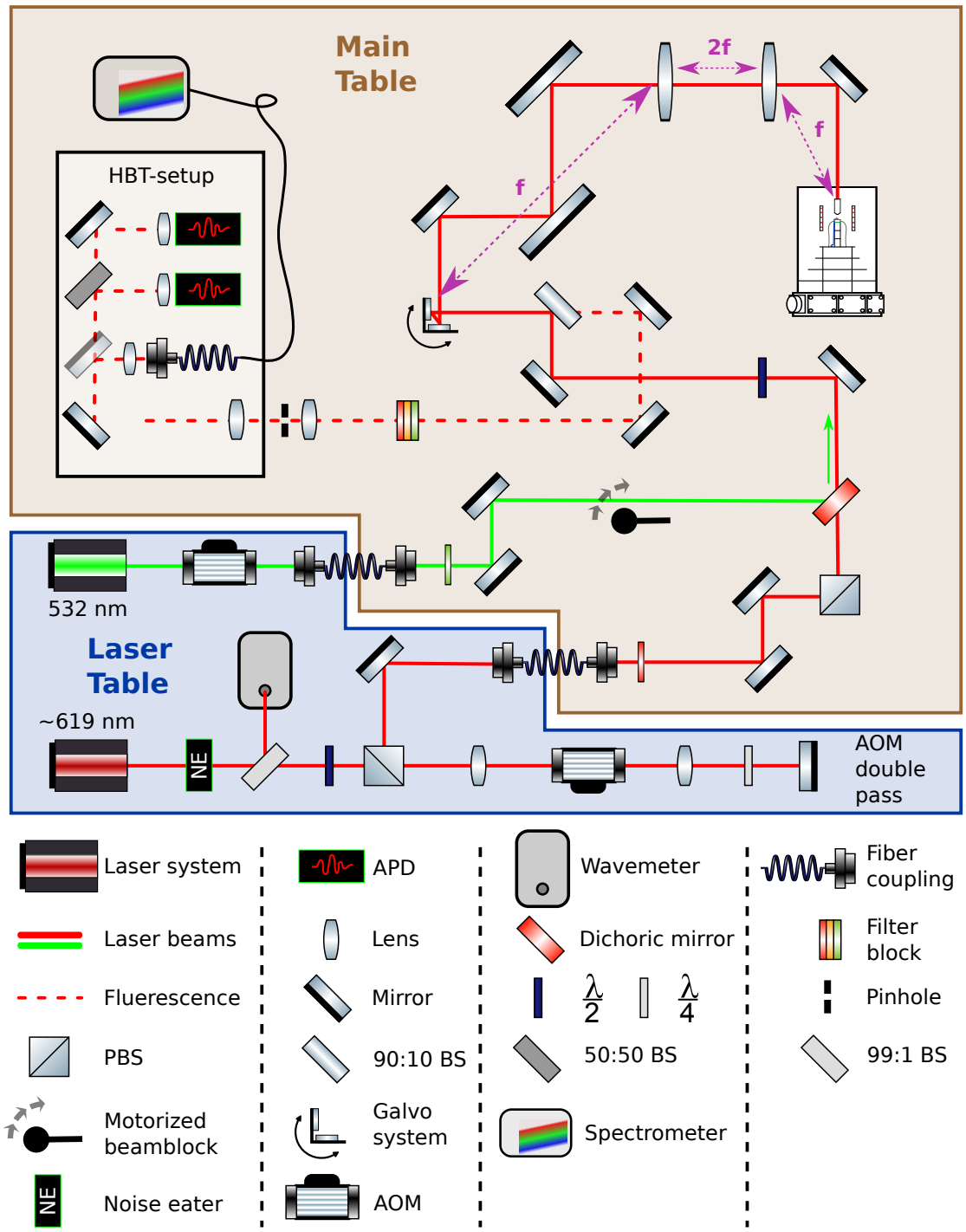

Figure C.1.: Optical setup of the experiment. The optical setup is separated on two optical tables. One table houses the laser systems and AOMs (blue border) and one table is for the experiment including the table-top cryostat and the components required for the photo-collection (brown border). Some of the components used in this graphic are from the ComponentLibrary by Alexander Franzen.

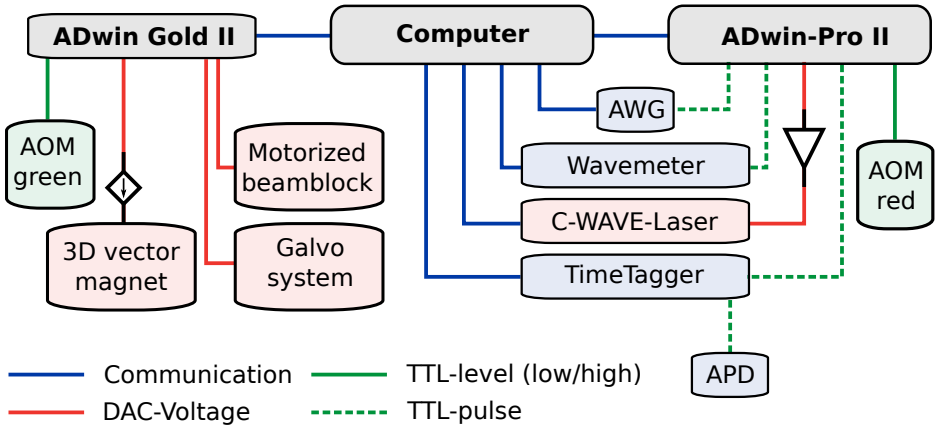

Figure C.2.: Experimental control is coordinated over a central computer. The ADwin-Pro II system is the heart of the logic architecture for time-critical control. The ADwin Gold II system is mainly used to generate highly stable analog voltages for the galvanometers and the vector magnets.

splitter (BSN10, Thorlabs), which is later used to separate excitation from fluorescence. To account for both the dipole orientation of the emitter and the polarization sensitivity of the downstream optical components, a $\lambda/2$-waveplate (WPH05M-633, Thorlabs) is placed in front of the beam splitter.

Excitation is scanned across the sample using a galvo mirror system (GVS212 with GPS011 power supply, Thorlabs), which directs the beam into the cryostat. The system enables sub-20 nm spatial scan-resolution and a total scanning range of approximately 100 µm via a 4f-configuration. The 4f-system, composed of two-inch diameter lenses (ACT508-300-A, $f = 300$ mm, Thorlabs), is crucial for maintaining a large scan range over the ~ 1.2 m beam path between the galvo system and the back aperture of the objective, while avoiding beam clipping.

Fluorescence is spectrally filtered using an additional filter block (BLP01-532R-25, FF01-593/LP-25, LP01-633R-25, Semrock). The filtered signal is focused through a pinhole (P30HK, Thorlabs) onto an avalanche photodiode (SPCM-AQRH-16, Excelitas) using an achromat-doublet lens (AC254-030-A, Thorlabs).

For correlation measurements, a 50 : 50 beam splitter (BWS10, Thorlabs) allows splitting the fluorescence to two APDs. However, to reduce the dark count rate, only a single APD is used throughout the experiments presented. If needed, PL spectra are recorded using a fiber-coupled spectrometer (SP-2500i, Princeton Instruments), with a flip mirror (RD-KLS, Radiant Dyes Laser) diverting the beam path accordingly.

C.2. Experimental Hardware and Synchronization

The overall experimental control is coordinated via a central computer that interfaces with all critical components using custom Python scripts. Communication and synchronization across subsystems are handled in real-time, to ensure correct timing and repeatable

operation. The ADwin-Pro II system is the heart of the logic architecture, which functions as the primary timing controller. It outputs both TTL and analog signals, allowing precise synchronization of laser pulses, microwave triggering, and other timing-sensitive tasks throughout the setup.

Arbitrary waveform generator All microwave pulses used for spin control, including ODMR and advanced gate sequences for coherent manipulation, are generated using an arbitrary waveform generator (AWG70001A, Tektronix). Pulse sequences are designed and uploaded via Python and triggered by TTL signals from the ADwin-Pro II. A typical sampling rate of 50 GS/s is used for waveform generation. However, due to the current organization of the logic structure, each pulse sequence must be generated and uploaded as a single waveform-block. This constraints long or complex pulse sequences, such as coherent control protocols with $n \geq 32$ pulses due to memory limitations. A waveform generated at 50 GS/s is restricted to a maximum wavelength of approximately 20 ms. Thus, for $n \geq 32$, we reduce the sampling rate to 12 GS/s to increase the possible waveform duration. This trade-off leads to slight degradation in pulse shape and results in a reduced π-pulse fidelity.

Wavemeter and resonant laser system Resonant excitation is provided by a tunable continuous-wave laser (C-WAVE vis, Hübner), actively stabilized to a high-resolution wavemeter (WS7, HighFinesse) for long-term frequency stability. The ADwin-Pro II is responsible for pulsing of the laser. Since the selected SnV centers exhibit excellent spectral stability over extended periods (days to weeks), active feedback and dynamic retuning has not been necessary, and no automation has been implemented so far. For PLE measurements, the ADwin-Pro II is used to scan the internal piezo cavity of the C-WAVE (over a piezo amplifier; E-836.1G, PI Ceramic GmbH) while simultaneously triggering both the wavemeter and the TimeTagger (Swabian Instruments) for synchronized data acquisition.

Auxiliary control and magnet system The ADwin Gold II serves as a secondary control unit dedicated to non-time-critical operations. Most importantly, it is used to generate highly stable analog voltages. When DC voltages for components like the galvo system or the 3D-vector magnet are supplied from the same unit that is used for triggering (i.e., the ADwin-Pro II), cross-talk from the TTL outputs can induce small fluctuations in the analog lines. These fluctuations can affect the laser beam position on the sample and the magnetic field strength. Both are highly sensitive to voltage stability. By outsourcing these analog outputs to the ADwin Gold II, we avoid such interference. Another very important point is to make the system foolproof: if the ADwin-Pro II is overloaded by incorrectly entering pulse sequences or processdelays, the processor hangs up, making a reboot necessary. This would reset voltages across the device and cause the vector magnets to quench. In addition, the ADwin Gold II is responsible for triggering the green AOM for charge repumping, as well as actuating the motorized beam block on the main optical table.

C.3. Dilution Refrigerator

All measurements were performed in a table-top dilution refrigerator featuring an 'inverted' design, originally developed by Alain Benoit and Wolfgang Wernsdorfer. A cross-sectional schematic of the cryostat is shown in Figure C.3. In contrast to commercial systems, the inverted configuration places the coldest component, the mK-plate, at the top of the setup. This architecture allows easier optical access from above via windows. The concept for integrating optical access along with the design of the mK stage was realized by Marcel Schrodin.[3] The system offers several advantages, including a fast cooldown to temperatures ≤ 100 mK within approximately 6 h, simple mounting of the 3D-vector magnets without the need of soldering the connections and user friendly access to the mK-plate.

The cryostat features five temperature stages arranged vertically. Thermal isolation between stages is achieved through low-conductivity stainless-steel mounts and reflective thermal shields attached to each plate. Two closed-loop cooling circuits are used. The first, a ^{4}He cooling loop, precools the system to approximately 4 K using liquid helium from a Pulse tube refrigerator. The second circuit, a ^{3}He/^{4}He cooling loop, enables further cooling into the mK regime. For a detailed description of the technical details and the working principle of a comparable cryostat, we refer to [162].

C.3.1. Vector Magnet and Sample Mounting Architecture

Figure C.4 (a) shows the 3D-vector magnet for precise control of external magnetic fields that is housed within a dilution refrigerator on top of the 4 K shield. The vector magnet was designed, simulated and fabricated by Marcel Schrodin (Karlsruhe Institute of Technology). It is optimized for fast connection with the high temperature superconductor cables (black cables with yellow (coil-x), red (coil-y) and blue (coil-z) markers). The housing components are galvanically plated in gold. The precise calibration of the vector magnet is discussed in Section C.3.2. As is shown in (b), microwaves are delivered to the sample via bonding wires connecting the flexible coplanar waveguide to the on-chip CPW. Thermalization of the cold finger is ensured by silver strands mounted onto the milli-Kelvin plate. The cold finger is mounted onto piezoelectric steppers (2 ANPx101/RES/LT, ANPz101/RES/LT, ANC300-controller, Attocube). The sample mounting scheme is detailed in the lower row of the figure. The cold finger is optimized for thermal contact by feeding silver strands through a hole and compressing them with a copper piece. The flexible CPW is soldered to the sample holder. A top view of the cold finger with a sample glued to the surface is shown, alongside the wire-bonded sample that is used in [1]. To optimize thermal contact in the newer devices, we glue the sample using a mixture of two-component glue and silver powder. Additionally, bonding pads are fabricated on the diamond samples to allow for wire bonding to the silicon wafer.

[3] Commercially available cryostats with optimized design and faster cooldown times ($\sim$ 3 h), integrated into optical tables for access from the side, are offered by Qinu [161].

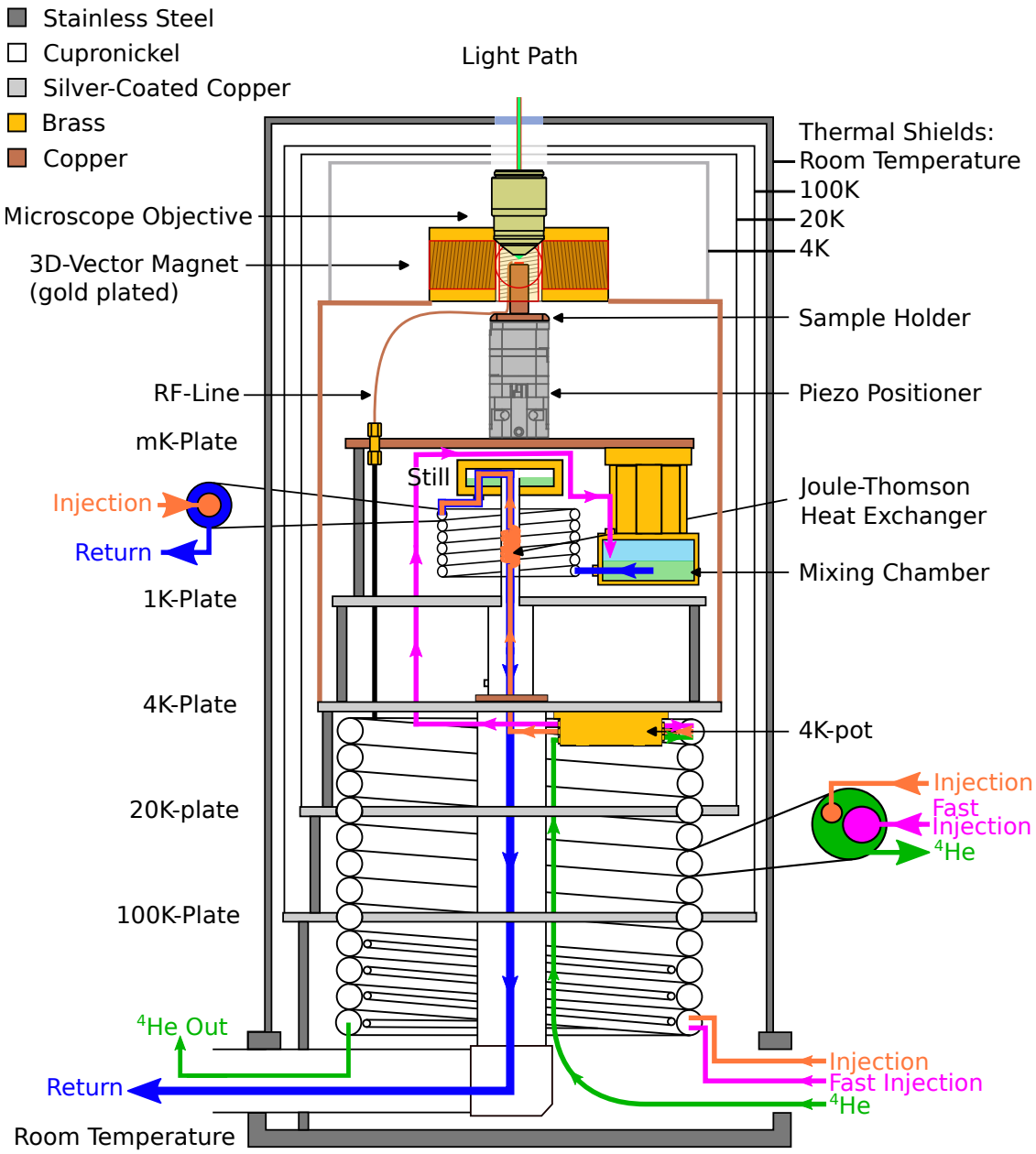

Figure C.3.: Cross-section of the dilution refrigerator. The optical path of the confocal setup enters from the top. The objective is thermally anchored to the 4K stage. The sample is positioned on an xyz–nanopositioner to allow precise spatial control. The diagram illustrates the four thermal shields from room temperature down to 4 K and the five temperature-stages (100 K, 20 K, 4 K, 1 K, mK). Additionally, the 3D-vector magnet is depicted. It is mounted in the 4 K-shield fabricated from copper for mechanical stability and better thermalization. The flow paths of the cryogenic fluids in the two cooling circuits are color-coded: the injection (orange) and fast injection (magenta) of the ^{3}He/^{4}He loop, as well as the ^{4}He loop (green). The figure has been adapted from Julian Schaal's masters thesis [159].

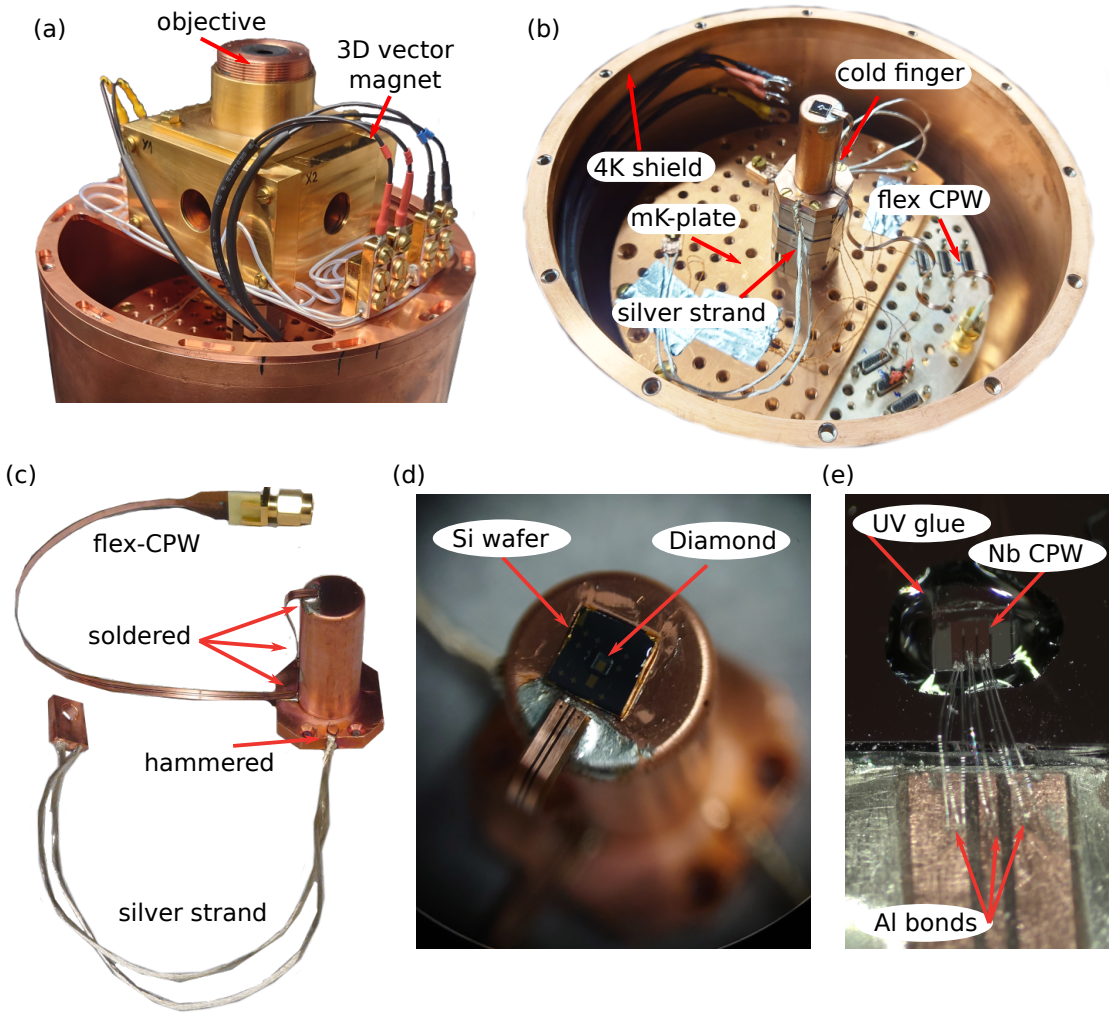

Figure C.4.: (a) shows the 4 K shield along with the 3D-vector magnets. (b) presents the milliK plate of the cryostat. Microwaves are delivered to the sample on the cold finger via bonding wires, which connect the flexible CPW to the on-chip NC-CPW/SC-CPW. Additionally, the cold finger is thermalized through silver strands mounted onto the milli-Kelvin plate. (c) shows the cold finger. Silver strands are fed through a hole and hammered with a piece of copper to improve contact with the copper holder. The flexible CPW is soldered to the sample holder. (d) top view of the cold finger with a sample glued onto the surface. (e) shows the wire boded sample that is used in the main part of [1].

C.3.2. Calibration of the DC Magnetic Field

The initial estimation of the magnetic field is conducted through COMSOL simulations, which generally exhibit a low margin of error. However, given the high sensitivity of the quenching factors to errors in the magnetic field strength, a further refinement of the field measurement is performed using the SnV center as an intrinsic magnetometer. To achieve the highest possible precision, we analyze the response of the surrounding ^{13}C nuclear spin bath in both parallel and perpendicular dc field orientations relative to the SnV axis. This approach allows an accurate determination of the absolute current

dependence of the magnetic field coils for all vector components, ensuring consistency in all subsequent measurements. The applied magnetic field strength is extracted from the Larmor precession of the nuclear spin, given by $\gamma_{^{13}\mathrm{C}} = 10.7084\,\mathrm{MHz\,T^{-1}}$.

To improve consistency, a field modulation technique is implemented during any field adjustment, where the magnetic field undergoes oscillations to asymptotically converge to the target value. For spin-echo measurements with the field aligned along the SnV axis, the observed modulation of the Hahn echo signal is well described by a phenomenological model:

$$p_{\parallel}(\tau) = A \cdot \exp\left(B \cdot \sin^4(2\pi f \cdot \tau + \varphi) - \frac{\tau}{T_{\mathrm{damp}}}\right) + a \cdot \tau + \mathrm{DC} \tag{C.1}$$

This expression accounts for additional couplings to remote ^{13}C nuclear spins. As evident from the Hahn-echo decay presented in Figure C.5 (a), we incorporate an artificial damping time and a linear drift term. The extracted fit parameters are in good agreement with a Lorentzian fit to the FFT spectrum of the echo signal, but yielding a better uncertainty compared to the FFT. A similar procedure is applied for spin-echo measurements with the field perpendicular to the SnV axis (y-component), depicted in Figure C.5 (c). In this configuration, the coupling to a proximal ^{13}C nuclear spin becomes visible (fast oscillation of the signal). We use an alternative fit function adapted from the well-established model for NV centers coupled to a proximal ^{13}C spin [15]:

$$p_{\perp}(\tau) = A \cdot \sin\left(2\pi f_1 \cdot \tau\right)^2 \cdot \sin\left(2\pi f_2 \cdot \tau\right)^2 + \mathrm{DC} \tag{C.2}$$

Here, one frequency component corresponds to the collective bath of ^{13}C spins, while the other arises from the direct coupling to the proximal nuclear spin. As previously observed in NV centers [15], the Larmor precession of the proximal nuclear spin is enhanced, allowing us to attribute the higher frequency component to this interaction. The expected Larmor precession frequency of the bath is given by:

$$f_{\mathrm{larmor}} = \cdot\gamma_{^{13}\mathrm{C}} \cdot B = \cdot 10.7084\,\mathrm{MHz\,T^{-1}} \cdot 100\,\mathrm{mT} = 1.070\,84\,\mathrm{MHz} \tag{C.3}$$

From the ratio between the measured and expected precession frequencies, a refined determination of the magnetic field amplitude is obtained:

$$B_{\mathrm{par}} = 96.7(2)\,\mathrm{mT}, \tag{C.4}$$

$$B_{\mathrm{perp}} = 94.5(4)\,\mathrm{mT}. \tag{C.5}$$

To ensure robust modeling in subsequent Hamiltonian fits and orbital quenching factor estimations, we conservatively estimate an upper bound on the systematic uncertainty of the magnetic field coils to be 0.5 %, to account for potential hysteresis effects. For completeness, Table C.1 provides the current-to-field conversion factors for the laboratory-frame 3D-vector magnet, alongside the quantization axes of the three SnV centers (A-C).

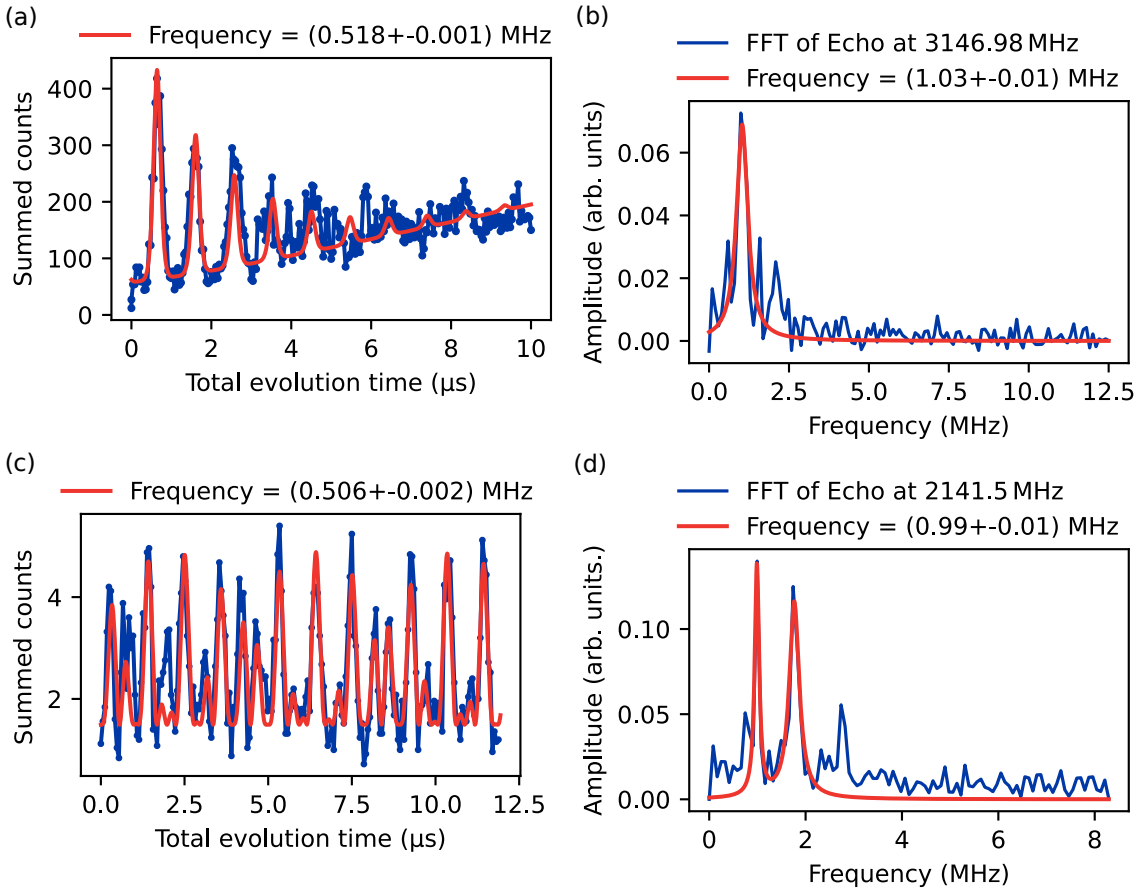

Figure C.5.: Hahn-echo signal for magnetic field aligned parallel (a) and perpendicular (c) to the SnV axis. The echo modulation arises from coupling to the ^{13}C bath, with an additional beat pattern observed in (c) due to coupling to a proximal nuclear spin. The corresponding FFT spectra are shown in (b) and (d). This figure is adapted from Figure 10 in Reference [1]

Table C.1.: Estimated parameters for the magnetic field coils in the laboratory frame and the corresponding SnV quantization axes. The uncertainties are given as standard errors.

Coil Axis	**Magnetic Field** ($\mathrm{mT\,A^{-1}}$)
X	−45.7(2)
Y	61.5(3)
Z	133.5(6)
SnV Quantization Axes (Lab Frame)	
SnV	**Quantization Axis (X, Y, Z)**
A	(-0.081, 0.834, -0.546)
B	(0.011, 0.722, 0.692)
C	(-0.015, 0.883, -0.468)

D. Details on Coplanar Waveguides

In the following, we briefly outline the calculation of the characteristic impedance of a coplanar waveguide with finite-width ground planes. Additionally, we summarize the attenuation characteristics arising from dielectric and conductor losses for both normal-conducting and superconducting CPWs. The following section is based on the book *Coplanar Waveguide Circuits, Components, and Systems* by Rainee N. Simons [106].

This book provides a comprehensive analysis of the propagation characteristics of many different CPW configurations. Interested readers are strongly encouraged to read the chapters covering conventional CPWs, conductor-backed CPWs, and CPWs with finite-width ground planes.[1] The quasi-closed-form expressions for the conductor attenuation in the CPW structures presented in the book are mainly based on the works of Christopher Holloway on normal-conducting [164] and superconducting [165] CPWs.

D.1. Characteristic Impedance of FW-CPWs

The following section summarizes the important formulas for calculating the characteristic impedance of FW-CPW with two dielectric layers, accounting for both the diamond substrate of the sample and an underlying substrate, such as a silicon wafer. Please note, that in contrast to the derivations in the referenced book, we have swapped the indices of the dielectrics and heights in Figure D.1. The characteristic impedance, as derived from transmission line theory is approximated by:

$$Z_0 = \sqrt{\frac{L}{C}} \tag{D.1}$$

for a lossless TEM-mode with equivalent inductance L and the equivalent capacitance C per unit length [163]. The inductance can be expressed by the capacitance if the phase velocity v_{ph} is known. The latter depends on the effective dielectric constant $\varepsilon_{\mathrm{eff}}$, which is a measure of how the electromagnetic field is distributed between the different dielectric layers. With

$$v_{\mathrm{ph}} = \frac{1}{\sqrt{LC}} = \frac{c'}{\sqrt{\varepsilon_{\mathrm{eff}}}}, \quad \text{and} \quad \varepsilon_{\mathrm{eff}} = \frac{C}{C_0} \quad \text{we get} \quad Z_0 = \frac{1}{C v_{\mathrm{ph}}} = \frac{1}{c'\sqrt{C \cdot C_0}}. \tag{D.2}$$

[1] For an additional interesting read on coplanar waveguide integrated circuits, we refer to the book of Ingo Wolff [163].

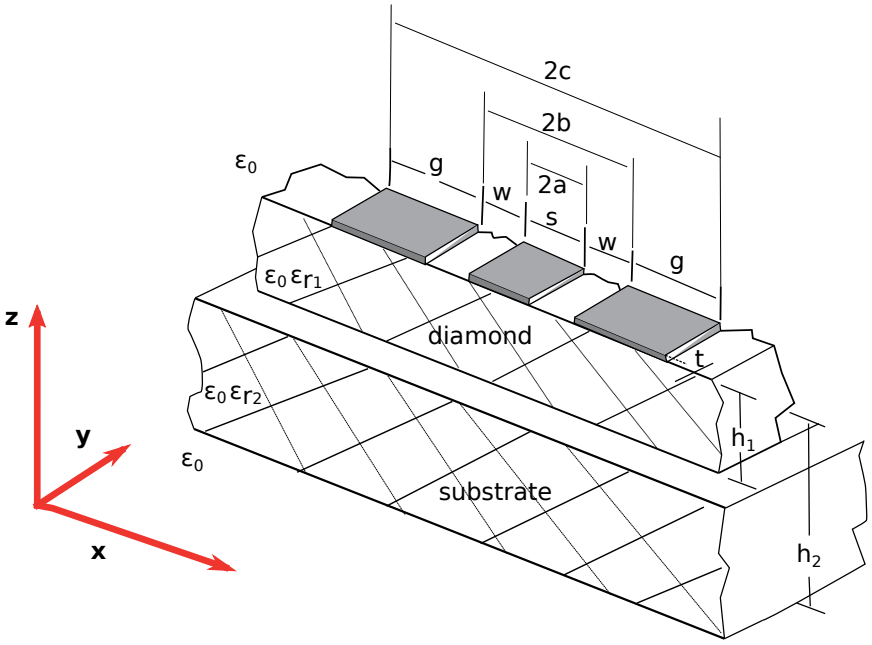

Figure D.1.: Extended schematic representation of a coplanar waveguide with finite-width ground planes. The CPW consists of two dielectric layers with relative permittivities ε_{r1} and ε_{r2} and thicknesses h_1 and h_2, respectively. The geometrical parameters of the structure are specified in two ways to match the formulation of the attenuation equations. Inspired by [106].

Here c' is the speed of light.

$$C = C_0 + C_1 + C_2 \tag{D.3}$$

is the total capacitance per unit length of the CPW and C_0 is the capacitance per unit length of the CPW if no dielectric is present and for a FW-CPW, it is given as:

$$C_0 = 4\varepsilon_0 \frac{K(k')}{K(k)}. \tag{D.4}$$

K is the complete elliptical integral of the first kind and its arguments depend on the geometry of the FW-CPW described in Figure D.1:

$$k = \frac{c}{b}\sqrt{\frac{b^2 - a^2}{c^2 - a^2}}, \tag{D.5}$$

$$k' = \sqrt{1 - k^2}. \tag{D.6}$$

Next, we determine the capacitance C_1 of the first dielectric region in the diamond with ε_{r1} and the capacitance C_2 in the second dielectric region in the substrate with ε_{r1}:

$$C_1 = 2\varepsilon_0(\varepsilon_{r1} - \varepsilon_{r2})\frac{K(k'_{h1})}{K(k_{h1})}, \tag{D.7}$$

and

$$C_2 = 2\varepsilon_0(\varepsilon_{r2} - 1)\frac{K(k'_{h2})}{K(k_{h2})}, \tag{D.8}$$

where:

$$k_{hi} = \frac{\sinh(\pi c/2h_i)}{\sinh(\pi b/2h_i)} \sqrt{\frac{\sinh^2(\pi b/2h_i) - \sinh^2(\pi a/2h_i)}{\sinh^2(\pi c/2h_i) - \sinh^2(\pi a/2h_i)}}, \tag{D.9}$$

$$k'_{hi} = \sqrt{1 - k_{hi}^2}. \tag{D.10}$$

Note, that the heights h_i in Figure D.1 are given as the total heights from the distance to the metallic layer. A closer look at the respective capacities reveals, the iterative pattern to extend the calculation of the total capacity for multiple layers, including layers on top of the metal conductors. Basically, each capacitance term is calculated based on the difference in relative permittivity $\varepsilon_{\mathrm{ri}}$ between two adjacent layers:

- C_1 is the difference between ε_1 and $\varepsilon_{\mathrm{r2}}$,
- C_2 is the difference between $\varepsilon_{\mathrm{r1}}$ and $\varepsilon_{\mathrm{vacuum}} = 1$.

D.2. Attenuation Characteristics of Conventional and Superconducting CPWs

Dielectric losses: In the following, we summarize the formulas to determine the attenuation of FW-CPWs. The calculations have been adapted, where necessary, to include the second dielectric layer, in contrast to [106]. The total attenuation α is

$$\alpha = (\alpha_{\mathrm{c}} + \alpha_{\mathrm{d}}) \quad \mathrm{Np\,m^{-1}}. \tag{D.11}$$

Please note, that the attenuation is expressed in the units of Nepers per meters. To express the losses in $\mathrm{dB\,m^{-1}}$ the value has to be converted accordingly. The dielectric losses are given as:

$$\alpha_{\mathrm{d}} = \sum_i \frac{\pi}{\lambda_0} \frac{\varepsilon_{\mathrm{ri}}}{\sqrt{\varepsilon_{\mathrm{eff}}}} q_i \tan\delta_{\mathrm{li}} \quad \mathrm{Np\,m^{-1}}. \tag{D.12}$$

Each dielectric layer contributes to the dielectric losses by the amount of the EM-wave that is present in the respective volume, which is expressed through the filling factor q_i. Therefore, we sum over the dielectric layers i with their relative permittivity $\varepsilon_{\mathrm{ri}}$ and dielectric loss tangent $\tan\delta_{\mathrm{li}}$. The free space wavelength in meters is λ_0. As defined in equation D.2, $\varepsilon_{\mathrm{eff}}$ is the effective dielectric constant, that can be expressed with the filling factor as:

$$\varepsilon_{\mathrm{eff}} = 1 + q_1(\varepsilon_{\mathrm{r1}} - \varepsilon_{\mathrm{r2}}) + q_2(\varepsilon_{\mathrm{r2}} - 1). \tag{D.13}$$

With equation D.3, we can express q_i by:

$$q_i = \frac{1}{2} \frac{K(k'_{hi})}{K(k_{hi})} \frac{K(k)}{K(k')} \tag{D.14}$$

The arguments of the complete elliptic integrals of the first kind are already given in equations D.5 and D.9.

Conductor losses: The attenuation constant α_c due to conductor loss is given by:

$$\alpha_c = \frac{R_{\mathrm{sm}} b^2}{16 Z_0 [K^2(\tilde{k})](b^2 - a^2)} \left\{ \frac{1}{a} \ln\left(\frac{2a\,(b-a)}{\Delta\,(b+a)} \right) + \frac{1}{b} \ln\left(\frac{2b\,(b-a)}{\Delta\,(b+a)} \right) \right\} \quad \mathrm{Np\,m^{-1}}. \tag{D.15}$$

The argument of complete elliptic integrals of the first kind is:

$$\tilde{k} = \frac{a}{b} \tag{D.16}$$

The surface resistance R_{sm} given by:

$$R_{sm} = \omega\mu t \,\mathrm{Imaginary}\left(\frac{\cot(k_c t) + \csc(k_c t)}{k_c t} \right) \quad \begin{cases} \mu = \mu_0 \mu_r & \text{for normal conductors,} \\ \mu = \mu_0 & \text{for superconductors.} \end{cases} \tag{D.17}$$

The permeability is $\mu = \mu_0 \mu_{\mathrm{r}}$, where $\mu_0 = 4\pi \cdot 10^{-7}\ \mathrm{H\,m^{-1}}$ is the magnetic permeability of free space and the relative permeability $\mu_{\mathrm{r}} \approx 1$ for gold. The angular frequency

$$\omega = 2\pi f, \tag{D.18}$$

is given via the frequency of operation f in cycles/s.

The complex wavenumber k_c is given by :

$$k_c = \omega\sqrt{\mu_0 \varepsilon_0}\sqrt{1 - j\frac{\sigma}{\omega\varepsilon_0}} \qquad \text{for normal conductors,} \tag{D.19}$$

$$k_c = \sqrt{\left(\frac{1}{\lambda_{\mathrm{p}}}\right)^2 + 2j\left(\frac{1}{\delta_{\mathrm{nf}}}\right)^2} \qquad \text{for superconductors.} \tag{D.20}$$

For the normal conducting metal the conductivity is σ, for the superonductor we have the magnetic penetration depth:

$$\lambda_{\mathrm{p}} = \sqrt{\frac{1}{\mu_0 \omega \sigma_2}}, \tag{D.21}$$

and normal fluid skin depth:

$$\delta_{\mathrm{nf}} = \sqrt{\frac{2}{\mu_0 \omega \sigma_1}}. \tag{D.22}$$

For the superconductor the complex conductivity is given as:

$$\tilde{\sigma} = \sigma_1 + j\sigma_2, \tag{D.23}$$

therefore σ_1 is the conductivity of the normal fluid, while σ_2 is the conductivity of the super fluid in the two-fluid model described in Section 3.1. Since λ_{p} is not determined in our measurements, we adopt values from literature.

D.3. Details on Superconducting Waveguides

Critical field measurements In the following we discuss the magnetic field dependent input return loss (RL) measurements of the SC-CPW shown on the top right of Figure B.1 operating in reflection configuration. The field measurements of the SC-CPW sample are presented in Figure D.2, with the left column corresponding to measurements at 5.8 K and the right column to measurements at 50 mK. The magnetic field sweeps are performed in the x, y, and z directions (first, second and third row). The data points are color-coded to match with the PLE and T_1 measurements discussed in Section 3.3 of the main text (red for 20 MHz, blue for 1 GHz, green for 2 GHz and additionally purple for 3 GHz). For better visualization, the data are offset in the y direction.

For all plots, it is evident that the RL at 20 MHz remains constant throughout the field sweeps, indicating a DC-like behavior and confirming the discussion in the main text regarding the frequency dependence of dissipated power in superconducting waveguides (see Section 3.1). In contrast, the behavior in the GHz regime differs between the two temperature regimes and also between the sweep directions. For the sweeps in x direction the RL mostly decreases with field strength at both temperatures to a very small extent. The sweeps in y direction are equivalent at both temperatures and show continuous increase in RL.

As explained in the main text (Section 3.3), the strong AC losses are likely due to magnetic flux penetrating the superconductor and the resulting formation of vortices. These vortices are locally normal-conducting and their movement leads to energy dissipation. This effect is pronounced for magnetic field oriented perpendicular to the film, i.e. in z-direction. Here, the strong applied field allows for the determination of the temperature dependent critical field at the elevated temperature of 5.8 K. The critical field B_{c2} is reached at approximately 1 T, indicated by the sharp increase in the input return loss. This value is already an order of magnitude higher than the field strengths used in the coherent control measurements discussed in the main text. At 50 mK, the critical magnetic field of niobium exceeds the maximum field strength achievable with the coils, which is limited to 1.33 T in the pure z direction. Consequently, we are unable to measure the critical field at such low temperatures, as the applied magnetic field remains insufficient to break the superconductivity.

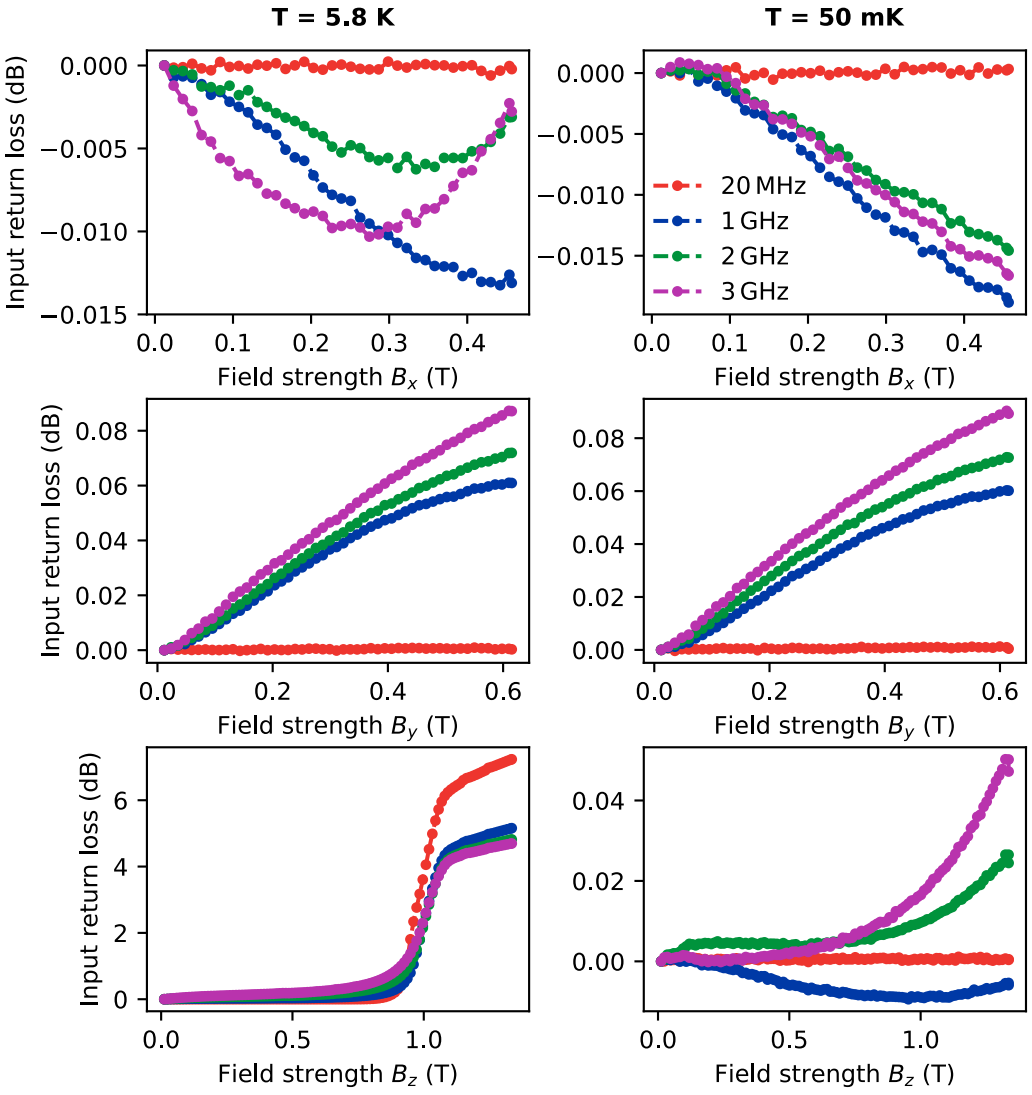

Figure D.2.: Field measurements of the SC-CPW sample at 5.8 K (left) and 50 mK (right). The rows show the magnetic field sweeps in x, y, and z direction, respectively. The data points are color-coded to match the PLE measurements and T_1 measurements of the main text and are offset in y. The critical field is reached at about 1 T at 5.8 K, as is visible by the sharp increase of the input return loss S11. The magnetic field coils are not strong enough to break the superconductivity at 50 mK.

E. Details on Measurements Techniques

E.1. Photoluminescence Excitation

For PLE measurements, the frequency of the resonant laser needs to be tuned across the resonance of the optical transitions. The C-WAVE supports mode-hop free tuning by varying the length of its internal reference cavity via an analog control voltage. This input voltage can be adjusted between 0 V and 100 V, allowing a continuous frequency shift of up to approximately 20 GHz.

As described in Figure C.1, the laser frequency is controlled via the ADwin-Pro II system. The analog output provides 16-bit resolution over an −10 V to 10 V range for its DAC. This output is connected to a piezo amplifier (E-836.1G, PI Ceramic GmbH) with a gain factor of 1:10, which in turn drives the internal piezo cavity of the laser. For high-resolution spectral scans, we use slow sweep rates of approximately 28 MHz s^{-1} (converted from voltage). During the sweep, the ADwin-Pro II simultaneously triggers both the wavemeter and the TimeTagger to synchronize data acquisition. The voltage sweep follows a sawtooth pattern, as illustrated in Figure E.1.

Due to occasional laser instabilities, such as brief power drops that cause the wavemeter to lose signal, the measured frequency trace may contain gaps or discontinuities. [1] To eliminate these artifacts, the wavemeter data is fitted with a second-order polynomial, which smooths the trace and interpolates missing points. The frequency data are then matched to the count-traces of the TimeTagger.

E.1.1. Angular Magnetic Field Sweeps

For the angular magnetic field sweeps, the magnetic field strengths in the laboratory frame needs to be converted into voltages first, that can be applied to the current sources via the ADwin Gold II system. The current sources convert the applied voltage linearly into current, i.e., a voltage of 1 V results in a current of 1 A through the magnetic coils. The coil calibration values, i.e., the field strength per ampere of current, are listed in Table C.1.

This voltage-conversion is implemented in Python. A custom script calculates the required voltages either in the laboratory frame or in the SnV frame. For the latter, three orthogonal

[1] Instabilities mostly arise from loud noise, causing the laser to lose its lock, and vibrations from walking or shutting doors around the lab.

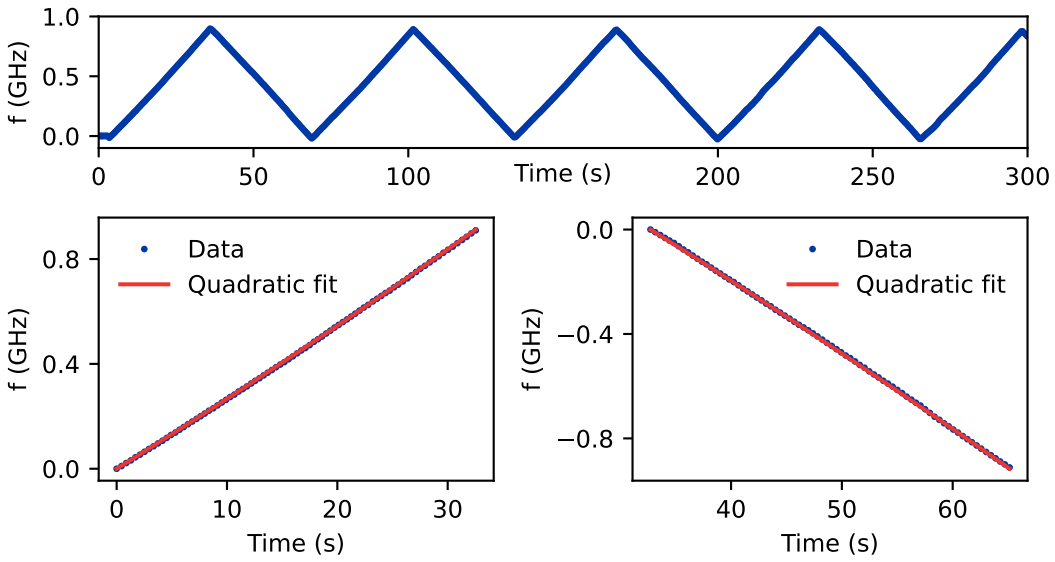

Figure E.1.: This figure shows raw wavemeter data of the laser frequency over time (top plot) and two exemplary quadratic fits (bottom plots) acquired during a PLE scan.

axes are first defined such that the SnV-z-axis aligns with the quantization axis of the SnV center. For the SnV-x and SnV-y axes, it is advantageous to define them such that their projections onto the xy-plane of the lab frame are aligned with either the lab x- or y-axis, respectively. [2] This is helpful to understand interactions, such as the angular dependence of the Rabi-frequency, discussed in Section 4.1.2, as this makes it easier to represent the corresponding vector components and symmetry dependencies, when rotating the magnetic field in the SnV-frame.

On the ADwin system, a background script runs continuously that determines the output voltages from the DAC. Through the Python interface, new bit values corresponding to the desired voltages can be sent, allowing for dynamic adjustment of the magnetic field without the need to first ramp down the coils. The voltages are then updated at a controlled rate of $\mathrm{d}V = 0.1\,\mathrm{V\,s^{-1}}$. The Python script monitors whether the new voltage values (and thus the corresponding magnetic field) have been applied. Once confirmed, it initiates the PLE measurement.

[2] In our experiment, we use square diamond membranes cut along the ⟨110⟩ directions and a (001) surface.

Bibliography

[1] I. Karapatzakis, J. Resch, M. Schrodin, P. Fuchs, M. Kieschnick, J. Heupel, L. Kussi, C. Sürgers, C. Popov, J. Meijer, C. Becher, W. Wernsdorfer, and D. Hunger, "Microwave control of the tin-vacancy spin qubit in diamond with a superconducting waveguide", Phys. Rev. X **14**, 031036 (2024).

[2] I. Karapatzakis and D. Hunger, "Supraleitende Mikrowellenkontrolle von Zinn-Fehlstellen", Physik in unserer Zeit **56**, 6–7 (2025).

[3] R. A. Millikan, "Radioactive substances and their radiations", Science **38**, 29–30 (1913).

[4] R. Yokota, "Color Centers of Quartz and Fused Quartz", J. Phys. Soc. Jpn. **7**, 222–223 (1952).

[5] K. Przibram, "Verfärbung und Lumineszenz durch Becquerelstrahlen V nebst verwandten Erscheinungen", Z. Phys. **130**, 269–292 (1951).

[6] R. K. Sheline, D. E. Sharp, and W. J. Arner, "Color Centers in Glass", J. Chem. Phys. **19**, 1422–1423 (1951).

[7] L. Pincherle, "Energy Levels of F-Centres", Proc. Phys. Soc. A **64**, 648 (1951).

[8] D. Clark C., D. R. William, and B. Dyer H., "The absorption spectra of irradiated diamonds after heat treatment", Proc. R. Soc. London A - Math. Phys. Sci. **237**, 75–89 (1956).

[9] G. Davies, S. C. Lawson, A. T. Collins, A. Mainwood, and S. J. Sharp, "Vacancy-related centers in diamond", Phys. Rev. B **46**, 13157–13170 (1992).

[10] N. B. Manson, X.-F. He, and P. T. H. Fisk, "Raman heterodyne detected electron-nuclear-double-resonance measurements of the nitrogen-vacancy center in diamond", Opt. Lett. **15**, 1094–1096 (1990).

[11] A. Lenef and S. C. Rand, "Electronic structure of the N-V center in diamond: Theory", Phys. Rev. B **53**, 13441–13455 (1996).

[12] N. B. Manson, X.-F. He, and P. T. H. Fisk, "Raman heterodyne studies of the nitrogen-vacancy centre in diamond", J. Lumin. **53**, 49–54 (1992).

[13] A. Gruber, A. Dräbenstedt, C. Tietz, L. Fleury, J. Wrachtrup, and C. von Borczyskowski, "Scanning Confocal Optical Microscopy and Magnetic Resonance on Single Defect Centers", Science **276**, 2012–2014 (1997).

[14] J. Wrachtrup, S. Y. Kilin, and A. P. Nizovtsev, "Quantum computation using the 13C nuclear spins near the single NV defect center in diamond", Opt. Spectrosc. **91**, 429–437 (2001).

[15] L. Childress, M. V. G. Dutt, J. M. Taylor, A. S. Zibrov, F. Jelezko, J. Wrachtrup, P. R. Hemmer, and M. D. Lukin, "Coherent dynamics of coupled electron and nuclear spin qubits in diamond", Science **314**, 281–285 (2006).

[16] T. Gaebel, M. Domhan, I. Popa, C. Wittmann, P. Neumann, F. Jelezko, J. R. Rabeau, N. Stavrias, A. D. Greentree, S. Prawer, et al., "Room-temperature coherent coupling of single spins in diamond", Nat. Phys. **2**, 408–413 (2006).

[17] S. Prawer and A. D. Greentree, "Diamond for Quantum Computing", Science **320**, 1601–1602 (2008).

[18] J. M. Taylor, P. Cappellaro, L. Childress, L. Jiang, D. Budker, P. R. Hemmer, A. Yacoby, R. Walsworth, and M. D. Lukin, "High-sensitivity diamond magnetometer with nanoscale resolution", Nat. Phys. **4**, 810–816 (2008).

[19] C. Hepp, T. Müller, V. Waselowski, J. N. Becker, B. Pingault, H. Sternschulte, D. Steinmüller-Nethl, A. Gali, J. R. Maze, M. Atatüre, and C. Becher, "Electronic structure of the silicon vacancy color center in diamond", Phys. Rev. Lett. **112**, 036405 (2014).

[20] T. Iwasaki, F. Ishibashi, Y. Miyamoto, Y. Doi, S. Kobayashi, T. Miyazaki, K. Tahara, K. D. Jahnke, L. J. Rogers, B. Naydenov, et al., "Germanium-Vacancy Single Color Centers in Diamond", Sci. Rep. **5**, 1–7 (2015).

[21] E. Neu, C. Hepp, M. Hauschild, S. Gsell, M. Fischer, H. Sternschulte, D. Steinmüller-Nethl, M. Schreck, and C. Becher, "Low-temperature investigations of single silicon vacancy colour centres in diamond", New Journal of Physics **15**, 043005 (2013).

[22] L. J. Rogers, K. D. Jahnke, T. Teraji, L. Marseglia, C. Müller, B. Naydenov, H. Schauffert, C. Kranz, J. Isoya, L. P. McGuinness, et al., "Multiple intrinsically identical single-photon emitters in the solid state", Nat. Commun. **5**, 1–6 (2014).

[23] A. Sipahigil, K. D. Jahnke, L. J. Rogers, T. Teraji, J. Isoya, A. S. Zibrov, F. Jelezko, and M. D. Lukin, "Indistinguishable Photons from Separated Silicon-Vacancy Centers in Diamond", Phys. Rev. Lett. **113**, 113602 (2014).

[24] H. Bernien, B. Hensen, W. Pfaff, G. Koolstra, M. S. Blok, L. Robledo, T. H. Taminiau, M. Markham, D. J. Twitchen, L. Childress, and R. Hanson, "Heralded entanglement between solid-state qubits separated by three metres", Nature **497**, 86–90 (2013).

[25] B. Hensen, H. Bernien, A. E. Dréau, A. Reiserer, N. Kalb, M. S. Blok, J. Ruitenberg, R. F. L. Vermeulen, R. N. Schouten, C. Abellán, W. Amaya, V. Pruneri, M. W. Mitchell, M. Markham, D. J. Twitchen, D. Elkouss, S. Wehner, T. H. Taminiau, and R. Hanson, "Loophole-free bell inequality violation using electron spins separated by 1.3 kilometres", Nature **526**, 682–686 (2015).

[26] N. Kalb, A. A. Reiserer, P. C. Humphreys, J. J. W. Bakermans, S. J. Kamerling, N. H. Nickerson, S. C. Benjamin, D. J. Twitchen, M. Markham, and R. Hanson, "Entanglement distillation between solid-state quantum network nodes", Science **356**, 928–932 (2017).

[27] P. C. Humphreys, N. Kalb, J. P. J. Morits, R. N. Schouten, R. F. L. Vermeulen, D. J. Twitchen, M. Markham, and R. Hanson, "Deterministic delivery of remote entanglement on a quantum network", Nature **558**, 268–273 (2018).

[28] M. Pompili, S. L. N. Hermans, S. Baier, H. K. C. Beukers, P. C. Humphreys, R. N. Schouten, R. F. L. Vermeulen, M. J. Tiggelman, L. dos Santos Martins, B. Dirkse, S. Wehner, and R. Hanson, "Realization of a multinode quantum network of remote solid-state qubits", Science **372**, 259–264 (2021).

[29] M. K. Bhaskar, R. Riedinger, B. Machielse, D. S. Levonian, C. T. Nguyen, E. N. Knall, H. Park, D. Englund, M. Lončar, D. D. Sukachev, and M. D. Lukin, "Experimental demonstration of memory-enhanced quantum communication", Nature **580**, 60–64 (2020).

[30] P.-J. Stas, Y. Q. Huan, B. Machielse, E. N. Knall, A. Suleymanzade, B. Pingault, M. Sutula, S. W. Ding, C. M. Knaut, D. R. Assumpcao, Y.-C. Wei, M. K. Bhaskar, R. Riedinger, D. D. Sukachev, H. Park, M. Lončar, D. S. Levonian, and M. D. Lukin, "Robust multi-qubit quantum network node with integrated error detection", Science **378**, 557–560 (2022).

[31] C. M. Knaut, A. Suleymanzade, Y.-C. Wei, D. R. Assumpcao, P.-J. Stas, Y. Q. Huan, B. Machielse, E. N. Knall, M. Sutula, G. Baranes, et al., "Entanglement of nanophotonic quantum memory nodes in a telecom network", Nature **629**, 573–578 (2024).

[32] C. Bradac, W. Gao, J. Forneris, M. E. Trusheim, and I. Aharonovich, "Quantum nanophotonics with group iv defects in diamond", Nature Communications **10**, 5625 (2019).

[33] L. J. Rogers, K. D. Jahnke, M. W. Doherty, A. Dietrich, L. P. McGuinness, C. Müller, T. Teraji, H. Sumiya, J. Isoya, N. B. Manson, et al., "Electronic structure of the negatively charged silicon-vacancy center in diamond", Phys. Rev. B **89**, 235101 (2014).

[34] C. Hepp, "Electronic structure of the silicon vacancy color center in diamond", PhD thesis (SciDok - Der Wissenschaftsserver der Universität des Saarlandes, 2014).

[35] K. D. Jahnke, A. Sipahigil, J. M. Binder, M. W. Doherty, M. Metsch, L. J. Rogers, N. B. Manson, M. D. Lukin, and F. Jelezko, "Electron–phonon processes of the silicon-vacancy centre in diamond", New Journal of Physics **17**, 043011 (2015).

[36] S. Meesala, Y.-I. Sohn, B. Pingault, L. Shao, H. A. Atikian, J. Holzgrafe, M. Gündo ğan, C. Stavrakas, A. Sipahigil, C. Chia, R. Evans, M. J. Burek, M. Zhang, L. Wu, J. L. Pacheco, J. Abraham, E. Bielejec, M. D. Lukin, M. Atatüre, and M. Lon čar, "Strain engineering of the silicon-vacancy center in diamond", Phys. Rev. B **97**, 205444 (2018).

[37] K. Kuruma, B. Pingault, C. Chia, M. Haas, G. D. Joe, D. R. Assumpcao, S. W. Ding, C. Jin, C. J. Xin, M. Yeh, et al., "Engineering Phonon-Qubit Interactions using Phononic Crystals", arXiv, `10.1038/s41567-024-02697-5` (2023).

[38] G. Thiering and A. Gali, "Ab initio magneto-optical spectrum of group-iv vacancy color centers in diamond", Phys. Rev. X **8**, 021063 (2018).

[39] J. C. Boschero, N. M. P. Neumann, W. van der Schoot, T. Sijpesteijn, and R. Wezeman, "Distributed Quantum Computing: Applications and Challenges", arXiv, 10.48550/arXiv.2410.00609 (2024).

[40] M. Caleffi, M. Amoretti, D. Ferrari, J. Illiano, A. Manzalini, and A. S. Cacciapuoti, "Distributed quantum computing: A survey", Comput. Networks **254**, 110672 (2024).

[41] D. Barral, F. J. Cardama, G. Díaz-Camacho, D. Faílde, I. F. Llovo, M. Mussa-Juane, J. Vázquez-Pérez, J. Villasuso, C. Piñeiro, N. Costas, et al., "Review of Distributed Quantum Computing: From single QPU to High Performance Quantum Computing", Computer Science Review **57**, 100747 (2025).

[42] M. Ruf, N. H. Wan, H. Choi, D. Englund, and R. Hanson, "Quantum networks based on color centers in diamond", J. Appl. Phys. **130**, 10.1063/5.0056534 (2021).

[43] F. Arute, K. Arya, R. Babbush, D. Bacon, J. C. Bardin, R. Barends, R. Biswas, S. Boixo, F. G. S. L. Brandao, D. A. Buell, et al., "Quantum supremacy using a programmable superconducting processor", Nature **574**, 505–510 (2019).

[44] V. Hassija, V. Chamola, A. Goyal, S. S. Kanhere, and N. Guizani, "Forthcoming applications of quantum computing: peeking into the future", IET Quantum Commun. **1**, 35–41 (2020).

[45] J. Preskill, "Quantum Computing in the NISQ era and beyond", Quantum **2**, 79 (2018).

[46] C. Monroe, R. Raussendorf, A. Ruthven, K. R. Brown, P. Maunz, L.-M. Duan, and J. Kim, "Large-scale modular quantum-computer architecture with atomic memory and photonic interconnects", Phys. Rev. A **89**, 022317 (2014).

[47] IBM Quantum, *Ibm quantum roadmap 2025*, Accessed: 2025-03-03, 2025.

[48] D. P. DiVincenzo, "The Physical Implementation of Quantum Computation", Fortschr. Phys. **48**, 771–783 (2000).

[49] M. Kjaergaard, M. E. Schwartz, J. Braumüller, P. Krantz, J. I.-J. Wang, S. Gustavsson, and W. D. Oliver, "Superconducting Qubits: Current State of Play", Annu. Rev. Condens. Matter Phys., 369–395 (2020).

[50] C. Wang, X. Li, H. Xu, Z. Li, J. Wang, Z. Yang, Z. Mi, X. Liang, T. Su, C. Yang, et al., "Towards practical quantum computers: transmon qubit with a lifetime approaching 0.5 milliseconds", npj Quantum Inf. **8**, 1–6 (2022).

[51] B. E. Kane, "A silicon-based nuclear spin quantum computer", Nature **393**, 133–137 (1998).

[52] A. Chatterjee, P. Stevenson, S. De Franceschi, A. Morello, N. P. de Leon, and F. Kuemmeth, "Semiconductor qubits in practice", Nat. Rev. Phys. **3**, 157–177 (2021).

[53] T. Koch, C. Godfrin, V. Adam, J. Ferrero, D. Schroller, N. Glaeser, S. Kubicek, R. Li, R. Loo, S. Massar, G. Simion, D. Wan, K. D. Greve, and W. Wernsdorfer, *Industrial 300 mm wafer processed spin qubits in natural silicon/silicon-germanium*, 2024.

[54] A. Zwerver, T. Krähenmann, T. Watson, L. Lampert, H. C. George, R. Pillarisetty, S. Bojarski, P. Amin, S. Amitonov, J. Boter, et al., "Qubits made by advanced semiconductor manufacturing", Nature Electronics **5**, 184–190 (2022).

[55] J. M. Pino, J. M. Dreiling, C. Figgatt, J. P. Gaebler, S. A. Moses, M. S. Allman, C. H. Baldwin, M. Foss-Feig, D. Hayes, K. Mayer, et al., "Demonstration of the trapped-ion quantum CCD computer architecture", Nature **592**, 209–213 (2021).

[56] C. D. Bruzewicz, J. Chiaverini, R. McConnell, and J. M. Sage, "Trapped-ion quantum computing: Progress and challenges", Appl. Phys. Rev. **6**, 10.1063/1.5088164 (2019).

[57] T. M. Graham, Y. Song, J. Scott, C. Poole, L. Phuttitarn, K. Jooya, P. Eichler, X. Jiang, A. Marra, B. Grinkemeyer, et al., "Multi-qubit entanglement and algorithms on a neutral-atom quantum computer", Nature **604**, 457–462 (2022).

[58] M. A. Nielsen and I. L. Chuang, *Quantum Computation and Quantum Information* (Cambridge university press, 2010).

[59] H. Edlbauer, J. Wang, T. Crozes, P. Perrier, S. Ouacel, C. Geffroy, G. Georgiou, E. Chatzikyriakou, A. Lacerda-Santos, X. Waintal, et al., "Semiconductor-based electron flying qubits: review on recent progress accelerated by numerical modelling", EPJ Quantum Technology **9**, 21 (2022).

[60] P. Magnard, S. Storz, P. Kurpiers, J. Schär, F. Marxer, J. Lütolf, T. Walter, J.-C. Besse, M. Gabureac, K. Reuer, et al., "Microwave Quantum Link between Superconducting Circuits Housed in Spatially Separated Cryogenic Systems", Phys. Rev. Lett. **125**, 260502 (2020).

[61] C. H. Bennett, G. Brassard, C. Crépeau, R. Jozsa, A. Peres, and W. K. Wootters, "Teleporting an unknown quantum state via dual classical and Einstein-Podolsky-Rosen channels", Phys. Rev. Lett. **70**, 1895–1899 (1993).

[62] S. D. Barrett and P. Kok, "Efficient high-fidelity quantum computation using matter qubits and linear optics", Phys. Rev. A **71**, 060310 (2005).

[63] G. Pieplow, C. G. Torun, J. H. D. Munns, F. M. Herrmann, A. Thies, T. Pregnolato, and T. Schröder, *Quantum electrometer for time-resolved material science at the atomic lattice scale*, 2024.

[64] L. De Santis, M. E. Trusheim, K. C. Chen, and D. R. Englund, "Investigation of the stark effect on a centrosymmetric quantum emitter in diamond", Phys. Rev. Lett. **127**, 147402 (2021).

[65] D. D. Sukachev, A. Sipahigil, C. T. Nguyen, M. K. Bhaskar, R. E. Evans, F. Jelezko, and M. D. Lukin, "Silicon-vacancy spin qubit in diamond: a quantum memory exceeding 10 ms with single-shot state readout", Phys. Rev. Lett. **119**, 223602 (2017).

[66] A. Faraon, P. E. Barclay, C. Santori, K.-M. C. Fu, and R. G. Beausoleil, "Resonant enhancement of the zero-phonon emission from a colour centre in a diamond cavity", Nat. Photonics **5**, 301–305 (2011).

[67] T. Iwasaki, Y. Miyamoto, T. Taniguchi, P. Siyushev, M. H. Metsch, F. Jelezko, and M. Hatano, "Tin-vacancy quantum emitters in diamond", Phys. Rev. Lett. **119**, 253601 (2017).

[68] Y. Narita, P. Wang, K. Ikeda, K. Oba, Y. Miyamoto, T. Taniguchi, S. Onoda, M. Hatano, and T. Iwasaki, "Multiple tin-vacancy centers in diamond with nearly identical photon frequency and linewidth", Phys. Rev. Appl. **19**, 024061 (2023).

[69] X. Guo, A. M. Stramma, Z. Li, W. G. Roth, B. Huang, Y. Jin, R. A. Parker, J. Arjona Martínez, N. Shofer, C. P. Michaels, C. P. Purser, M. H. Appel, E. M. Alexeev, T. Liu, A. C. Ferrari, D. D. Awschalom, N. Delegan, B. Pingault, G. Galli, F. J. Heremans, M. Atatüre, and A. A. High, "Microwave-based quantum control and coherence protection of tin-vacancy spin qubits in a strain-tuned diamond-membrane heterostructure", Phys. Rev. X **13**, 041037 (2023).

[70] E. I. Rosenthal, C. P. Anderson, H. C. Kleidermacher, A. J. Stein, H. Lee, J. Grzesik, G. Scuri, A. E. Rugar, D. Riedel, S. Aghaeimeibodi, G. H. Ahn, K. Van Gasse, and J. Vu čkovi ć, "Microwave spin control of a tin-vacancy qubit in diamond", Phys. Rev. X **13**, 031022 (2023).

[71] I. B. W. Harris and D. Englund, "Coherence of group-iv color centers", Physical Review B **109**, 085414 (2024).

[72] K. Senkalla, G. Genov, M. H. Metsch, P. Siyushev, and F. Jelezko, "Germanium vacancy in diamond quantum memory exceeding 20 ms", Phys. Rev. Lett. **132**, 026901 (2024).

[73] A. M. Stramma, "The tin-vacancy centre in diamond: a coherent spin-photon interface for quantum network nodes", PhD thesis (Apollo - University of Cambridge Repository, 2024).

[74] A. Sipahigil, R. E. Evans, D. D. Sukachev, M. J. Burek, J. Borregaard, M. K. Bhaskar, C. T. Nguyen, J. L. Pacheco, H. A. Atikian, C. Meuwly, et al., "An integrated diamond nanophotonics platform for quantum-optical networks", Science **354**, 847–850 (2016).

[75] M. K. Bhaskar, D. D. Sukachev, A. Sipahigil, R. E. Evans, M. J. Burek, C. T. Nguyen, L. J. Rogers, P. Siyushev, M. H. Metsch, H. Park, et al., "Quantum Nonlinear Optics with a Germanium-Vacancy Color Center in a Nanoscale Diamond Waveguide", Phys. Rev. Lett. **118**, 223603 (2017).

[76] M. E. Trusheim, B. Pingault, N. H. Wan, M. Gündoğan, L. De Santis, R. Debroux, D. Gangloff, C. Purser, K. C. Chen, M. Walsh, et al., "Transform-Limited Photons From a Coherent Tin-Vacancy Spin in Diamond", Phys. Rev. Lett. **124**, 023602 (2020).

[77] A. E. Rugar, S. Aghaeimeibodi, D. Riedel, C. Dory, H. Lu, P. J. McQuade, Z.-X. Shen, N. A. Melosh, and J. Vučković, "Quantum Photonic Interface for Tin-Vacancy Centers in Diamond", Phys. Rev. X **11**, 031021 (2021).

[78] P. Wang, T. Taniguchi, Y. Miyamoto, M. Hatano, and T. Iwasaki, "Low-temperature spectroscopic investigation of lead-vacancy centers in diamond fabricated by high-pressure and high-temperature treatment", ACS Photonics **8**, 2947–2954 (2021).

[79] M. W. Doherty, N. B. Manson, P. Delaney, F. Jelezko, J. Wrachtrup, and L. C. L. Hollenberg, "The nitrogen-vacancy colour centre in diamond", Phys. Rep. **528**, 1–45 (2013).

[80] I. P. Radko, M. Boll, N. M. Israelsen, N. Raatz, J. Meijer, F. Jelezko, U. L. Andersen, and A. Huck, "Determining the internal quantum efficiency of shallow-implanted nitrogen-vacancy defects in bulk diamond", Opt. Express **24**, 27715–27725 (2016).

[81] N. Kalb, P. C. Humphreys, J. J. Slim, and R. Hanson, "Dephasing mechanisms of diamond-based nuclear-spin memories for quantum networks", Phys. Rev. A **97**, 062330 (2018).

[82] M. Ruf, M. J. Weaver, S. B. van Dam, and R. Hanson, "Resonant Excitation and Purcell Enhancement of Coherent Nitrogen-Vacancy Centers Coupled to a Fabry-Perot Microcavity", Phys. Rev. Appl. **15**, 024049 (2021).

[83] L. J. Rogers, K. D. Jahnke, M. H. Metsch, A. Sipahigil, J. M. Binder, T. Teraji, H. Sumiya, J. Isoya, M. D. Lukin, P. Hemmer, and F. Jelezko, "All-optical initialization, readout, and coherent preparation of single silicon-vacancy spins in diamond", Physical Review Letters **113**, 263602 (2014).

[84] G. Pieplow, M. Belhassen, and T. Schröder, "Efficient microwave spin control of negatively charged group-iv color centers in diamond", Phys. Rev. B **109**, 115409 (2024).

[85] J. Görlitz, D. Herrmann, G. Thiering, P. Fuchs, M. Gandil, T. Iwasaki, T. Taniguchi, M. Kieschnick, J. Meijer, M. Hatano, A. Gali, and C. Becher, "Spectroscopic investigations of negatively charged tin-vacancy centres in diamond", New Journal of Physics **22**, 013048 (2020).

[86] J. Maze Rios, "Quantum manipulation of nitrogen-vacancy centers in diamond: From basic properties to applications", PhD thesis (Harvard University, Massachusetts, Jan. 2010).

[87] F. S. Ham, "Dynamical jahn-teller effect in paramagnetic resonance spectra: orbital reduction factors and partial quenching of spin-orbit interaction", Phys. Rev. **138**, A1727–A1740 (1965).

[88] M. Mohseni, L. Razinkovas, V. Žalandauskas, G. Thiering, and A. Gali, *Magneto-optical properties of group-iv–vacancy centers in diamond upon hydrostatic pressure*, 2024.

[89] M. H. Metsch, K. Senkalla, B. Tratzmiller, J. Scheuer, M. Kern, J. Achard, A. Tallaire, M. B. Plenio, P. Siyushev, and F. Jelezko, "Initialization and readout of nuclear spins via a negatively charged silicon-vacancy center in diamond", Phys. Rev. Lett. **122**, 190503 (2019).

[90] NIST Standard Reference Database 121, *Bohr magneton in hz/t*, online, `https://physics.nist.gov/cgi-bin/cuu/Value?mubshhz` Accessed: (28.02.2024).

[91] NIST Standard Reference Database 121, *Electron gyromagnetic ratio*, online, `https://physics.nist.gov/cgi-bin/cuu/Value?eqgammae` Accessed: (28.02.2024).

[92] J. Görlitz, D. Herrmann, P. Fuchs, T. Iwasaki, T. Taniguchi, D. Rogalla, D. Hardeman, P.-O. Colard, M. Markham, M. Hatano, and C. Becher, "Coherence of a charge stabilised tin-vacancy spin in diamond", npj Quantum Information **8**, 45 (2022).

[93] K. Ikeda, Y. Chen, P. Wang, Y. Miyamoto, T. Taniguchi, S. Onoda, M. Hatano, and T. Iwasaki, *Charge state transition of spectrally stabilized tin-vacancy centers in diamond*, 2024.

[94] R. E. Evans, A. Sipahigil, D. D. Sukachev, A. S. Zibrov, and M. D. Lukin, "Narrow-linewidth homogeneous optical emitters in diamond nanostructures via silicon ion implantation", Phys. Rev. Appl. **5**, 044010 (2016).

[95] P. Tamarat, T. Gaebel, J. R. Rabeau, M. Khan, A. D. Greentree, H. Wilson, L. C. L. Hollenberg, S. Prawer, P. Hemmer, F. Jelezko, and J. Wrachtrup, "Stark shift control of single optical centers in diamond", Phys. Rev. Lett. **97**, 083002 (2006).

[96] S. Aghaeimeibodi, D. Riedel, A. E. Rugar, C. Dory, and J. Vu čkovi ć, "Electrical tuning of tin-vacancy centers in diamond", Phys. Rev. Appl. **15**, 064010 (2021).

[97] T. Fließbach, *Elektrodynamik: lehrbuch zur theoretischen physik ii* (Springer-Verlag, 2022).

[98] Element Six, *Cvd diamond handbook*, `https://e6cvd.com/media/wysiwyg/pdf/E6_CVD_Diamond_Handbook_A5_v10X.pdf`, Element Six (Harwell, Oxfordshire, UK, 2020).

[99] E. I. Rosenthal, S. Biswas, G. Scuri, H. Lee, A. J. Stein, H. C. Kleidermacher, J. Grzesik, A. E. Rugar, S. Aghaeimeibodi, D. Riedel, M. Titze, E. S. Bielejec, J. Choi, C. P. Anderson, and J. Vu čkovi ć, "Single-shot readout and weak measurement of a tin-vacancy qubit in diamond", Phys. Rev. X **14**, 041008 (2024).

[100] M. H. Appel, A. Tiranov, A. Javadi, M. C. Löbl, Y. Wang, S. Scholz, A. D. Wieck, A. Ludwig, R. J. Warburton, and P. Lodahl, "Coherent spin-photon interface with waveguide induced cycling transitions", Phys. Rev. Lett. **126**, 013602 (2021).

[101] H.-P. Breuer and F. Petruccione, *The theory of open quantum systems /*, 1. publ., repr., Literaturangaben (Oxford Univ. Press, Oxford [u.a.] : 2003).

[102] D. Manzano, "A short introduction to the lindblad master equation", AIP Advances **10**, 025106 (2020).

[103] G. Bayer, R. Berghaus, S. Sachero, et al., "Optical driving, spin initialization and readout of single SiV^- centers in a fabry-perot resonator", Communications Physics **6**, 300 (2023).

[104] C. J. Foot, *Atomic physics*, Vol. 7, Oxford Master Series in Physics (Oxford University Press, Oxford, 2005), p. 344.

[105] C. Cohen-Tannoudji, B. Diu, and F. Laloë, *Quantenmechanik, band 2*, 5. Auflage, De Gruyter Studium (De Gruyter, 2019).

[106] R. N. Simons, *Coplanar waveguide circuits, components, and systems*, Available in both print (ISBN: 978-0-471-16121-9) and electronic (ISBN: 978-0-471-22475-4) formats. (John Wiley & Sons, Inc., New York, 2001).

[107] C. Wen, “Coplanar waveguide: a surface strip transmission line suitable for nonreciprocal gyromagnetic device applications”, IEEE Transactions on Microwave Theory and Techniques **17**, 1087–1090 (1969).

[108] M.-S. Kao and C.-F. Chang, *Understanding electromagnetic waves* (Springer, Cham, Switzerland, 2020).

[109] C. Veyres and V. F. Hanna, “Extension of the application of conformal mapping techniques to coplanar lines with finite dimensions”, International Journal of Electronics **48**, 47–56 (1980).

[110] S. M. Anlage, “Microwave superconductivity”, IEEE Journal of Microwaves **1**, 389–402 (2021).

[111] J. Rairden and C. Neugebauer, “Critical temperature of niobium and tantalum films”, Proceedings of the IEEE **52**, 1234–1238 (1964).

[112] S. A. Wolf, J. J. Kennedy, and M. Nisenoff, “Properties of superconducting rf sputtered ultrathin films of nb”, Journal of Vacuum Science and Technology **13**, 145–147 (1976).

[113] H. London, “The high-frequency resistance of superconducting tin”, Proceedings of the Royal Society of London. Series A. Mathematical and Physical Sciences **176**, 522–533 (1940).

[114] H. London, “Production of heat in supraconductors by alternating currents”, Nature **133**, 497–498 (1934).

[115] J. I. Gittleman and B. Rosenblum, “Microwave properties of superconductors”, Proc. IEEE (Inst. Elec. Electron. Engrs. **Vol: 52**, `10.1109/PROC.1964.3301` (1964).

[116] A. I. Gubin, K. S. Il’in, S. A. Vitusevich, M. Siegel, and N. Klein, “Dependence of magnetic penetration depth on the thickness of superconducting nb thin films”, Phys. Rev. B **72**, 064503 (2005).

[117] R. F. Wang, S. P. Zhao, G. H. Chen, and Q. S. Yang, “Absolute measurement of penetration depth in a superconducting film by the two-coil technique”, Applied Physics Letters **75**, Published 13 December 1999, 3865–3867 (1999).

[118] B. W. Maxfield and W. L. McLean, “Superconducting penetration depth of niobium”, Phys. Rev. **139**, A1515–A1522 (1965).

[119] H. Yamada, A. Meier, F. Mazzocchi, S. Schreck, and T. Scherer, “Dielectric properties of single crystalline diamond wafers with large area at microwave wavelengths”, Diamond and Related Materials **58**, 1–4 (2015).

[120] A. Tanwar, K. Gupta, P. Singh, et al., “Dielectric parameters and a.c. conductivity of pure and doped poly (methyl methacrylate) films at microwave frequencies”, Bulletin of Materials Science **29**, 397–401 (2006).

[121] D. B. Tuckerman, M. C. Hamilton, D. J. Reilly, R. Bai, G. A. Hernandez, J. M. Hornibrook, J. A. Sellers, and C. D. Ellis, “Flexible superconducting nb transmission lines on thin film polyimide for quantum computing applications”, Superconductor Science and Technology **29**, 084007 (2016).

[122] V. Hizhnyakov, H. Kaasik, and I. Sildos, "Zero-phonon lines: the effect of a strong softening of elastic springs in the excited state", physica status solidi (b) **234**, 644–653 (2002).

[123] V. Hizhnyakov, V. Boltrushko, H. Kaasik, and I. Sildos, "Phase relaxation in the vicinity of the dynamic instability: anomalous temperature dependence of zero-phonon line", Journal of Luminescence **107**, Proceedings of the 8th International Meeting on Hole Burning, Single Molecule, and Related Spectroscopies: Science and Applications, 351–358 (2004).

[124] C. Arend, J. N. Becker, H. Sternschulte, D. Steinmüller-Nethl, and C. Becher, "Photoluminescence excitation and spectral hole burning spectroscopy of silicon vacancy centers in diamond", Phys. Rev. B **94**, 045203 (2016).

[125] V. Sedov, K. Boldyrev, V. Krivobok, S. Nikolaev, A. Bolshakov, A. Khomich, A. Khomich, A. Krasilnikov, and V. Ralchenko, "Siv color centers in si-doped isotopically enriched 12c and 13c cvd diamonds", physica status solidi (a) **214**, 1700198 (2017).

[126] A. Razgulov, S. Lyapin, A. Novikov, and E. Ekimov, "Low-temperature photoluminescence study of gev centres in hpht diamond", Journal of Luminescence **242**, 118556 (2022).

[127] J.-W. Fan, I. Cojocaru, J. Becker, I. V. Fedotov, M. H. A. Alkahtani, A. Alajlan, S. Blakley, M. Rezaee, A. Lyamkina, Y. N. Palyanov, Y. M. Borzdov, Y.-P. Yang, A. Zheltikov, P. Hemmer, and A. V. Akimov, "Germanium-vacancy color center in diamond as a temperature sensor", ACS Photonics **5**, 765–770 (2018).

[128] A. Razgulov, S. Lyapin, A. Novikov, and E. Ekimov, "Low-temperature photoluminescence study of SnV centers in HPHT diamond", Diamond and Related Materials **116**, 108379 (2021).

[129] C. T. Nguyen, D. D. Sukachev, M. K. Bhaskar, B. Machielse, D. S. Levonian, E. N. Knall, P. Stroganov, C. Chia, M. J. Burek, R. Riedinger, H. Park, M. Lon čar, and M. D. Lukin, "An integrated nanophotonic quantum register based on silicon-vacancy spins in diamond", Phys. Rev. B **100**, 165428 (2019).

[130] R. Berman, F. E. Simon, and J. M. Ziman, "The thermal conductivity of diamond at low temperatures", Proceedings of the Royal Society of London. Series A, Mathematical and Physical Sciences **220**, 171–183 (1953).

[131] A. Yurgens, *Temperature distribution in large bi2212 mesas*, 2010.

[132] A. I. Krivchikov and A. Je.zowski, "Thermal conductivity of glasses and disordered crystals", arXiv: Disordered Systems and Neural Networks (2020).

[133] C. V. Raman, "The heat capacity of diamond between 0 and 1000° k", Proceedings of the Indian Academy of Sciences-Section A **46**, 323–332 (1957).

[134] W. DeSorbo, "Specific heat of diamond at low temperatures", The Journal of Chemical Physics **21**, 876–880 (1953).

[135] L. Evans, *Partial Differential Equations, Second edition*, Vol. 19 (American Mathematical Society, Mar. 2010).

[136] D. R. Poirier and G. H. Geiger, "Conduction of heat in solids", in *Transport phenomena in materials processing* (Springer International Publishing, Cham, 2016), pp. 281–327.

[137] D. K. Finnemore, T. F. Stromberg, and C. A. Swenson, "Superconducting Properties of High-Purity Niobium", Phys. Rev. **149**, 231–243 (1966).

[138] T. Matsushita et al., *Flux pinning in superconductors*, Vol. 164 (Springer, 2007).

[139] W. Buckel and R. Kleiner, *Supraleitung: grundlagen und anwendungen* (John Wiley & Sons, 2013).

[140] Y. B. Kim, C. F. Hempstead, and A. R. Strnad, "Flux-Flow Resistance in Type-II Superconductors", Phys. Rev. **139**, A1163–A1172 (1965).

[141] J. Bardeen and M. J. Stephen, "Theory of the Motion of Vortices in Superconductors", Phys. Rev. **140**, A1197–A1207 (1965).

[142] G. S. Park, C. E. Cunningham, B. Cabrera, and M. E. Huber, "Vortex pinning force in a superconducting niobium strip", Phys. Rev. Lett. **68**, 1920–1922 (1992).

[143] D. Janjušević, M. S. Grbić, M. Požek, A. Dulčić, D. Paar, B. Nebendahl, and T. Wagner, "Microwave response of thin niobium films under perpendicular static magnetic fields", Phys. Rev. B **74**, 104501 (2006).

[144] W. R. Hudson and R. J. Jirberg, *Superconducting properties of niobium films*, Vol. 6380 (National Aeronautics and Space Administration, 1971).

[145] R. Debroux, C. P. Michaels, C. M. Purser, N. Wan, M. E. Trusheim, J. Arjona Martínez, R. A. Parker, A. M. Stramma, K. C. Chen, L. de Santis, E. M. Alexeev, A. C. Ferrari, D. Englund, D. A. Gangloff, and M. Atatüre, "Quantum control of the tin-vacancy spin qubit in diamond", Phys. Rev. X **11**, 041041 (2021).

[146] R. A. Parker, J. Arjona Martínez, K. C. Chen, A. M. Stramma, I. B. Harris, C. P. Michaels, M. E. Trusheim, M. Hayhurst Appel, C. M. Purser, W. G. Roth, D. Englund, and M. Atatüre, "A diamond nanophotonic interface with an optically accessible deterministic electronuclear spin register", Nature Photonics **18**, 156–161 (2024).

[147] E. Knill, D. Leibfried, R. Reichle, J. Britton, R. B. Blakestad, J. D. Jost, C. Langer, R. Ozeri, S. Seidelin, and D. J. Wineland, "Randomized benchmarking of quantum gates", Phys. Rev. A **77**, 012307 (2008).

[148] R. de Sousa, "Electron spin as a spectrometer of nuclear spin noise and other fluctuations", in *Electron spin resonance and related phenomena in low-dimensional structures*, Vol. 115, edited by M. Fanciulli, Topics in Applied Physics (Springer, Berlin, Heidelberg, 2009), pp. 183–220.

[149] R. Hanson, V. V. Dobrovitski, A. E. Feiguin, O. Gywat, and D. D. Awschalom, "Coherent dynamics of a single spin interacting with an adjustable spin bath", Science **320**, 352–355 (2008).

[150] G. de Lange, Z. H. Wang, D. Ristè, V. V. Dobrovitski, and R. Hanson, "Universal dynamical decoupling of a single solid-state spin from a spin bath", Science **330**, 60–63 (2010).

[151] P. London, J. Scheuer, J.-M. Cai, I. Schwarz, A. Retzker, M. B. Plenio, M. Katagiri, T. Teraji, S. Koizumi, J. Isoya, R. Fischer, L. P. McGuinness, B. Naydenov, and F. Jelezko, "Detecting and polarizing nuclear spins with double resonance on a single electron spin", Phys. Rev. Lett. **111**, 067601 (2013).

[152] Ł. Cywiński, R. M. Lutchyn, C. P. Nave, and S. Das Sarma, "How to enhance dephasing time in superconducting qubits", Phys. Rev. B **77**, 174509 (2008).

[153] Z.-H. Wang, G. de Lange, D. Ristè, R. Hanson, and V. V. Dobrovitski, "Comparison of dynamical decoupling protocols for a nitrogen-vacancy center in diamond", Phys. Rev. B **85**, 155204 (2012).

[154] B. A. Myers, A. Das, M. C. Dartiailh, K. Ohno, D. D. Awschalom, and A. C. Bleszynski Jayich, "Probing surface noise with depth-calibrated spins in diamond", Phys. Rev. Lett. **113**, 027602 (2014).

[155] N. Bar-Gill, L. M. Pham, C. Belthangady, D. Le Sage, P. Cappellaro, J. R. Maze, M. D. Lukin, A. Yacoby, and R. Walsworth, "Suppression of spin-bath dynamics for improved coherence of multi-spin-qubit systems", Nature Communications **3**, 858 (2012).

[156] J. Medford, Ł. Cywiński, C. Barthel, C. M. Marcus, M. P. Hanson, and A. C. Gossard, "Scaling of dynamical decoupling for spin qubits", Phys. Rev. Lett. **108**, 086802 (2012).

[157] M. J. Biercuk and H. Bluhm, "Phenomenological study of decoherence in solid-state spin qubits due to nuclear spin diffusion", Phys. Rev. B **83**, 235316 (2011).

[158] K. J. Brown, E. Chartier, E. M. Sweet, D. A. Hopper, and L. C. Bassett, "Cleaning diamond surfaces using boiling acid treatment in a standard laboratory chemical hood", Journal of Chemical Health & Safety **26**, 40–44 (2019).

[159] J. Schaal, "Fabrication and characterization of superconducting coplanar waveguides for spin qubit control in diamond", Master's thesis (Karlsruhe Institute of Technology, 2024).

[160] A. Franzen, *Componentlibrary*, `https://www.gwoptics.org/ComponentLibrary/`, Licensed under Creative Commons Attribution-NonCommercial 3.0 Unported License, 2023.

[161] Qinu, *Qinu website*, Accessed: 2025-03-28, 2025.

[162] A. Zilz, "Investigation of the rarefied gas flow in the pumping tube of a ^{3}he/^{4}he dilution refrigerator", Master's thesis (Karlsruhe Institute of Technology, 2022).

[163] I. Wolff, *Coplanar microwave integrated circuits* (John Wiley & Sons, Inc., Hoboken, New Jersey, 2006).

[164] C. Holloway and E. Kuester, "A quasi-closed form expression for the conductor loss of cpw lines, with an investigation of edge shape effects", IEEE Transactions on Microwave Theory and Techniques **43**, 2695–2701 (1995).

[165] J. Booth and C. Holloway, "Conductor loss in superconducting planar structures: calculations and measurements", IEEE Transactions on Microwave Theory and Techniques **47**, 769–774 (1999).